UNSW
SYDNEY

Impacts of extreme events on the ocean thermal structure over the North West Shelf of Australia:

Part 1. The hydrodynamic drivers of the 2012/2013 marine heatwave;

and Part 2. Effects of tropical cyclones on the ocean thermal balance.

Anna Maggiorano

A thesis in fulfilment of the requirements for the degree of
Doctor of Philosophy

School of Science

The University of New South Wales, Canberra

October 2021

Thesis Title

Impacts of extreme events on the ocean thermal structure over the North West Shelf of Australia: Part 1. The hydrodynamic drivers of the 2012/2013 marine heatwave; and Part 2. Effects of tropical cyclones on the ocean thermal balance.

Thesis Abstract

The North West Shelf (NWS) of Australia is an ecologically sensitive region susceptible to extreme ocean and atmospheric events driven by large-scale and climate variability. This thesis investigates the drivers of the 2012/2013 strong marine heatwave (MHW) and how tropical cyclones (TCs) affect the temperature and energy of the ocean in the NWS region.

In part 1, a high-resolution regional numerical model based on the Regional Ocean Modelling System (ROMS) is implemented to simulate the variability of the upper ocean temperature and circulation in order to understand the mechanisms that drive the evolution of the 2012/2013 MHW. An upper ocean heat budget is used to quantify the roles of air-sea heat flux and ocean circulation in the development of extreme temperature anomalies over the continental shelf. Results indicate that during December 2012 an increase of net air-sea heat flux combined with positive horizontal advective heat flux anomaly led to development of the MHW. During the peak in January-February 2013 high-temperature anomalies were maintained by a combination of a decrease in negative heat advection and vertical mixing cooling and a decrease in net air-sea flux warming. The delayed onset of the 2012–2013 Australian monsoon resulted in alongshore wind anomalies on the NWS which in turn caused the advection and mixing anomalies.

Part 2 focuses on characterizing the changes produced by TCs over the NWS of Australia on the ocean structure and ocean thermal energy budget using a 20-year composite of cyclone data (1996-2016) created from Bluelink ReANalysis data (BRAN). The passage of a TC can have strong effects over a large area as the strong winds cause vertical mixing and upwelling through the water column near the TC core as well as downwelling in the periphery of the TC circulation. Cold temperature anomalies develop at the ocean surface beneath the TC core in response to strong mixing and deep upwelling driven by surface divergence and Ekman pumping. In the TC outer circulation surface cold anomalies also develop. However, in the subsurface warm temperature anomalies appear below the mixed layer due to wind-driven mixing across the mixed layer. In the month following the passage of the TC, the surface cold temperature anomalies recover relatively quickly due to air-sea fluxes, while the subsurface warm anomalies take longer to recover, mostly due to a reduction in mixing once the TC has left the region.

Different TC and ocean characteristics such as location with respect to the shelf edge, period of the year, intensity and translation speed, and the presence of a barrier layer are examined to assess their effects on thermal changes occurring in the ocean. Stronger cold anomalies develop at the surface over the shelf locations, over locations with a shallow or non-existent barrier layer, for strong TCs (category 3 or above on the Australian intensity category scale), and for slow-moving (< 4 m/s) TCs. The period of the year influences the recovery of the surface anomalies, which happens faster for TCs between December and February than for TCs that occur during or after March. The warm anomalies in the subsurface are stronger for more intense TCs and over locations with a shallow barrier layer as the vertical mixing processes are more efficient.

Ocean heat content (OHC) integrated heat through the water column is examined as a proxy for the energy exchange between the atmosphere and ocean during the TC passage. The processes that produce changes in OHC during and after the passage of the TC are separated into regions near the TC core, in the TC outer structure, and at different depths in the ocean during the passage and the subsequent 30-day recovery period. The OHC in the top 500 m of the region within 1000 km from the TC centre recovers more than 30 days after the passage of the TC. During the passage of the TC the majority of the OHC losses are located beneath the TC core and in the surface layer, while the OHC increases in the subsurface layer in the region between 500 and 1000 km from the TC centre. When the temperature anomalies start to recover, the OHC increases at a stronger rate in the surface layer due to the air-sea heat fluxes and in the TC core region where the strong upwelling relaxes to downwelling. Strong TCs produce an overall increase in the OHC within a month after the TC passage, while weak TCs of categories 1 and 2 cause an overall decrease in the OHC.

ORIGINALITY STATEMENT

☑ I hereby declare that this submission is my own work and to the best of my knowledge it contains no materials previously published or written by another person, or substantial proportions of material which have been accepted for the award of any other degree or diploma at UNSW or any other educational institution, except where due acknowledgement is made in the thesis. Any contribution made to the research by others, with whom I have worked at UNSW or elsewhere, is explicitly acknowledged in the thesis. I also declare that the intellectual content of this thesis is the product of my own work, except to the extent that assistance from others in the project's design and conception or in style, presentation and linguistic expression is acknowledged.

COPYRIGHT STATEMENT

☑ I hereby grant the University of New South Wales or its agents a non-exclusive licence to archive and to make available (including to members of the public) my thesis or dissertation in whole or part in the University libraries in all forms of media, now or here after known. I acknowledge that I retain all intellectual property rights which subsist in my thesis or dissertation, such as copyright and patent rights, subject to applicable law. I also retain the right to use all or part of my thesis or dissertation in future works (such as articles or books).

For any substantial portions of copyright material used in this thesis, written permission for use has been obtained, or the copyright material is removed from the final public version of the thesis.

AUTHENTICITY STATEMENT

☑ I certify that the Library deposit digital copy is a direct equivalent of the final officially approved version of my thesis.

UNSW is supportive of candidates publishing their research results during their candidature as detailed in the UNSW Thesis Examination Procedure.

Publications can be used in the candidate's thesis in lieu of a Chapter provided:

- The candidate contributed **greater than 50%** of the content in the publication and are the "primary author", i.e. they were responsible primarily for the planning, execution and preparation of the work for publication.
- The candidate has obtained approval to include the publication in their thesis in lieu of a Chapter from their Supervisor and Postgraduate Coordinator.
- The publication is not subject to any obligations or contractual agreements with a third party that would constrain its inclusion in the thesis.

☑ The candidate has declared that **some of the work described in their thesis has been published and has been documented in the relevant Chapters with acknowledgement**.

A short statement on where this work appears in the thesis and how this work is acknowledged within chapter/s:

> Part of my literature review, methodology and a result chapter is based the a published paper: Maggiorano, A., Feng, M., Wang, X. H., Ritchie, L., Stark, C., Colberg, F., & Greenwood, J. (2021). Hydrodynamic drivers of the 2013 marine heatwave on the North West Shelf of Australia. Journal of Geophysical Research: Oceans, 126(3), e2020JC016495.
> At the beginning of the relevant chapters the following statement has been added: Note: sections of this chapter are based on a published paper.
> Maggiorano, A., Feng, M., Wang, X. H., Ritchie, L., Stark, C., Colberg, F., & Greenwood, J. (2021). Hydrodynamic drivers of the 2013 marine heatwave on the North West Shelf of Australia. Journal of Geophysical Research: Oceans, 126(3), e2020JC016495.

Candidate's Declaration

I declare that I have complied with the Thesis Examination Procedure.

Abstract

The North West Shelf (NWS) of Australia is an ecologically sensitive region susceptible to extreme ocean and atmospheric events driven by large-scale and climate variability. This thesis investigates the drivers of the 2012/2013 strong marine heatwave (MHW) and how tropical cyclones (TCs) affect the temperature and energy of the ocean in the NWS region.

In part 1, a high-resolution regional numerical model based on the Regional Ocean Modelling System (ROMS) is implemented to simulate the variability of the upper ocean temperature and circulation in order to understand the mechanisms that drive the evolution of the 2012/2013 MHW. An upper ocean heat budget is used to quantify the roles of air-sea heat flux and ocean circulation in the development of extreme temperature anomalies over the continental shelf. Results indicate that during December 2012 an increase of net air-sea heat flux combined with positive horizontal advective heat flux anomaly led to development of the MHW. Despite a decrease in net air-sea flux warming, during the peak in January-February 2013 high-temperature anomalies were maintained by a combination of positive anomalies of heat advection and vertical mixing. The delayed onset of the 2012–2013 Australian monsoon resulted in alongshore wind anomalies on the NWS which in turn caused the advection and mixing anomalies.

Part 2 focuses on characterizing the changes produced by TCs over the NWS of Australia on the ocean structure and ocean thermal energy budget using a 20-year composite of cyclone data (1996-2016) created from Bluelink ReANalysis data (BRAN). The passage of a TC can have strong effects over a large area as the strong winds cause

vertical mixing and upwelling through the water column near the TC core as well as downwelling in the periphery of the TC circulation. Cold temperature anomalies develop at the ocean surface beneath the TC core in response to strong mixing and deep upwelling driven by surface divergence and Ekman pumping. In the TC outer circulation surface cold anomalies also develop. However, in the subsurface warm temperature anomalies appear below the mixed layer due to wind-driven mixing across the mixed layer. In the month following the passage of the TC, the surface cold temperature anomalies recover relatively quickly due to air-sea fluxes, while the subsurface warm anomalies take longer to recover, mostly due to a reduction in mixing once the TC has left the region.

Different TC and ocean characteristics such as location with respect to the shelf edge, period of the year, intensity and translation speed, and the presence of a barrier layer are examined to assess their effects on thermal changes occurring in the ocean. Stronger cold anomalies develop at the surface over the shelf locations, over locations with a shallow or non-existent barrier layer, for strong TCs (category 3 or above on the Australian intensity category scale), and for slow-moving (< 4 m/s) TCs. The period of the year influences the recovery of the surface anomalies, which happens faster for TCs between December and February than for TCs that occur during or after March. The warm anomalies in the subsurface are stronger for more intense TCs and over locations with a shallow barrier layer as the vertical mixing processes are more efficient.

Ocean heat content (OHC) integrated heat through the water column is examined as a proxy for the energy exchange between the atmosphere and ocean during the TC passage. The processes that produce changes in OHC during and after the passage of the TC are separated into regions near the TC core, in the TC outer structure, and at different

depths in the ocean during the passage and the subsequent 30-day recovery period. The OHC in the top 500 m of the region within 1000 km from the TC centre recovers more than 30 days after the passage of the TC. During the passage of the TC the majority of the OHC losses are located beneath the TC core and in the surface layer, while the OHC increases in the subsurface layer in the region between 500 and 1000 km from the TC centre. When the temperature anomalies start to recover, the OHC increases at a stronger rate in the surface layer due to the air-sea heat fluxes and in the TC core region where the strong upwelling relaxes to downwelling. Strong TCs produce an overall increase in the OHC within a month after the TC passage, while weak TCs of categories 1 and 2 cause an overall decrease in the OHC.

Acknowledgements

This work would never have been completed without the help and support of many people I met during my PhD journey, and I would like to express my sincere gratitude to them.

First of all, thanks to my supervisor Liz Ritchie, who supported me, taught me how to be a researcher and constantly inspired me with her great passion. Many thanks also to Clair Stark, who always encouraged and helped me giving me plenty of good advice whenever I needed it. Thanks to Scott Tyo who, despite joining the supervisory team at a late stage, gave me insightful suggestions for my work.

Many thanks go to Ming Feng and the exciting opportunity he gave me to work with his CSIRO group and the CSHOR project. Thanks also to Xiao Hua Wang, who helped me getting started on my PhD journey.

I want to offer my gratitude to Susan Wijffels and Robin Robertson for being my mentors and to all the participants to the voyage IN2019_V06 on the Research Vessel Investigator. It has been a truly inspiring experience from which I learned a lot.

I also deeply thank all my UNSW colleagues that were always ready to help and give suggestions. In particular Isabel Jalon Rojas and Yuwei Hu, who made the difference when I was stuck and have always been great friends for me, inside and outside the working environment. I also really want to thank my friend Mona Bahri, who during these years gave me tons of great suggestions which always proved right, always encouraged me during the hard times and has been a role model to follow.

I want to give special thanks to my partner Leo, who made these years in Australia an amazing adventure, always being there for me and having confidence in me

no matter what. Many thanks also to my family, who encouraged me and supported me through this journey.

Finally, I want to thank all the good friends I met in Australia, too many to name them all, who made these years a fantastic experience filled with awesome memories that I will treasure forever, and to the country that welcomed us and never failed to amaze me with its stunning natural beauty.

Publications during PhD study

Maggiorano, A., Feng, M., Wang, X. H., Ritchie, L., Stark, C., Colberg, F., & Greenwood, J. (2021). Hydrodynamic drivers of the 2013 marine heatwave on the North West Shelf of Australia. *Journal of Geophysical Research: Oceans*, 126(3), e2020JC016495.

Table of Contents

List of Figures

List of Tables

List of Abbreviations

ADCP – Acoustic Doppler Current Profiler

AUSMI – Australian Monsoon Index

BOM – Bureau Of Meteorology

BRAN – Bluelink ReANalysis

BT – Best Track

CARS – CSIRO Atlas for Regional Seas

CCI – Climate Change Initiative

ECMWF – European Centre for Medium-Range Weather Forecast

ENSO – El Niño Southern Oscillation

ESA – European Space Agency

ILD – Isothermal Layer Depth

IMOS – Integrated Marine Observing System

IOD – Indian Ocean Dipole

IPO – Interdecadal Pacific Oscillation

ITF – Indonesian Throughflow

MHW – Marine Heatwave

MJO – Madden-Julian Oscillation

ML – Mixed Layer

MLD – Mixed Layer Depth

MPI – Maximum Potential Intensity

NWS – North West Shelf

OHC – Ocean Heat Content

OFAM – Ocean Forecasting Australia Model

PDO – Pacific Decadal Oscillation

RMSE – Root Mean Square Error

SLP – Sea Level Pressure

SSH – Sea Surface Height

SSS – Sea Surface Salinity

SST – Sea Surface Temperature

TC – Tropical Cyclone

XBT – expendable bathythermograph

Chapter 1. Introduction

1.1 The context of this study

The Australian North West Shelf (NWS) is the region located between the North West Cape and Bonaparte Archipelago off the coast of Western Australia. The region is characterized by an unusual broad shallow shelf that extends on average 300 km from the coast and covers around 720,000 km^2 (Purcell and Purcell, 1988). The NWS is home to a unique environment with numerous coral reefs and other marine habitats and harbours a large variety of marine species including several protected species such as dugongs, turtles, and whale-sharks (Condie and Andrewartha, 2008). Furthermore, this region is one of the most economically relevant marine regions in Australia as it hosts a multi-billion oil and gas industry (North West Shelf Project; Acil Tasman Ltd, 2009; Government of Western Australia, Stastic Digest 2018-2019).

The ocean circulation off the coast of Western Australia differs from the equatorward currents usually found on the eastern boundary of subtropical oceans. It is mainly characterized by currents that carry warm, fresh tropical waters southward: the Holloway Current on the NWS; and the Leeuwin Current south of the North West Cape, in Fig. 1.1 (Feng et al., 2003; Thompson, 1984). The Holloway current is weaker and broader than the Leeuwin current and flows westward along the shelf boundary. The flow on the NWS is also influenced by flow that originates in the Pacific Ocean and arrives in the Indian Ocean through the Indonesian Archipelago (Clarke & Liu, 1994; Godfrey & Ridgway, 1985; Smith et al., 1991; Wijffels et al., 2007). Furthermore, the region is characterized by one of the strongest tidal flows on the

planet, which triggers the formation of internal waves at the edge of the shelf and drives ocean mixing (Egbert and Ray, 2000; Holloway, 1983).

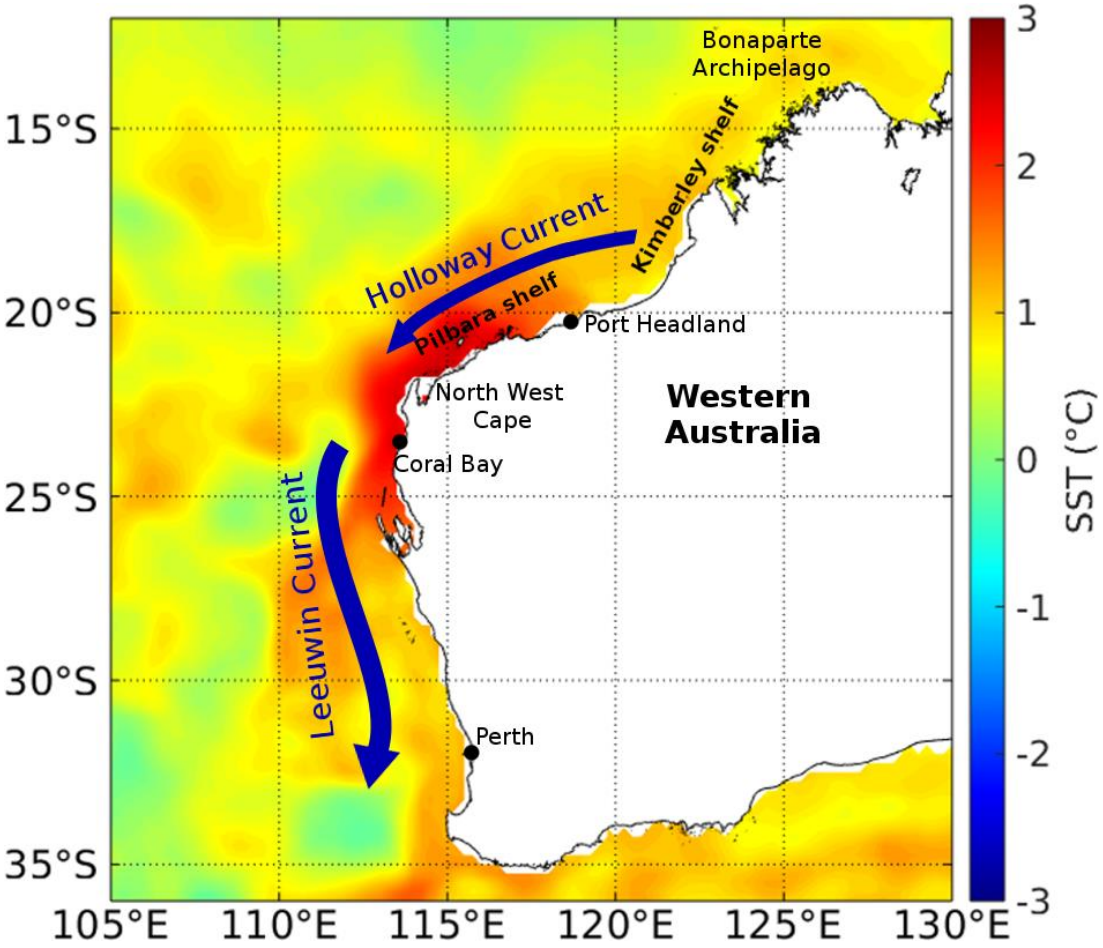

Figure 1.1: Area of interest, with the main currents and geographical locations indicated. SST anomalies during the peak of the MHW in January and February 2013 compared to a 30-year climatology (1987-2016) calculated with ERA 5 data are also shown.

The NWS region is influenced by several modes of climate variability, which affect the atmospheric and ocean circulations and can drive extreme ocean and atmospheric events. The atmospheric circulation over the NWS is strongly influenced

by the Australian monsoon, with easterly trade winds from April to October and westerly monsoonal winds between November and March (Godfrey and Ridgway, 1985; Suppiah, 1992). In the Indian Ocean the Indian Ocean Dipole (IOD) influences the sea surface temperature (SST) in the eastern part of the basin, which in turn affect the general atmospheric circulation over the NWS (Saji et al., 1999). The Madden-Julian Oscillation (MJO) is an intraseasonal variability mode in the atmosphere, which influences atmospheric convection in the tropics and drives signals that propagate down the NWS coast (Marin and Feng, 2019). Furthermore, the El Niño Southern Oscillation (ENSO) and the Pacific Decadal Oscillation (PDO) climate signals in the Pacific Ocean propagate via the Indonesian region to the NWS (Feng et al., 2015; Wijffels & Meyers, 2004).

The west coast of Australia is subject to marine heatwaves (MHWs), which occur when SSTs are warmer than the long term mean for an extended period of time (Feng et al., 2013; Hobday et al., 2016). MHWs can have strong effects on the ecology and economy of a region as they impact the fauna and flora and can lead to mass marine mortality events as reported by Garrabou et al. (2008) for the 2003 event in the Mediterranean, by Mills et al. (2013) for the 2012 event in the Atlantic and by Oliver et al. (2017) for the 2015/2016 event in the Tasman Sea. Strong MHWs during the Australian 2010/2011 and 2012/2013 summers have impacted the ecosystem along more than 2000 km on the NWS and in the southern part of the Australian West coast with coral bleaching and fish mortality (Caputi et al., 2015; Lafratta et al., 2017; Wemberg et al., 2012).

The frequency and intensity of these extreme events is projected to change in the future as the climate changes. Oliver et al. (2018) studied MHWs on a global scale

between 1925 and 2016, and reported that the frequency, duration and intensity of MHWs increased in recent years, with patterns of change that appear to be strictly connected with increasing ocean temperature. According to Frölicher et al. (2018), the probability of MHW events will increase in future years and MHWs will be more frequent and extreme.

The region is also affected by tropical cyclones (TCs) with several TCs forming and moving through the region each year (Dufois et al., 2018; Harper et al., 2008). These storms can impact and damage infrastructure and natural landscapes (Mendelsohn et al., 2012). On the NWS in particular, TCs disrupt the oil and gas industry as well as impact other infrastructure in the region causing significant economic losses. Strong TC-induced currents can produce storm surges and strong sediment resuspension on the shelf damaging the reefs and coastal environment and causing significant damage to the ecology (De'Ath et al., 2012; Dufois et al., 2018). TCs also impact the temperature and salinity of the ocean along their track and alter the ocean heat content (OHC) of a region for a period of several days to months after their passage (Parks et al 2001; Pasquero and Emanuel, 2007; Price et al, 2008). Strong vertical mixing due to the intense TC winds cools the surface of the water and warms the subsurface. While the SSTs restore to the climatological values within a few weeks, the anomalies in the subsurface can remain for longer periods and be transported out of the region, modifying the OHC of the whole ocean (Emanuel, 2001; Pasquero and Emanuel, 2007; Sriver and Huber, 2007).

TC activity is also projected to change as the climate changes because of ocean warming, sea-level rise and atmospheric circulation changes (Knutson et al., 2010). Webster et al. (2005) studied the changes on TC activity during a 35-year period and

reported an increase in the most intense storms. In the future the impact on TC activity could differ depending on the basin and the region considered, but in general there may be an increase in the frequency of high intensity storms and on the damage and economic losses from TC activity (Knutson et al., 2010; Mendelsohn et al., 2012; IPCC 2021). More recently, Kossin (2018) suggested that the translation speed of TCs in the future could be reduced as a result of a slower atmospheric circulation, and there could be more rainfall in the same location. In the Australian region Hassim and Walsh (2008) reported an increase of TC intensity and duration in the past three decades in Western Australia but not over the Australian east coast.

Given the extreme ecological sensitivity of the region, understanding extreme events such as MHWs and TCs and their impacts in the region, is important for understanding, monitoring and mitigating their impacts into the future. The purpose of this study is to investigate the physical processes that caused a strong MHW to develop on the NWS during the summer of 2012/2013 and more generally how TCs affect the temperature and energy budget of the ocean in the NWS region.

The 2012/2013 MHW resulted in unusually high SST anomalies during January and February 2013 of greater than 3°C that were mostly confined northeast of the North West Cape in the south-western region of the NWS (Fig. 1.1) (Xu et al., 2018). The MHW caused coral bleaching and other significant ecological impacts (Feng et al. 2015; Xu et al., 2018), stressing the importance of understanding the driving mechanisms behind the evolution of this strong MHW event. Two strong cyclones influenced the ocean temperature and its changes during the summer 2012/2013 MHW: Narelle, which passed offshore parallel to the shelf in the middle of January, and Rusty, which moved towards the coast at the end of February (Dufois

et al., 2017, 2018; Smith et al. 2015). Both cyclones reached category 4 intensity and produced strong currents and temperature responses in the ocean that could have impacted the ecology of the region (Dufois et al., 2017, 2018) as well as the development and decay of the MHW. Because of the importance of these two TCs in potentially driving the MHW evolution, it is also important to put them in the context of the general impact of TCs on the ocean temperature and currents in the NWS region. Understanding these processes is of crucial importance to be able to project their impacts in a changing climate and to protect the environment and the infrastructure of this unique and sensitive region.

1.2 The objectives and the structure of the thesis

This thesis is divided in two parts. Part 1 studies the drivers of the strong 2012/2013 MHW and Part 2 contains a discussion on how TCs affect the temperature and energy budget of the ocean in the NWS region.

I have three main objectives in this thesis:

(1) to study the physical processes that caused the development of a strong MHW during the 2012/2013 summer on the NWS of Australia.

(2) Study the general impact of TCs on the ocean temperature and the factors that influence the ocean response to TCs in the NWS region.

(3) Study the ocean energy changes driven by TCs in the NWS region.

The thesis is structured as follows. The introduction is provided in Chapter 1. Chapter 2 provides a discussion of previous research on the NWS ocean circulation, MHWs and the impact of TCs on ocean structure. The methodology and data used in this study are provided in Chapter 3. Chapter 4 provides the analysis and results of the 2012/2013 MHW investigation. Chapter 5 provides a composite analysis of how TCs affect the ocean temperature and currents using 20 years of TCs in the NWS region. The study on how the ocean energy changes following the passage of a TC on the NWS region is provided in Chapter 6. Finally, a summary and conclusions along with potential future work is presented in Chapter 7.

Chapter 2. Background

Note: sections of this chapter are based on a published paper.

Maggiorano, A., Feng, M., Wang, X. H., Ritchie, L., Stark, C., Colberg, F., & Greenwood, J. (2021). Hydrodynamic drivers of the 2013 marine heatwave on the North West Shelf of Australia. *Journal of Geophysical Research: Oceans*, 126(3), e2020JC016495.

2.1 The NWS ocean circulation

The ocean circulation off the coast of Western Australia is characterized by the presence of a poleward current, called the Leeuwin current, in the region south of the North West Cape, and the Holloway current on the NWS (Fig. 1.1).

South of the North West Cape, the Leeuwin current (Fig. 1.1) is a narrow poleward surface flow, which is relatively warm and composed of lower salinity water compared to the surrounding waters (Thompson, 1984). It carries tropical waters southward along the west coast of Western Australia and causes the SST in the region to be warmer than temperatures at corresponding latitudes in other basins (Thompson, 1984; Feng et al., 2003). The Leeuwin current is driven by the large north-south pressure gradient present along the Australian west coast and flows against a prevailing equatorward wind (Godfrey and Ridgway, 1985; Smith et al., 1991; Thompson, 1984). Even though the wind is not the driving force of the currents along the west coast of Australia, it influences the currents' strength and their annual cycle (Feng et al., 2003; Smith et al., 1991). In fact, due to the wind pattern in the Indian

Ocean, which is strongly modulated by the Indo-Australian Monsoon, this current is stronger during the Australian autumn and winter and weaker during the Australian spring and summer (Feng et al., 2003). Furthermore, the strength of the Leeuwin current varies inter-annually with ENSO and is stronger during La Niña and weaker during El Niño years (Feng et al., 2003).

The NWS is characterized by a wide shelf which is divided into the Kimberly Shelf in the north and the Pilbara shelf in the south (Fig. 1.1), in the region just north of the North West Cape. Holloway and Nye (1985) analysed 19 months of current data collected in 1982-1983 in the Pilbara Shelf region and reported an evident south-westward flow, which was especially strong between February and July. This flow was more recently named the Holloway current by D'Adamo et al. (2009), in Fig. 1.1. The Holloway current appears to be driven from a steric high gradient in opposition to the wind stress, with a similar mechanism as already reported for the Leeuwin current south of North West Cape by Godfrey and Ridgway (1985), but compared to the Leeuwin current the Holloway current flow is weaker and broader (Cresswell et al., 1993; Holloway, 1995).

More recently, a study of the Holloway current using IMOS mooring data showed the presence of a south-eastward flow all year round, with an annual mean transport of 1 Sv and a peak of 2 Sv during the Australian autumn, connected to the weakening of the Australian summer monsoon, which allows the accumulated water to flow southward (Bahmanpour et al., 2016). According to Bahmanpour, et al. (2016), the mooring station closer to the coast showed that alongshore currents follow the reversal of the winds over the region. In fact, the westerly winds during summer drive

upwelling favourable north-eastward alongshore surface currents, bringing cold water over the shelf (Condie & Adrewartha, 2008).

The sea level in the NWS region appears to differ from the sea level changes in the central Indian Ocean, but to be strictly connected to the sea level changes arriving from the Pacific, which is propagated by Kelvin and Rossby waves, with a strong interannual variability connected with ENSO (Clarke and Liu, 1994; Wijffels and Meyers, 2004). Rossby waves interacting with coastally trapped Kelvin waves propagating poleward along the coast of the NWS appear to also drive a semi-annual and intraseasonal fluctuation of the Holloway current, which appears to be influenced by the variation in atmospheric convection driven by the MJO (Marin et al., 2019; Marshall and Hendon, 2014). Moreover, Wyrtki (1987) studied the sea level differences between the two oceans, finding that the signal is connected with the monsoon seasonal variability and the gradient is stronger in July and August and weaker in January and February.

The ocean currents in the northern part of the NWS are directly connected with the Indonesian throughflow (ITF), which is the flow of water that arrives into the Indian Ocean from the Pacific Ocean through the Lombok, Ombai, and Timor straits (Wijffels et al., 2008). There are two major remote northern sources for the warm low salinity flow in the Indonesian Australian basin. The first source of warm water is Pacific Ocean water that comes from the South East Asian seas, while the second source is the tropical Indian Ocean water that is carried into the basin by the South Java current (D'Adamo et al., 2009). The flow between the Pacific and the Indian Oceans develops as a pressure gradient between the western Pacific and the eastern Indian Ocean is established due to the presence of trade winds that cause an increase

in the sea level at the western boundary of the Pacific Ocean and a corresponding decrease at the eastern boundary of the Indian Ocean (Wyrtki, 1987). The ITF transport is influenced by monsoon winds and it is stronger during the Australian winter (south-east monsoon) and weaker during the Australian summer (north-west monsoon) (Meyers et al., 1995; Sprintall et al., 2009, Wyrtki, 1987). The pathways of these currents and the ways in which their water is conveyed into the Leeuwin current was investigated by Domingues et al. (2007) using a particle tracking model and by Wijeratne et al. (2018) using a comparison between a numerical model and observations. The ITF is found to be strongly connected with ENSO events, which also influence the transport between different passages, and its transport is stronger during La Niña (Wijeratne et al., 2018).

The NWS of Australia is also characterized by strong tides and is one of the regions of major tidal energy dissipation on the globe (Egbert and Ray, 2000). The interaction of strong barotropic tidal currents with the shelf slope in presence of density stratification produces internal waves of tidal frequency whose energy can propagate onshore and dissipate on the continental shelf or can propagate offshore and dissipate in the deep ocean. This phenomenon was first observed and studied on the NWS in a location off from Dampier by Holloway, (1983), who described the characteristics of the semidiurnal internal tides on the shelf and noticed that the spring-neap tide cycle was not well defined in the region, suggesting a formation of internal tide in deep water over a large section of the shelf. Moreover, semidiurnal internal tides in the region appear to be influenced by the seasonal cycle, having a maximum amplitude in January, when the water is more stratified, and presenting a decay in amplitude between April and June as the stratification decreases (Holloway, 1984;

Van Gastel et al., 2009). Rayson et al. (2021) argued that internal tides on the NWS could be subjected to significant interannual variability and that there is a strong variability between different site locations, however they also noted a decrease in the semidiurnal internal tide around October, connected with the ITF seasonal variability. In more recent years, different numerical models have been developed to study the semidiurnal internal tides on the NWS of Australia and to assess the energy flux connected with them. In particular, Holloway (2001) estimated how the energy is transferred from the barotropic tide to the baroclinic tide and suggested that the energy dissipated by the baroclinic mode is very important for the mixing in the deep ocean. The connection of strong tides on the NWS of Australia with the mixing of the water column were further analysed by Katsumata, (2006), who suggested that the tidal mixing is responsible for the heating and cooling of the ocean up to a few degrees on a monthly scale.

2.2 Marine heatwaves and the Ningaloo Niño

MHWs often develop on the NWS of Australia, with an increase of frequency in recent years (Feng et al., 2013). Hobday et al. (2016) defined a MHW as a "prolonged discrete anomalously warm water event that can be described by its duration, intensity rate of evolution and spatial extent". They quantified the heatwaves based on the calculation of a 90^{th} percentile temperature threshold using 30 years of climatology data. Moreover, the categorization of MHWs based on the intensity was then specified by Hobday et al. (2018), according to how many times the difference between the 90^{th} percentile threshold and the climatology temperature data has been

overcome during the event. A global analysis of MHW between 1950 to 2016 (Holbrook et al., 2019), suggested there had been an increase of events reported over the years and studied the connections between the development of MHWs and their drivers for different regions globally. Furthermore, MHWs are often reported and studied just in the top layer of the ocean due to the higher availability of data; however, in some cases MHWs have been reported to extend below the mixed layer (ML) (Benthuysen et al., 2018; Schaeffer and Roughan, 2017). MHWs in some cases can last for a very long time. For example, the 2014/2015 MHW in the North Pacific Ocean lasted for more than a year and the 2015/2016 MHW in the Tasman Sea lasted for 251 days (Di Lorenzo and Mantua, 2016; Oliver et al., 2017).

Off the coast of Western Australia, the major SST variability mode of the coast is referred to as Ningaloo Niño and is a key driver of MHWs in the region. A positive Ningaloo Niño is associated with anomalously warm SSTs extending off the western Australian coast between approximately 22 and 32°S (Kataoka et al., 2014). A typical Ningaloo Niño event usually starts to develop in September-October and peaks in the middle of the Australian summer in January-February (Feng et al., 2013; Kataoka et al., 2014, 2018; Marshall et al., 2015).

Marshall et al. (2015) analysed the evolution of Ningaloo Niños for a 50-year period and found that during their development an anomalous atmospheric cyclonic circulation develops over the NWS, which decreases the wind speed along the coast. The anomalous northerly surface winds trigger two main processes that lead to the development of the phenomena: a reduction in evaporation and latent heat loss, which enhances warming; and an increase in the Leeuwin Current advection that drives the positive SST anomalies further south (Marshall et al., 2015). However, the positive

feedback on SST caused by heat loss reduction due to the lower wind speed (Marshall et al., 2015) was opposed by Tozuka & Oettli (2018), who argued that the increase of SST and reduced wind speed trigger a negative feedback. In fact, according to Tozuka & Oettli (2018), the increase of SST and reduced wind speed enhance convection and cloud formation and reduce shortwave radiation over the region.

Kataoka et al. (2014; 2017) studied the development of Ningaloo Niño and identified two modes: a locally amplified mode and a non-locally amplified mode, which are connected to the presence or absence, respectively, of positive northerly wind anomalies over the coastal region that causes downwelling. According to Kataoka et al. (2014), in the locally amplified mode the SST warm anomalies off the west coast of Australia produce low sea level pressure in the overlying atmosphere, which triggers northerly wind anomalies along the coast that cause anomalous downwelling. The non-locally amplified case mostly co-occurs during La Niña conditions in the Pacific Ocean, which forces positive sea surface height (SSH) and SST anomalies in the tropics, then the SSH anomalies, along with warmer SSTs, propagate south through coastal Kelvin waves (Kataoka et al., 2014; Kusunoki et al., 2020). Another difference reported by Kataoka et al. (2014) that distinguishes the locally amplified mode from the non-locally amplified mode is the presence of positive sea level pressure (SLP) anomalies over the Australian continent, which are present only in the locally amplified case.

Modes of climate variability, such as ENSO, the IOD, the MJO, the PDO or the Interdecadal Pacific Oscillation (IPO), can drive MHWs in the region (Holbrook et al., 2019). Zhang et al. (2018) studied the mechanisms involved in the generation of Ningaloo Niños and found out that approximately 40% of the cases were correlated

with the presence of La Niña in the Pacific, in 30% of the cases it was correlated with the positive phase of the IOD, and in the other 30% other phenomena such as MJO or the Australian monsoon might have triggered the development of the MHW.

La Niña conditions in the Pacific Ocean that enhance the Leeuwin current and the advection of warm water southward, could trigger a Ningaloo Niño event (Feng et al. 2015). The connection between La Niña and the development of a MHW along the west coast of Australia was used by Doi et al. (2013) to predict the development of the Ningaloo Niño a few months in advance using a numerical model. On the other hand, the possibility that a Ningaloo Niño could develop without the presence of La Niña conditions was further shown by Kataoka et al. (2018), who ran a general circulation model with suppressed ENSO, and reported almost no changes in the development of marine heat waves in the region, meaning that La Niña is not a necessary condition for the development of a Ningaloo Niño off the south coast of Western Australia. Furthermore, a study by Zhang et al. (2017), who considered a broader region of the eastern Indian Ocean suggested that both polarities of ENSO could drive MHWs at different latitudes: El Niño drives weak positive SST anomalies in the tropical region; while La Niña drives stronger SST anomalies further south.

The suppressed phase of the MJO can influence the development of a Ningaloo Niño as it modulates the wind stress over the region affecting the shortwave and latent heat fluxes (Marshall and Hendon, 2014). In the northern part of the NWS MHWs mostly peak during phase 2-5 of the MJO while in the southern part of the Australian west coast the peak is delayed and mostly occurs during phase 3-6 of the MJO (Zhang et al., 2017).

A positive IOD event during the previous Australian winter may also contribute to the development of a Ningaloo Niño event in the following summer as it induces easterly anomalies over the equatorial Indian Ocean and anticyclonic wind anomalies over the southern Indian Ocean. This, in turn, induces cyclonic anomalies off the NWS and northerly wind anomalies over the NWS that could initiate the warming in the months before the MHW peak (Zhang et al., 2018).

Furthermore, an increase in ocean temperatures and in the frequency of these events off the coast of Western Australia has been observed since the late 1990s, related to the shift to the negative phase of the PDO (Feng et al., 2015). In fact, the negative phase of the PDO causes a heat modulation of the ITF and cyclonic wind anomalies, which are related to an enhancement in the poleward transport along the coast (Feng et al., 2015; Pearce and Feng, 2007).

A very strong MHW connected with La Niña was observed along the west coast of Australia in the summer of 2010/2011 (Benthuysen et al., 2014; Pearce and Feng, 2013; Xu et al., 2018). The first analysis of the development of this phenomenon with in situ mooring stations and satellite-based SST data was conducted by Pearce and Feng (2013). They studied the SST anomalies with respect to the climatology in a wide area, which extended from the North West Cape to Cape Leeuwin, and from the coast to 200 km offshore. The reported SST anomalies were up to 3°C, especially concentrated in the surface warm layer (Pearce and Feng, 2013). Furthermore, this phenomenon also had important consequences for the ecosystem and marine biota with coral bleaching and tropical fish moving to unusually southern waters (Pearce and Feng, 2013). Benthuysen et al. (2014) studied the dynamics of the 2010/2011 Ningaloo Niño event with a numerical model and calculated the heat budget of the

region in order to determine the mechanisms responsible for the extreme SSTs; they found out that anomalous southward advection due to a stronger Leeuwin current was the cause of the warming.

Another important Ningaloo Niño event occurred in the summer of 2012/2013 (Feng et al., 2015; Xu et al., 2018). The difference between this event and the 2010/2011 MHW was highlighted in Xu et al., (2018). In particular, the regions where the extreme high SSTs were observed differ between the two events. In 2010/2011 the MHW extended further south in a broader region along the West Coast of Australia whereas in 2012/2013 it remained confined in a smaller region just north of the North West Cape, as shown in Fig. 1.1 (Xu et al., 2018). Furthermore, a survey conducted by Lafratta et al. (2017) in March 2017 found that most of the corals near Onslow, in the NWS where the 2012/2013 MHW peaked, were bleached, possibly due to the thermal stress caused by the MHW.

Dufois et al. 2018 noted an increase in TC activity on the NWS during three consecutive Ningaloo Niño years (2011-2012-2013) and hypothesised that higher SSTs caused by a Ningaloo Niño event could cause an increase in TCs' development over the region. During summer 2012/2013 two TCs developed and moved through the NWS. Narelle developed during a monsoon trough at the beginning of January north of Timor and moved southward offshore along the shelf while Rusty developed at the end of February and had a perpendicular trajectory towards the coast (Dufois et al., 2017, 2018; Smith et al., 2015).

2.3 Tropical cyclone effects on the ocean

The tropical regions of Australia and the NWS in particular, are often impacted by TC activity (Dufois et al., 2018; Harper et al., 2008). TCs and their associated strong winds induce strong dynamical responses in the ocean, driving strong surface currents (Price et al., 1994). In the ML strong, near-inertial currents develop after the passage of a TC and can remain for many days, driving upwelling and mixing (Price, 1981; Price et al., 1994; Shay & Elseberry, 1987), The processes are illustrated in the schematic in Fig. 2.1. Furthermore, TCs usually drive a strong temperature response in the ocean, with significant cooling at the sea surface, known as the "cold wake", and warming below the ML on each side of the TC track (Cheng et al., 2015; Price, 1981).

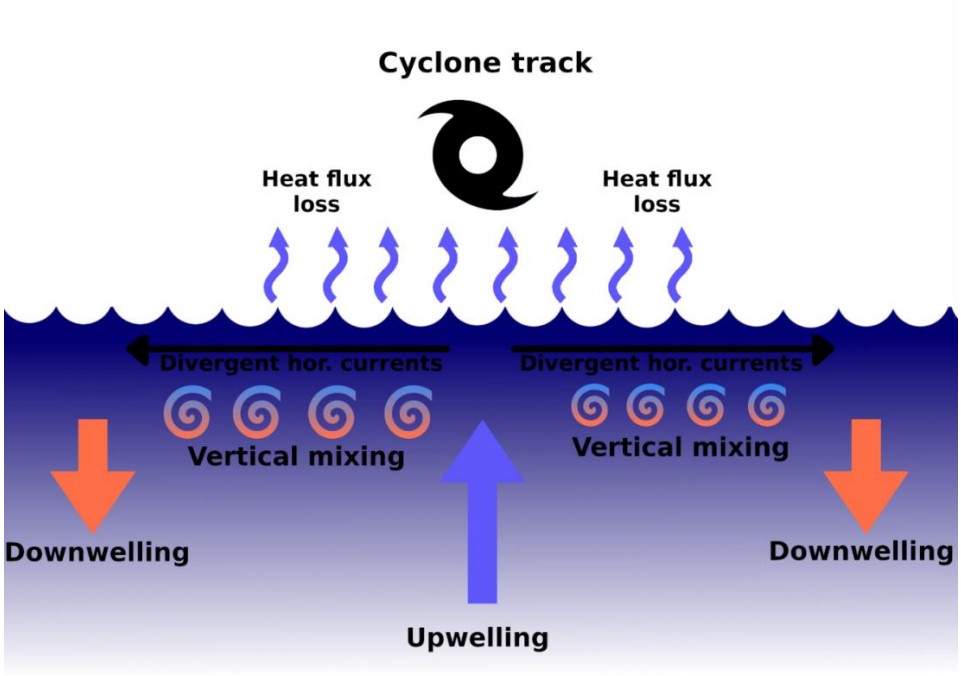

Figure 2.1: Schematic of the processes happening in the ocean during a TC passage. The arrows indicate current movements and the colours the effect on the ocean temperature (orange indicates warming, blue indicates cooling).

As explained by Ginis (2002) the dynamic response of the ocean to a TC is dominated by two modes: a barotropic mode associated with displacement of the sea surface and a baroclinic mode, which is associated with displacements of the interface between the ML and the subsurface layer. The barotropic mode is geostrophically adjusted and produces a circulation pattern stretched in the along-track direction, while the baroclinic response in associated with a near-inertial oscillating wake (Ginis, 2002; Price et al., 1983).

The circular wind stress pattern of a TC produces divergent currents at the surface of the ocean, which force an upward movement of the water below and lift the isotherm under the TC track (Ginis, 2002; Price, 1981; Price et al., 1983, 1994), Fig. 2.1. The intensity of this upward motion strongly depends on the Froude Number *Fr*:

$$Fr = \frac{Uh}{Cn} \tag{2.1}$$

where *Uh* is the translation speed of the storm and *Cn* is the speed of the first baroclinic mode. The lower the Froude number and slower moving the storm, the stronger the geostrophic currents are compared to the near-inertial waves, and the stronger the upwelling of isotherms (Ginis, 2002; Price et al., 1983, 1994). Zedler (2009) studied the current response to a westward moving storm in the Northern Hemisphere and found stronger upwelling and vertical mixing for slow-moving storms with the maximum upwelling region shifted to the left of the track due to the asymmetry of the Coriolis force on the north and south of the track.

Shay et al. (1989) studied the vertical structure of the near-inertial baroclinic ocean currents excited by the passage of a TC and found divergent currents in the ML associated with inertial pumping and opposite currents in the thermocline below.

Because the current vector rotates with depth, this causes the ML currents to be in an opposite direction compared to the layer below, which produces a strong shear at the base of the ML and drives mixing and ML entrainment (Shay, 2019). Price et al. (1994) studied the current response to the passage of TCs and reported that in most of the cases the response is dominated by near-inertial currents that remain for many days after the TC passage and have an e-folding time of 5-10 days. Currents in the ML have a rightward (leftward) bias in the Northern (Southern) Hemisphere, with stronger currents and horizontal transport at the right (left) of track (Price et al., 1994). In the thermocline, currents appear to decay with depth and have nearly constant direction (Price et al., 1994).

The TC strong winds and associated dynamic response of the ocean drive strong thermal changes in the ocean through different processes (Fig. 2.1). The strong shear between the ML currents and thermocline currents produces entrainment of the ML with the colder layer below, the upward motion due to Ekman pumping below the TC drives upwelling of isotherm cooling the water through the whole depth, and the ocean loses heat to the atmosphere through surface fluxes (Price, 1981).

Dare and McBride (2010) studied the SST response to several TCs using satellite data and comparing the local SST with a climatological SST dataset for the same day of the year and location. They reported that cold SSTs peak between one day before the TC to 7 days after and that for the majority of TCs the maximum SST anomaly occurs 1 day after the TC passage (Dare and McBride 2010). Mei and Pasquero (2013) studied SST anomalies calculated with respect to the mean SST averaged over the months prior the TC passage and analysed the SST response after removing the seasonal cycle. They reported a temperature decrease 1-2 days before

the TC passage and on average they found that the SST cold anomaly peaked the day after the TC.

The SST response is influenced by the strength of the TC and its translation speed. The SST cools more significantly and the spatial extension of the cold wake is larger for intense and slow-moving TCs (Dare and McBride 2010; Haakman et al. 2019; Mei and Pasquero 2013; Price, 1981). In particular, the intensity of the storm is important as it influences the strength of the upwelling, which reduces the mixed layer depth (MLD) and enhances the entrainment of the colder water underneath (Price, 1981). The translation speed affects the residence time, and so a slow-moving storm produces larger horizontal divergent currents and vertical shear at the bottom of the ML, generating deeper mixing and cooling (Price, 1981). Furthermore, Mei and Pasquero (2013) argued that the effect of translation speed is more significant in the tropics, while in the subtropics the ML is shallower and thus with a shorter residence time storms can generate near-inertial currents strong enough to significantly cool the ML.

The cooling of the SST is stronger on the right of the track in the Northern Hemisphere and on the left in the Southern Hemisphere (D'Asaro, 2003; Jullien et al. 2012; Price, 1981). This rightward (leftward) bias occurs because the wind stress of the TC is asymmetric and on the right (left) side in the Northern (Southern) Hemisphere, its turning rate is comparable with the turning rate of an inertial motion, and there is a near resonant coupling with ML velocity, which enhances mixing at the bottom of the ML (Price, 1981; Price et al., 1983). This displacement of maximum SST cold anomalies from the TC track is larger for fast-moving TCs (Mei and Pasquero 2013; Price, 1981).

Below the ocean surface, warm anomalies develop in the layer below the ML where the warmer water from the ML is entrained and mixed with the cooler water underneath (Cheng et al., 2015; Price, 1981) (Fig. 2.2). These warm subsurface anomalies are more pronounced to the right (left) of track in the Northern (Southern) Hemisphere, beneath the region where there is maximum entrainment and surface cooling (Price, 1981).

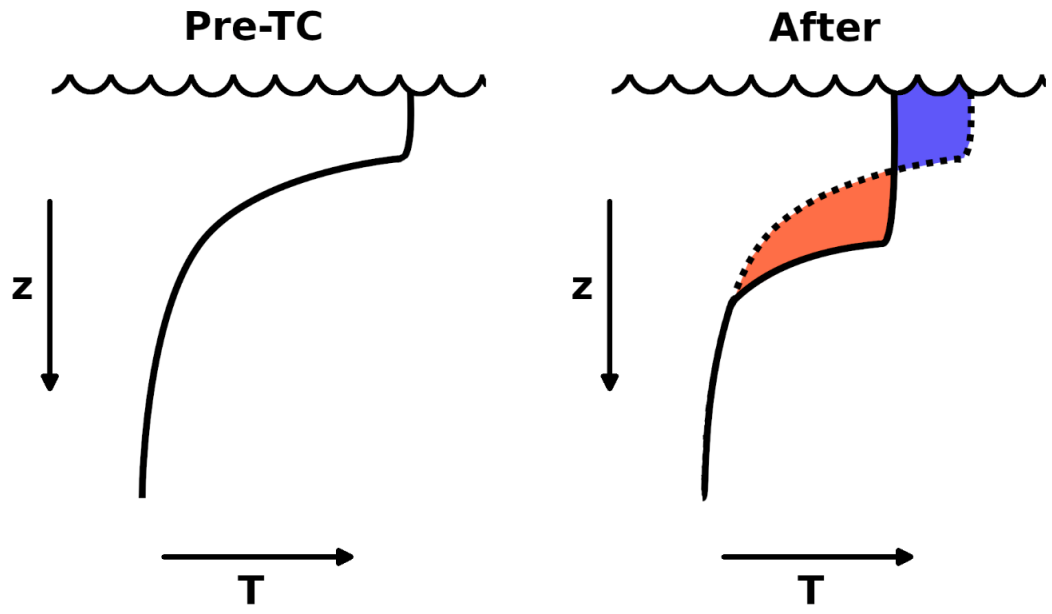

Figure 2.2: Schematic of the development of temperature anomalies following the MLD entrainment driven by the passage of a TC. The cold anomalies at the surface are expected to recover quickly due to solar radiation, while the subsurface warm anomalies could be stored for a longer period.

According to Cheng et al. (2015), who compared the cross-track ocean thermal response of all TCs and tropical storms between 2004 and 2012 globally, during the forced stage in the first three days after the storm passage, the thermal changes under

the storm eye produced cold anomalies near the surface, a warmer layer underneath (stronger on the right of the track) and cold anomaly underneath. This structure is similar to the one reported by Zhang et al. (2016) and Zhang et al. (2019), who studied the ocean temperature response to a typhoon in the South China Sea and found a three-layer structure with surface cooling and subsurface warming due to vertical mixing and further cooling in the lower layer due to upwelling. In addition, according to Zhang et al. (2016) in the days following the typhoon the thermocline moved up and down following pumping from near-inertial currents with opposite phase in the ML and in the thermocline. In general, the temperature response of the ocean is much stronger for more intense TCs and for strong TCs (cat >3) the subsurface warming is comparable in magnitude to the surface cooling, while for weaker TCs the surface fluxes play a major role in cooling and there is less entrainment and subsurface warming (Cheng et al. 2015; Park et al. 2011).

Several studies focused on assessing the importance of the different processes in cooling the ocean during the passage of a TC. According to Price (1981), the entrainment of the ML is the most effective cooling process, while the heat loss to the atmosphere is less effective for the cooling of the sea surface. Price et al. (1994) studied the response to the “forced stage”, the period during the actual TC passage (time scale based on the TC residence time, of around half a day), with a one-dimensional ocean model. They reported that while in the upper part of the water column the response is dominated by vertical mixing, upwelling is the major contributor to the heat budget in the lower water column and that it can overwhelm the subsurface warming from vertical mixing (Price et al., 1994). Vincent et al. (2012) used a global circulation model to study the cooling by different TCs and reported that

while for more intense TCs the vertical mixing is the major factor for cooling, for less intense TCs and further away from the track most of the cooling can be explained by heat fluxes. Lateral temperature advection may pay an important role for cooling during more intense TCs and for the recovery of the cold anomalies (Vincent et al., 2012). Recently, Lin et al. (2017) studied the upwelling response to several typhoons in the western North Pacific and reported that upwelling of cold water contributes to cooling marginally in the surface layer and more significantly in the subsurface and in the deeper ocean, with a major effect for intense and slow-moving TCs. Further away from the ocean track the upwelling below the TC centre is compensated by downwelling, which might cause an increase in SST (Cheng et al., 2015; Oey et al., 2006; Jaimes and Shay, 2015). Another case study focused on calculating the heat budget of a Typhoon cold wake showed that the majority of the cooling is due to vertical mixing, with some upwelling contribution to cooling on the left and downwelling contribution to warming in the front and sides, and horizontal advection that modulated the temperature anomalies over a larger area (Zhang et al., 2019). Huang et al. (2009) studied the heat budget of the cooling after the passage of Hurricane Frances and reported that vertical mixing was the major contributor to the cooling, while horizontal advection contributed only in some locations to the spatial pattern of SST, and vertical advection was important under the eye of the TC. The cold wake of hurricane Frances was also studied by D'asaro et al. (2007) , who confirmed the dominance of mixing compared to the air-sea heat flux to cool the ocean SST.

The magnitude of the cold surface anomalies is influenced by the state of the ocean prior the TC (Haakman et al., 2019; Vincent et al., 2012). In the subsurface, cooling is greater during the warming season when the pre-TC ML is shallower than

during the cooling season (Park et al. 2011). Haakman et al. (2019) studied the SST response for TCs from 2002 to 2018 for different upper ocean stratification conditions by calculating the thickness of the barrier layer and potential energy and found out that the SST cooling is larger for thinner barrier layers, as less energy is required to mix the warm ML water with cooler water underneath. On the contrary, the presence of a thick barrier layer and salinity stratification inhibits the entrainment and can reduce the cooling induced by the passage of a TC (Wang et al, 2011).

A thicker pre storm MLD reduces the cooling effect of upwelling and vertical mixing in the surface layer but enhances upwelling and cooling in the layers below (Lin et al., 2017). The importance of the ocean conditions prior the arrival of the TC is further confirmed by Mei et al. (2015), who compared the SST response to TCs in the South China Sea and in the North Western Pacific and concluded that although the TC characteristics are the most important to determine the response, for the same TC forcing the response is larger in the South China Sea, which is characterized by a shallower ML and a stronger stratification below the ML. During the slow-moving Typhoon Kai-Tak, SST cooling up to 10.8 °C was measured, which appeared to be favoured by a particularly warm water and shallow ML before the TC passage (Chiang et a. 2011). Chaudhuri et al. (2019) studied the effect of strong stratification conditions before the passage of cyclone Phailin in the Bay of Bengal and reported that the presence of a thick barrier layer reduced vertical mixing, which remained confined into a nearly isothermal layer and produced little SST cooling. Steffen and Bourassa (2018) studied the changes in the barrier layer due to the passage of a TC and found significant differences in the different basins: in the Atlantic the barrier layer changes are mostly driven by the deepening of the isothermal layer, while there are no

significant changes in the eastern Pacific. In the central Pacific, the freshening of the surface layer due to precipitation is the major driver of the changes in stratification.

Geostrophic currents associated with an eddy can modulate the heat and mass budget of the ML and the TC-induced cooling and warming anomalies in the subsurface and away from the track (Jacob et al., 2000; Jaimes and Shay, 2009; Jaimes et al., 2011). Jaimes et al. (2009) studied the ML cooling over a warm-core and cold-core eddy during Hurricane Katrina and Hurricane Rita in the North Atlantic in 2005 and found a stronger and larger ML velocity response over the cold-core eddy where the ML was shallower. This produced stronger cooling caused by enhanced vertical mixing and upwelling. Jaimes et al. (2011) studied the response to the TC passage over a cold-core and warm-core eddy with a numerical model and found that during the forced stage the upwelling/downwelling response also depended on the underlying geostrophic currents, with upwelling favoured over cold-core eddies. The background currents modulate the vertical dispersion of near-inertial energy, with more rapid dispersion and less mixing over the warm-core eddy compared with the cold-core eddy. Furthermore, downwelling away from the TC track could be significant over warm anticyclonic mesoscale features, as reported by Jaimes and Shay (2015) for a warm-core eddy during Hurricane Isaac.

Pre-TC ocean conditions can also be important for the intensification of TCs. Lin et al. (2008) studied the development of supertyphoons in the Western North Pacific and found that in some regions passing over warm ocean features is fundamental for typhoons to intensify. Furthermore, the intensification appears to depend on both the pre-TC MLD and the translation speed of the TC since fast-moving TCs can intensify over shallow warm ocean features while slow-moving TCs require

a deeper subsurface warm layer in order to intensify (Lin et al., 2009). Balaguru et al. (2015) suggested that accounting for the ocean stratification could improve the prediction of TC intensification especially over the eastern Pacific, where the thermocline is shallow and the effects of mixing canbe stronger. Moreover, the ocean surface cooling caused by a TC could have a negative feedback effect on TC intensification (Jaimes et al. 2009, Oey et al. 2009, Shay et al. 2000). As reported for Hurricanes Katrina, Rita and Opal in the North Atlantic, TCs intensify over warm core eddies where the ML is deeper and the surface cooling less intense and weaken over cold-core eddies where the SST cooling was stronger (Jaimes et al. 2009, Shay et al. 2000).

Furthermore, when sea spray is lifted in the air at a cooler temperature than the ocean, it releases sensible heat to the atmosphere, and, if it evaporates, which does not always happen, it can absorb latent heat from the atmosphere (Andreas and Emanuel, 2001). These processes affect the development of a TC, and a bulk formulation that accounts for the sea spray could significantly improve the simulation of TC intensification (Andreas and Emanuel, 2001; Wang et al., 2001; Zheng et al., 2008).

Price et al. (2008) studied the recovery time of the SST in the wake of different TCs and reported that it usually takes around 5 to 20 days for the SST to be restored to pre-TC conditions. However, Park et al. (2011) studied the temperature restoration using ARGO float data and reported that only the top layer restores to the pre-TC SST in this time period, while near-surface cooling below the first few meters takes significantly longer to recover. This is further confirmed by Mrvaljevic et al. (2013), who studied the cold wake of typhoon Fanapi and reported that the e-folding time for the recovery of the cold anomalies was almost double in the subsurface layer compared

to the surface. Hart et al. (2007) studied the MPI (maximum potential intensity) anomaly after passage of a TC and reported that while the atmosphere recovers in approximately one week the ocean takes 1-2 months, with stronger TCs, which produce stronger cooling, taking longer.

The warming following the passage of a TC is correlated with the amplitude of the cooling, and the central and coolest part of the wake warms faster than the surrounding region (Price et al., 2008). According to Dare and McBride (2010) the recovery time could be divided in an immediate partial recovery that happens quite fast and in a slow recovery after this. Furthermore, the recovery time is influenced by the intensity of the TC because more intense TCs lead to more intense cooling, which takes more time to fully recover (Dare and McBride, 2010).

Price et al. (2008) concentrated on the recovery of the cold wakes of two TCs, one that warmed quickly and one that warmed slowly, and suggested that the recovery times depends mostly on the air-sea fluxes. Major warming occurs during periods of light winds and clear skies, which are positively correlated with a large amplitude of the SST diurnal cycle (Price et al., 2008). Furthermore, Mei and Pasquero 2012 argued that baroclinic instability, which produces restratification of the upper ocean after the passage of a TC plays a significant role in the temperature recovery to pre-TC conditions. In fact, after a TC passage a strong horizontal temperature gradient develops between the centre of the cold anomalies and the surrounding water, and in the following period the effect of the baroclinic instability will be to re-stratify the ocean pushing the warmer and less dense water on the sides of the centre of the cold anomalies over the colder and denser water (Mei and Pasquero, 2012). Moreover, in the period following a TC passage, the cold surface thermal anomalies propagate

westward through Rossby waves and may move out of the region which was directly influenced by the TC (Jansen et al., 2010; Vincent et al., 2012).

It has been postulated that subsurface warm anomalies (Fig. 2.2) could remain for several months and contribute to the ocean heat transport from tropical regions to the pole (Emanuel 2001; Sriver and Huber 2007, Sriver et al. 2008). Emanuel (2001) calculated the ocean heat uptake in the tropical region due to vertical mixing from all TCs recorded during 1996 and suggested that this could be equilibrated by a net ocean heat transport out of the tropics. Sriver and Huber (2007) calculated that if all the heat mixed downward by TCs is balanced by heat transport towards the poles, approximately 15% of the ocean heat transport could be associated with TCs. However, Jansen et al. (2010) argued that the heat uptake by TC stored in the subsurface is released back to the atmosphere in winter when the ML deepens and only a fraction of it contributes to the ocean heat transport. This was further confirmed by Vincent et al. (2012) who found that only 1/10th of the TC heat uptake was transported poleward using a global ocean model.

Pasquero and Emanuel (2008) used a general circulation model to study heat anomalies following the passage of a TC and reported that a fraction of the warm subsurface anomaly remains in the region for more than a year and that the warm subsurface water appears to be advected in the equatorial band. The equatorward transport of the warm anomalies was further confirmed by Jansen et al. (2009), who calculated zonally averaged heat transport with a global model and argued that if the mixing due to TCs is enhanced in both the subtropics and the tropics there is a poleward transport, but if the mixing is enhanced only in the subtropical bands most of the transport is towards the equatorial band and poleward transport is decreased.

Sriver et al. (2010) used a global model and further confirmed that the presence of TCs results in an overall increase of OHC and warmer equatorial regions. Jullien et al. (2012) studied the impact of TCs in the South Pacific and suggested that the passage of a TC leaves a signature that lasts through to the following winter, with warming anomalies in the subsurface and a cold surface anomaly that is not fully restored during the TC season. Bueti et al. (2014) studied the OHC changes due to TCs in different basins and found that in some cases a TC can increase the ocean heat uptake of about 10%, with warm anomalies transported towards the tropics.

On the NWS, Davidson and Holloway (2001) studied the influence of the passage of a TC on internal tides using mooring data and simulation of three TCs passing at different distances from the shelf and parallel to it and of one TC perpendicular to the shelf. They reported strong near-inertial oscillations after the TC and a reduction of semidiurnal internal tides in the region, with internal oscillations after the TC passage that last longer at depth (Davidson and Holloway, 2001). According to Davidson and Holloway (2001), the passage of a TC with a track parallel to the shelf produces a well-mixed water column over the shelf and advection of water up or down the shelf slope depending on the distance of the TC from the coast, with strong upwelling for TCs closer to the coast and downwelling for TCs outside the shelf, while the TCs with track perpendicular to the coast triggers downwelling before the TC passage and strong upwelling after.

Rayson et al. (2015) studied the ocean currents and energy response to four TCs that passed within 150 km of a mooring on the NWS using a numerical model and they found that the influence of semidiurnal tides was an important driver of the ocean circulation following a TC, along with the TC induced near-inertial currents. In

this region the inertial currents decay much faster on the shelf than in the open ocean and during spring tides, when the tidal currents are stronger (Rayson et al. 2015). Furthermore Rayson et al. (2015) looked at the ocean temperature response following a TC on the NWS and found that its passage produces cooling beneath the centre of the storm due to upwelling, entrainment and air-sea heat fluxes, which could account for up to 50% of the heat loss, and warming caused by downwelling at 100 m depth on the left of the TC track close to the shelf edge. Moreover, on the NWS TC activity can produce strong sediment transport, trigger strong wave activity, and can generate coastally trapped waves that can travel along the coast and influence the sea level further south along the coast (Dufois et al., 2017, 2018; Eliot and Pattiaratchi, 2010).

More studies of the effect of the passage of a TC on the ocean cooling have been conducted in other continental shelf regions. On the shelf in the South China Sea Chu et al. (2000) studied the response of TC Ernie and reported a similar response in the open ocean and near the coast, with alternating patterns of downwelling and upwelling near the coast caused by convergence and divergence. Mitchell et al. (2005) and Teague et al. (2007) studied the response of Hurricane Ivan over the continental shelf of the U.S. and reported stronger currents response on the left of track, probably due to the bathymetry, and strong downwelling before the TC passage and upwelling along the shelf slope after the TC passage. The forced stage response resulted in an overlapping of surface and bottom Ekman layer and after the TC passage they found a quasi-homogeneous water column due to vertical mixing (Mitchell et al., 2007).

2.4 Significance of this study

2.4.1 Part 1: Study of the summer 2012/2013 MHW

Previously the 2012/2013 MHW had not been defined using the comprehensive categorization based on the duration and intensity by Hobday et al. (2018), which is necessary to assess the spatial and temporal extent of this event in a quantitative and objective way. Furthermore, although Xu et al. (2018) studied the difference in drivers between the 2012/2013 over the southern part of the NWS and the MHW and the 2010/2011 MHW that extended on the southern part of the West coast, an analysis of the 2012/2013 MHW compared to a regional climatology is still lacking. In particular, the advection patterns over the shelf on the southern part of the NWS region need further investigation as they had an important role on maintaining the MHW for a long period (Xu et al., 2018) and the large scale and climate drivers of the MHW need to be studied.

In this thesis, an objective analysis of the 2012/2013 MHW over the NWS following Hobday's metric and an in-depth study of the MHW regional and large-scale drivers compared to a 7-year model climatology will be conducted to assess the causes that led to the development of this event.

2.4.2 Part 2: Tropical cyclone effects on the ocean over the NWS region

The response of the ocean to the passage of a TC is influenced by several factors and can be different in different basins (Mei et al., 2015) and a comprehensive study of the average temperature and currents response on the NWS region has not been conducted yet. In particular, how the response changes over the continental shelf or the deep ocean, the effect of the season at which the TC occurs on the ocean

recovery, of the TC characteristics such as the intensity and translation speed and of the ocean stratification at the moment of the TC passage have not been analysed over the NWS region.

Several questions on how TCs influence the OHC, when their passage can lead to an increase of the ocean energy and where the extra energy is transported are still unanswered. How TCs drive OHC changes over different basins and in particular over the NWS region has not been studied yet. Furthermore, how TCs with different intensity and translation speed and happening in different periods can drive different patterns of temperature anomalies and OHC changes has not been fully defined and has not been studied in the eastern Indian Ocean region. The magnitude of the OHC increase following a TC is still subject to debate, and whether the warm temperature anomalies induced in the subsurface resurface in winter or are stored in the ocean for longer is still unknown. Moreover, it is not clear if the warm anomalies induced from the passage of a TC over the NWS remain in the region or are advected away and whether they are advected poleward or equatorward.

In this thesis a composite approach is used to study the temperature and currents changes driven by the passage of a TC on the NWS region, with a focus on the difference between on-shelf and off-shelf locations, the effect of the season, of the intensity and translation speed of the TC and of the ocean stratification. The OHC changes induced by TCs with different characteristics over the NWS region and the processes responsible for these changes are analysed.

Chapter 3. Methodology

Note: sections of this chapter are based on a published paper.

Maggiorano, A., Feng, M., Wang, X. H., Ritchie, L., Stark, C., Colberg, F., & Greenwood, J. (2021). Hydrodynamic drivers of the 2013 marine heatwave on the North West Shelf of Australia. *Journal of Geophysical Research: Oceans*, 126(3), e2020JC016495.

3.1 Data

3.1.1 Satellite sea surface temperature

SST data from the European Space Agency (ESA) SST Climate Change Initiative v.2 (CCI SST, https://cds.climate.copernicus.eu/cdsapp#!/home) (Merchant et al., 2019) were used to validate the MHW model and BRAN (Bluelink ReANalysis) dataset for the TC – ocean analysis. CCI SST is daily mean blended multi-sensor and gap-filled, created from infrared satellite data at a grid resolution of 0.05° latitude/longitude. The interpolated level 4 (L4) reanalysis CCI SST was used, which represents a multi-satellite estimate of daily mean SST at 20 cm nominal depth.

3.1.2 In-situ ocean currents

In-situ velocity measurements from the Integrated Marine Observing System (IMOS, 2019) shelf moorings PIL200 and PIL100 (red triangles in Fig. 3.1) were used to validate the MHW model velocities. The mooring data was collected during 2012–2014. Mooring velocities are measured throughout the water column using an upward looking Acoustic Doppler Current Profiler (ADCP). The temporal resolution of the

mooring measurements is 10 minutes, which have been averaged daily to compare with BRAN and model daily output. The vertical resolution is 8 m for PIL 100 and 10 m for PIL 200.

3.1.3 ERA5 reanalysis data

Hourly atmospheric (heat flux, evaporation, precipitation and wind stress) and SST data used in the MHW model were sourced from the European Centre for Medium-Range Weather Forecast (ECMWF) ERA 5 dataset (C3S, 2017). The ERA 5 data were provided on a regular grid with a 0.25° latitude/longitude resolution.

3.1.4 Bluelink model and reanalysis data

The Bluelink eddy-resolving Ocean Forecasting Australia Model-3 (OFAM3, Oke et al., 2013) was used to initialize ocean temperature and salinity for the MHW model, and the BRAN dataset was used for both the MHW and TC - ocean analyses. For the MHW analysis, BRAN provided the sea surface salinity (SSS) model forcing and was used as a model validation tool for horizontal currents, and for the TC - ocean study BRAN was the primary data source, using 3D fields of temperature, vertical and horizontal currents and surface air-sea fluxes.

BRAN is a reanalysis dataset for the global ocean, providing 3-dimensional (3D) output of temperature, salinity, horizontal and vertical currents, sea level, and air-sea heat flux components as short- and long-wave radiation and sensible and latent heat flux at the ocean surface (Oke et al., 2013, Schiller et al., 2020). BRAN has daily resolution on a 0.1° latitude/longitude grid and 51 vertical depth levels (Oke et al., 2013). BRAN assimilates OFAM3 data with satellite altimetry, satellite SST and in situ temperature and salinity data from Argo floats, expendable bathythermographs

(XBTs) and field surveys using the Bluelink ocean data assimilation system (BODAS; Oke et al., 2008) every 3-7 days (Schiller et al., 2020). OFAM3 is an uncoupled ocean model with a horizontal spatial resolution of 1/10° for all longitudes between 75°S and 75°N, 5 m vertical resolution down to 40 m depth, 10 m vertical resolution to 200 m depth, and vertical mixing based on the K-epsilon scheme (Schiller et al., 2020). In reanalysis mode, OFAM3 is forced with ERA-Interim (Dee and Uppala, 2009) surface heat, freshwater, and momentum fluxes with 1.5° latitude/longitude horizontal resolution and 3-hourly temporal resolution (Schiller et al., 2020). Tidal dynamics are not represented in the implementation of BRAN, which could be a limitation in simulating dynamical processes over the NWS as the region is characterized by strong tides that induce internal waves and that have strong influence on several ocean processes.

3.1.5 CSIRO Atlas of Regional Seas climatology

The temperature data from the CSIRO Atlas for Regional Seas (CARS 2009) climatology, (https://researchdata.edu.au/csiro-atlas-regional-cf14-standard/15297, Rigdway et al., 2002) was used to validate the model MLD. CARS 2009 climatology has 0.5° latitude/longitude horizontal resolution and 56 fixed depth levels with 10 m resolution within the first 100 m (Rigdway et al., 2002).

3.1.6 Tropical cyclone tracks

TC track data were accessed from the Australian Bureau of Meteorology (BOM) best track (BT) database (http://www.bom.gov.au/cyclone/tropical-cyclone-knowledge-centre/databases/). The BT database provides TC track positions typically every 6 hours (but occasionally more frequently for special cases and near land).

3.1.7 Argo float data

Argo float (IMOS, 2020) temperature data were used to validate BRAN temperature anomalies after the passage of a TC. Argo is a system of profiling floats, which measure temperature, salinity, pressure and oxygen from the surface to a depth of 2000 m. Argo floats measure the ocean profile every 10 days at various locations. From the surface they descend to approximately 1000 m depth, where they drift following the currents for approximatively 10 days. They then descend further to 2000 m depth and ascend to the surface in around 3 hours while collecting data (Jayne et al., 2017).

3.2 Marine heatwave methods

3.2.1 The MHW numerical model

To study the 2012/2013 MHW we ran a 3D ocean circulation model of the Australian NWS based on the Regional Ocean Modelling System (ROMS) (Marchesiello et al., 2003; Shchepetkin & McWilliams, 2005). The model configuration was used previously for connectivity studies and is described in Feng et al. (2016). This high-resolution model provides additional benefit over OFAM3 in two main aspects: one is to capture the strong semidiurnal tidal signals as well as the associated internal tides in the region, which improves estimates of the vertical mixing in the temperature budget; and the other is to better capture the coastal warming signals which are crucial for marine assets such as coral reefs.

The model domain covers the Pilbara Shelf and Ningaloo Reef region (Feng et al., 2016, between 17°S and 23°S and 110°E and 119°E, Figure 3.1); approximately 900 km off the coast between Coral Bay in the south of the North West Cape and Port Hedland in the north. The horizontal resolution is approximately 1 km. In the vertical there are 30 grid layers defined by terrain following stretched-coordinates (S-coordinates) with a minimum depth of 5 m. The model was run between April 2009 and June 2016 to capture average conditions and the 2012/2013 MHW event.

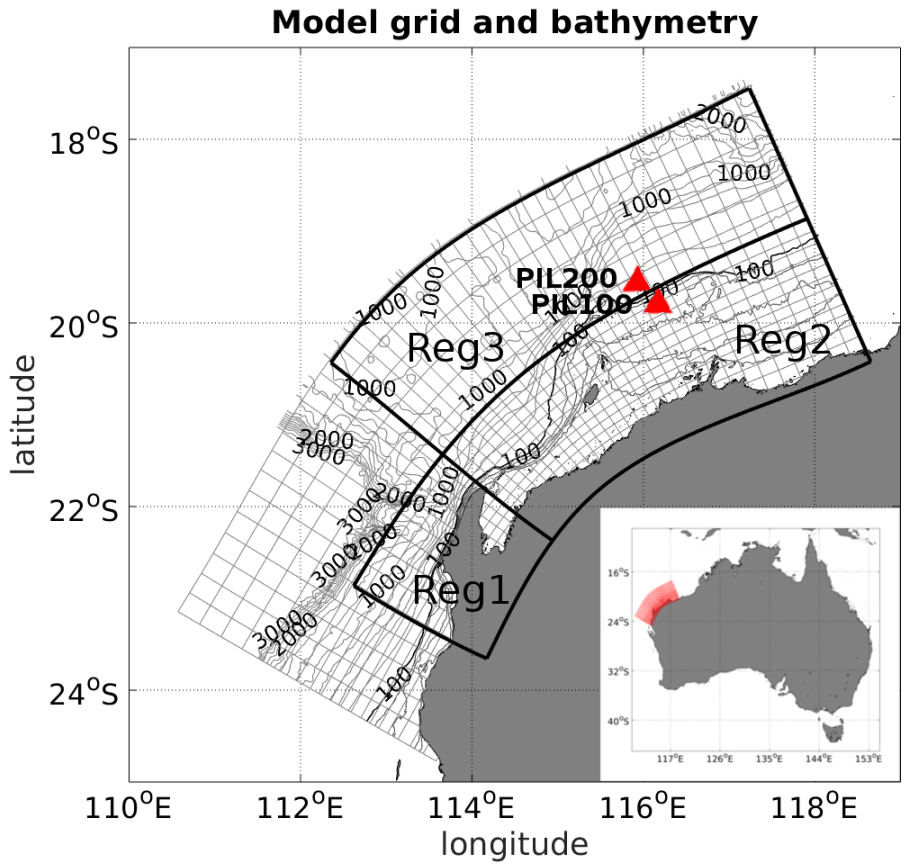

Figure 3.1: Model domain with model grid (every 10th line) and coastal bathymetry every 20 m to 100 m and every 200 m to 3000 m. The IMOS mooring stations used for validation are indicated by solid red triangles. The three regions highlighted are the regions considered for the heat budget study.

The model is initialized with daily temperature and salinity data from OFAM3. Model surface forcing is different to that used previously by Feng et al. (2016) as we used the hourly ERA5 atmospheric data of heat flux, evaporation, precipitation, wind stress and SLP. Using hourly forcing allows the model to capture the diurnal SST cycle, which in some conditions can be strong over the NWS (Zhang et al., 2016) and improves the model ability to capture TC influences. The forcing data were re-interpolated by ROMS on the model grid. Hourly SST data are from ERA 5, while SSS data are interpolated from BRAN.

Boundary conditions are provided by the TPXO7.2 global model for tidal forcing (Egbert et al., 1994; Egbert & Erofeeva, 2002), with the same tidal constituents used by Feng et al. (2016). Except for the surface forcing, the open-boundary conditions described by Feng et al. (2016) are also used, including: the Flather condition (Flather, 1976; Flather & Heaps, 1975) for the normal component of barotropic velocity; the Chapman condition for surface elevation (Chapman, 1985) and 3D open boundary conditions using a combination of clamped and radiation nudging open boundary conditions. In addition, the model surface heat flux (Q_{ROMS}) was corrected based on Barnier et al. (1994):

$$Q_{ROMS} \approx Q + dQ/dSST(T_{ROMS} - SST) \qquad (3.1)$$

where Q is the heat flux from ERA5 and dQ/dSST = 40 W m^{-2} C^{-1} is the correction coefficient for low latitudes (Barnier et al., 1994). Hourly SST values from ERA 5 have been used in equation 3.1. The model SSS was restored towards observed SSS. The model does not consider tidal wetting of mud flats. Non-local K-Profile was

used in the vertical mixing parameterization, which is a specific parameterisation developed by Large et al. (1994).

3.2.1.1 Current validation

The MHW model was developed and previously validated by Feng et al. (2016) for regional connectivity studies, where model surface and tidal currents were validated against moorings. Current validation for this study used the IMOS moorings and BRAN. The summer average of model, mooring and BRAN horizontal velocity components at all mooring locations from the surface to 100 m are shown in Fig. 3.2. The model overestimated the strength of the currents near the surface, with standard deviation between 0.15 and 0.20 m/s for northward (V) and eastward (U) components at PIL100 (Region 2) and between 0.21 and 0.29 m/s at PIL200 (Region 3) but overall captured the general features of the profiles (Fig. 3.2).

Model validation of U and V in the first layer against PIL100 and PIL200 from November 2012 to March 2013 (averaged over the top 50 m) are shown in Fig. 3.3. The model captures the general features of the timeseries well, with some differences - probably due to the lack of mooring data at depths closer to the surface where the model has a finer resolution, especially for PIL200 which sits at a greater depth.

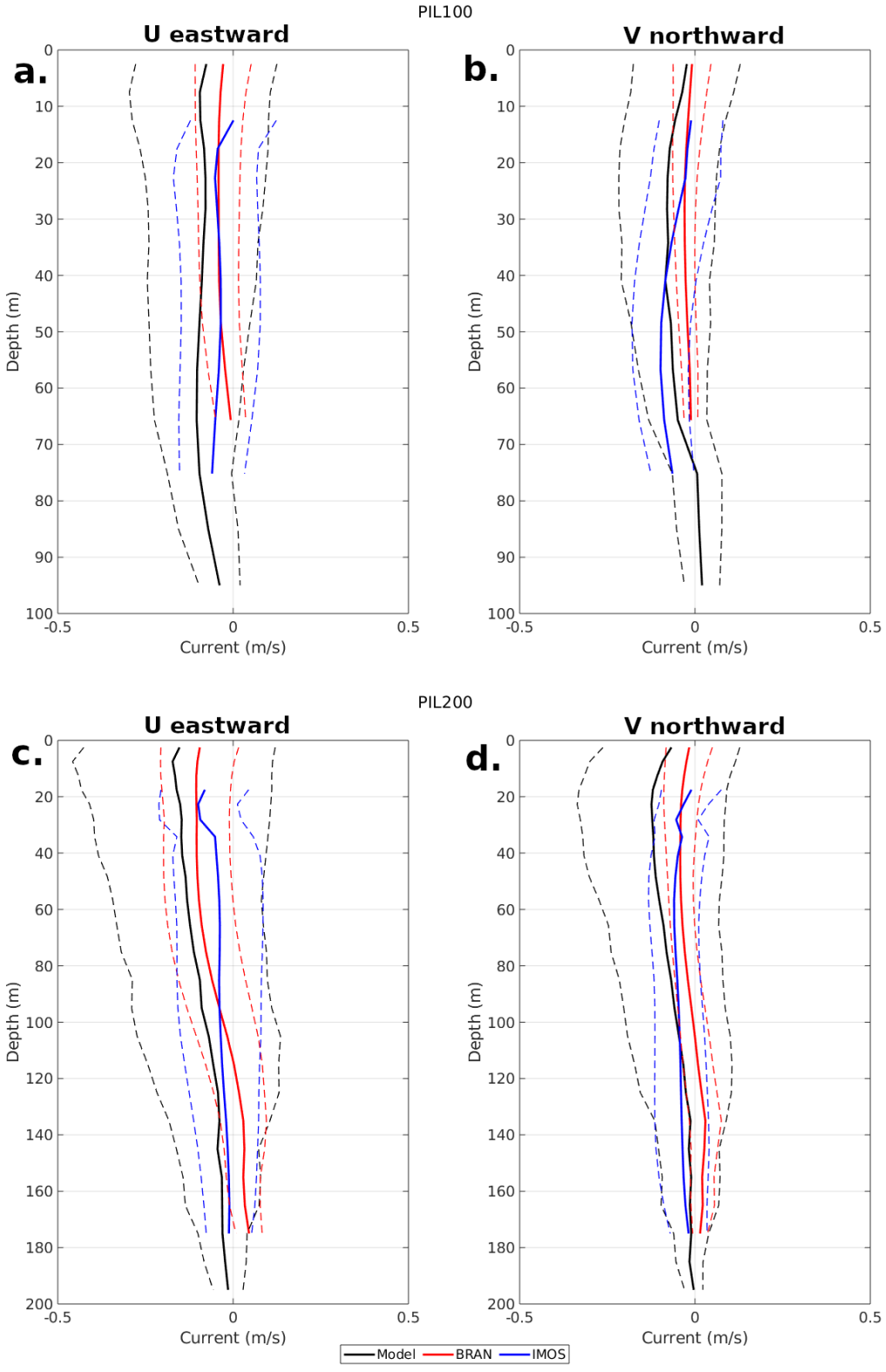

Figure 3.2: Season averaged U and V current profiles at mooring station: (a), (b) PIL100; and (c), (d) PIL200 using the model (black), BRAN data (red), and mooring data (blue). The dashed lines indicate the standard deviation.

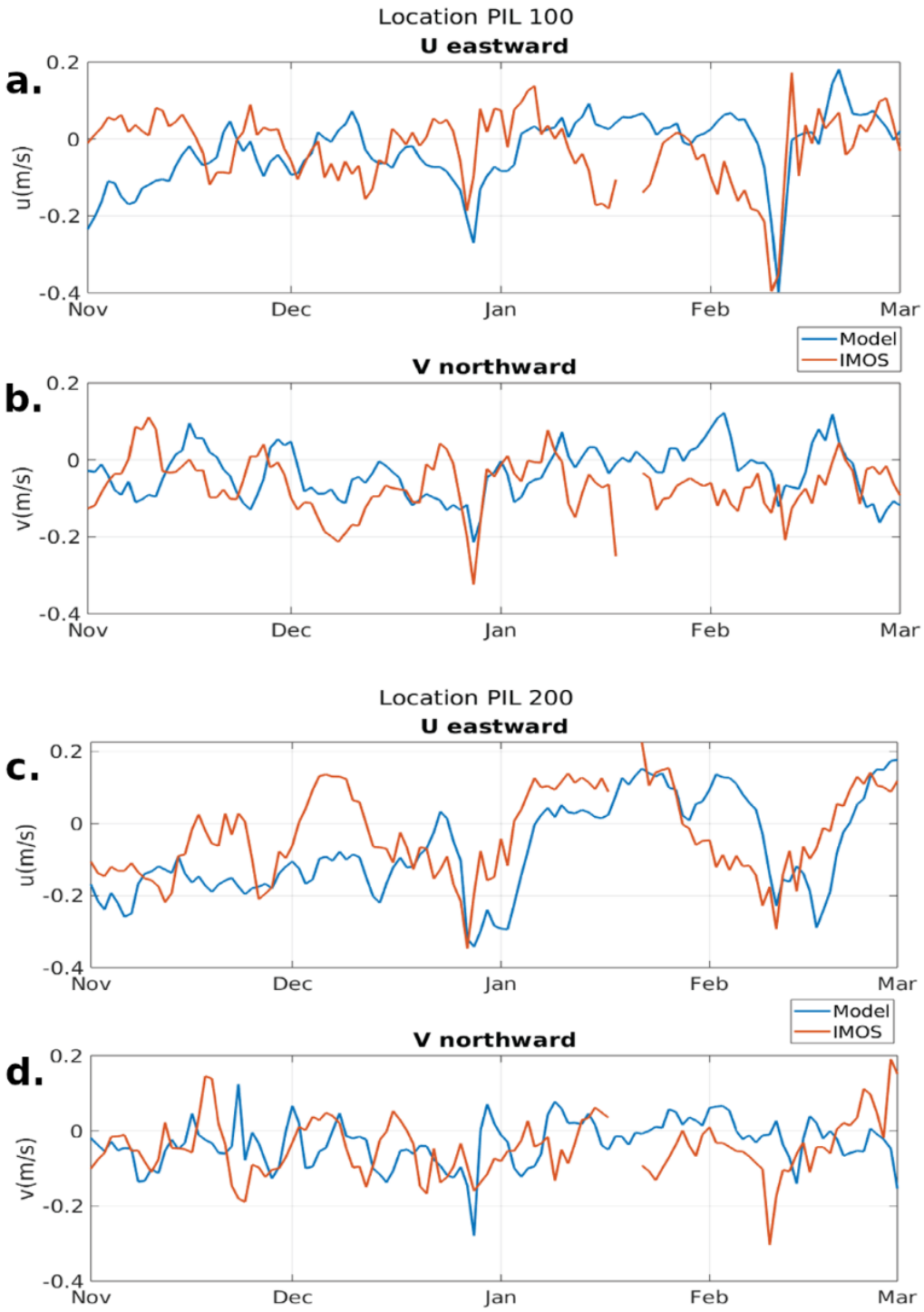

Figure 3.3: Modelled (blue line) and mooring (red line) for: (a), (c) eastward (U); and (b), (d) northward (V) velocity components averaged over the top 50 m at mooring locations: (a), (b) PIL100 (Region 2); and (b), (c) PIL200 (Region 3) covering the period prior to, during and after the 2012/2013 MHW between 1 November 2012 and 1 March 2013.

Root mean square errors (RMSE) between model currents and BRAN (in the whole domain, interpolated at each BRAN grid point) and between model and moorings (averaged over the entire column at the mooring locations) ranged between 0.13 and 0.17 m/s for U and V (Table 3.1), probably due to the different resolutions and spatial interpolation of data. Additional differences could be partially due to the use of different atmospheric forcing of the model compared with BRAN and the data assimilation procedure of BRAN. Differences between model and mooring in the top 50 m (Fig. 3.2) could again be due to the lower vertical resolution of the moorings closer to the surface. Model bias was small, ranging from values lower than 0.01 to 0.02 m/s for U and V (Table 1), indicating the absence of systematic errors in ROMS.

Table 3.1: Comparisons of eastward (U) and northward (V) current velocities between the ROMS model output, PIL100 and PIL200 moorings (column averaged) and BRAN (surface and column averaged) datasets. The results were calculated comparing the model output interpolated at IMOS mooring locations and at the same grid points as BRAN.

	U RMSE(m/s)	V RMSE(m/s)	U bias (m/s)	V bias (m/s)
PIL200	0.15	0.13	-0.002	0.009
PIL100	0.17	0.13	-0.0006	0.02
BRAN	0.15	0.15	0.005	-0.002

3.2.1.2 SST validation

The model surface temperatures were approximated with the first layer temperatures between 0.5 m and 3.5 m depths and validated against CCI SST (Fig. 3.4). On average, the bias varied between +0.5 °C in the summer to -0.5 °C in the winter, possibly because of the boundary conditions from the parent model, a bias in the hourly forcing applied from ERA5, or model vertical turbulence that could simulate over mixing particularly in the deeper region 3. Fig. 3.4 (right) shows the bias for the different regions; in region 2 model SST compares better with CCI data, probably due to finer model vertical resolution near the surface over the shelf. The distribution of RMSEs in the model domain shows larger differences in the south (south of the North West Cape, Fig. 3.4 left). Overall, RMSEs during the entire model period was < 1°C and correlation > 0.93.

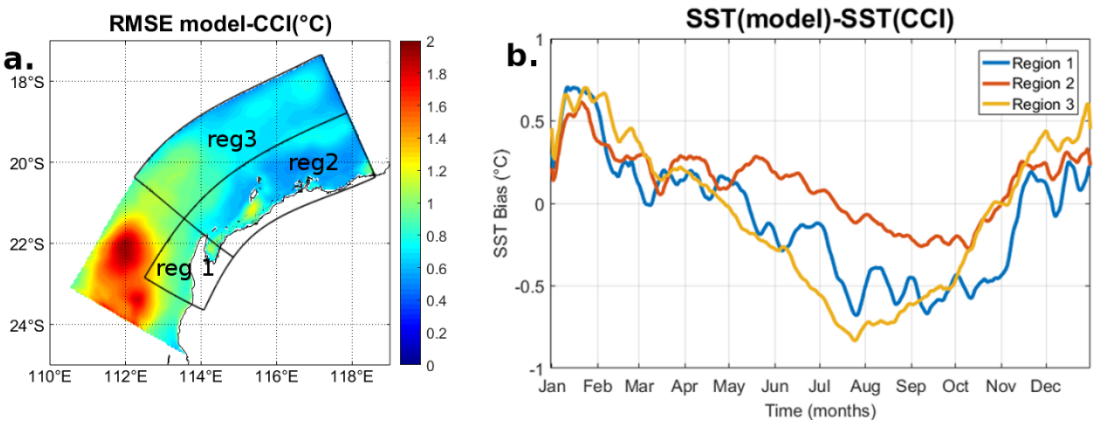

Figure 3.4: (a) Mean RMSE for SST data in the model domain; and (b) domain-averaged bias between model SST and CCI SST in the three regions. Correlation coefficient over the whole domain is > 0.93.

Fig. 3.5 compares 20-day average CCI SST anomalies to model SST anomalies between December 2012 and March 2013 and shows that the model successfully captures the spatial pattern and magnitude during the MHW development, peak period and decay (Fig. 3.5, columns 3 and 4). In particular, the difference between the model and CCI anomalies (Fig. 3.5, column 3) are larger near the south-western border and along the coast, where the bathymetry is shallower and there are fewer sigma layers than at other locations. Fig. 3.5, column 4, shows the correlation pattern between CCI and model anomalies, with lower correlation near the south-west part of the domain and higher correlation in region 2, where the model captures the MHW better.

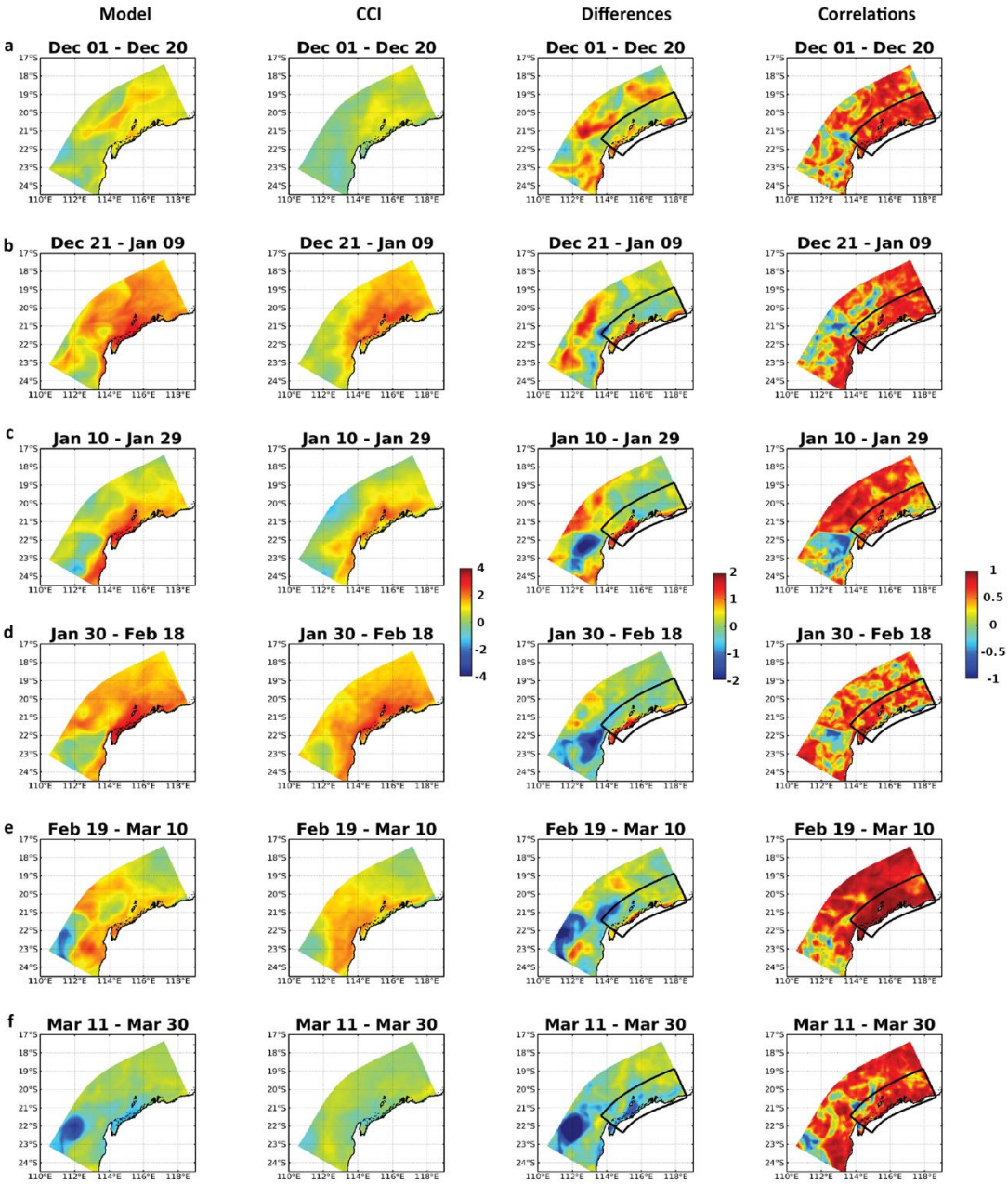

Figure 3.5: Modelled SST anomalies (1st column), CCI SST anomalies (2nd column), difference between model and CCI anomalies (3rd column), and correlations (4th column) as 20- day averages for; (a) 1-20 December; (b) 21 December - 9 January; (c) 10 - 29 January; (d) 30 January - 18 February; (e) 19 February - 10 March; and (f) 11 - 30 March. Region 2 is shown by the black box in columns 3 and 4.

3.2.2 Marine heatwave analysis

SST anomalies were analysed using the method and categorization of MHW events described by Hobday et al. (2016; 2018), which defines a MHW as SST anomalies higher than the 90th percentile threshold for more than 5 consecutive days. The cumulative intensity of the MHW was calculated as the cumulative sum of temperature anomalies during the corresponding MHW period. To do this, a 30-year climatology of the region based on CCI SST data from 1986 to 2016 was developed.

To highlight the spatial differences of MHW development, SST anomalies were compared to the 30-year climatology in the three regions shown in Fig. 3.1: along Ningaloo reef (Region 1); on the shelf north of North West Cape (Region 2); and just off the shelf (Region 3). In addition, for a more complete MHW analysis, the anomalous warm summer of 2012/13 was compared to a shorter 7-year climatology period (model climatology) covering the years of the model run (late 2009 to early 2016). This allows a comparison between the modelled features of summer 2012/2013 and other years to identify the anomalies that drove the MHW development.

3.2.3 Atmospheric forcing

To analyse the atmospheric circulation over a larger region during MHW development, monthly averaged wind and SLP data from ERA5 were used. The atmospheric conditions for three months during summer 2012/2013 were compared with the 30-year monthly mean climatology. A 30-year daily climatology based on the ERA 5 850 hPa zonal wind field during summer was used to calculate the Australian Monsoon Index (AUSMI) and analyse the Australian monsoon onset date and strength, following the method by Kajikawa et al. (2010) which is based on reversal of the winds to westerlies north of Australia. Kajikawa et al. (2010) defined the AUSMI as the 850

hPa zonal wind averaged over the area between 5 °S - 15 °S and 10 °E - 130 °E. The onset day is calculated as the first day after 1 November which satisfies the following conditions: on the onset day and during the 5 days after, the averaged AUSMI must be > 0; in the subsequent four pentads the AUSMI must be positive in at least three pentads; and the accumulative four-pentad mean AUSMI >1 m/s (Kajikawa et al., 2010).

3.2.4 Heat budget calculation

The change of temperature over time is driven by multiple factors, such as advection of temperature by currents, fluxes of heat between ocean and atmosphere, and vertical mixing (which transfers warm surface water to the ocean subsurface and colder subsurface water up to the surface). These forcings were analysed by calculating the upper ocean heat budget to a depth just below the ML (described below).

The time rate of change in temperature is governed by the following equation:

$$\frac{\partial T}{\partial t} = -\boldsymbol{u_H} \cdot \nabla_H T - w\frac{\partial T}{\partial z} + \nabla_H \cdot (\kappa_H \nabla_H T) + \frac{\partial}{\partial z}\left(\kappa_V \frac{\partial T}{\partial z}\right) \qquad (3.2)$$

where T is the model temperature, u_H and w are the horizontal and vertical velocities, z is depth, ∇_H is the horizontal gradient operator, κ_H and κ_V are the horizontal and vertical diffusivities. The first and second terms of the right-hand side represent the horizontal and vertical advection, the third is the horizontal diffusion and the last term is the vertical diffusion, which represents the change in temperature due to air-sea heat fluxes and vertical mixing. The total advection (horizontal plus vertical) and total vertical diffusion terms in equation 3.2 are calculated by the model while running in

diagnostic mode with daily timesteps. The horizontal diffusion term κ_H is very small and is considered a residual.

Equation 3.2 was volume averaged over region 2 and over a fixed depth surface layer of 15 m (justification provided below), and integrated in time to evaluate the contribution of each term to the development of anomalously high temperatures:

$$\frac{1}{V}\int_{\Delta t}\int_{V}\frac{\partial \mathrm{T}}{\partial \mathrm{t}}dV\,\mathrm{dt} = -\frac{1}{V}\int_{\Delta t}\int_{V}(\boldsymbol{u_H}\cdot\nabla_H T)dV\,dt - \frac{1}{V}\int_{\Delta t}\int_{V}\left(w\frac{\partial T}{\partial z}\right)dV\,\mathrm{dt} + \frac{1}{V}\int_{\Delta t}\int_{A}\left(\kappa_V\frac{\partial \mathrm{T}}{\partial \mathrm{z}}\right)_{z0}\mathrm{d}A'\,\mathrm{dt} + \frac{1}{V}\int_{\Delta t}\int_{A}\left(\frac{Q_{net}}{\rho_0\,cp} - \frac{(Q_{solar})_{z0}}{\rho_0\,cp}\right)\mathrm{d}A'\,dt + Res \tag{3.3}$$

where V is the volume in the region, A is area and Δt is time period. The first and second terms of the right-hand side represent horizontal and vertical advection, the third is vertical mixing at the base of the volume and the fourth is the surface flux contribution, calculated considering the incoming net heat flux at the surface minus solar radiation that penetrates at the base of the volume.

The horizontal advection term has been calculated considering its contribution at each open boundary of the study region:

$$-\frac{1}{V}\int_{\Delta t}\int_{V}\left(\boldsymbol{u_H}\cdot\nabla_H(T-T_0)\right)dV\ \mathrm{dt}$$

$$=-\frac{1}{V}\int_{\Delta t}\left[\int\int_{NE}u_{s(T-T_0)}dydz-\int\int_{SW}u_{s(T-T_0)}dydz\right.$$

$$\left.-\int\int_{NW}v_{s(T-T_0)}dxdz\right]\mathrm{dt}$$

(3.4)

where u_s is the alongshore velocity, v_s is the cross-shelf velocity and T_0 is the average temperature of the control volume and is used as the reference temperature in the heat advection calculation, following the approach by Lee et al. (2004) and Feng et al. (2008). As explained by Lee et al. (2004), when the volume is conserved changes in the reference temperature do not affect the total advection, but when evaluating the temperature advection in a single direction, this is not the case. When the mass is not conserved, as when evaluating advection through a side, the unbalanced mass is assumed to be at the reference temperature, which would be 0°C if the term T_0 in equation 3.4 were missing. Instead, using the domain's mean temperature as a reference temperature T_0, we can evaluate the impact of heat advection at the borders of the domain on the mean temperature change. A similar approach was used by Wilkin (2006).

The vertical advection has been calculated as the difference between total advection (provided by model diagnostics) and horizontal advection. In this way, we can distinguish advection contributions across different boundaries. After closing the budget for the control volume, a 15-day moving average filter was applied to each heat budget term to eliminate advection due to the spring-neap tidal cycle, for visualization.

The MLD in region 2 was calculated to determine the depth of the heat budget and identify MLD changes throughout the event. We used the method and algorithm described in Lorbacher et al. (2006) based on the shallowest extreme curvature of near surface layer temperature profiles. This method assumes that the first local extreme temperature or density curvature profile is a distinguishing feature of the depth to which the most recent mixing events penetrate.

The MLD during summer months was evaluated using model data and CARS 2009 climatology for comparison (Fig. 3.6). The MLD calculated with CARS 2009 data and with the model temperature profile (averaged in the model region) are comparable (Fig. 3.6). In fact, despite the different horizontal and vertical resolutions, the model and CARS 2009 MLD are within 5 to 10 m of each other (Fig. 3.6).

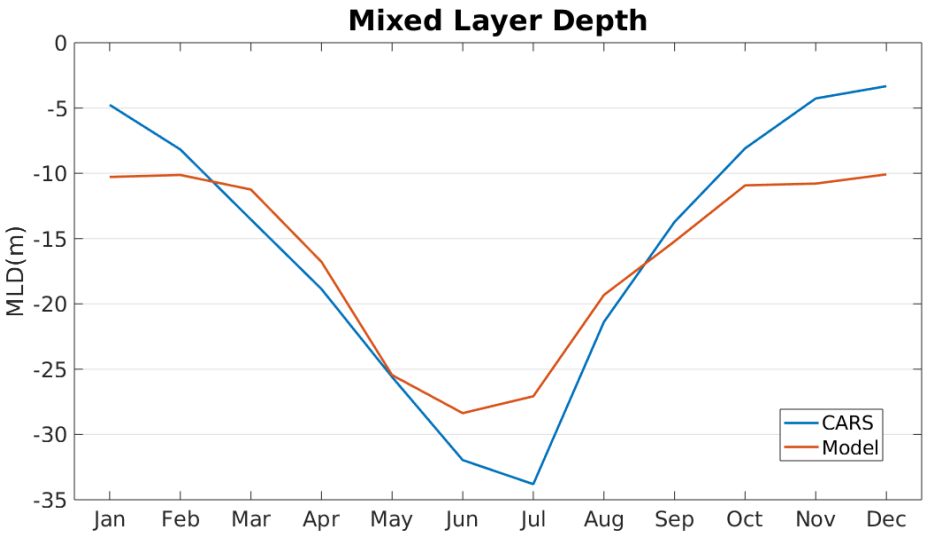

Figure 3.6: Monthly averaged MLD calculated with model data (red) and with CARS climatology (blue).

3.3 Tropical cyclone - ocean methods

3.3.1 Tropical cyclone composites

To study the characteristics of the thermal and dynamic ocean response to the passage of TCs in the Northwestern Australia region, a 20-year (1996-2016) composite of the ocean response was constructed comprising 85 TCs using temperature, salinity, and horizontal and vertical velocity data from BRAN. Every 6-hourly data point of each TC from the BOM BT database in the region between 105 °E and 130 °E and 5 °S and 30 °S (Fig. 3.7) was considered separately, for a total of 1396 data points during the 20-year period. Temperature composites were analysed to identify the common ocean energy response features including onset of temperature anomalies, maximum cooling at the surface, development of warm anomalies in the subsurface, and recovery times of these temperature changes.

To study the response of the ocean in different conditions TCs were composited by different criteria, including: all TCs during the study period, deep ocean and shelf regions, intensity and translation speeds, and cooling and warming seasons, with each described below.

First, TC impacts were grouped into “on shelf”, for data points located over bathymetry shallower than 200 m, and “deep ocean” for deeper locations, due to the unique bathymetry of the NWS. The TC data points on shelf were further divided according to the most common directions of motion with respect to the shelf: parallel (towards south-west) and perpendicular (towards the coast). TCs moving over the deep ocean close to the shelf edge and parallel to it (in the region 110 °E - 127 °E and 13 °S - 22 °S) were also separated by their distance to the coast to consider the influence of

the shelf edge. As a TC travels parallel to the coast (but slightly offshore), the wind over the shelf blows mostly parallel to the coast and it is expected to drive shelf Ekman downwelling which could further increase subsurface heat gain.

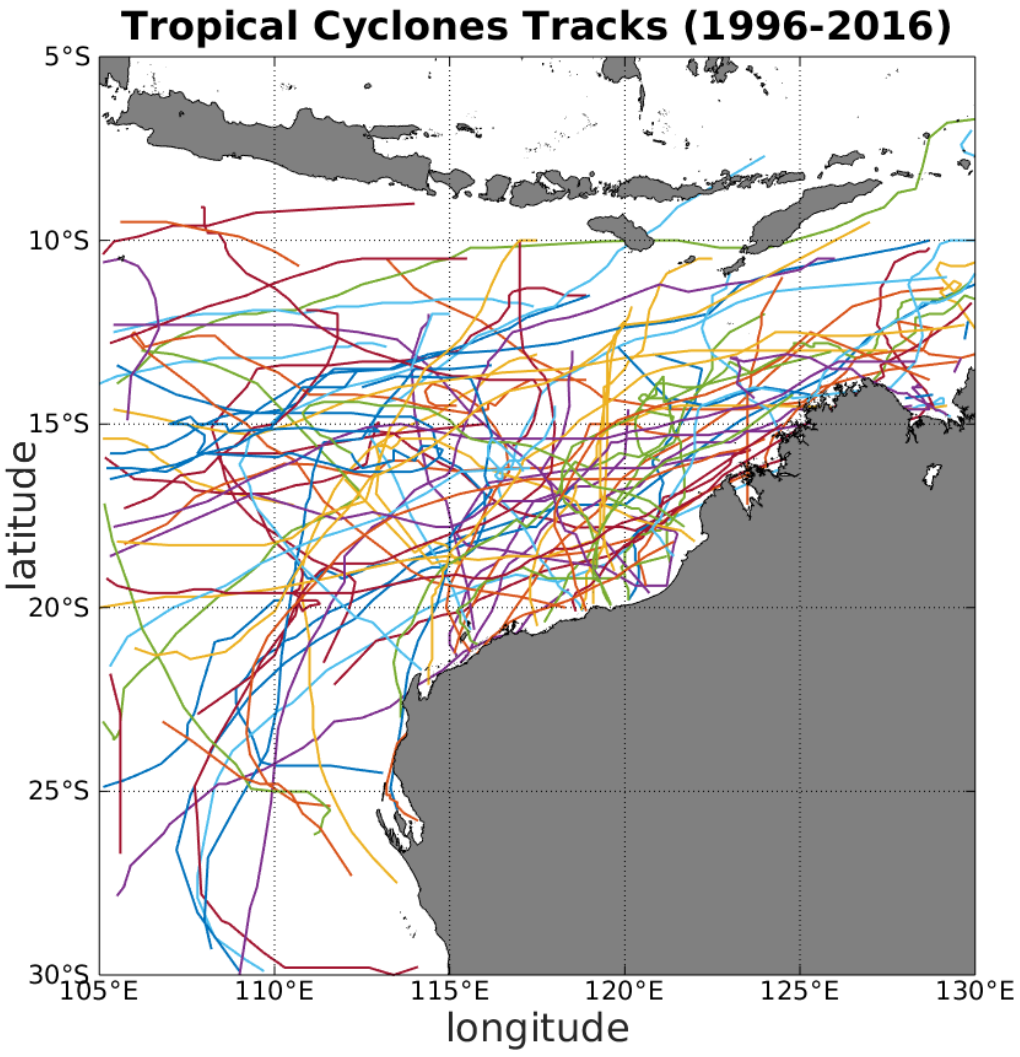

Figure 3.7: 85 Western Australia TC tracks from 1996 – 2016 used in the TC - ocean analysis.

As the TC data points over the shelf show more variability in current and temperature response, only deep ocean data points were considered for further analysis. Deep ocean TCs were separated based on intensity category and translation speed, to study the thermal responses induced by different TC dynamics. Intensity categories include: Cat 1 (34-47 kts), Cat 2 (48-63 kts), Cat 3 (64-85 kts), and Cat 4/5 (> 85 kts). TC translation speeds were divided into very slow (< 2 m/s), slow (2-4 m/s), fast (4-6 m/s) and very fast (> 6 m/s) based on the definition by Lin et al. (2017). These categories have been further simplified into weak (Cat 1-2) and strong (Cat 3 and above), fast (> 4 m/s) and slow (< 4 m/s).

Analysis was also performed based on the time of year in which the TC develops: “warming season” between November and February, and “cooling season” during or after March. This analysis assesses not only the effect of the pre-existing ocean temperatures and stratification on ocean temperature changes, but also the seasonal effect on their recovery after the TC passage, due to winter ML deepening.

The impacts of upper ocean structure were also analysed to assess the influence of pre-existing surface layer stratification. Entrainment of cold subsurface water into the ML could be inhibited across a barrier layer, which exists where a strong halocline (and hence density gradient) is present above the thermocline and the ML does not correspond to the isothermal layer (Chi et al., 2014). The barrier layer is defined as the layer separating the top of the thermocline (where the surface temperatures begin to decrease by 0.5 °C, also called isothermal layer) and the base of the surface ML, defined by a density threshold criteria (Chi et al., 2014). The presence of a barrier layer was determined by calculating the difference between the isothermal layer depth (ILD) and the MLD, following Haackman et al. (2019), where the ILD was calculated as the

depth at which the surface temperature decreases by 0.5 °C and the MLD has been calculated as the depth where the surface density increases by 0.1 kg/m^3. Then the influence of the barrier layer was assessed by calculating the mean barrier layer 3 days before the TC passage. This TC composite analysis has been separated into deep and shallow barrier layer cases, with 5 m being the threshold separating data points located over deep and shallow barrier layers. A value of 5 m was chosen as it is the minimum thickness required to alter the TC -ocean interactions (Haackman et al., 2019; Wang et al., 2011).

3.3.2 Temperature and ocean current analysis

To analyse energy changes during the forcing stage (from two days prior to five days after TC passage) and recovery stage (six to thirty days after TC passage), daily temperature anomalies were calculated as the difference from the seasonal climatology and as the difference from two days prior to TC passage. For the seasonal climatology, a daily 20-year regional ocean climatology was calculated to a depth of 2000 m at each BRAN grid point. To remove any strong seasonal signal, a 11-day moving average was then applied to the 20-year climatology. To further reduce the effects of non-TC related processes, the temperature changes were further analysed by subtracting the seasonal anomaly on each day from the seasonal anomaly two days before the arrival of the TC at each location. Two days prior to TC arrival was chosen because the influence of the TC outer windfield should be negligible. These temperature anomalies were used throughout for the temperature and OHC analyses. The choice to analyse the ocean condition for a maximum of 30 days after the TC forcing was to limit the effect of longer-term processes which could influence the

dynamics of the region (such as the passage of other TCs, or non-TC upwelling / downwelling events).

A variety of spatial averages and TC cross-track profiles of temperature, vertical currents and horizontal current divergence were used to explore the complexity of the ocean response. One-hundred km radius average profiles were calculated to demonstrate the features and dynamics driving the main column cooling region, which contains the primary upwelling region directly underneath the TC. Composite cross-track sections extending to distances of 1000 km either side of the track perpendicular to the TC direction of motion were analysed to encompass all processes, including mixing (which typically occurs to the left of track in the Southern Hemisphere to distances of 900 km, and down to no more than 500 m) and downwelling (which occurs out to distances of more than 500 km from the track and down to 1000 m). The composite MLD was also studied as its changes induced by the TC passage are strongly connected with the vertical mixing processes which cool the ocean surface and warm the subsurface. To assess the influence of the presence of a thick barrier layer on the mixing processes and on the development of the temperature anomalies the annulus region between 100 km and 300 km from the track has been considered. This annulus region was chosen to exclude the region of maximum upwelling beneath the track and focus on the surrounding region where the cooling is still significant and the MLD entrainment is driving the cooling.

A student t-test was used to compare the inner core values of SST, temperature at 300-m depth and vertical velocity at 100 m depth for the several cases considered. P-values less than 0.05 were considered as statistically significant.

3.3.3 BRAN validation for TC ocean response

BRAN SST analysis of the TC-induced temperature anomalies are validated against CCI SST, and BRAN temperature profiles are compared to Argo profiles. It is noted that BRAN was not designed for modelling the ocean under TC conditions, and the drag coefficient parameterization implemented in BRAN may not be best suited for this purpose and could overestimate ocean mixing. Furthermore, BRAN is forced at the surface by the ERA-Interim dataset which tends to underestimate TC intensity because of its relatively coarse resolution (Aijaz et al., 2019), which may have a tendency to reduce the ocean mixing.

Figure 3.8 shows the comparison between CCI and BRAN SST for 1396 TC composites. Each daily temperature value is calculated as the temperature anomaly on that day minus the temperature 2 days prior to the TC arrival at that location (without removing the seasonal cycle of temperature). There is a reasonable comparison between the two datasets, with BRAN developing a slightly colder wake compared to the CCI data between -1 and +5 days after the TC arrival. The CCI largest temperature anomaly occurs approximately one day later than in the BRAN analysis (Fig. 3.8), on Day 6 after the passage of the TC compared to Day 5 for BRAN. This delay may be partially due to uncertainties in SST satellite data over cloudy regions after the passage of a TC (Merchant et al., 2019). However, the traces are comparable, including the rate of recovery and eventual -0.2°C residual cooling that remains more than 30 days after the TC passage (Fig. 3.8). This demonstrates that the BRAN data are appropriate to analyse TC-induced thermal changes in the ocean.

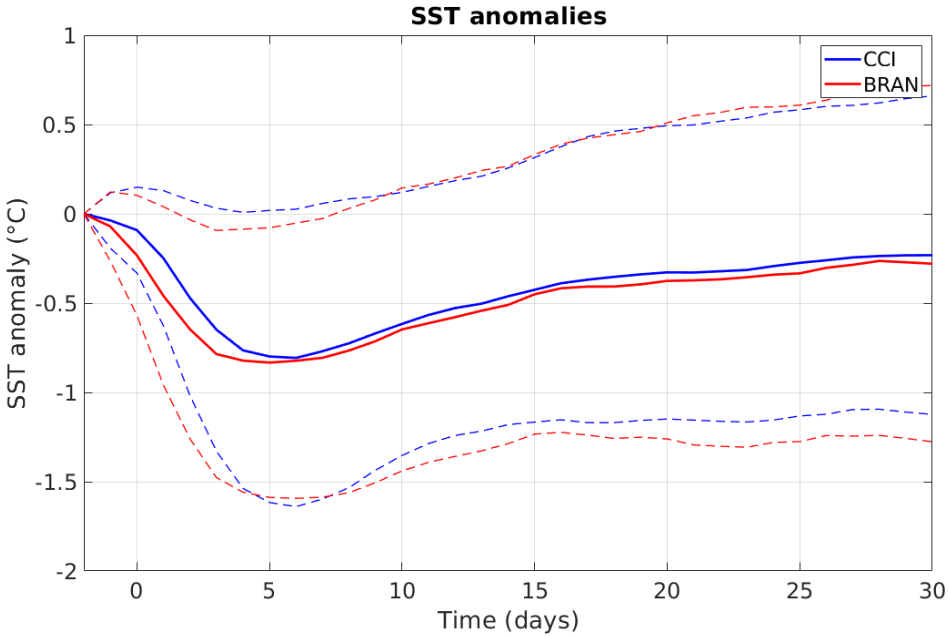

Figure 3.8: CCI SST anomalies (blue line) compared to BRAN SST anomalies (red line) for 1396 composited TC data points, centred on TC location. Data are averaged over 100 km radius, and anomalies are calculated by subtracting the average SST 2 days before TC arrival from each daily average. Dashed lines show standard deviation.

The cross-track temperature anomalies timeseries for the 20-year composites separated into TCs located over the shelf and TCs located over the deep ocean show good similarity between CCI SST and BRAN SST (Fig. 3.9). Both CCI and BRAN capture wider cold anomalies over the shelf locations (Fig. 3.9b and d) and narrower cold anomalies over the deep ocean (Fig. 3.9a and c). However, the CCI and BRAN composites over the shelf appear to differ as BRAN captures stronger cold anomalies shifted to the left of the track (Fig. 3.9b and d), perhaps due to the coarser spatial resolution that makes it more difficult to capture the complex dynamics near the coast in the BRAN model.

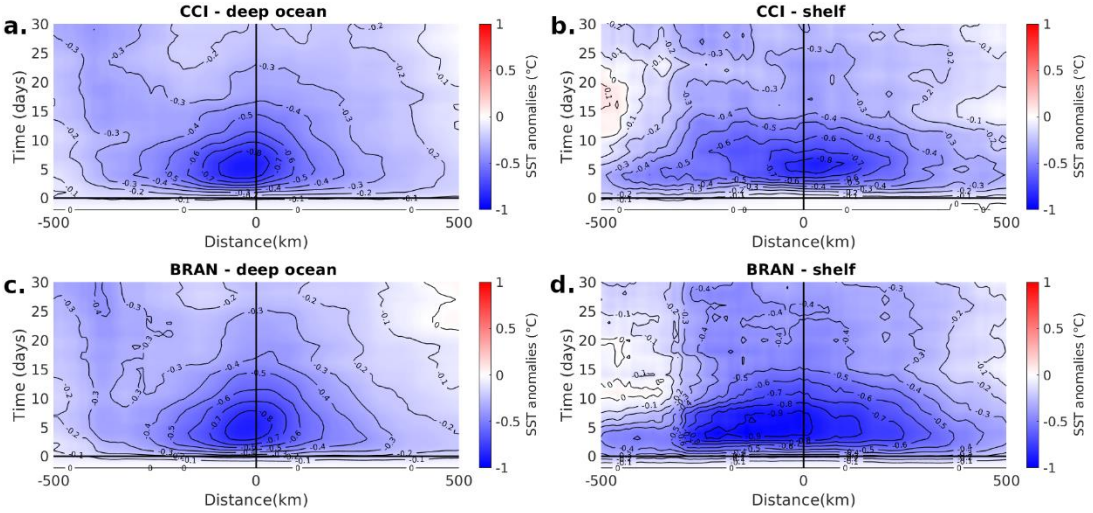

Figure 3.9: Cross-track SST anomaly compared to 2 days before the TC passage, centred on the TC centre for: (a), (b) CCI; and (c), (d) BRAN for all data points: (a), (c) over the deep ocean (using 459 data points); and (b), (d) on the shelf using 937 data points) extending to 30 days after the TC passage.

Timeseries comparisons between Argo float data and BRAN were performed for 21 TCs, for which Argo float data in the proximity of the track were available. As can be seen for TCs Narelle (Fig. 3.10), Nicholas (Fig. 3.11) and Quong (Fig. 3.12), there was good agreement between Argo observations and BRAN data, particularly below the surface after the TC passage. Any differences are mostly due to the interpolation to fill the temporal gaps between Argo floats (which are measured every 10 days, at the dashed lines in the top panels of Figs. 3.10, 3.11 and 3.12) to the daily BRAN data.

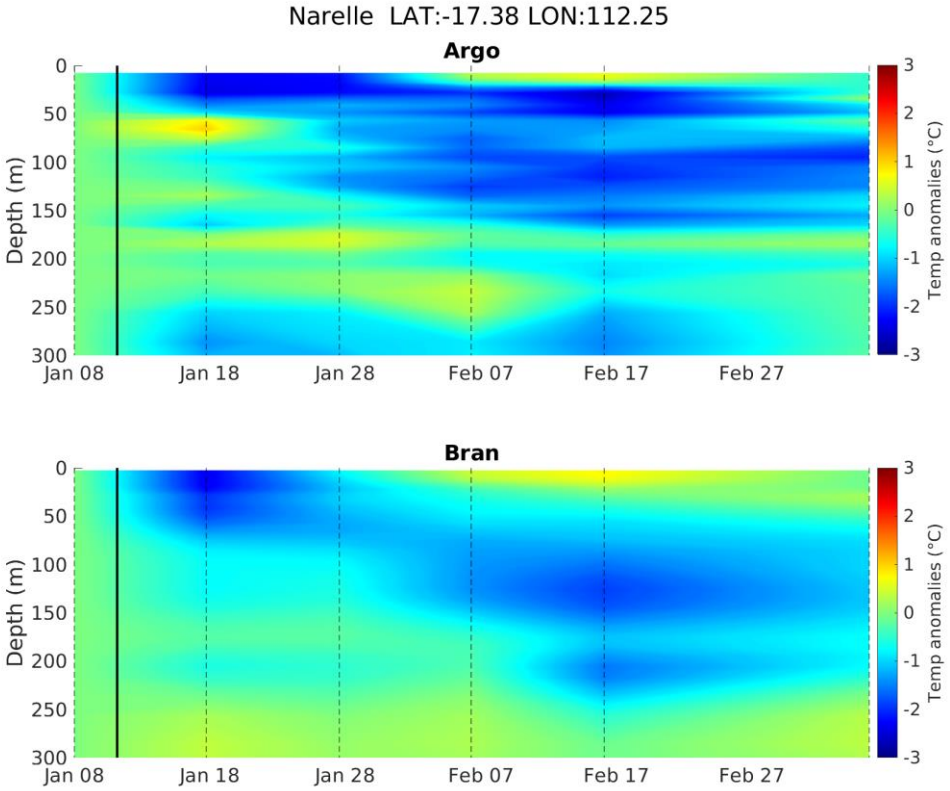

Figure 3.10: Temperature-depth profiles for Argo (top) and BRAN (bottom) at 17.38 °S, 112.25 °E before (left of the solid black line), during (at the solid black line), and after (right of the solid black line) the passage of TC Narelle (2013). The dashed vertical lines represent the days that Argo profiles were recorded at this location.

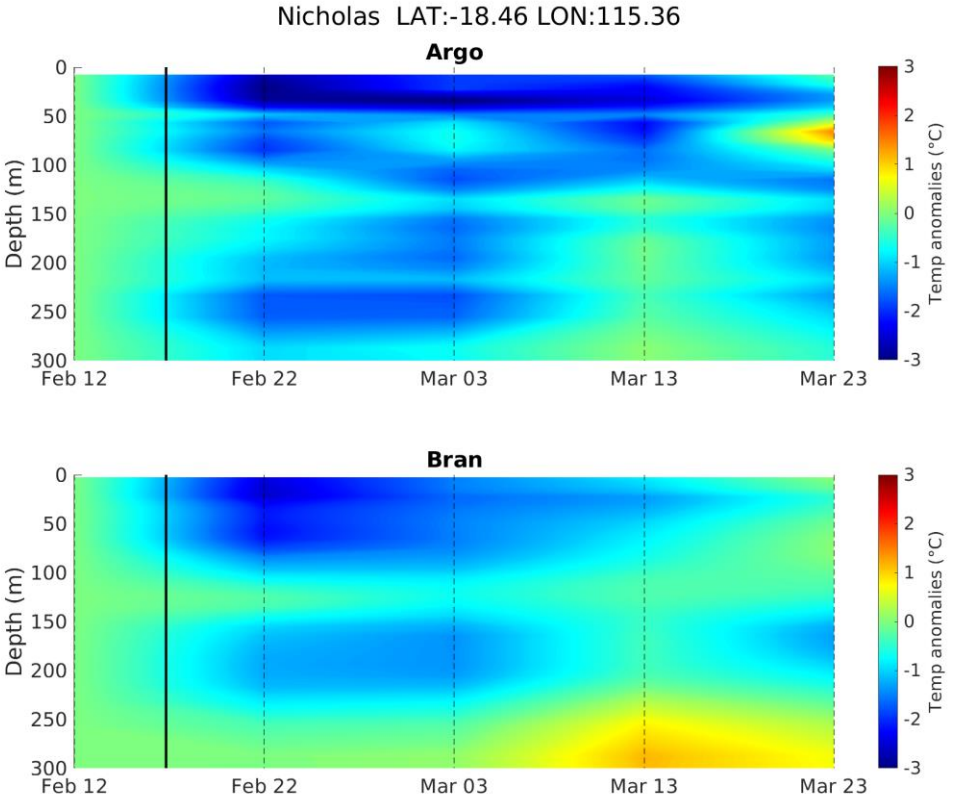

Figure 3.11: As in Fig. 3.10 but for TC Nicholas (2008).

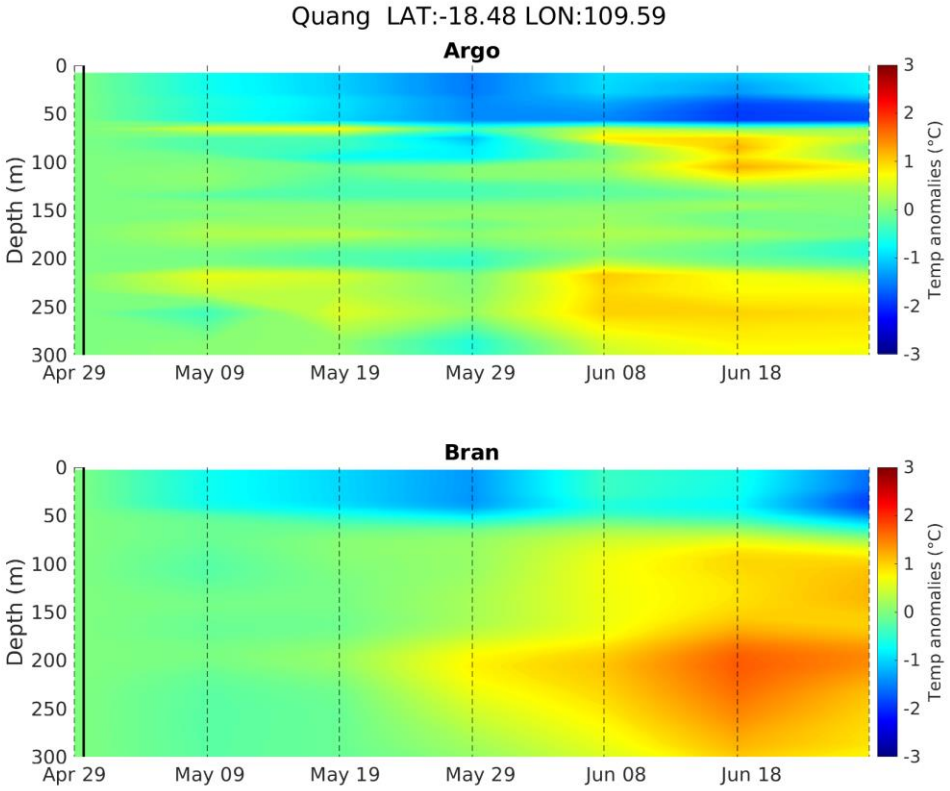

Figure 3.12: As in Fig. 3.10 but for TC Quang (2015).

Overall, these comparisons provide confidence that BRAN represents the ocean temperatures well during and after the passage of a TC. Therefore, the analyses of TC induced temperature changes will be conducted using BRAN data.

3.3.4 Ocean Heat Content changes due to tropical cyclones

The total OHC (the integrated water column temperature profile) within a large region is expected to increase with the passage of a TC, because during the recovery stage the surface cold anomalies recover quickly due to air-sea fluxes while the subsurface warm anomalies remain for longer, (Emanuel., 2001, Sriver and Huber, 2007). To assess the overall lasting thermal changes due to a TC we calculated the

OHC anomaly between depths z_1 and z_2 compared to 2 days before the TC passage after removing the seasonal cycle:

$$OHC_{rate} = c_p \int_{z_2}^{z_1} \rho(z)\big(T(z) - T_{clim}(z)\big)dz \qquad (3.5)$$

where c_p is the sea water specific heat content, which is considered constant and equal to 3985 J g^{-1} C^{-1} (Glenn et al., 2016), $\rho(z)$ is the density of the water column at each depth between z_1 and z_2, $T(z)$ is the temperature profile and $T_{clim}(z)$ is the climatological temperature profile. Removing the climatology from the temperature profile ignores seasonal changes in the month following the TC.

The OHC was averaged in the region within 100 km (inner core region), 500 km (outer core region) and 1000 km radius (whole region) around the TC centre and in the annulus region of radius between 500 km and 1000 km from the track (outer region). Layers of different depths from the surface of the ocean, 50 m layers between the surface and 1000 m deep and 500 m layers from the surface to 2000 m deep are studied to assess the OHC changes induced by TCs at different depths and distances from the track due to different physical processes. To study the recovery of the OHC cold anomalies driven by the passage of a TC and to assess where the major warming happens during the month following the TC passage, the OHC changes from Day 5 are analysed. The OHC changes of TC data points with different characteristics were composited to study a general deep ocean case, the difference in the OHC changes driven by warming season versus cooling season TCs, and the differences driven by different TC translation speed and intensity.

3.3.5 Tropical cyclone heat budget

OHC changes are driven by several processes including horizontal advection, upwelling and downwelling (or vertical advection), vertical mixing, and air-sea heat fluxes. To separate the processes that affect the OHC changes the OHC budget was calculated following Huang et al. (2009):

$$OHC_{rate} \approx Hadv + Vadv + Vdiff \tag{3.6}$$

where OHC_{rate} is the time rate of OHC change and on the right hand side are horizontal advection ($Hadv$), vertical advection ($Vadv$), and the vertical diffusion ($Vdiff$) terms, which includes the vertical mixing and the air-sea heat fluxes terms. The horizontal diffusion is generally negligible in the ocean and the term is therefore neglected in eq. 3.6.

We expect strong contributions by vertical advection, which is due to upward or downward transport of temperature by the vertical currents and can be used as proxy for the upwelling beneath the track and downwelling further away on the side. The strong TC winds and their circular pattern force strong horizontal currents at the surface of the ocean. The horizontal advection represents the heat transported away from the region beneath the TC centre by the divergent horizontal currents, or towards the track in the following period when the horizontal currents reverse and converge towards the track.

For this budget analysis, the temperature climatology has not been considered and the seasonal cycle has not been removed for simplicity. The time rate of change of the OHC was calculated as

$$OHC_{rate} = c_p \int_{z_2}^{z_1} \rho(z) T(z) dz\,, \tag{3.7}$$

and the horizontal and vertical advection terms were calculated using BRAN temperature and velocity data as

$$Hadv = -\mathrm{c_p}\rho \cdot \boldsymbol{u_H} \cdot \nabla_H T = -c_p \rho \left(u \cdot \frac{\partial T}{\partial x} + v \cdot \frac{\partial T}{\partial y} \right), \tag{3.8}$$

and

$$V\mathrm{adv} = -\mathrm{c_p}\rho \cdot w \frac{\partial T}{\partial z}\,, \tag{3.9}$$

where the vertical diffusion term ($Vdiff$), which represents vertical mixing of the water masses and change in temperature due to air-sea heat fluxes, was approximated as the residual of equation (3.6).

Equation (3.6) was then integrated between the surface and 500 m to give

$$\int_{500}^{0} OHC_{rate}\, dz \approx \int_{500}^{0} Hadv\ dz + \int_{500}^{0} Vadv\ dz + \int_{500}^{0} Vdiff\ dz, \tag{3.10}$$

which was used to analyse the temporal change of the OHC along the cross-track direction.

To understand the processes which contribute to OHC changes at different depths during the forcing and recovery stages, equation (3.6) was integrated in time using several integration periods

$$OHC \approx \int_{t_1}^{t_2} Hadv\ dt + \int_{t_1}^{t_2} Vadv\ dt + \int_{t_1}^{t_2} Vdiff\, dt\,, \tag{3.11}$$

including the “whole period” (day -2 to day 30), the “forcing stage” (Day -2 to Day 5, when the most cooling is expected to happen), and the “recovery stage” (Day 5 to Day 30) to assess which processes contribute to the recovery of the cold anomalies and to the development of warm anomalies after the TC has left the region.

Chapter 4. The 2012/2013 Marine Heat Wave on Australia's North West Shelf

Note: sections of this chapter are based on a published paper.

Maggiorano, A., Feng, M., Wang, X. H., Ritchie, L., Stark, C., Colberg, F., & Greenwood, J. (2021). Hydrodynamic drivers of the 2013 marine heatwave on the North West Shelf of Australia. *Journal of Geophysical Research: Oceans*, 126(3), e2020JC016495.

4.1 Introduction

During the austral summer of 2012/2013 a particularly strong MHW developed on the NWS, beginning in December 2012 and peaking in February 2013 (Feng et al. 2015; Xu et al. 2018). This MHW resulted in warm SST anomalies during January and February of over 3°C that were mostly confined northeast of the North West Cape in the south-western region of the NWS (Fig. 2.1) (Xu et al., 2018) and caused coral bleaching and other significant ecological impacts (Feng et al. 2015; Xu et al., 2018). The impacts of the MHW stresses the importance of understanding the driving mechanisms behind the evolution of this strong event. Xu et al. (2018) compared this MHW to 2010/2011 event. They found that the 2010/2011 event occurred over a larger area further to the south and was driven by a stronger poleward heat advection due to a more intense La Niña event, while the 2012/2013 event was mostly confined north-east of the North West Cape and was driven by higher surface heat fluxes into the

ocean (Feng et al. 2015; Xu et al., 2018). Here we explore in more detail the 2012/2013 MHW using a high-resolution ocean model with diurnal forcing, which provides a better temporal resolution than previous work. Specifically, differences between the 2012/2013 summer conditions and climatological conditions in the region, as well as the connection between the 2012/2013 MHW and its large-scale forcing, are investigated. Xu et al. (2018) identified that different advection patterns on the NWS lead to differences in development between the two MHW events, but the advection patterns were not fully investigated. We further investigate the advection patterns over the shelf region, particularly during the temperature increase in summer 2012/2013 compared to climatology, to better understand the cause of the MHW's long duration.

4.2 The marine heatwave period

CCI SST data were used to define MHW peaks during late 2012 and early 2013 following the metrics described by Hobday et al. (2016; 2018) (Fig. 4.2) in the three regions highlighted in Fig. 4.1.

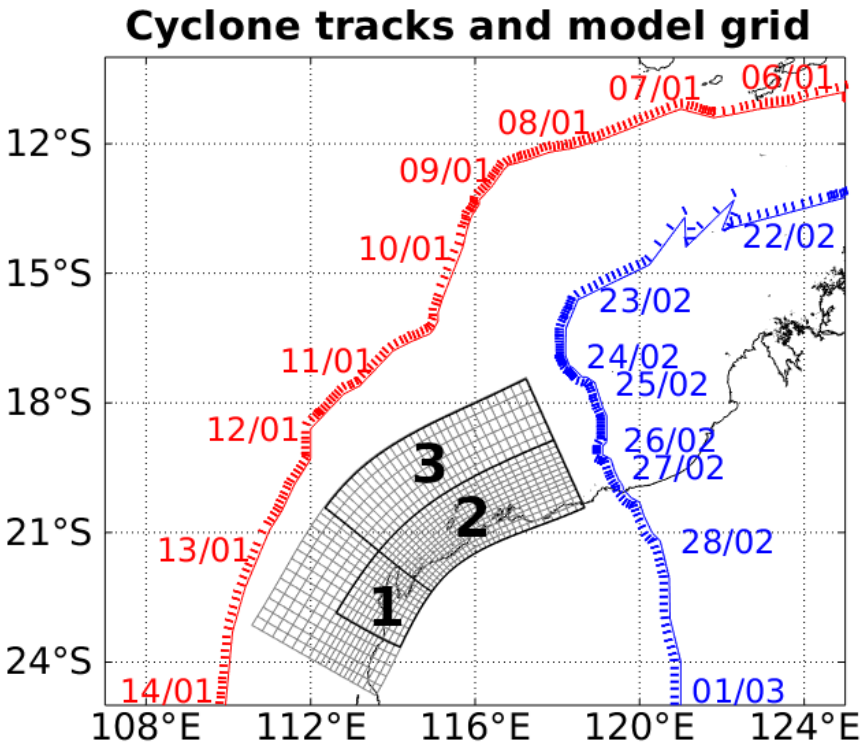

Figure 4.1: Study region with model grid with the three regions for the MHW study highlighted and the track of TC Narelle (in red) and Rusty (in blue).

The three regions experienced different MHW days, although the overall MHW period was approximately the same. Region 1 experienced temperature anomalies above the 90th percentile threshold from 25 December to 7 March (72 consecutive MHW days). In Region 2 the MHW developed and decayed earlier from 13 December to 2 March (lasting 79 consecutive days). Two peaks in the MHW, separated by more than 5 days, developed in Region 3: the first from 20 December to 11 January (22 consecutive days); and the second from 28 January to 2 March (33 consecutive days). Between these two peaks the SST anomalies remained positive, and this cooler period was probably due to the passage of TC Narelle (early-mid January 2013) just offshore from Region 3 (Fig. 4.1). The MHW in Region 2 exceeded

the threshold of twice the difference between the 90th percentile and the 30-year SST climatology of the region (Fig. 4.2) between 17 and 23 February and can be categorized as a strong MHW (Hobday et al., 2018). The cumulative intensity of the MHW was 146 °C day in Region 1, 131 °C day in Region 2, and in Region 3 was 34°C day for the first peak and 50°C day for the second peak (a total cumulative intensity of 84 °C day).

Fig. 4.2 also shows SST anomalies from the 30-year CCI climatology (used to define the MHW period) and from 7-year (2009-2016) CCI and model climatology for model validation. The anomalies calculated using a 7-year climatology are lower than the 30-year CCI climatology anomalies for both CCI and the model. However, the SST anomalies to 7-year model and CCI climatology compare well with the 30-year CCI anomalies and have the same temporal evolution.

The focus of the remaining analysis will be mostly on MHW development and characteristics in Region 2. This region was chosen as it is where the MHW overcame the threshold to be classified as a strong MHW (Fig. 4.2) and the model had the best agreement with observations (Figs. 4.2e and 3.5). For the heat budget time integration, two periods were considered: the fast warming period, from the minimum temperature anomalies to the first MHW peak, and the peak period of the MHW, between the first and last temperature anomaly peaks (Fig. 4.2e).

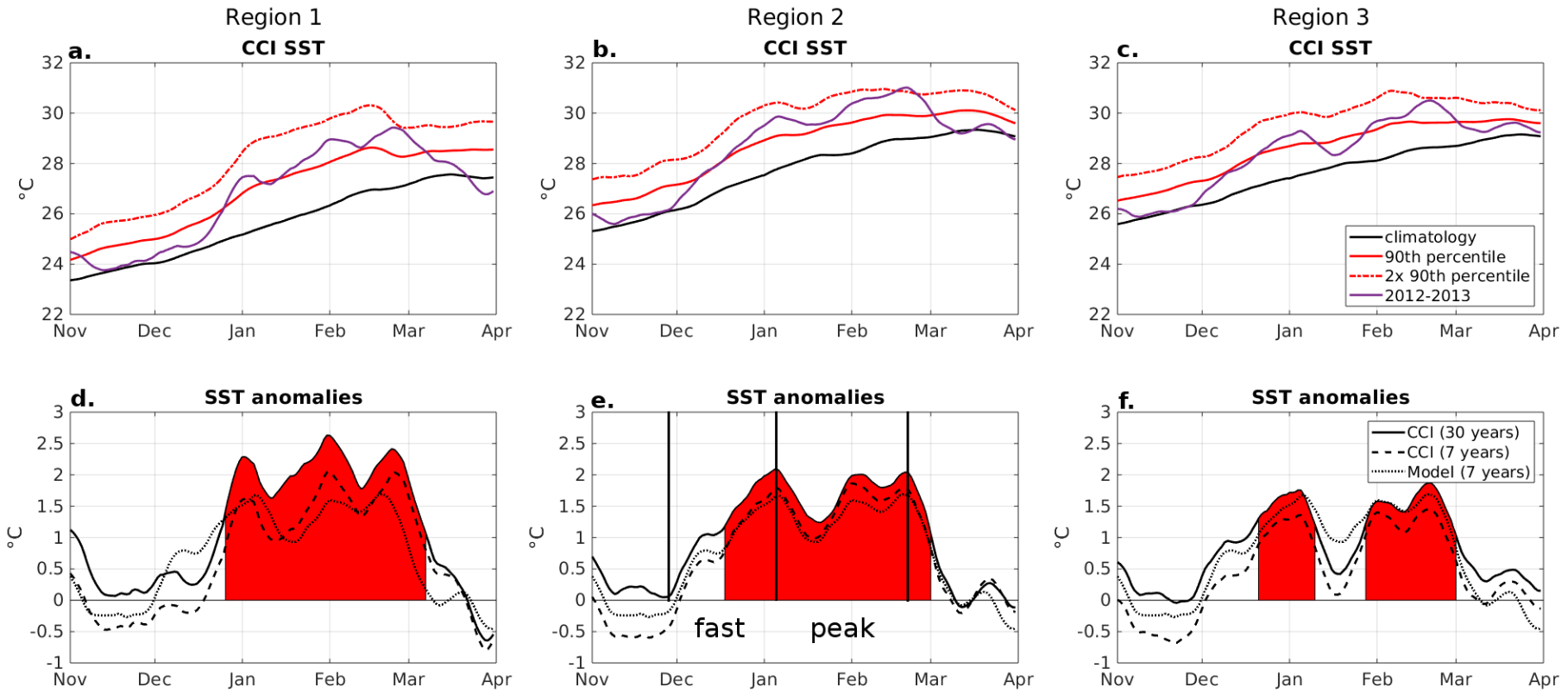

Figure 4.2: 30-year CCI SST climatology (black line), 90th percentile (solid red line), twice the 90th percentile (dotted red line) and SST (purple line) for the period between November 2012 and April 2013 for: (a) Region 1; (b) Region 2; and (c) Region 3. SST anomalies from the 30-year CCI climatology (solid black line) and from the 7-year model (black dashline) and CCI (broken black line) climatology for the period between November 2012 and April 2013: (d) Region 1; (e) Region 2; and (f) Region 3. The MHW periods are shaded in red.

4.3 Marine heatwave development

In region 2 uniformly distributed positive SST anomalies of approximately 1°C were evident starting in December 2012 (Fig. 4.3a), in agreement with regionally averaged SST anomaly timeseries (Fig. 4.2). During late December and the beginning of January, temperatures gradually increased (Fig. 4.2b and 4.2e) and the 20-day average shows SST anomalies up to 3°C (Fig. 4.3b). This corresponds to the first peak of the MHW indicated in Fig. 4.2e. Temperatures then decreased slightly at the end of January onshore just northwest of Dampier and also offshore in the northeast of the domain (Fig. 4.3c), and then increased again to between 3 and 4 °C during February (Fig. 4.3d), corresponding to the second peak. Compared to the first peak, these anomalies were higher in the southern part of the domain and along the coast (Fig. 4.3d). From late February, SST anomalies decreased, indicating the beginning of the MHW decay. The anomalies during the last 10 days of February and first 10 days of March were still positive in the southern part and became neutral in the north (Fig. 4.3e). By the end of March, the MHW had decayed and there were negative SST anomalies in the southern part (Fig. 4.3f).

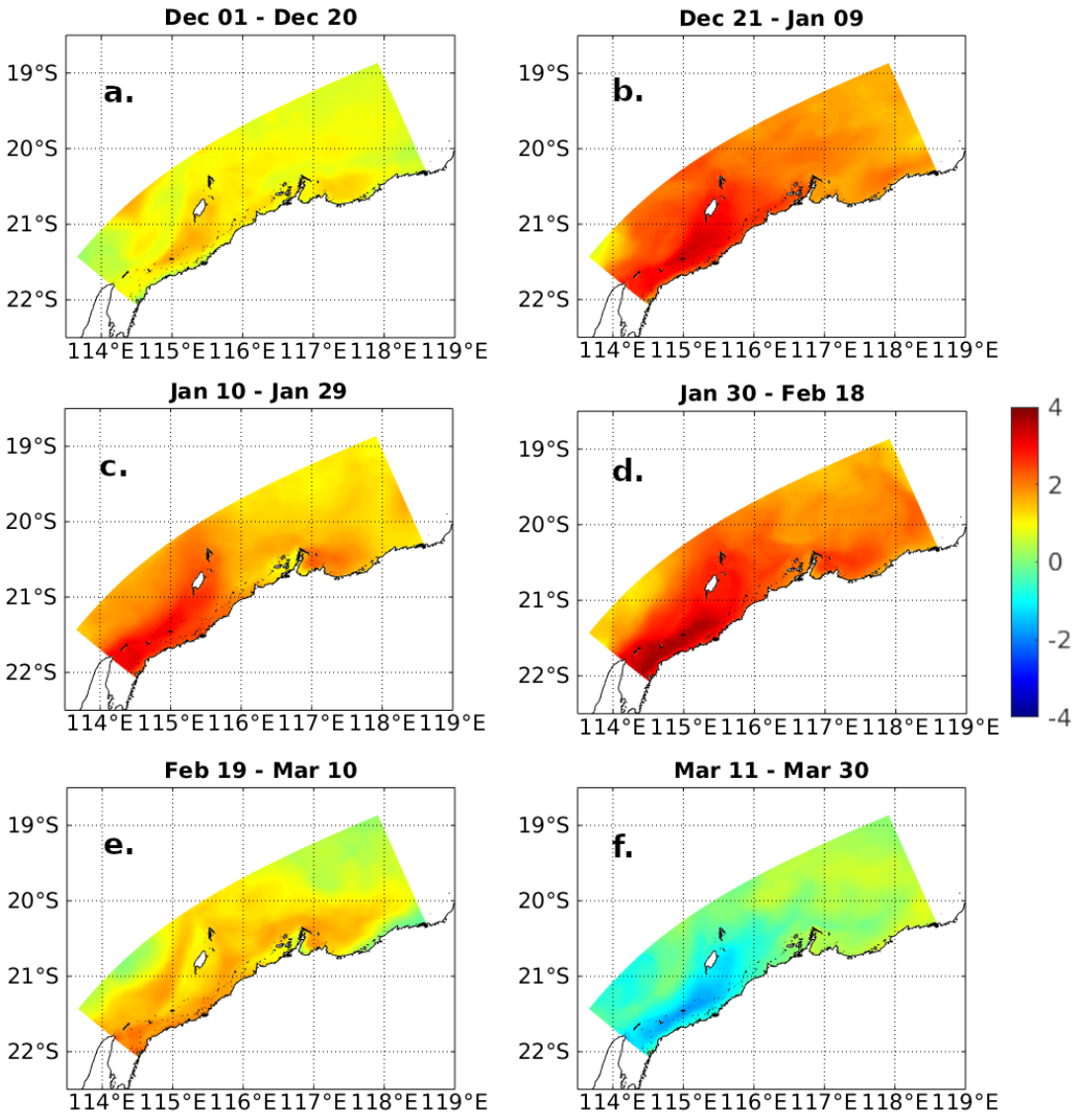

Figure 4.3: Modelled SST anomalies in region 2 as 20-day averages for: (a) 1 - 20 December; (b) 21 December - 9 January; (c) 10 - 29 January; (d) 30 January - 18 February; (e) 19 February - 10 March; and (f) 11 - 30 March.

Fig. 4.4 shows the temporal evolution of the spatially averaged temperature profile and the MLD from the model. In the model climatology, the upper ocean becomes steadily more stratified and the isotherms below the ML gradually deepen between November and March. During summer 2012/2013, the SST increases faster

during December and the water is warmer than normal below the surface due to a faster deepening of isotherms. Significant temperature anomalies above 2°C are evident up to 120 m depth (Fig. 4.4c). Anomalies at subsurface between 60 and 120 m are already positive during November and December, one month before the MHW develops at the surface. The maximum temperature anomaly during the middle of January was up to 4 °C (recorded between 60 and 100 m depth, Fig. 4.4c), at the same time when there was a small decrease in SST anomalies (Fig. 4.2e). Anomalies between 40 and 120 m appear to dissipate at the beginning of February, but last longer near the surface (Fig. 4.4c). At the end of February, the anomalies reduce throughout the water column, possibly following an upwelling event that could have been driven by the passage of TC Rusty just north of the domain (Fig. 4.1). However, the region considered is mostly over the continental shelf (Fig. 3.1) and the number of data points at higher depths is small, so the following analyses concentrates on the heat budget in the top part of the water column, just below the MLD.

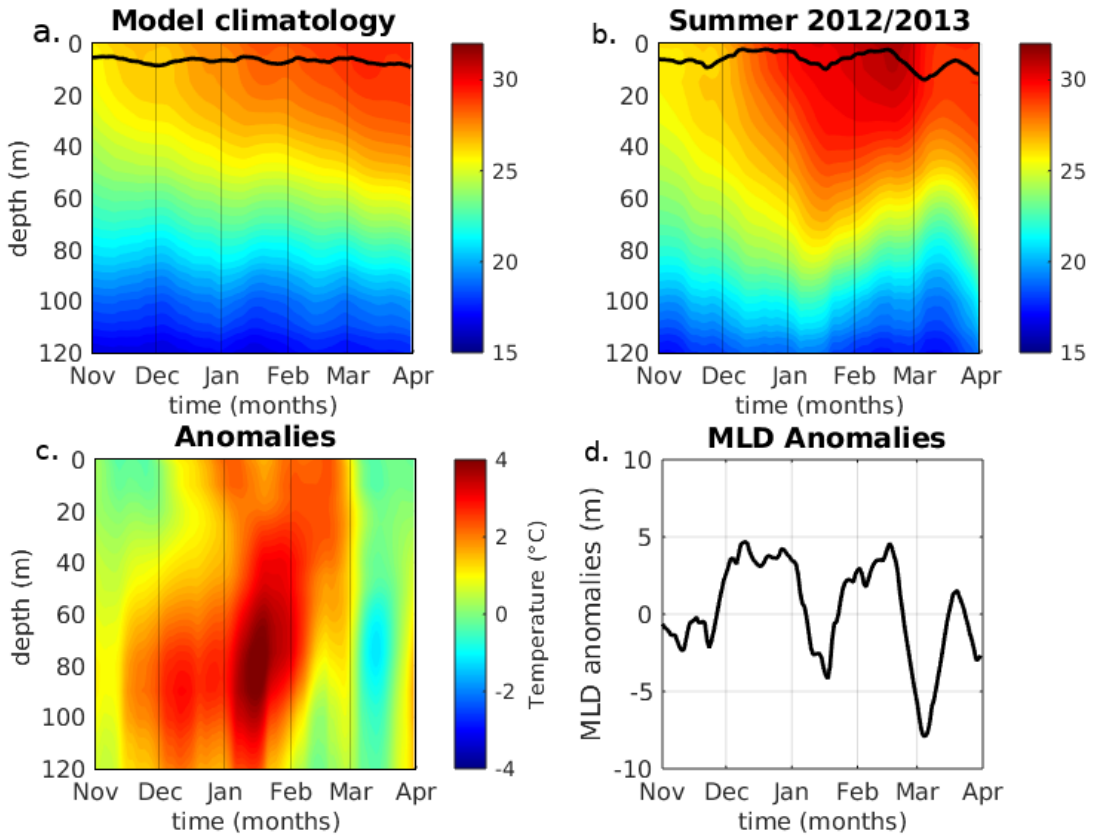

Figure 4.4: Averaged temperature profile (°C) for region 2 for: (a) the 7-year model climatology, with MLD overlaid with a black line, (b) summer 2012/2013 with MLD overlaid, (c) the temperature difference between (a) and (b), and (d) the MLD difference between (a) and (b). In (d), positive anomalies denote shallow MLD.

The region average MLD anomalies show a shallower MLD for most of the period between December and February, with two peaks of MLD deepening mid-January and end of February (Fig 4.4b), possibly caused by TCs Narelle (early-mid January, Fig. 4.1) and Rusty (end of February, Fig. 4.1).

The monthly average MLD (Fig. 4.5) is significantly shallower during December compared to model climatology especially in the northern part of the domain and slightly shallower during January and February (also shown if Fig. 4.4a,

b and d). The model MLD gradually begins to deepen leading into cooler months between March and April (Fig. 4.4).

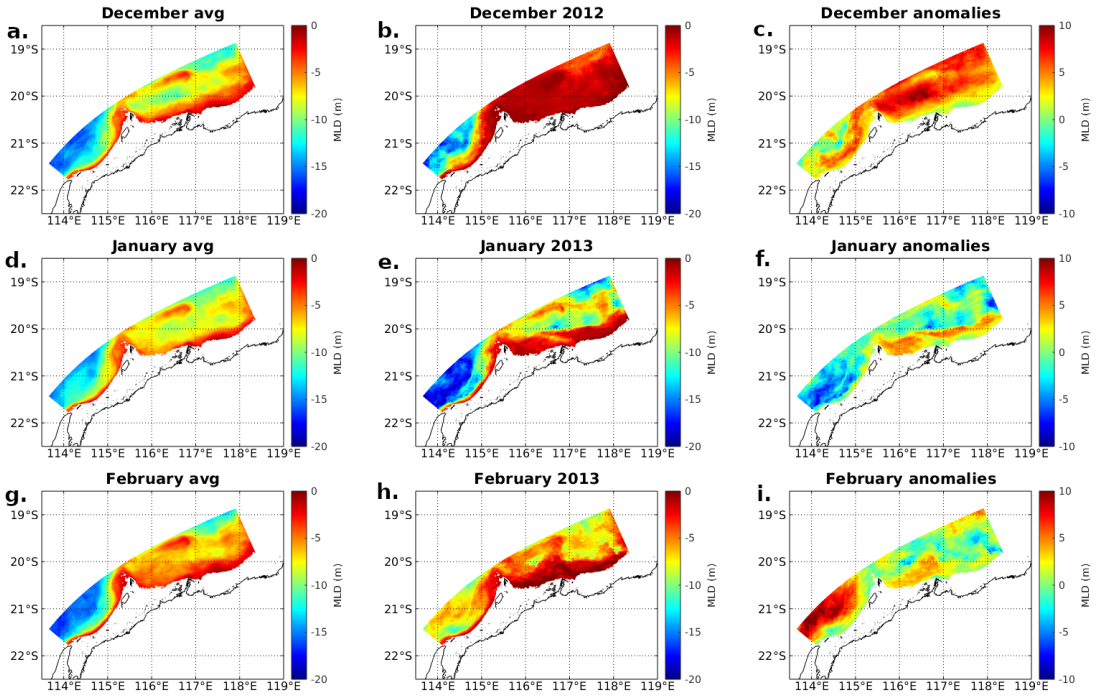

Figure 4.5: Average MLD for: (a), (d), (g) the model climatology; (b), (e), (h) summer 2012/2013; and (c), (f), (i) the difference between the two for the months of December, January and February in region 2.

4.4 Heat budget analysis

The ML is quite shallow during the summer months, rarely deepening below 15m, (Figs. 3.6 and 4.5) and based on the monthly mean model MLD (Fig. 4.5) a value of 15 m was chosen for the upper ocean heat budget analysis. Note that missing MLD values in Fig. 4.5 are due to bathymetry near the coast being shallower than the MLD.

The individual heat budget terms are shown in Fig. 4.6. We also tested a deeper layer of 20 m (the maximum depth reached by the ML in summer, Fig. 4.5) but found

no significant differences (Figs. 4.6 and 4.7). Fig. 4.6a and b shows that air-sea heat fluxes provide the major contribution to temperature increases during austral summer, as also reported by Santoso et al. (2010). The total contribution of the advection term for climatology is negative between the end of November and beginning of March (Fig. 4.6a), showing that heat is removed from region 2 during summer by both horizontal and vertical advection. Vertical mixing at the bottom of the control volume is normally negative and helps cool the surface layer (Fig. 4.6a).

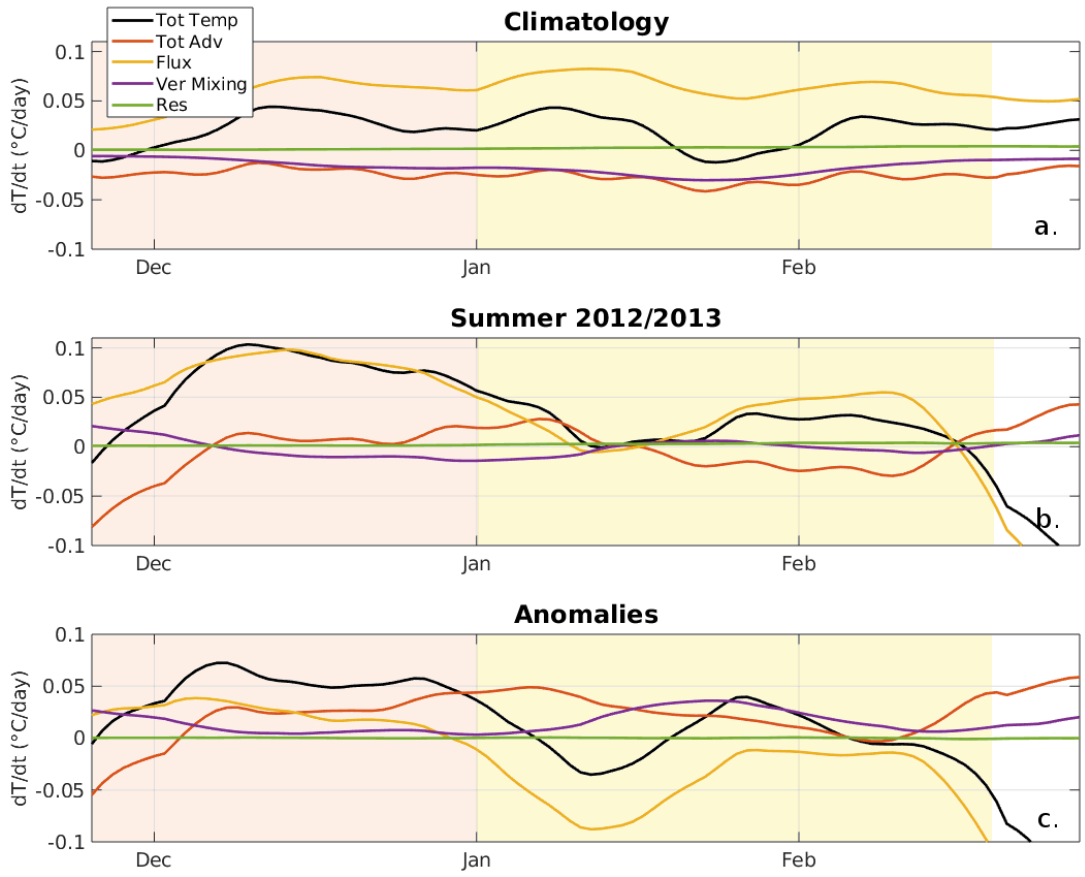

Figure 4.6: Individual heat budget terms (total temperature rate of change, total advection, air-sea net heat flux, vertical mixing at the bottom of the volume, and residuals), from eq. (1) volume averaged over region 2 and the upper 15 m of the water column for: (a) model climatology; (b) summer 2012/2013; and (c) the difference. Shaded regions indicate fast warming (red) and peak period (yellow).

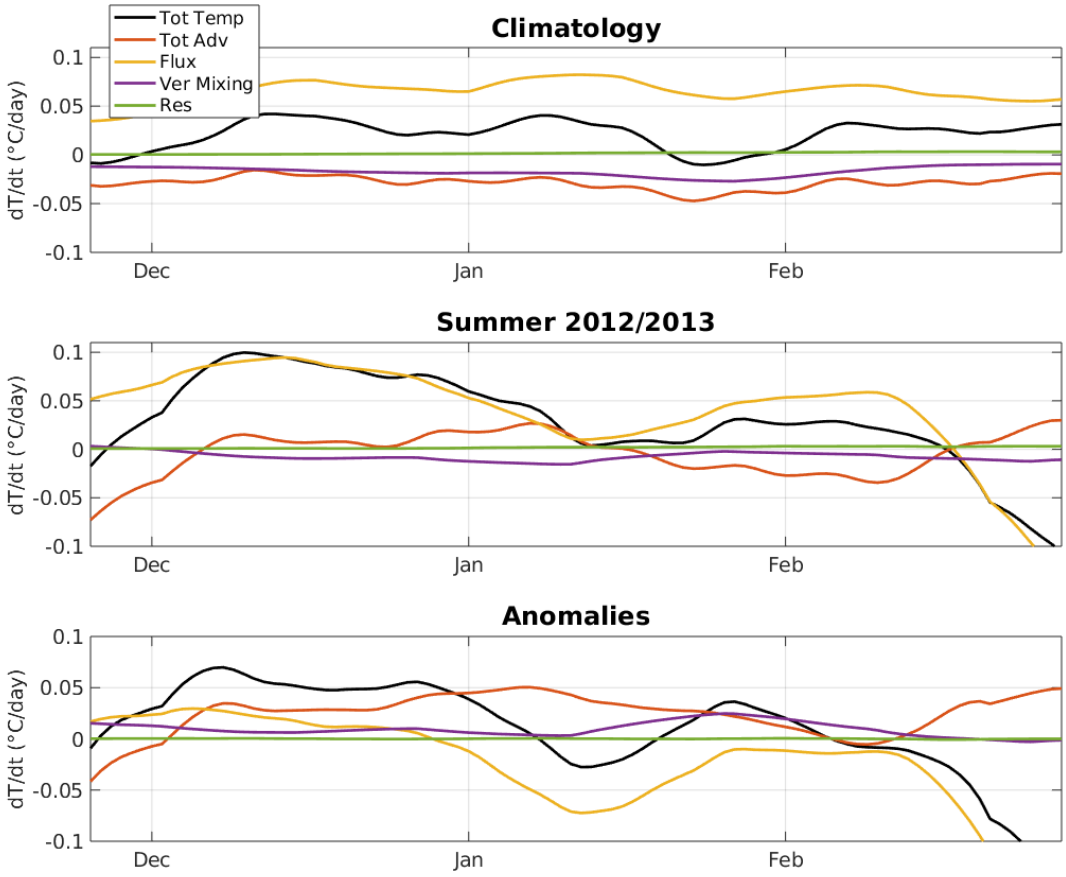

Figure 4.7: Same as figure 4.6 for the top 20 m of the water column.

At the end of November 2012, when SST anomalies began to develop, the steep increase in advection and an increase in net surface heat flux into the ocean drove a temperature increase (Fig. 4.6c). During December both the net surface heat flux and total advection anomalies were positive, adding heat into the region when the MHW developed, compared to climatology (Fig. 4.6c and Table 4.1).

Table 4.1: Time integrated heat budget terms (including horizontal, vertical and total advection, net surface flux, vertical mixing) for the climatological average, summer 2012/2013 and anomalies in the fast warming period (26 November- 1 January), in the peak warming period (1 January-20 February) and time integrated horizontal advection across the three open boundaries during the full period (26 November-20 February).

	Hadv (°C)	Vadv (°C)	tot adv (°C)	Net Sflux (°C)	Vmix (°C)	Tot (°C)	Res (°C)
Fast warming period							
climatology	-0.33	-0.48	-0.80	2.04	-0.46	0.82	0.04
2013	0.62	-0.46	0.16	2.94	-0.10	3.04	0.04
anomalies	0.95	0.02	0.97	0.90	0.35	2.22	0.00
Peak period							
climatology	-0.53	-0.91	-1.44	3.39	-1.06	1.05	0.16
2013	0.34	-0.62	-0.28	1.41	-0.17	1.13	0.16
anomalies	0.87	0.28	1.16	-1.98	0.89	0.07	0.01
Horizontal advection – Full period							
	advne (°C)	advsw (°C)	advnw (°C)	hadv (°C)			
climatology	-0.79	-0.41	0.35	-0.84			
2013	-0.22	-0.35	1.50	0.93			
anomalies	0.57	0.06	1.15	1.77			

At the beginning of January 2013, the net surface heat flux anomalies became negative, contributing to cooling in the region, but were opposed by positive horizontal advection and vertical mixing anomalies (Fig. 4.6c), which contributed to the long duration of the MHW. However, advection and vertical mixing were together weaker than anomalous surface cooling resulting in an overall slight decrease in temperature (Fig. 4.2e). Typically, stronger vertical mixing would cool the surface layer, contributing to a negative temperature change as shown in the climatology in Fig. 4.6a, but during the end of January and the beginning of February 2013 the vertical mixing was reduced, resulting in a temperature increase in the surface layer (Fig. 4.6c). By the end of January and beginning of February the net heat flux became positive (Fig. 4.6b), driving an increase in temperature. At the end of February, when SST anomalies began to weaken, a decrease of net surface heat flux into the ocean drove rapid cooling which was the main driver of the MHW decay (Fig. 4.6b, Table 4.1). The two negative heat flux anomaly periods at the beginning of January and end of February (Fig. 4.6c, indicating reduced heat flux into the ocean) could be the result of TCs Narelle (early to mid-January) and Rusty (end of February) near the region (Fig. 4.1).

The total advection term became weakly negative between January and February (Fig. 4.6b), while advection anomalies were positive during both months (Fig. 4.6c) mostly due to positive horizontal advection anomalies throughout the whole period (Fig. 4.8b and c). In fact, Table 4.1 suggests that the climatological horizontal advection was negative in the region, while during the MHW period the advection was slightly positive (Fig. 4.6b). The model climatology shows that heat advection at the north-eastern and south-western boundary were typically negative

(Fig. 4.8a and Table 4.1). In summer 2012/2013, the cooling effects of the advective component at the north-eastern boundary were significantly reduced (Table 4.1) with positive contributions from advection originating from an anomalous inflow from the north west, especially during December 2012 and the beginning of January (Fig. 4.8). At the north-western boundary the model climatology showed a positive advective flux, which during summer 2012/2013 was stronger than the climatology and provided a larger contribution to the temperature increase (Fig. 4.8c and Table 4.1). The vertical advection contributed to the anomalous warming especially during January and February 2013 (Fig. 4.8c, Table 4.1).

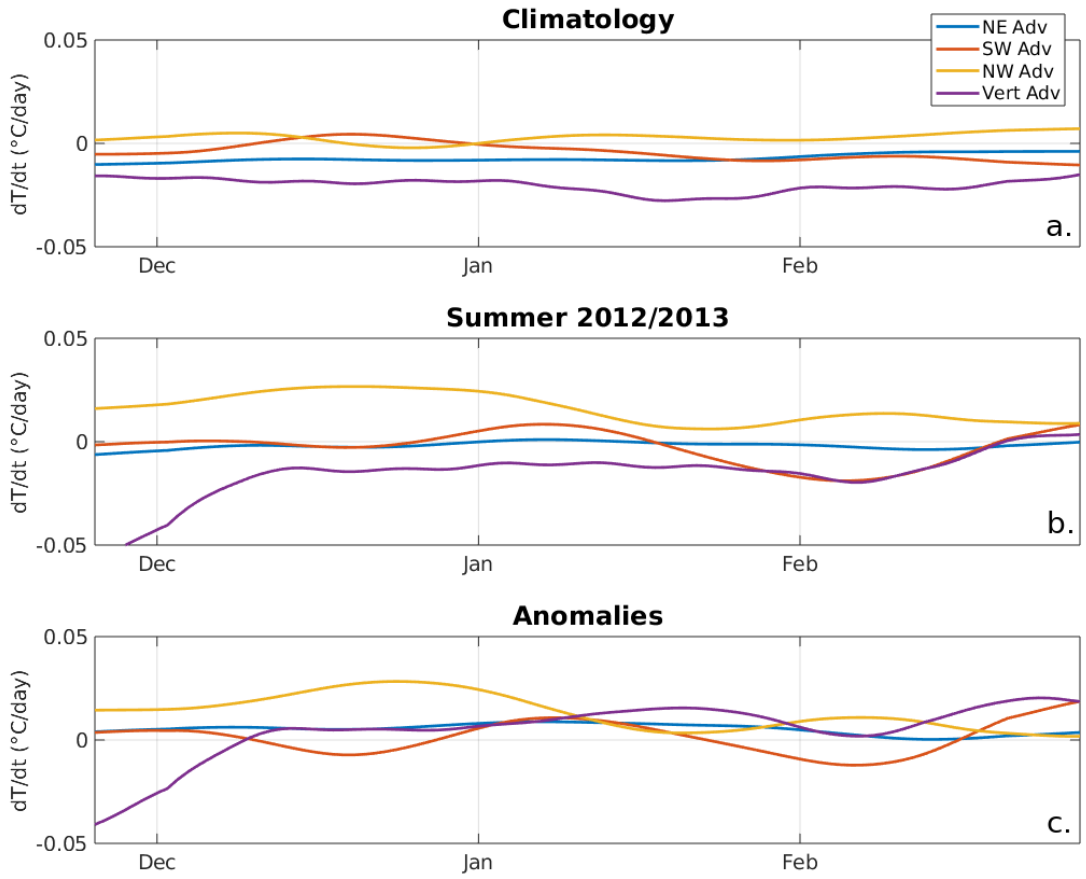

Figure 4.8: Advection terms from eq. (1) averaged over region 2 for: (a) the model

climatology; (b) the 2012/2013 MHW; and (c) the difference between the two.

It is worth noting that the residuals of the integrated budget were higher during the peak period, but this value was still an order of magnitude smaller than the total heat change.

4.5 Net surface heat flux

Positive surface heat flux anomalies (increased heat flux into the ocean) were present during December (Fig. 4.9c) however anomalies into the ocean during January (Fig. 4.8f) and February (Fig. 4.9i) were near zero or negative, suggesting less contribution to ocean heating from the surface heat flux in 2013 compared to other years. This is in accordance with the analysis by Xu et al. (2018), who documented a positive heat flux anomaly warming the ocean in December 2012, but not during the following months. Still, a shallower MLD (Figs. 4.4 and 4.5) during summer 2012/2013 could have constrained the surface heating in a shallower surface layer to sustain the SST anomalies.

The model net surface heat flux (Fig. 4.9) was corrected using observed SST and SSS values based on a flux correction method described by Barnier et al. (1994). Overall, the total net heat flux of the model compares well with the original forcing from ERA 5 (Figs. 4.9 and 4.10), indicating only small adjustment by the flux correction. In particular, the correction generally reduces the model heat flux, more significantly in December and January 2013 (Fig. 4.10, fourth column); this could

possibly underestimate the heat flux warm anomalies during December and overestimate the heat flux reduction in January and February.

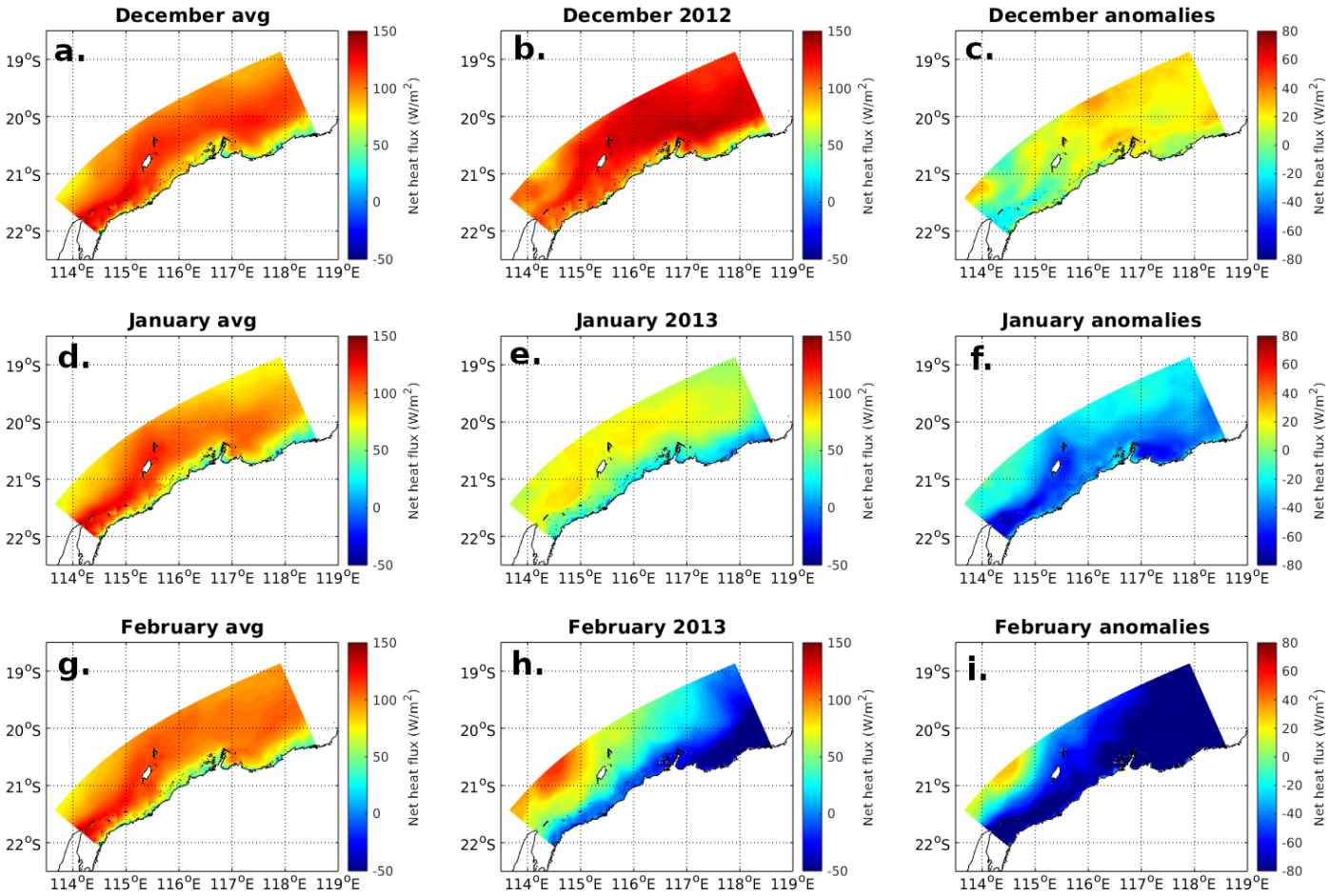

Figure 4.9: Monthly mean model net surface heat flux for: (a), (d), (g) the model climatology; (b), (e), (h) summer 2012/2013; and (c), (f), (i) the difference between the two for December, January and February in region 2.

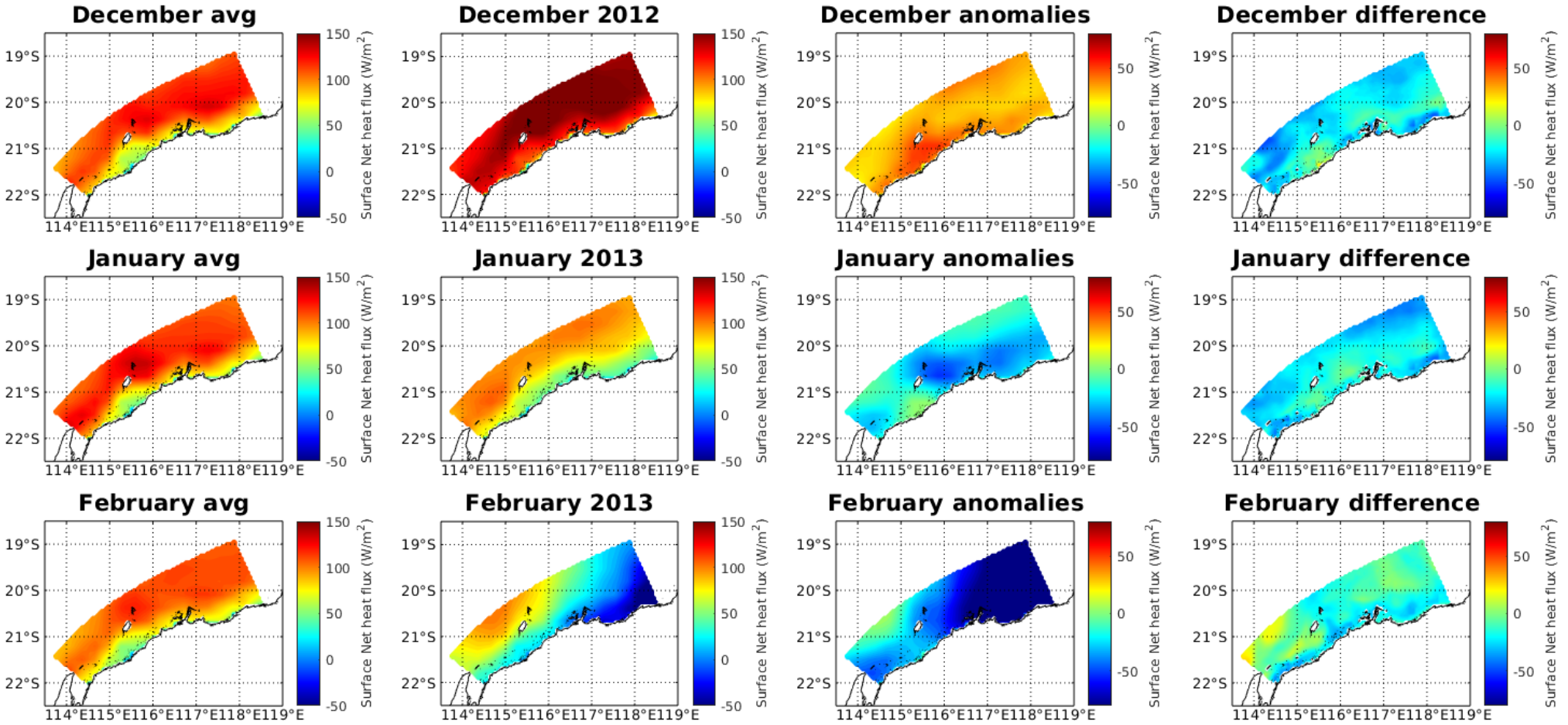

Figure 4.10: Same as Fig. 4.9 (first three columns) but from ERA5 data used to force the model; and difference between model net heat flux after the correction and ERA5 data (fourth column) during the MHW period.

Fig. 4.11 shows different components of surface heat flux from ERA 5 for December, January and February (also documented in Table 4.2 for each month separately). During December, the positive net surface heat flux anomaly was due to longwave radiation and latent heat flux, while shortwave solar radiation was reduced, possibly due to increased cloud cover (Fig. 4.11c). The negative net surface heat flux anomaly during January and February was due mostly to a strong increase in latent heat loss, especially significant in February, and a slight reduction in incoming solar radiation (Fig. 4.11c).

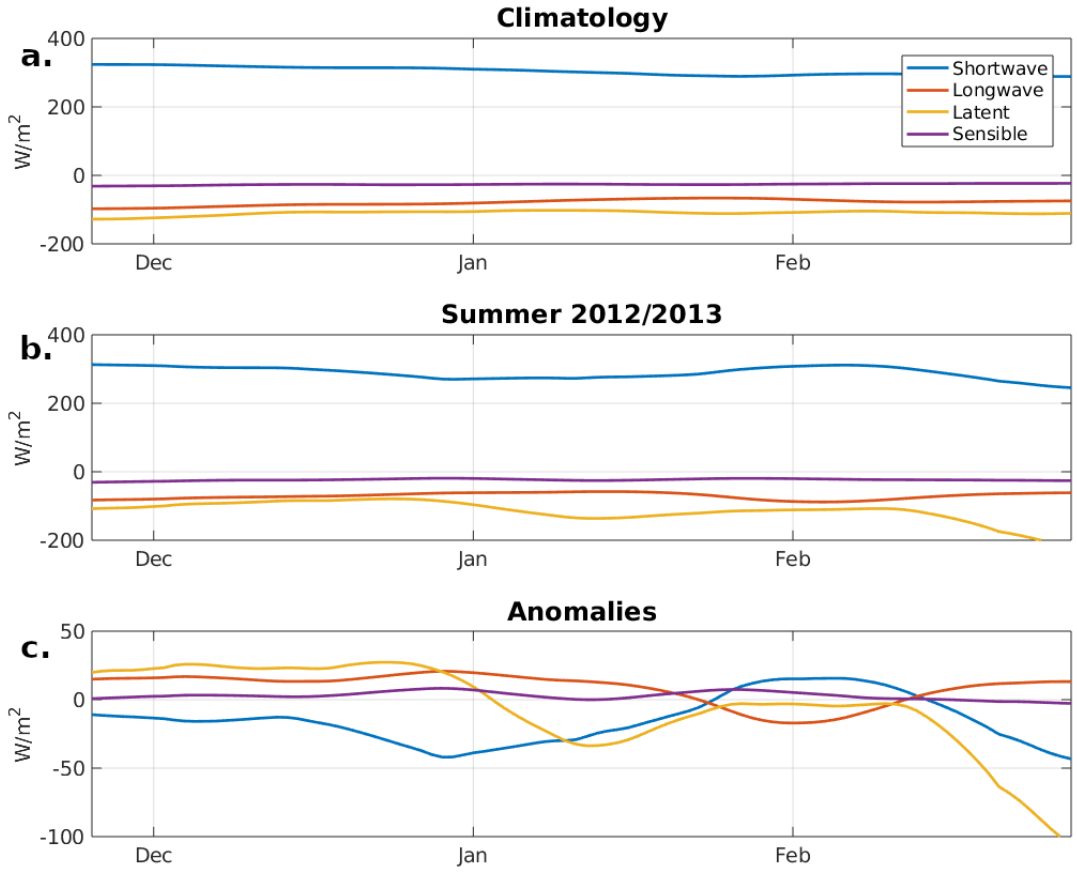

Figure 4.11: Heat flux components over Region 2 for December, January and February for: (a) model climatology; (b) summer 2012-2013; and (c) anomalies from ERA 5.

Table 4.2: Average heat flux components over region 2 for the month of December, January and February for model climatology period, summer 2012-2013 and anomalies from ERA 5 data.

year	Shortwave (W/m^2)	Longwave (W/m^2)	Latent (W/m^2)	Sensible (W/m^2)	Net (W/m^2)
December					
climatology	317	-79	-129	-6	103
2012	289	-61	-91	-2	135
anomalies	-28	18	38	4	32
January					
climatology	295	-62	-120	-7	106
2013	287	-59	-139	-6	83
anomalies	-8	3	-19	1	-23
February					
climatology	293	-70	-121	-6	96
2013	282	-68	-172	-9	33
anomalies	-11	2	-51	-3	-63

4.6 Ocean surface current analysis

The model current climatology (Fig. 4.12, left column) shows a north-eastward cold surface current in the southern part of the domain and over the shelf which was stronger during December (Fig. 4.12a) and weakened in January (Fig. 4.12d) and

February (Fig. 4.12g). These climatological conditions shows that upwelling in the region typically brings cooler subsurface water from below during summer (Fig. 4.8a). However, during summer 2012/2013 (Fig. 4.12, middle column) the shelf current was instead south-westward and hence unfavourable for upwelling. The effect of these anomalously unfavourable upwelling conditions contributing to higher temperatures is further demonstrated in Fig. 4.12 (right column) by the larger south-westward current anomaly and higher temperatures (positive anomalies), especially in the southern part and for December (Fig. 4.12c) and January (Fig. 4.12f). The anomalous south westward currents over the shelf are in agreement with an increase of horizontal along shore advection through the north-eastern border of the domain (Table 4.1). The shelf currents in February along the coast (Fig. 4.12h) and in the northern part differed from the climatology (Fig. 4.12g) less than during the previous months and the current was north-eastward, but with a strong south-westward current in the south.

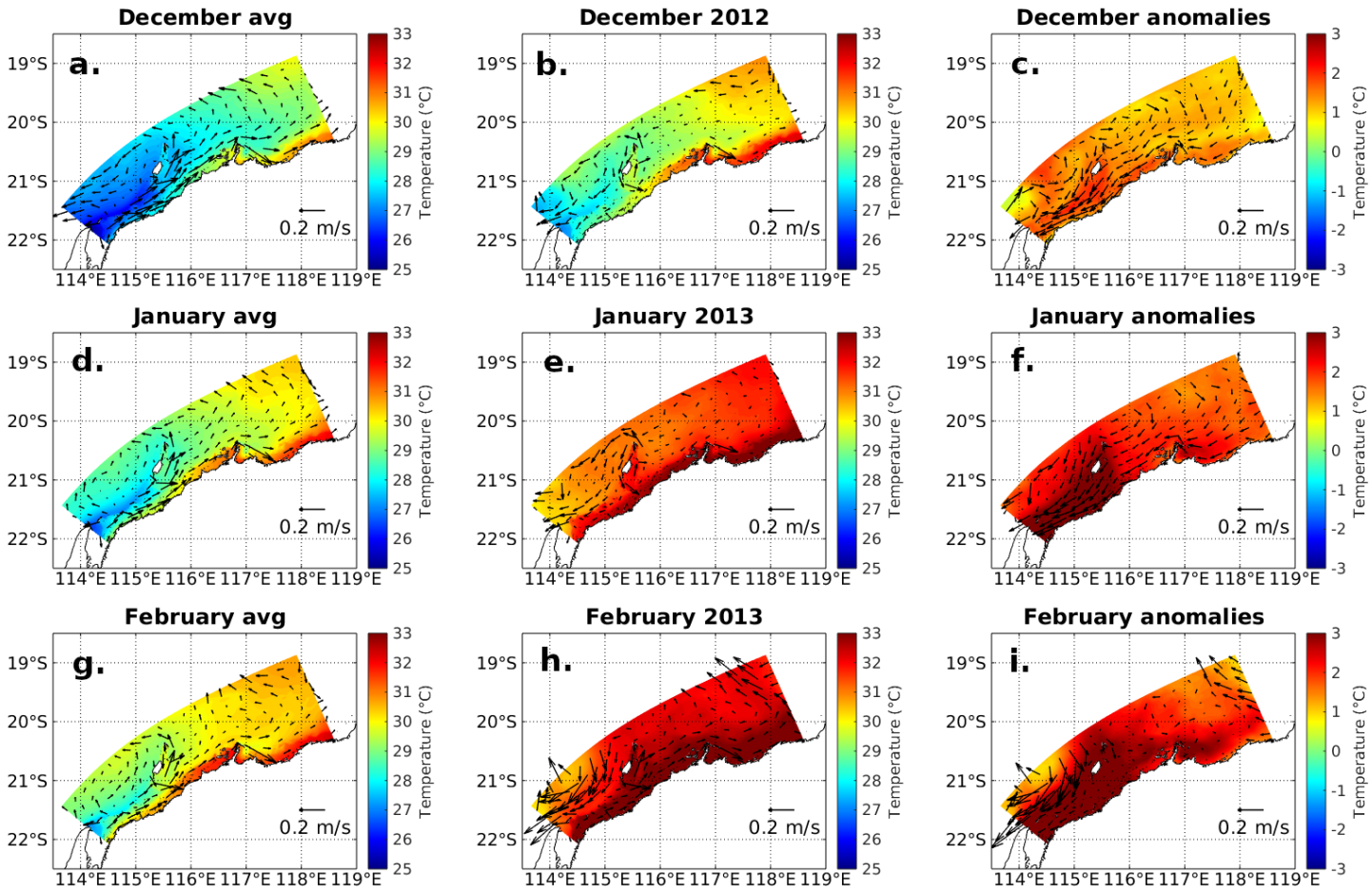

Figure 4.12: Monthly average surface currents and temperature for: (a), (d), (g) the model climatology; (b), (e), (h) summer 2012/2013; and (c), (f), (i) the difference between the two for December, January and February in region 2.

4.7 Wind speed and SLP

The surface wind forcing not only drives ocean currents, but also influences the mixing of the surface layer and air-sea latent heat fluxes. During a normal summer, an along-coast south-easterly monsoonal wind field develops (Fig. 4.13, left column), driving upwelling and bringing cooler subsurface water from below.

During November 2012 the wind and SLP anomalies were weak (Fig. 4.13i), and during December and January the wind speed over the whole NWS appeared to be reduced with respect to the 30-year climatological average (Fig. 4.13f, g, j, k). Reduced wind speed may explain the decrease in the MLD (Fig. 4.5) and reduction in vertical mixing contribution to cooling (e.g. Fig. 4.6b), and the decrease in latent heat flux losses during December (Fig. 4.12). Furthermore, while southwesterly monsoonal winds can normally induce upwelling events during the summer period (Godfrey & Ridgway, 1985), during summer 2012/2013 the weaker and more onshore winds over the region drove downwelling favourable conditions, reflected in a decrease of the contribution of vertical advection to cooling.

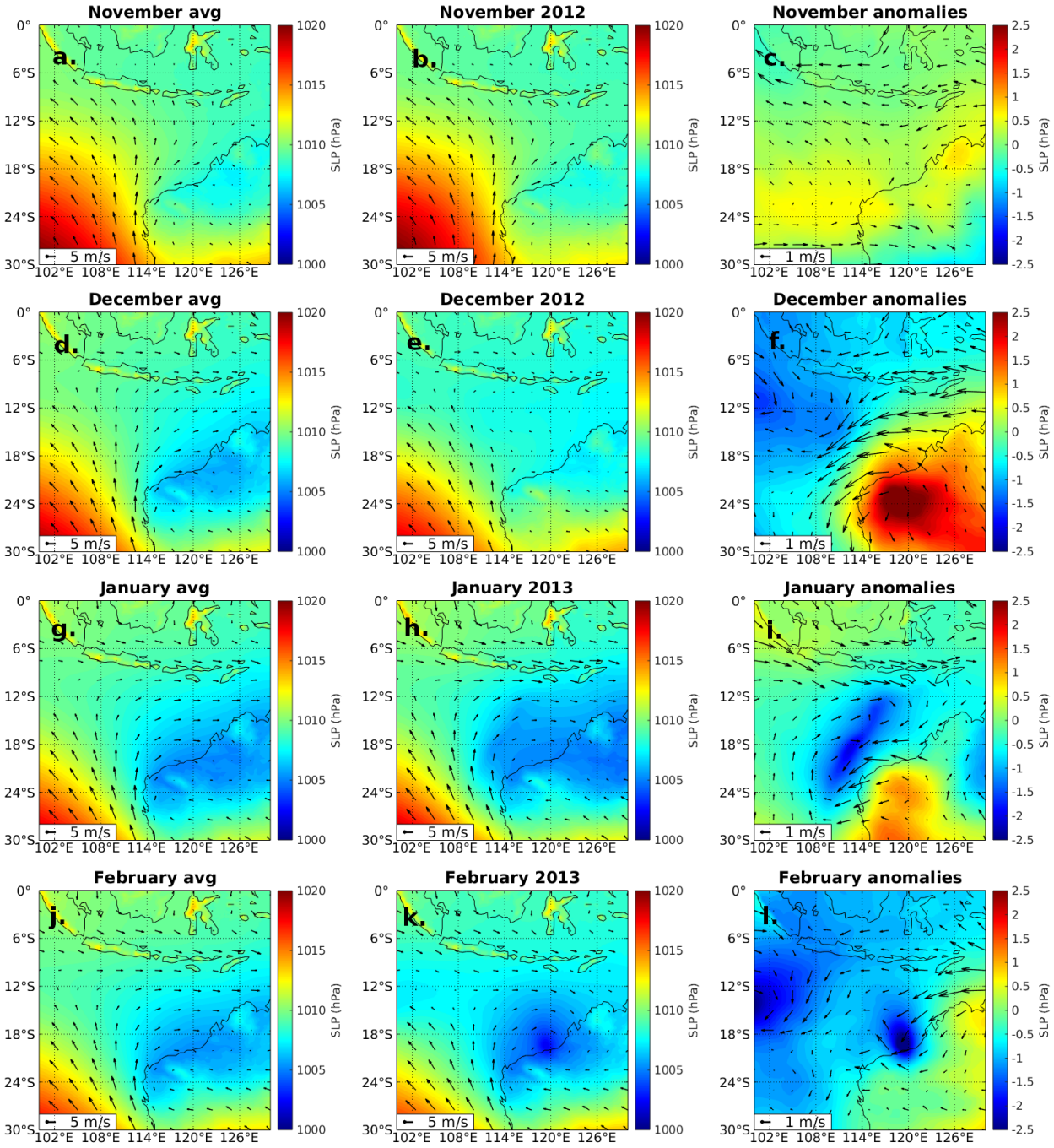

Figure 4.13: Wind speed and sea level pressure from monthly averaged ERA5 data for: (a), (d), (g), (h) the 30-year climatology; (b), (e), (h), (k) summer 2012/2013; and (c), (f), (i), (l) the difference (summer 2012/2013-climatology). (Note that the wind vector scale has been decreased from 5 m/s for the first 2 columns to 1 m/s for the much smaller wind anomalies in the 3rd column).

Reduced wind speed is also noticeable across the Indonesian-Australian Basin in December 2012, due to late onset of the Australian monsoon season (Godfrey & Ridgway, 1985; Holloway, 1995) during summer 2012/2013. Fig. 4.14a and b shows AUSMI calculated following Kajikawa et al. (2010) for 30-year climatology compared to summer 2012/2013. The onset date for the Australian monsoon during summer 2012/2013 was 2 January. Around the middle of January there was a strong monsoon burst with increased westerly wind speeds, and at the end of January and beginning of February a decrease in monsoon strength was followed again by a strengthening of monsoon at the end of the month.

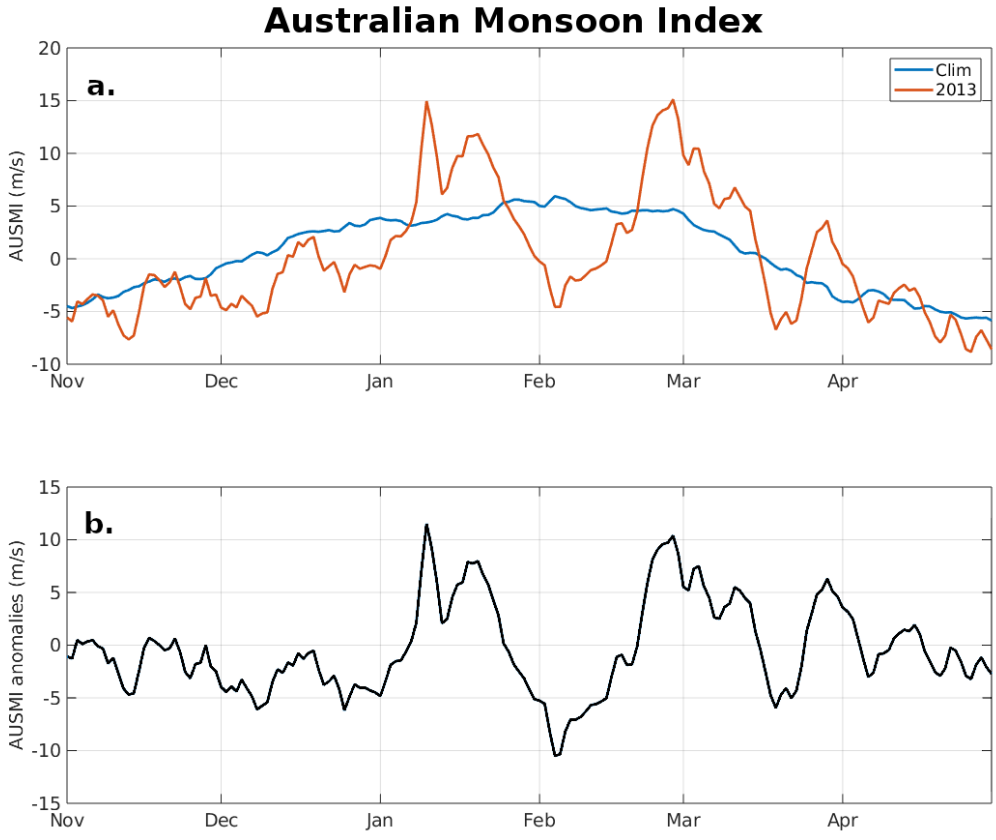

Figure 4.14: Australian monsoon index calculated with Kajikawa et al. (2010) method for: (a) 30-year climatology and summer 2012/2013; and (b) anomalies between the two.

Zhang et al. (2017) found most of the MHWs in the region occurred between phase 2 and 5 of MJO (bottom half of Fig. 4.15). The MJO was very weak for November and December and moved from phase 4 to 8 then phase 1 to 4 between January (red line, Fig. 4.15) and the last peak of the MHW at the end of February (yellow line, Fig.4.15 with days of the month written on each line). Both the first and last MHW peaks occurred during phase 4 (bottom right section of Fig. 4.15), which is in accordance with the results from Zhang et al. (2017). The active MJO phase over northern Australia (phase 4-5) corresponds to a burst in monsoon strength (Fig. 4.14a).

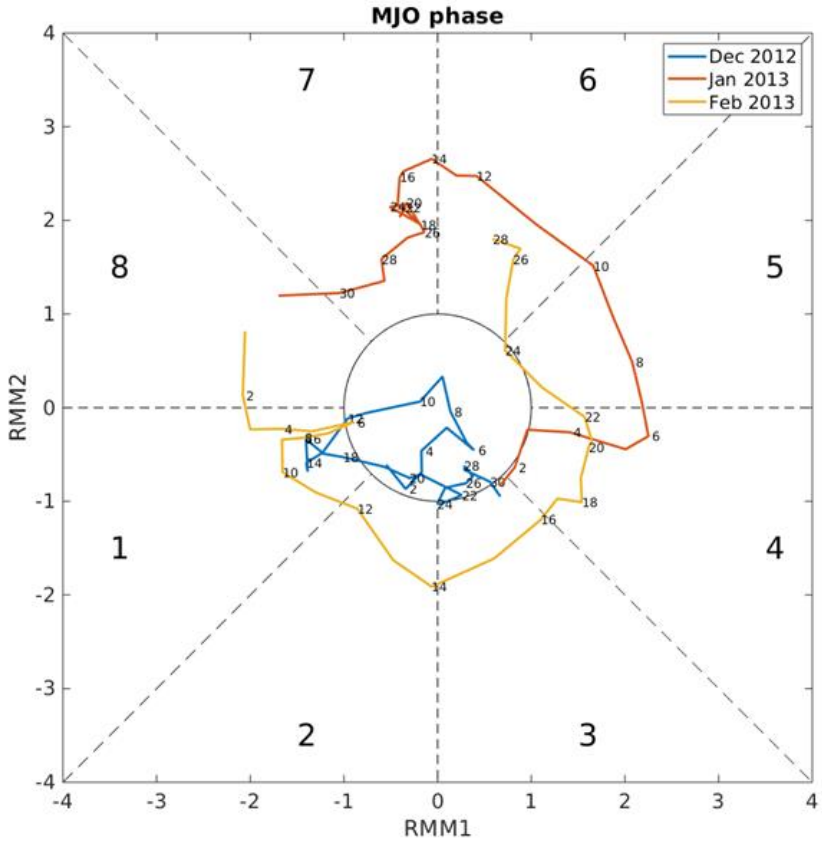

Figure 4.15: MJO phase diagram for the months of December 2012 (blue), January 2013 (red) and February 2013 (yellow); the numbers next to the lines denote the day of the month, while the numbers 1-8 on each section denote the MJO phase.

Fig. 4.13 shows that negative SLP anomalies occurred over the NWS after November and a centre of positive anomalies formed over the continent, which is particularly strong in December when the wind anomalies were the strongest and the MHW is developing. The regions of low monthly mean SLP anomalies in January and February appear to be in conjunction with TCs Narelle and Rusty passing over the NWS (Fig. 4.1). The SLP anomalies, however, may contribute to the wind anomalies that drove the ocean advection anomalies.

4.8 Summary and discussion

A MHW developed during Australian summer 2012/2013 north of the North West Cape over the NWS. Its evolution and hydrodynamic drivers were studied using a numerical model based on the ocean model ROMS, focusing on the inner shelf north of the North West Cape. The 2012/2013 MHW developed rapidly during the first half of December. Heat budget analysis shows that the rapid rise in upper ocean temperature was due to positive advection anomalies (contributing 44 % of the temperature anomalies during the fast warming period) and net air-sea heat flux anomalies, driving increased heat flux into the ocean and contributing 41 % of the anomalies, possibly associated with the delayed onset of the Australian monsoon (Godfrey & Ridgway, 1985; Holloway, 1995). Comparing summer 2012/2013 with a 7-year model climatology, there was a decrease of advective cooling during summer and a decrease in vertical mixing (which normally entrains colder water up), which played a key role in maintaining the warm anomalies on the shelf. A MLD temperature budget would follow the SST variability more closely as a shallower MLD during the

2012/2013 austral summer could provide a positive feedback to increase the SST anomalies, which is not analyzed in this study. The shallow MLD and stronger near surface stratification would reduce the cooling effect from vertical mixing during the evolution of the MHW. The delayed onset of the Australian monsoon, which usually begins around December 13, could have resulted in weaker north-easterly winds during the December 2012. These wind anomalies forced an anomalous south-westward flow over the NWS, bringing warmer northern waters to the region. Reduced wind speed is also responsible for reduced vertical mixing and MLD, which then contributes to warming.

Overall, the development of the 2012/2013 MHW over the inner NWS occurred during a non-canonical Ningaloo Niño (Feng et al., 2015). The anomalous warming on the NWS was not canonical, according to the Ningaloo Niño composite during the austral summer (Kataoka et al., 2014). In fact, during summer 2012/2013 the peak warming anomalies remained mostly confined in the region north of North West Cape, without extending to the southern part of the coast. Furthermore, while a Ningaloo Niño event is often connected to La Niña in the Pacific, during summer 2012/2013 ENSO was in a neutral state. During winter 2012 a positive IOD event occurred and, although Zhang et al. (2018) showed there could be a correlation between positive IOD phase the previous winter and the development of a MHW along the west coast, there is no evidence of this in the November temperature anomalies. This could be due to a shorter IOD phase in 2012, but further analysis is needed to confirm this.

The development of the MHW event could be attributed to the delayed onset of the Australian monsoon, which drove weaker winds over the NWS region during

December compared to the climatology upwelling favourable winds that usually develops during December. The alongshore current in the region, which contributed to the advection of warm water into the region, could also be driven by remote wind forcing from the Kimberley coast (Marin and Feng, 2019) and may have had a stronger effect during January. As shown in Fig. 4.10, SLP anomalies during December could correspond to a locally amplified Ningaloo Niño described by Kataoka et al. (2014), which happens when warm SST anomalies produce low SLP anomalies, triggering northerly wind anomalies that cause downwelling anomalies and further increase warming. However, it is not clear yet if the MHW event on the NWS involved local air-sea coupling, as in a locally amplified event. Our uncoupled regional ocean model results suggested that the air-sea heat input during the developing stage of the MHW played a crucial role in causing ocean temperature warming off the coast. We have used a flux correction as a proxy for the atmospheric feedback., but a regional coupled ocean-atmosphere model may better capture the feedback of atmospheric response to the MHW on the air-sea fluxes during MHW evolution and the influence of remote wind forcing from the Kimberly coast. Moreover, in our model the energy inflow of the baroclinic internal tides could be underestimated as the region considered does not include all the tides generation sites in northern part of the NWS, which could influence the generation of internal waves in the Pilbara region (Rayson et al., 2021).

Chapter 5. Tropical Cyclone Ocean Impacts on Australia's North West Shelf

5.1 Introduction

The NWS of Australia is affected by the passage of several TCs every year (Dufois et al., 2018; Harper et al., 2008). TCs have strong effects on the ocean thermal balance of a wide region beneath and around the track (Price, 1981), which differ from basin to basin (Mei et al., 2015), depending on the typical pre-TC ocean conditions such as the typical MLD and thermal stratification.

The effects of TCs over the NWS of Australia have been studied mostly in relation to sediment transport over the region and their ability to trigger strong internal waves at the shelf edge (Davidson et Holloway, 2001; Rayson et al., 2015). The thermal changes and temperature anomalies induced by a TC have been studied for four specific cases by Rayson et al. (2015). Davidson and Holloway (2001) used a numerical model to study the temperature changes over the shelf region induced by the passage of TCs moving parallel and perpendicular to the coast at several distances. However, a general study of average thermal changes induced by TCs over the ocean in the NWS region is still missing. Here, we use a composite approach to study average ocean response to TCs in the NWS region.

5.2 The TC composite

To produce the composites of TCs off the North West coast of Australia, 20 years of BRAN data from 1996 to 2016 were studied. The sample included 85 different TCs that passed over the region between 105° and 130°E and 5° to 30° S (Fig. 3.7). As every data point on the TC track is considered separately, this leads to 1396 TC data points used to build the composite.

Of all the TC data points on the NWS, 459 were located over the shelf (bathymetry < 200 m) and 937 were over the deeper ocean with depths reaching to 7000 m (Fig. 5.1b). The distribution of water depths below the centre of the TC for shelf data points and deep ocean data points is shown in Fig. 5.1. TC data points located over the shelf have an average depth of 67 m and are mostly over bathymetry < 100 m (Fig. 5.1a). One tenth of the locations over the deep ocean are closer to the shelf edge and have bathymetry < 500 m (Fig. 5.1b).

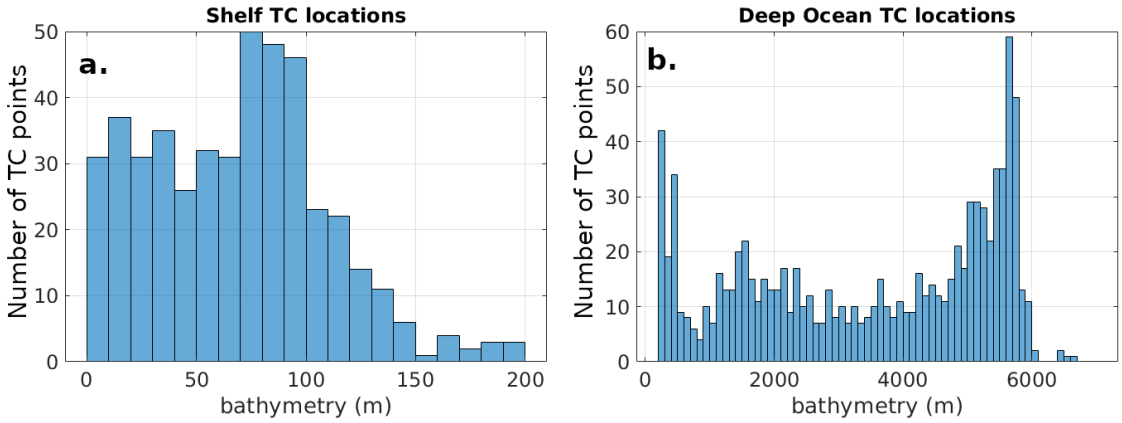

Figure 5.1: Distribution of the bathymetry below TC locations: (a) over the shelf; and (b) over the deep ocean.

The TC season over the NWS of Australia occurs during the warm season between November and May. The distribution of TC data points over the deep ocean by month is shown in Fig. 5.2. Of the cases studied, most are related to TCs that occurred in March (> 300 locations), while around half occurred in the other months between December and April. As the recovery of the temperature anomalies is influenced by the seasonal cycle of temperature, the locations are divided into warming season - for TCs between November and February - which recover when the surface temperature of the water is still warming due to the increased summer solar fluxes, and cooling season - for TCs during or after March. There are 434 TC locations representing warming season TCs and 483 during the cooling season.

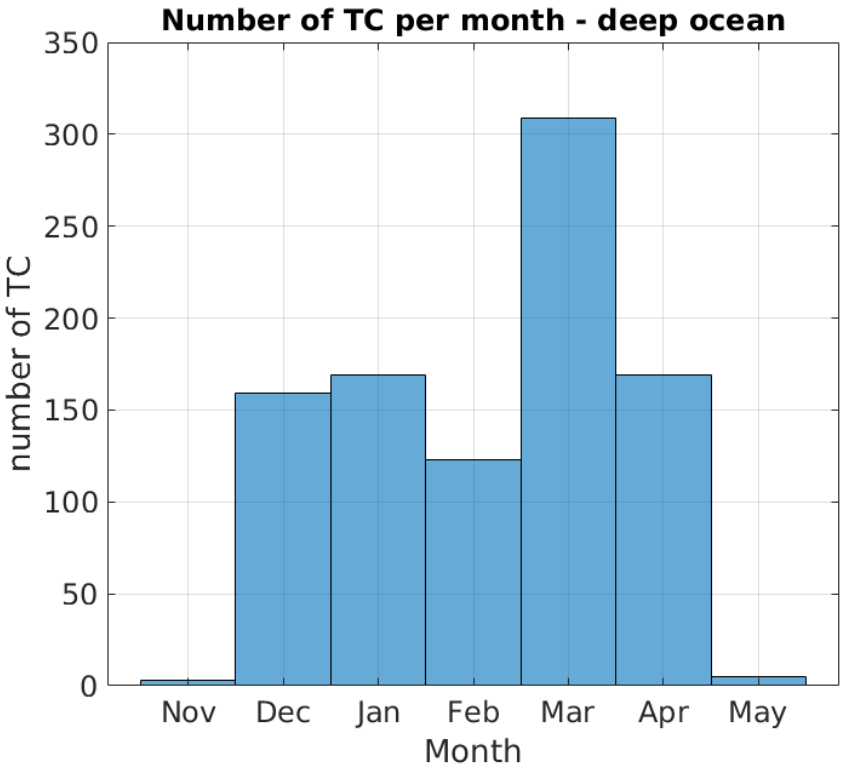

Figure 5.2: Monthly distribution of deep ocean TC data points.

The ocean thermal changes due to the passage of a TC depend strongly on the TC characteristics, in particular intensity and translation speed. Fig 5.3a shows the distribution of TC intensity considered in the composite for TC data points located over the deep ocean. The number of TC data points for each category decrease with increasing intensity, as weak TCs (Cat 1-2, 630 data points) are more common than strong TCs (cat 3-5, 306 data points). The distribution of TC locations with different translation speeds over the deep ocean (Fig. 5.3b) peaks between 3 and 4 m/s. The threshold for slow-moving and fast-moving TCs is set at 4 m/s, as this is the average translation speed of the composite TC data points. There are 460 slow-moving TC data points and 477 fast-moving TC data points.

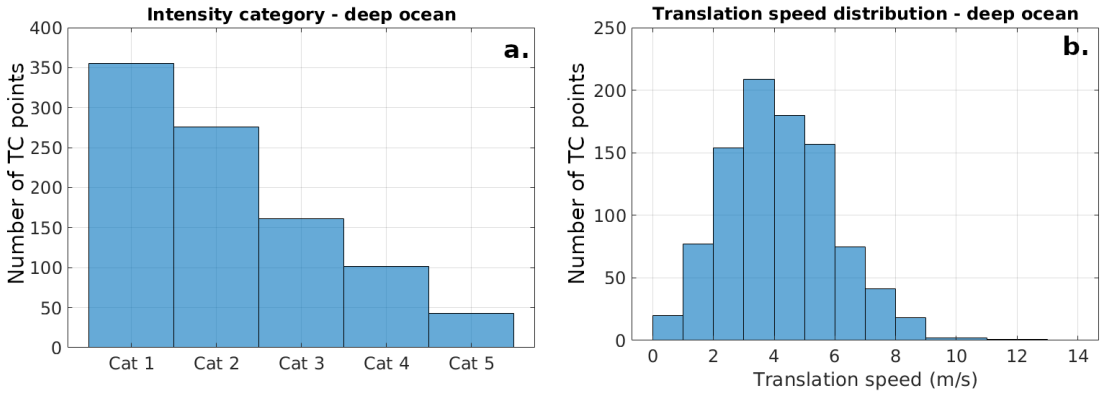

Figure 5.3: Distribution of: (a) TC intensity; and (b) TC translation speed for the data points over the deep ocean.

The presence of a barrier layer, which exists where a strong halocline (and hence density gradient) is present above the thermocline and the ML does not

correspond to the isothermal layer (Chi et al., 2014), prior to the passage of a TC inhibits vertical mixing and entrainment between the surface layer and the colder water underneath. Fig. 5.4a shows the average barrier layer distribution during the TC seasons (between December and March) calculated using a 20-year climatology. The regions with a deeper barrier layer - where mixing is expected to be more significantly reduced - are located mostly over the northern part (equatorward of 12°) and over the open ocean on the western border of the study region (Fig. 5.4a). Closer to the shelf edge the barrier layer is shallower and TC induced mixing is expected to increase. The missing data points near the coast in Fig. 5.4a occur where the bathymetry is shallow enough that the water column is well mixed. Figure 5.4b shows the distribution of the thickness of the barrier layer for TC locations over the deep ocean. The threshold for a deep barrier layer is set at 5 m and there are 472 Tc locations over a shallow barrier layer before the TC passage and 365 TC locations over a deep barrier layer.

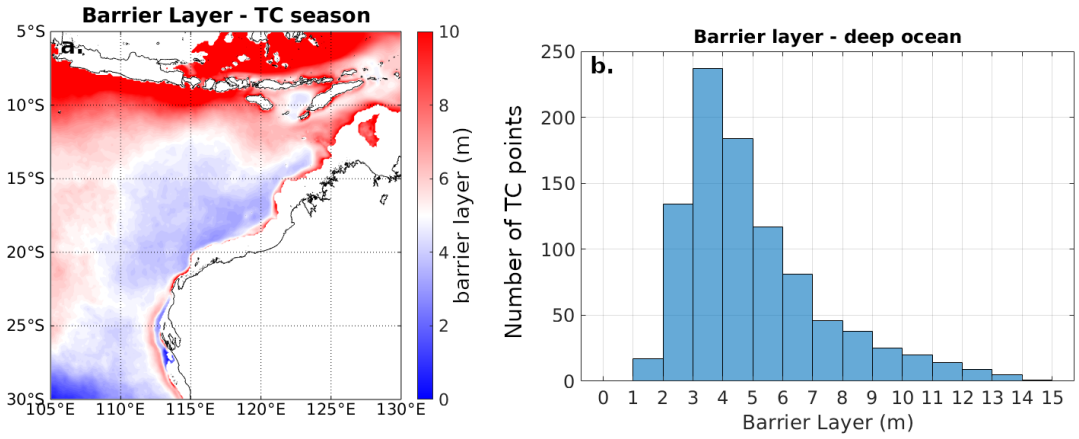

Figure 5.4: (a) Average barrier layer during the TC season (December-March); and (b) barrier layer distribution for all deep ocean TC data points. The missing points near the coast in (a) are located where the bathymetry is shallow and the water is well mixed through the water column.

However, the presence of a shallow or deep barrier layer is related to the season in which the TC occurs (Table 5.1). In fact, during the warming season, more than 70% of the TC data points occur over shallow barrier layer regions before a stable stratification develops in the ocean, while during the cooling season approximately 50% of the TC data points occur over shallow barrier layer regions and 50% occur over deep barrier layer regions (Table 5.1).

Table 5.1: Number of TC data points occurring over shallow and deep barrier layer regions during the warming and cooling seasons.

	Shallow barrier layer	**Deep barrier layer**
Warming season	325	129
Cooling season	247	235

5.3 General case

A 20-year composite of TCs over the North West of Australia is calculated from 1396 TC data points from 1996 to 2016. All composites are calculated relative to a fixed geographic location in order to investigate the ocean response and recovery after the TC has passed. The day on which the TC passes over the fixed geographic location is defined as Day 0 and daily composites are calculated over that location for up to 30 days after the TC passage. For comparison, all temperature composites are

calculated as an anomaly relative to the ocean state 2 days prior to the TC passage and the seasonal mean is also removed from the data prior to compositing.

The cross-track SST anomalies compared with 2 days prior to the passage of the TC are shown in Fig. 5.5. The horizontal line indicates the time the TC is located in that position (Day 0) and the vertical line at “0 km” indicates the centre of the TC, with the cross-section extending 1000 km to the left and right of the centre of the TC. On average, the surface cooling begins just prior to the day of the cyclone passage (Day 0) as the front quadrant of the TC begins to encroach on the area. Maximum surface cooling occurs from Day 4 to Day 6. Subsequently, the surface begins to recover quite rapidly through Day 17 then more slowly after that. However, in the month following the passage of the TC the cold SST anomalies beneath the track never fully recover to the pre-TC values (Fig. 5.5). The area of surface cooling extends over 600 km to each side of the track with maximum cooling within 100 km from the TC centre (Fig. 5.5). The cooling is slightly asymmetric with respect to the track with maximum SST cooling shifted slightly towards the left of the track. At the sides of the track, warm SST anomalies develop (Fig. 5.5). On the left side, warm anomalies start to develop beyond 800 km away from the track during the TC passage at Day 0 and Day 1 (Fig 5.5) and are still present at Day 30.

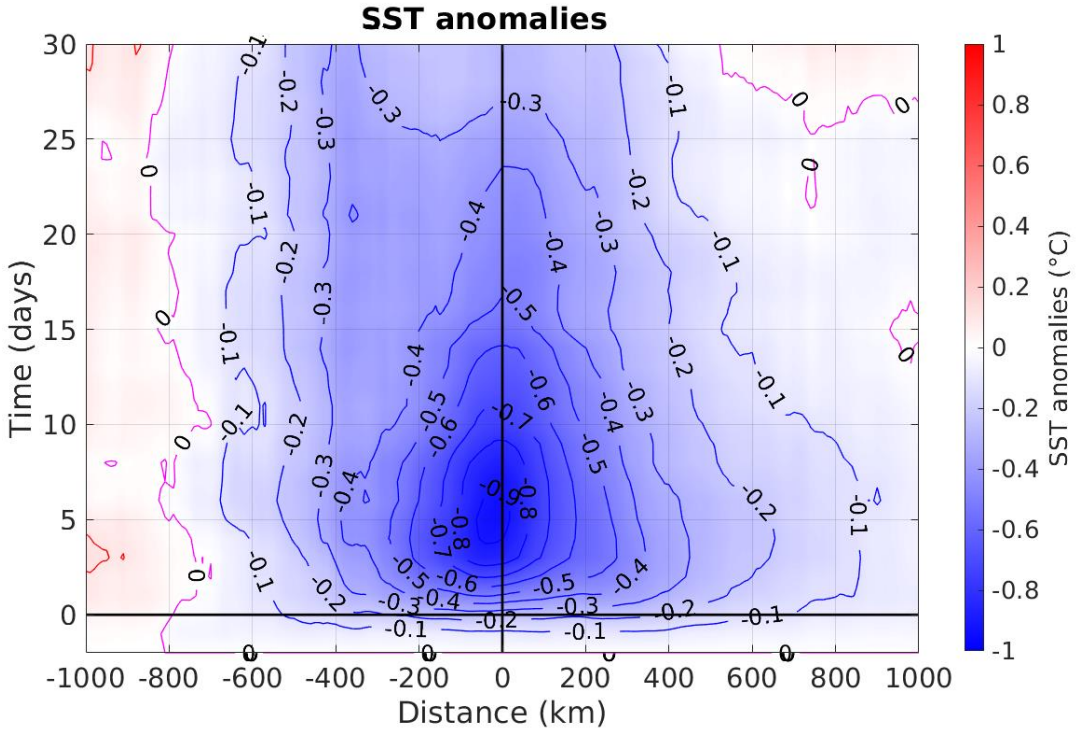

Figure 5.5: Cross-track Hovmoller diagram of SST anomaly (contours every 0.1 °C) relative to 2 days prior to the passage of the TC over time, composited for 20 years of TCs (1396 data points). The negative distances indicate the left of track and the positive distances are right of track.

On the day of the TC passage over the region (Day 0) there is strong heat loss from the ocean toward the atmosphere (Fig. 5.6e, negative heat flux cools the ocean and positive flux warms the ocean), which contributes to the development of the SST cold anomalies in Fig. 5.5. The heat loss into the atmosphere is asymmetric with respect to the track of the cyclone with a greater heat loss on the left of track (Fig. 5.6e). On Day 0, the incoming shortwave solar radiation is reduced within the region covered by the TC clouds (Fig. 5.6a), the longwave radiation heat loss is reduced within the region covered by the TC during its passage (Fig. 5.6b) and the latent and sensible heat loss towards the atmosphere is enhanced (Fig. 5.6c and d). In particular,

the latent heat flux loss is large enough to overcome the shortwave radiation reduction and it is stronger particularly over the left of the track, where the cyclone winds are maximised due to the alignment of the wind direction with the direction of movement of the cyclone (Fig. 5.6c). During the month following the TC passage, the net heat coming into the ocean (positive values in Fig. 5.7) contributes to the recovery of the temperature anomalies. In fact, while during the TC passage the net heat flux within 400 km from the track is negative and the ocean loses heat to the atmosphere (Fig. 5.6e and 5.7), from Day 2 the net heat flux returns positive in the region around the track. The positive net heat flux coming into the ocean drive warming at the ocean surface and drive the recovery of the cold anomalies (Fig. 5.5).

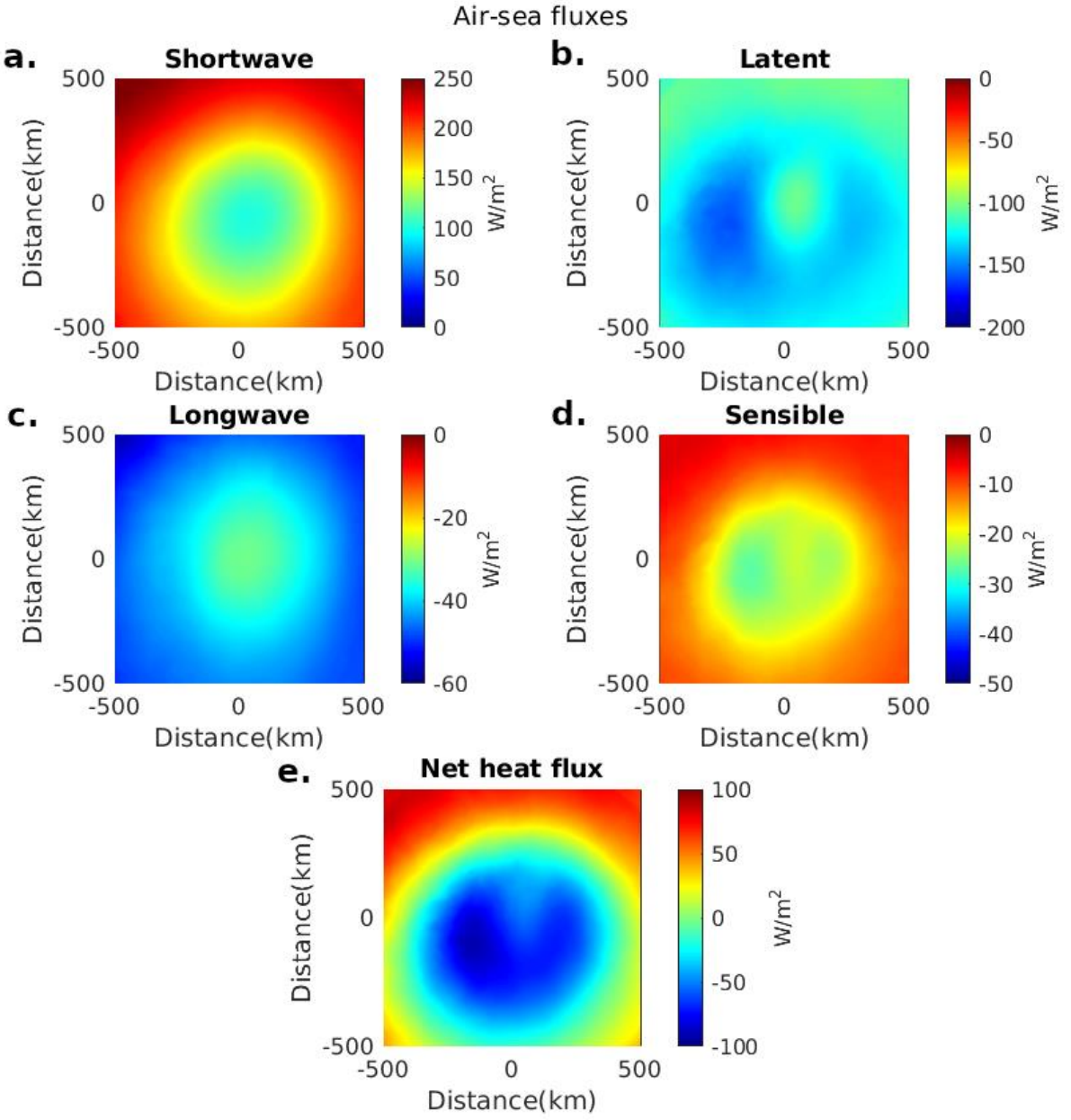

Figure 5.6: Components of the heat flux on Day 0 over the region: (a) Shortwave radiation; (b) latent heat flux; (c) longwave radiation; (d) sensible heat flux; and (e) net heat flux. Positive values represent heat warming the ocean and negative values represent heat loss from the ocean to the atmosphere.

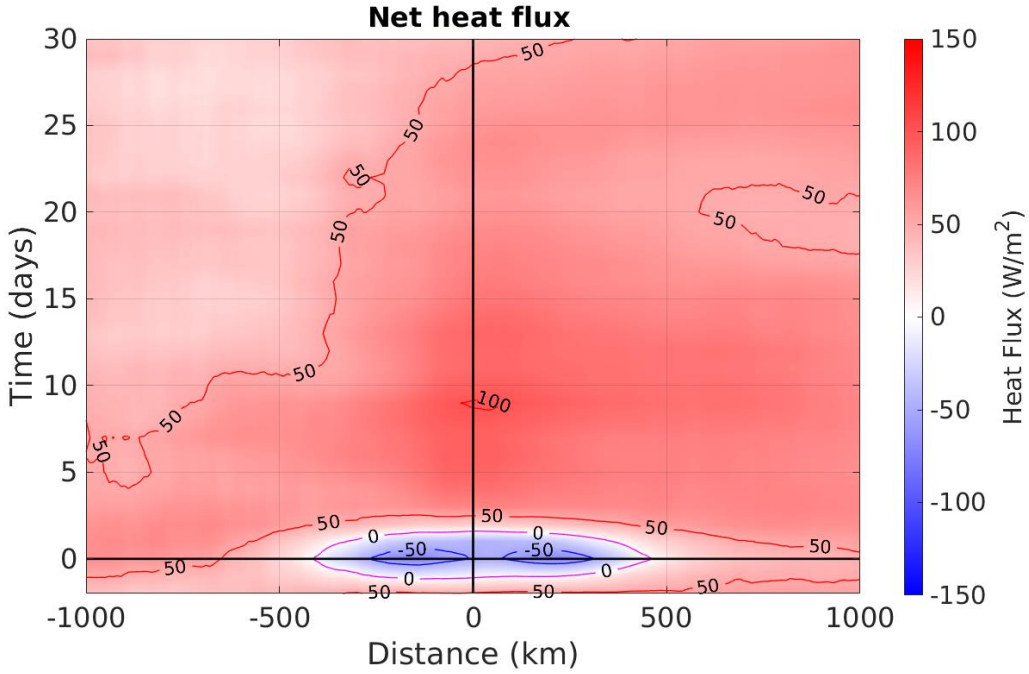

Figure 5.7: Cross-track Hovmoller diagram of the net heat flux (contours every 50 W/m^2) over time, composited for 20 years of TCs (1396 data points). Positive values represent heat warming the ocean and negative values represent heat loss from the ocean to the atmosphere.

The daily cross-section of temperature anomalies is shown in Fig. 5.8, the temperature daily rate of change in Fig. 5.9, and divergence and currents in Fig. 5.10 for the first 10 days after the TC passage. Within the ML the cooling extends horizontally to 800 km and reaches its maximum around day 4 to 6 (Fig. 5.8), with the maximum cooling rate occurring on the day of the TC passage (Day 0) and the day after (Day 1) and less cooling continuing up to Day 5 (Fig. 5.9). In the ML, horizontal currents appear to be much stronger and opposite in direction to the subsurface currents, indicating a strong vertical shear between the ML and the thermocline (Fig. 5.10). Strong vertical shear is expected to cause vertical mixing between the surface and the subsurface water below the ML and drive extensive surface cooling (Price,

1981; Shay et al., 1989). Below the ML, the majority of the cooling occurs within 200 km of the centre of the TC (Figs. 5.8 and 5.9). At depth, the cold anomaly is stronger under the location where the initial surface divergence and upward currents are strongest, suggesting that the majority of the cooling under 100 m is due to the upwelling of cold water rather than vertical mixing (Figs. 5.9 and 5.10). The upwelling is due to near-surface horizontal currents (Fig. 5.10) that produce strong divergence in the ML (0-40 m) and weak convergence below through a deep layer (from 50 to 500 m) driving Ekman pumping below the inner core of the TC (Fig. 5.10). Upwelling is strongest during Day 0 and Day 1 and is maximized right-of-track (Fig. 5.10). The stronger vertical currents during Day 0 and 1 coincide with the maximum cooling rate through the whole water column (Fig. 5.9). The recovery of temperatures below 100 m from Day 2 to 8 is accompanied by downwelling through the water column (Figs. 5.9 and 5.10). Stronger downward vertical currents occur every 5-6 days at the same time when the warming rate is stronger (Days 4 and 10 in Figs. 5.9 and 5.10).

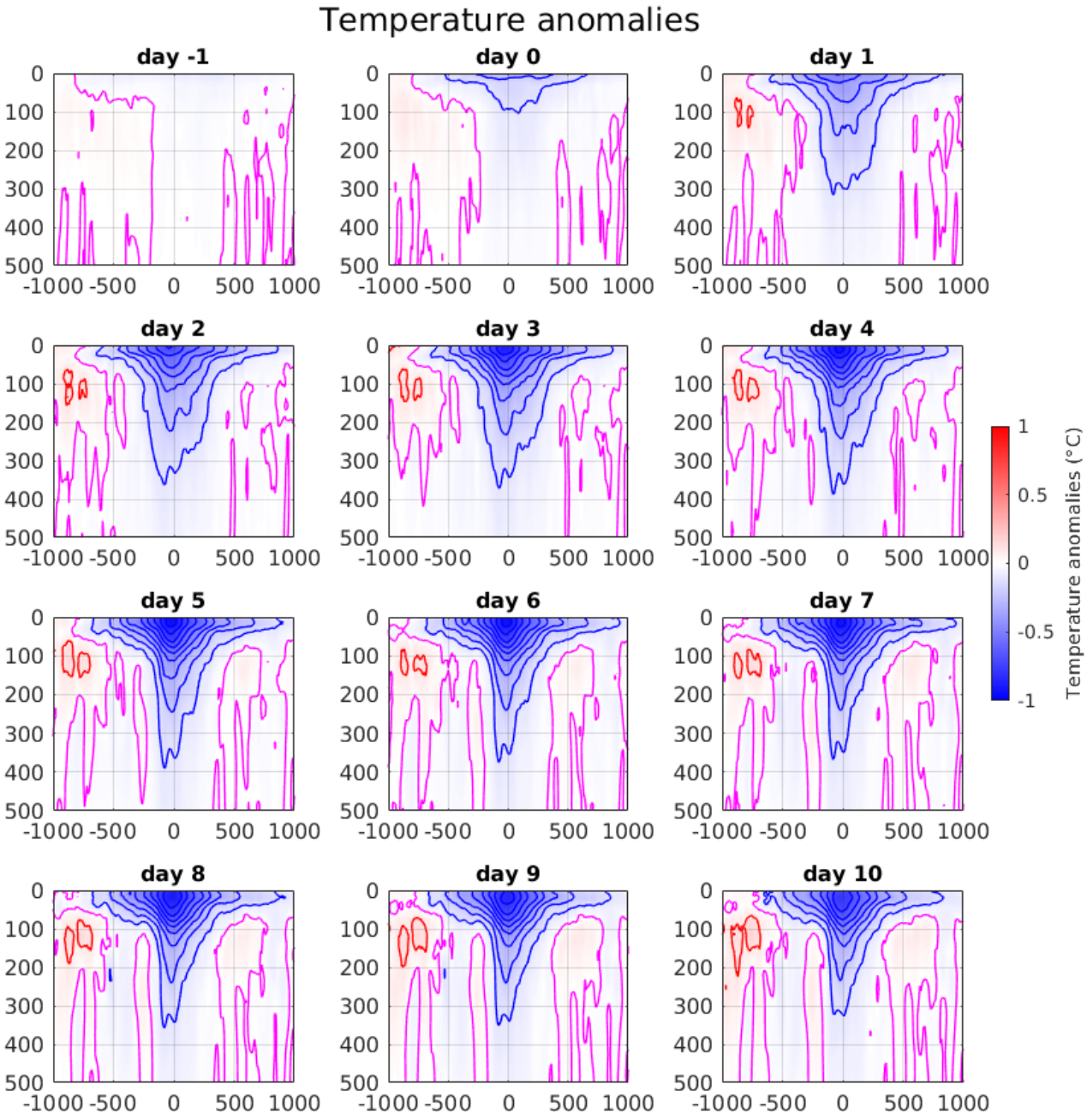

Figure 5.8: Cross-section temperature anomaly (contours every 0.1 °C) from the day before the TC passage to 10 days after, composited for 20 years of TCs (1396 data points).

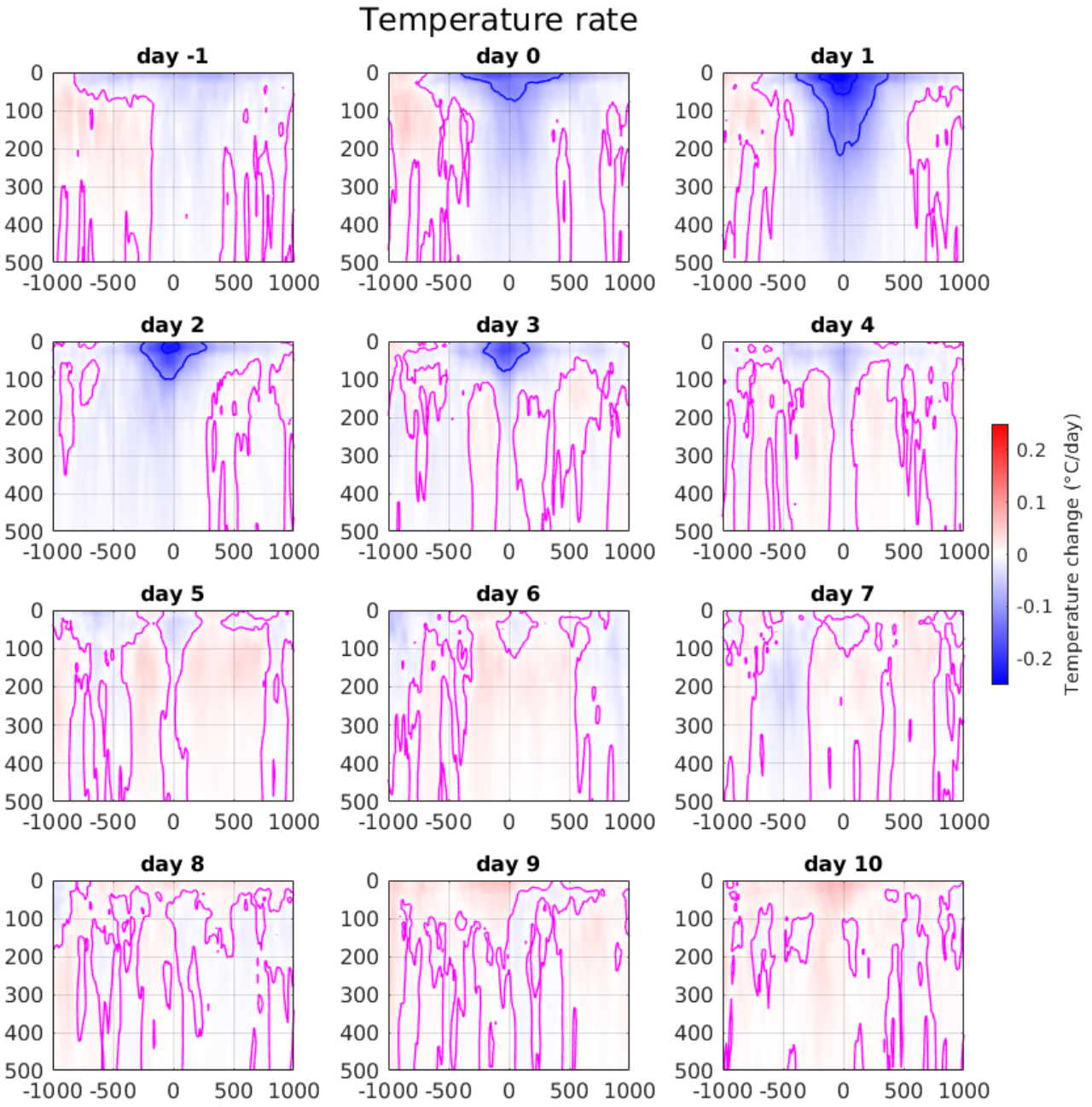

Figure 5.9: Cross-section of the daily rate of change of temperature (contours every 0.1 °C/day) from the day before the TC passage to 10 days after, composited for 20 years of TCs (1396 data points).

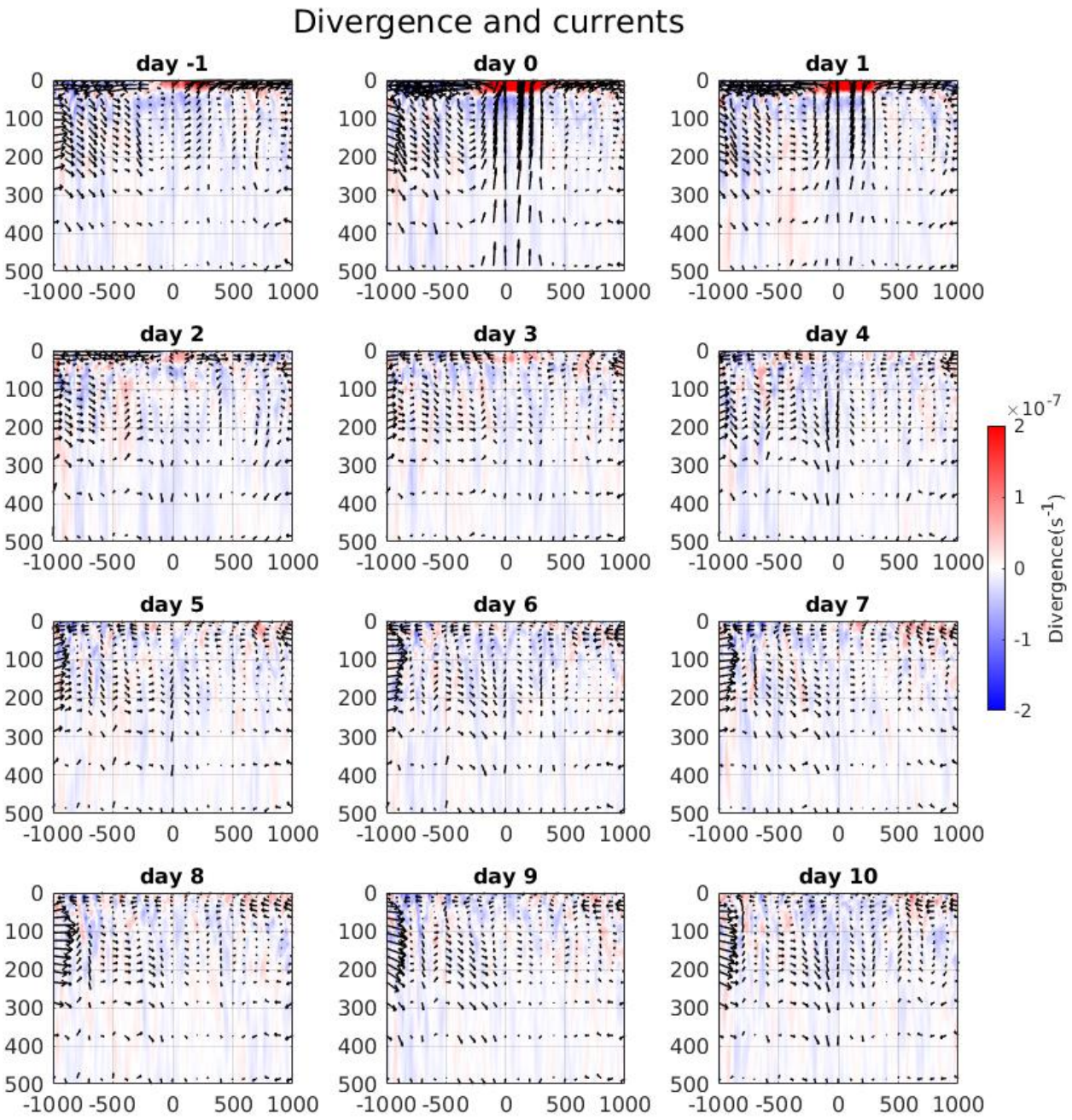

Figure 5.10: Cross sections of divergence (shaded) and currents (vectors) from the day before the TC passage to 10 days after, composited for 20 years of TCs (1396 data points). The vertical component of currents is magnified by 10^3 to help visualize the upward and downward movements.

Outside of 200 km of the TC centre substantial warming occurs below the ML (Figs. 5.8 and 5.9). This warming begins on the day prior to the arrival of the TC in the centre of the cross-track section and the positive warming rate lasts until approximately Day 6 after its passage (Fig. 5.9). The maximum warming is located at a depth between 100 and 200 m on the left of track, where the current shear between the ML and the subsurface is the strongest, and strong vertical mixing and ML entrainment likely occur (Figs. 5.9 and 5.10). Furthermore, weak downwelling in the region further from the TC centre compensating for the strong upwelling immediately below, could further contribute to the warming at the sides (Figs. 5.9 and 5.10).

Fig. 5.11 shows the cross-track temperature changes over time at specific depths to further investigate the different processes occurring within the water column. The central cold temperature anomalies decrease in area and intensity at increasing depths. Near the surface, colder temperature anomalies are shifted towards the left of track (Figs. 5.11a and 5.5), but between 95 and 195 m the colder region appears towards the right of track (Figs. 5.11c-e and 5.8). Cold anomalies beneath the track begin to decrease after Day 5 at every depth with different recovery rates: recovery is faster at 286 m (Fig. 5.11f) but between 95 and 195 m the recovery is slower than at the surface (Fig. 5.11c, d and e). At the sides of the track warm anomalies appear at 48 m depth over the left side and at 95 m depth over the right side (Fig. 5.11b). These warm anomalies build up earlier and are stronger over the left of the track between 48 and 145 m (Fig 5.11b, c and d). After Day 10, the time derivatives of the warm anomalies left of track are nearly zero and the warm anomalies are still present in the region 30 days after the TC passage (Fig. 5.11), taking much longer than the central cold anomalies to dissipate.

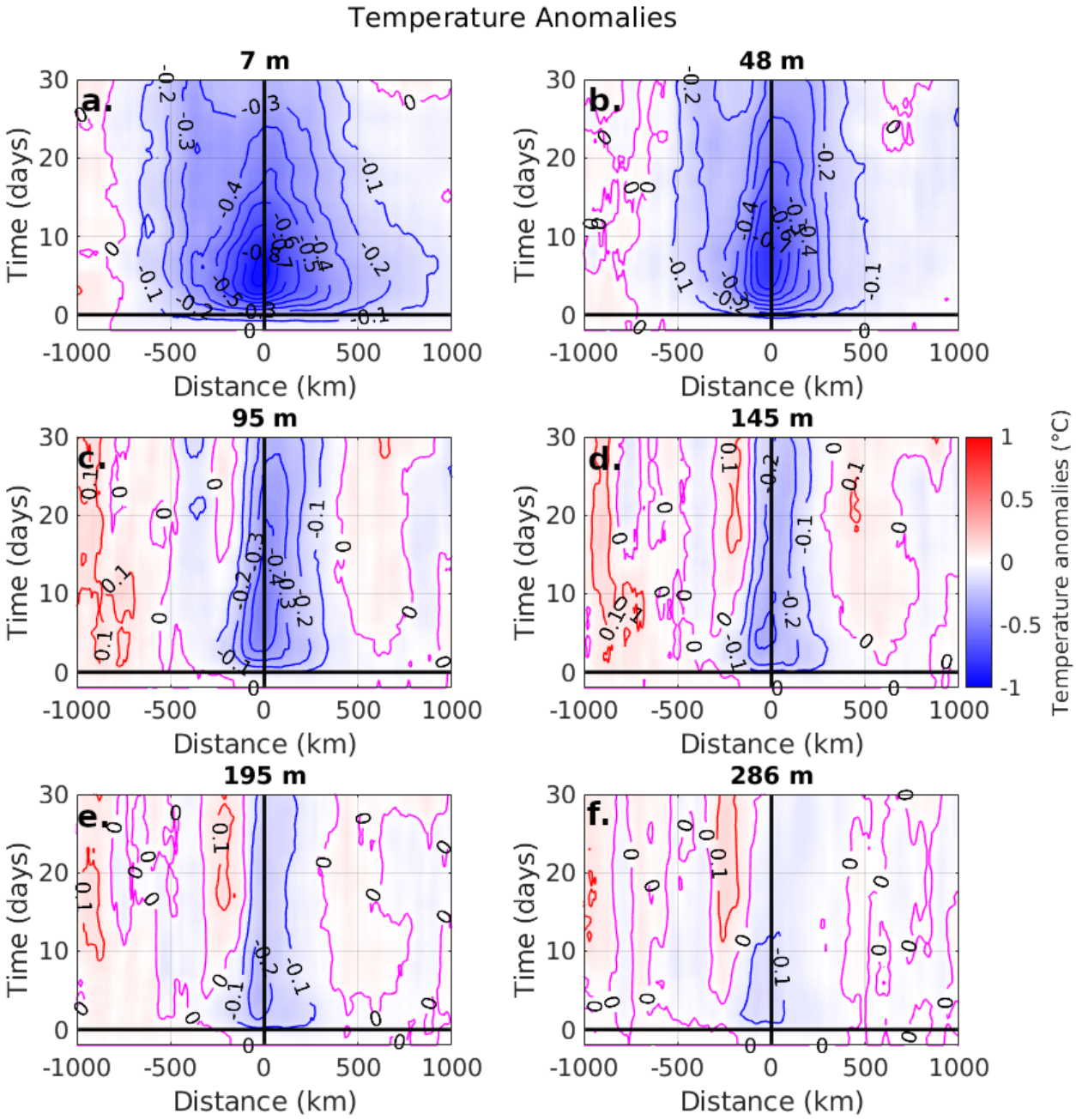

Figure 5.11: Cross-track Hovmoller diagram of temperature anomaly (contours every 0.1 °C) relative to 2 days prior to the passage of the TC over time, composited for 20 years of TCs (1396 data points) at increasing depths.

Cross-track vertical currents over time are shown in Fig. 5.12. On Day 0 there is strong upward vertical motion under the track, between 200 km at the left of the track and 400 km at the right of it (all depths, Fig. 5.12). This strong upward vertical motion at all depths is consistent with the location of the colder anomalies towards the right of the track at depths of 48 m and below shown in Fig. 5.11 and can also be seen in the vertical velocities shown in Fig. 5.12b, c, d, e and f), where the upwelling of the isotherms is expected to be the stronger cooling mechanism. At the sides of the strong upwelling region, the behaviour is quite different on each side of the track. On the left, at more than 300 km from the TC centre the vertical velocity on Day 0 is downward (Fig. 5.12b, c, d, e and f), possibly due to some downwelling motion that compensates the upwelling below the track. To the right of the track, the vertical velocity on Day 0 is upward as far out as 800 km, although it is weaker than below the track (Fig. 5.12b, c, d, e and f). From Day 3, the upwelling below the centre switches to a downward current that remains for over 30 days after the TC passage (Fig. 5.12c, d, e and f). This downward motion under the track from Day 3 likely drives the fast recovery of the cold anomalies at depths below 195 m (Fig. 5.11e and f) where downwelling is strongest and air-sea fluxes (which drive the recovery at the surface) do not penetrate. Beyond approximately 400 km from the centre, the general downward current on the left of the track and upward current on the right remains through the 30-day period (Fig. 5.12c, d, e and f).

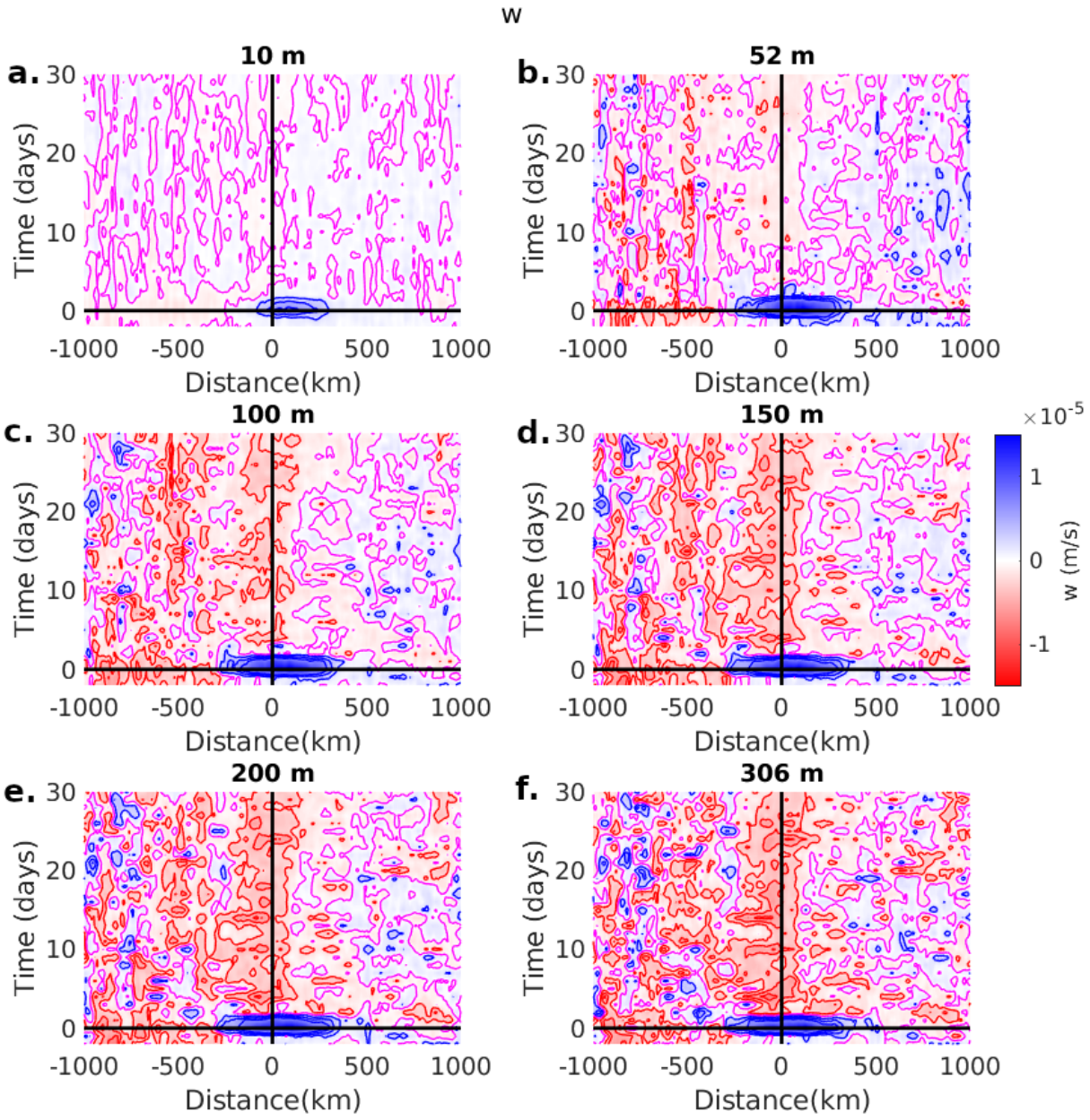

Figure 5.12: Cross-track Hovmoller diagram of vertical velocity (contours every 0.2 x10^{-6} m/s) over time, composited for 20 years of TCs (1396 data points) at increasing depths.

The change in MLD induced by the passage of the TC is shown in Fig. 5.13. As the cyclonic winds approach the region at Day -1 the MLD increases on both sides of the track at distances further than 200 km from it (Fig. 5.13) where the vertical shear of horizontal currents drives vertical mixing (Fig. 5.9). Beneath the TC centre, lowering of the isotherms by mixing is contrasted by upwelling of the isotherms (Fig. 5.12), and there are no significant changes in the MLD (Fig. 5.13). In the month following the passage of the TC, the MLD continues to deepen on the left of the track (Fg. 5.13 a), which is in agreement with a general downwelling regime (Fig. 5.12b, c and d). On the right of track, the MLD oscillates slightly, which is consistent with a weak and variable upwelling regime on the right of track (Fig. 5.12). The general deepening of the MLD in the period following the TC in Fig. 5.13 a, especially strong on the left of track, is mostly due to seasonal effects which have not been removed. The MLD anomaly compared to a 20-year climatology shows a greater MLD deepening following the passage of a TC on the right of track, which recovers more quickly than the MLD deepening on the left of track (Fig. 5.13 b). In fact, at Day 30 the MLD is recovered to the climatology values on the right of track, whereas between 200 and 600 km on the left of track, the MLD is approximately 4 m deeper than the climatology (Fig. 5.13b). As the MLD criteria is based on a density threshold, TC-related precipitation over the region could affect the deepening of the MLD as it produces a fresher surface layer.

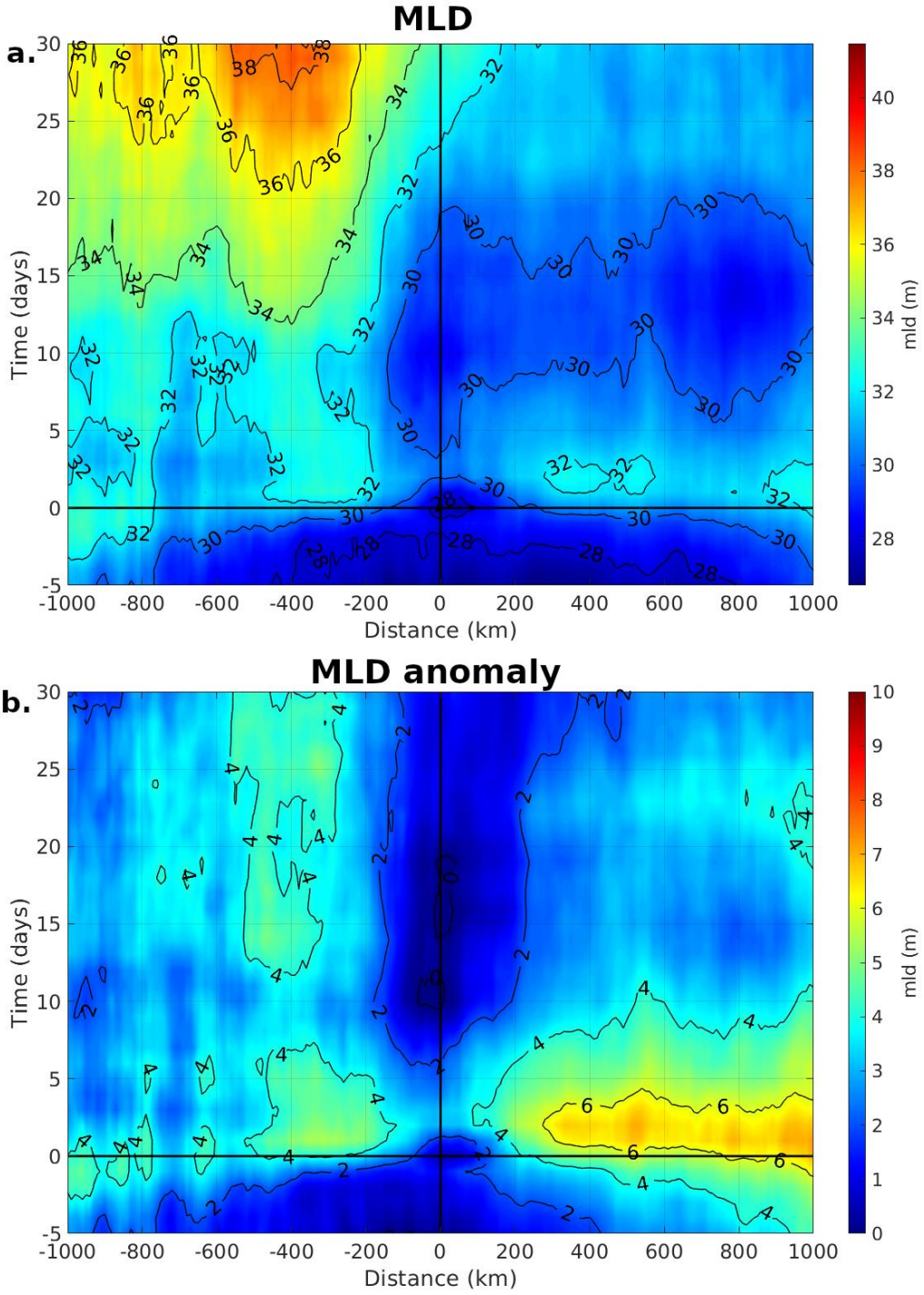

Figure 5.13: Cross-track Hovmoller diagram of: (a) MLD; and (b) MLD anomaly to 20-year climatology over time, composited for 20 years of TCs (1396 data points). Contours every 2 m.

Fig. 5.14 shows a composite of the vertical velocity, temperature anomalies, and divergence of horizontal currents averaged within 100 km of the TC centre, where the stronger cooling occurs. Fig. 5.14a shows the composite down to 2000 m depth and out to 30 days after the TC passage and Fig. 5.14b shows more detail down to 500 m and to Day 15. TCs trigger a strong current response in the column directly beneath the TC inner core typically out to 200 km at the left of track and 400 km at the right of it (Fig 5.10 and 5.12), with divergence of horizontal currents at the surface during Day 0 and Day 1 (Fig. 5.14b) which drives Ekman upwelling. Overall, the maximum cooling appears to be confined in the first 500 m near the surface, while the upward vertical currents reach deeper to 2000 m (Fig. 5.14a). Beneath the surface, the cooling reaches its maximum extent earlier at deeper depths. For example, below 200 m the maximum cooling occurs 2 days after the TC passage, while in the ML the cooling increases through Day 4 (Fig. 5.14b, black contours). At depth, the maximum cold anomaly is reached at the time when the vertical currents reverse from an upwelling regime under the TC to downwelling (Fig. 5.14b). After Day 2 the divergence of horizontal currents at the surface starts to diminish and reverse to convergence around Day 4, driving the reversal of the vertical currents after Day 2 (Fig. 5.14b) to downward, which reach 2000 m depth. At the surface, the cooling remains steady until 10 days after the passage of the TC, while below 150 m the temperature starts to recover around Day 5, alternating 2 days of stronger temperature increase with 2 days no change which corresponds to periods of stronger convergence at the surface and stronger downward vertical currents associated with the warming periods (Fig. 5.14b).

In the days following the TC it is expected that near inertial currents would develop and last for several days, creating alternating patterns of convergence and

divergence (Price et al., 1994; Shay & Elseberry, 1987). As the period of the inertial oscillation depends on latitude and TC translation speed, the overall inertial signal is expected to be significantly smoothed by the composite average. However, some signal remains, with stronger convergence and associated downwelling seen in Fig. 5.14b.

It is apparent from Figs. 5.11 and 5.14 that the recovery time of the temperature anomalies changes with depth. At the surface, the average e-folding time for the temperature recovery to pre-TC conditions is approximately 20 days, while in the subsurface between 100 and 150 m it is 25-30 days (Fig. 5.14c). Below 200 m depth the e-folding time decreases with depth. The faster recovery at the surface and at depths below 200 m is driven by different processes. At the surface, the recovery is driven by air-sea fluxes which heat the surface faster than the subsurface (Fig. 5.15). At depth, where the temperature anomalies are driven by the upwelling during the TC passage, the recovery is expected to be driven mostly by downwelling in the following days. This process could be the reason for the fast recovery below 300 m, where the maximum cold temperature anomalies are small (< 0.1°C, Fig. 5.14a and b) and recover as soon as the upwelled isotherms relax. Between 50 m and 200 m, where the solar radiation warming is low, but the cooling driven by the cyclone passage is still significant, the downwelling takes longer to recover the temperature anomaly and the e-folding time for the recovery reaches 30 days (Fig. 5.14b).

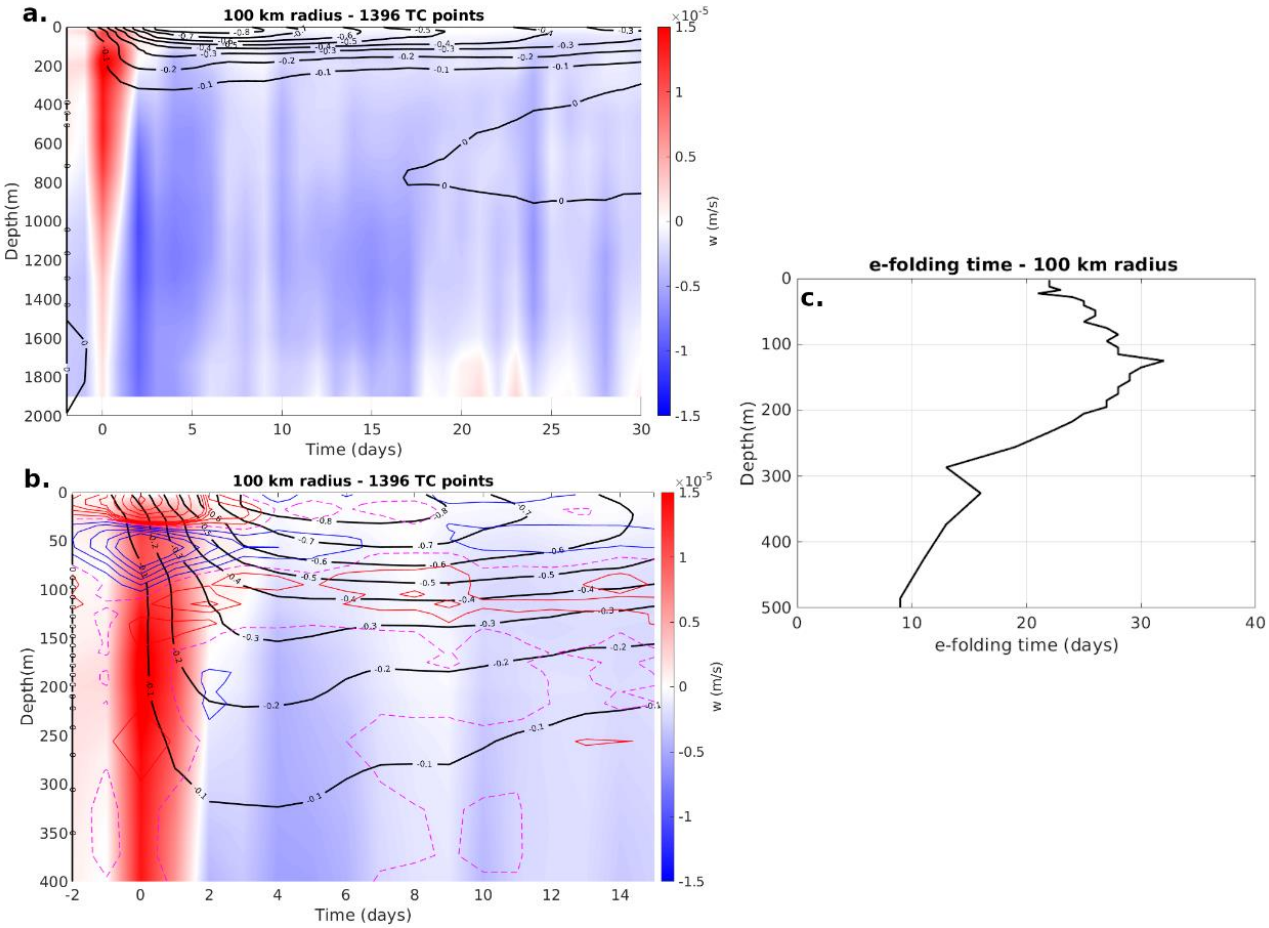

Figure 5.14: Depth-time cross-section of temperature anomalies (units: °C, black contours every 0.1°C), vertical velocities (units: m/s, shading), and divergence (units: x 10^{-8} s^{-1}, red (+ve) and blue (-ve) contours every 2 x10^{-8} s^{-1}) averaged over a 100 km radius circle centred on the TC for: (a) 30 days after the TC up to 2000 m depth; (b) 15 days after the TC up to 400 m depth; and (c) the e-folding time for the temperature recovery at different depths.

Fig. 5.15 further illustrates the connection between SST recovery at the surface and air-sea heat fluxes. From Day -2, when the TC clouds start to affect the area, the solar radiation and consequently the net heat flux entering the ocean start to diminish, with a negative peak on Day 0 and a recovery period up to Day 4. Between Day -1 and Day 2 the net heat flux is negative, as the heat loss towards the atmosphere from longwave, latent and sensible components are greatest (Fig. 5.6 for Day 0). A negative net heat flux at the surface drives an SST reduction, which is further enhanced by current-driven mechanisms such as upwelling and ML entrainment. After Day 5, the SST starts to recover at a faster rate until Day 15 and then more slowly afterwards. During this time (after Day 5), the shortwave heat flux is almost constant, while the net heat flux has a maximum between Day 5 to 10, then starts to decrease. The reduction of the net heat flux is to be expected: warmer SSTs increase latent heat loss to the atmosphere. There is good agreement between SST recovery being faster when the net heat flux is higher and slower, as the net heat flux entering the ocean diminishes (in accordance with Price et al., (2008) analysis).

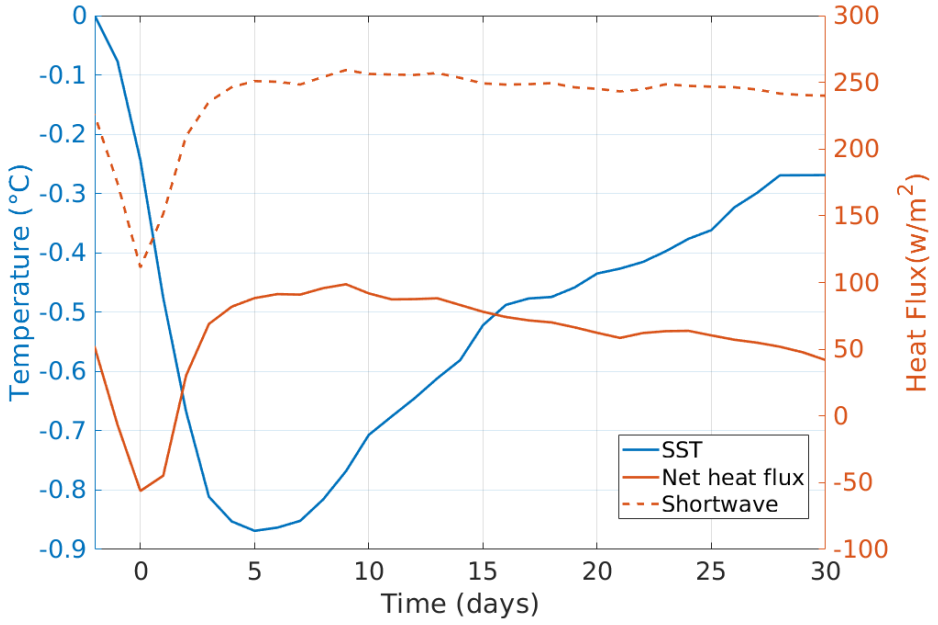

Figure 5.15: SST anomalies (blue line), net (full red line) and shortwave heat flux (dashed red line) change in time averaged over a 100 km radius circle centred on the TC centre. The net heat flux is positive as it warms the ocean and negative as it cools it. The positive shortwave heat flux is the amount of solar radiation entering the water at the ocean surface.

In summary, the passage of a TC over the NWS region triggers a strong temperature and current response over the ocean. TCs drive strong cold anomalies beneath the track and over a large surrounding surface area. These strong cold anomalies do not fully recover in the 30 days following the TC. Warm anomalies in the subsurface at the side of the track continue to increase in the month following the TC passage.

5.4 Comparison between the deep ocean and continental shelf

The NWS is characterised by a large shallow continental shelf area, and the effect of a TC over the shallower shelf is expected to be different from that over the deep ocean. Thus, this analysis separates the locations into over the shelf (< 200 m depth, 459 data points) and those located over the deep ocean (> 200 m depth, 937 data points).

Figs. 5.16 and 5.17 show that in general the cold anomalies are wider, extend deeper and are greater on the shelf (left columns of Figs. 5.16 and 5.17) compared with over the deep ocean (right columns). At the surface, the area of maximum cooling is shifted further to the left of the track for shelf data points compared with the deep ocean data points, and it is wider, expanding to 200 km on both sides of the track for shelf data points compared to 100 km on both sides for deep ocean data points (Fig. 5.16a and b). At 100 m depth, the cold anomalies beneath the track are larger for the TC data points over the shelf, while the warm anomalies on the sides of the track cover a larger area for deep ocean data points, especially over the right of the track (Fig. 5.16c and d). Furthermore, over the deep ocean the temperature anomalies diminish with depth, on the shelf at around 100 m deep there is an area where the cooling is lower than in the layer below (Fig. 5.17a, b). The larger cooling on the shelf below 100 m corresponds to strong upward vertical currents in the deeper layers (Fig. 5.16c, d, e and f and 5.16a and b), suggesting that the colder wake at depth could be driven by upwelling along the shelf edge. The cooling is most evident 2 days after the TC passage, when the strong upward vertical currents driven by the TC passage start to diminish.

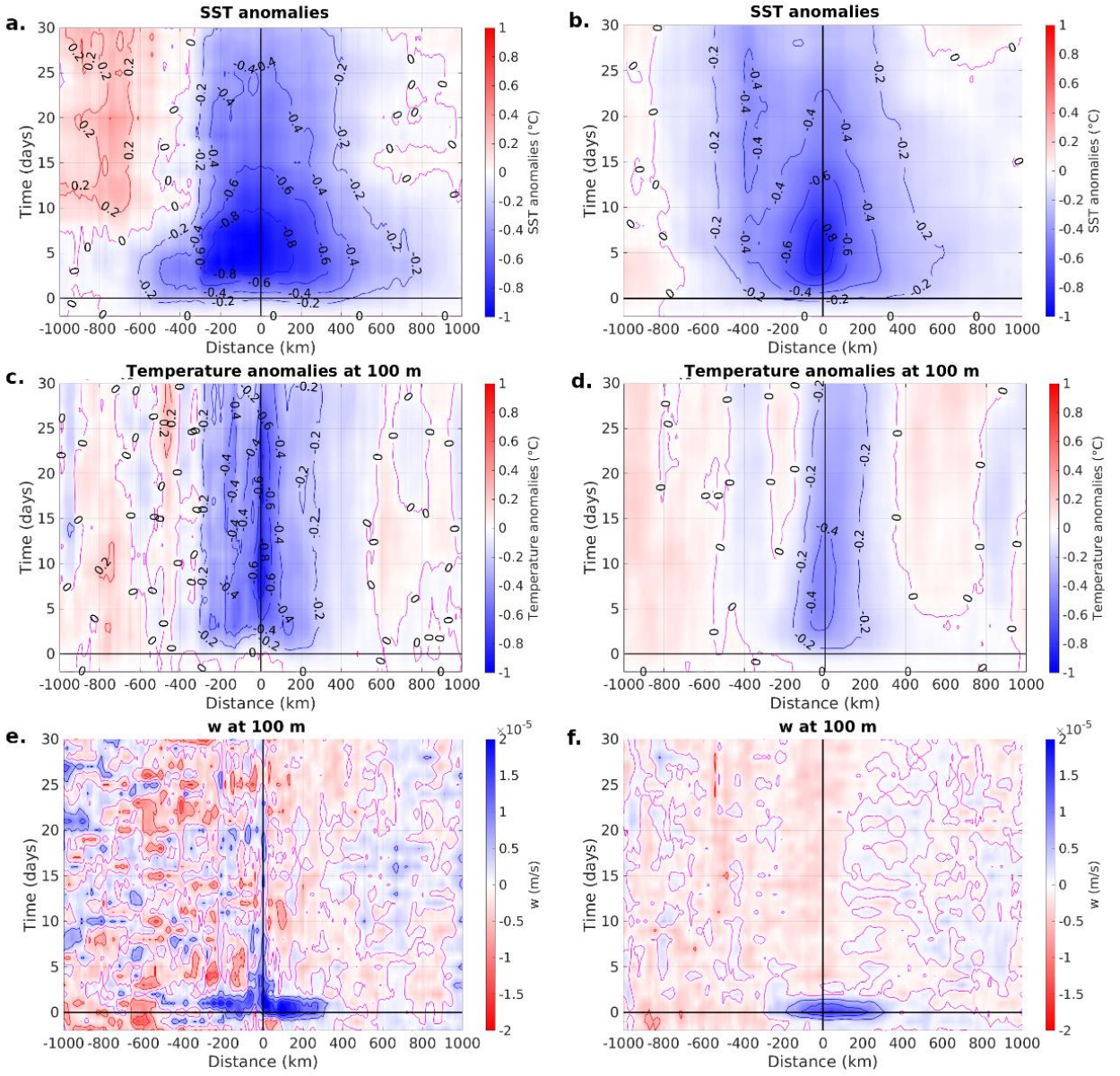

Figure 5.16: Cross-track Hovmoller diagram for shelf (left column, 459 TC data points) and deep ocean (right column, 937 TC data points): (a), (b) SST anomalies; (c), (d) temperature anomalies at 100 m depth (contours every 0.2 °C); and (e), (f) vertical currents at 100 m depth (contours every 0.5 x10^{-5} m/s).

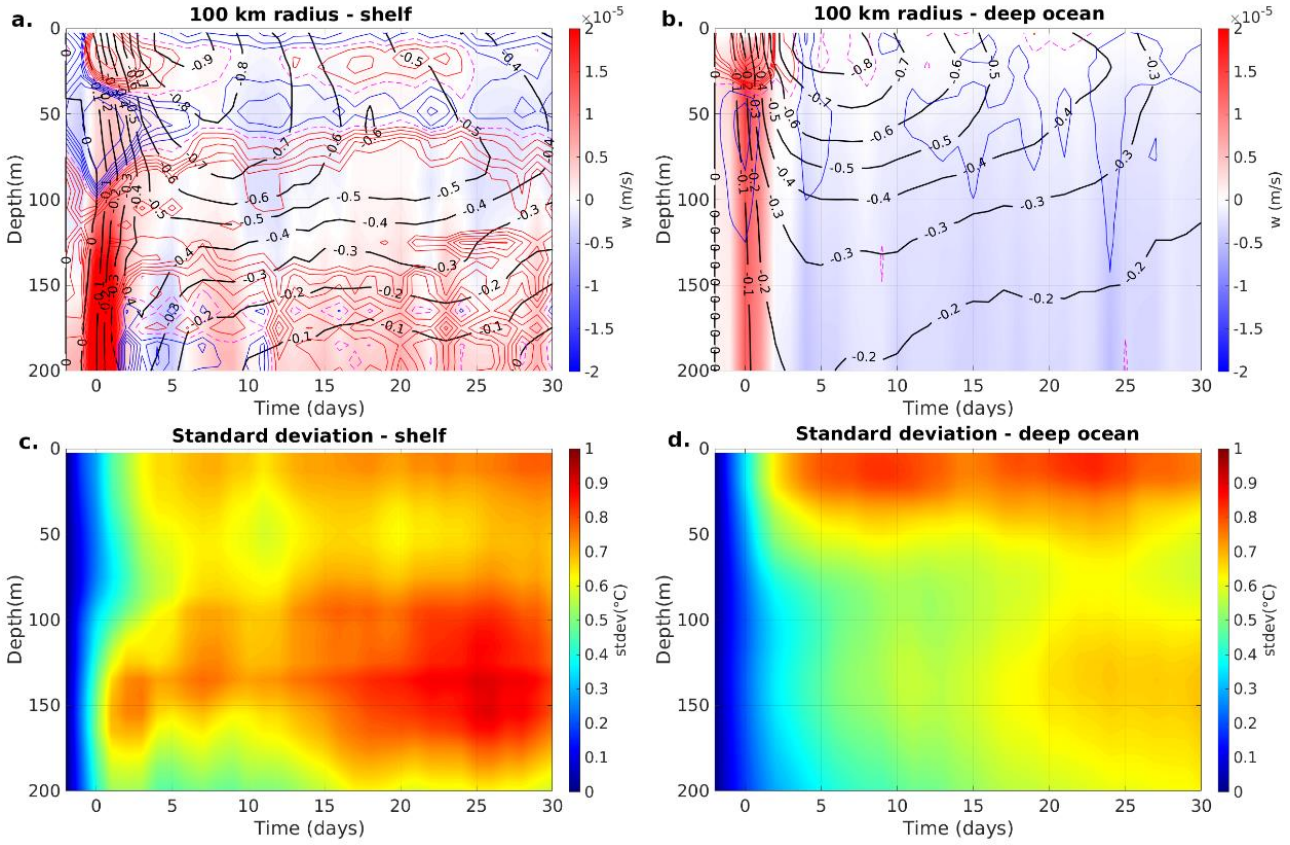

Figure 5.17: Depth-time cross-sections averaged over a 100 km radius circle centred on the TC to 200 m depth for shelf (left, 459 TC data points) and deep ocean (right, 937 TC data points) data points: (a), (b) temperature anomaly (black contours every 0.1 °C); vertical velocities (shaded, units: x 10^{-5} m/s) and divergence (units: x 10^{-8} s^{-1}, red (+ve) and blue (-ve) contours every 2 x10^{-8} s^{-1}); and (c), (d) the standard deviation of temperature (shading, Units: °C).

The interaction of the TCs with the shallower shelf region produces stronger upwelling below 100 m depth between Day -1 and Day 2 and is likely the reason that more cooling occurs over a larger horizontal and vertical area. There is higher variability below 100 m depth for shelf data points (Fig. 5.17c). This is possibly because the average bathymetry of the TC locations over the shelf is around 70 m and below 100 m depth a lower number of data points is included in the composite. Furthermore, the TC data points over the shelf that have bathymetry close to 200 m are likely close to the shelf edge, where strong upward or downward currents could develop along the slope. In fact, the noisier pattern of the vertical currents along the shelf edge could be dependent on the direction that the cyclone moves, which impact the oceanic response as the wind induced currents interact differently with the shelf slope (Davidson and Holloway, 2001). Because of this, it could be necessary to study each TC trajectory and the response of the shelf currents separately.

The e-folding temperature recovery time is slightly higher at the surface for shelf data points (Fig. 5.18), perhaps due to more intense cooling that develops over a larger area (Fig. 5.16a and c). For shelf data points, the subsurface recovery time is only slightly higher than at the surface because the water is often well mixed and the solar heat flux that drives the recovery is redistributed over the whole water column by tides and shelf currents. Near the shelf bottom (below 120 m) the e-folding time appears to be much shorter than at the same depth for the deep ocean cases (Fig. 5.18). The faster recovery of the cold anomalies over the shelf at these depths could be due to the strong downward currents that develop along the shelf following the strong upwelling and that quickly restores temperatures to pre-TC conditions (Fig. 5.17a).

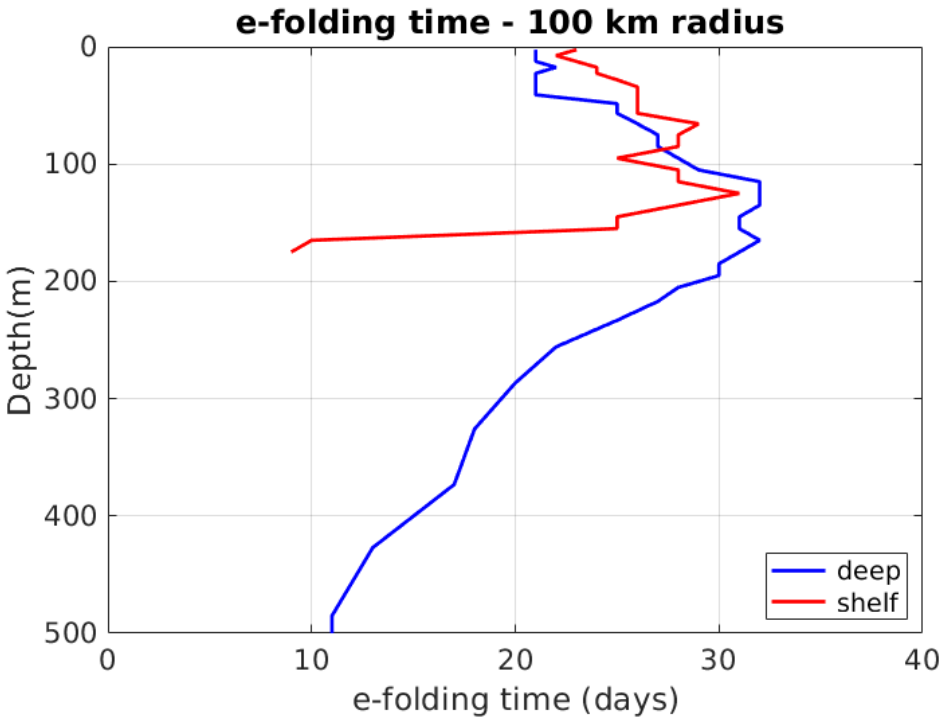

Figure 5.18: e-folding time for the temperature recovery at different depths for shelf and deep ocean data points.

5.4.1 TC direction of motion over the continental shelf

To study the effect of the direction of motion on the shelf a smaller region (110°-127° E ,13°-22°S) has been considered (Fig. 5.19). Within this smaller region, the coast was approximated by a straight line and the data points where the TC was moving parallel to the coast and toward the south-west (± 20°) and perpendicular to the coast and towards the coast (± 20°) were composited separately (Fig. 5.19). There are 341 data points where TCs moved parallel to the coast, of which 108 are on the shelf edge (bathymetry < 200 m), and 107 data points where TCs moved perpendicular to and towards the coast, with 53 over the shelf edge.

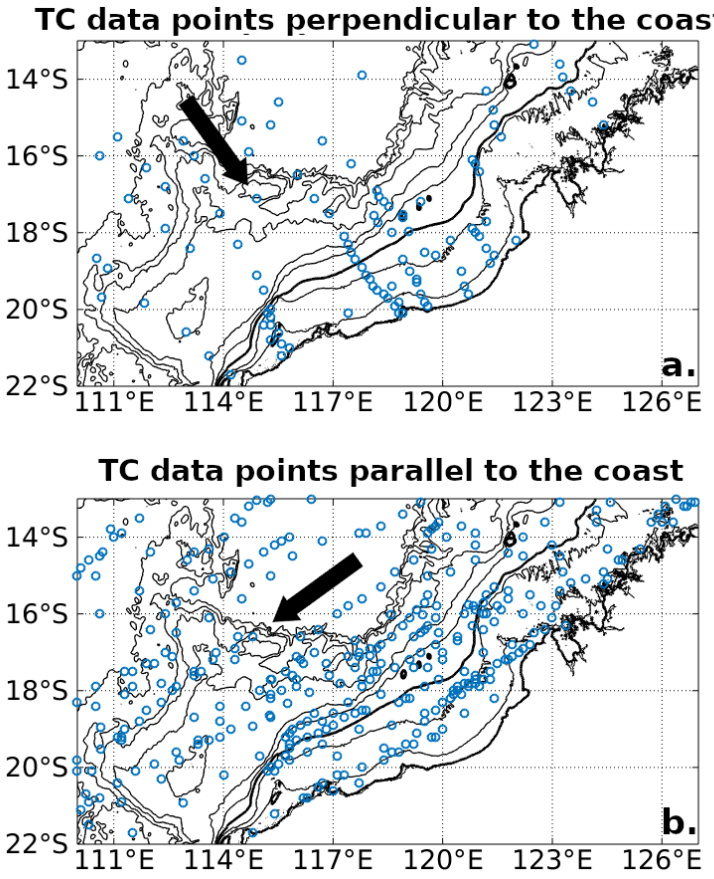

Figure 5.19: TC data points for TCs moving in proximity to the shallow region for (a) TCs moving perpendicular; and (b) TCs moving parallel to the coast. Bathymetry contours are at 30 m, 100 m, 200 m (thick line), 500 m, and then every 1000 m below 1000 m.

The data points over the shelf parallel or perpendicular to the coast are shown in the composite in Fig. 5.20. There are no data beyond 200 km on the left of track for TCs moving parallel to the coast due to the proximity to the coast. At the surface, the temperature anomaly composite (Fig. 5.20a and b) shows greater variability with the distance from the track for TCs that move perpendicular toward the coast, which may be due to variations in the bathymetry the TC passes over, or more generally the stronger horizontal currents over the shelf.

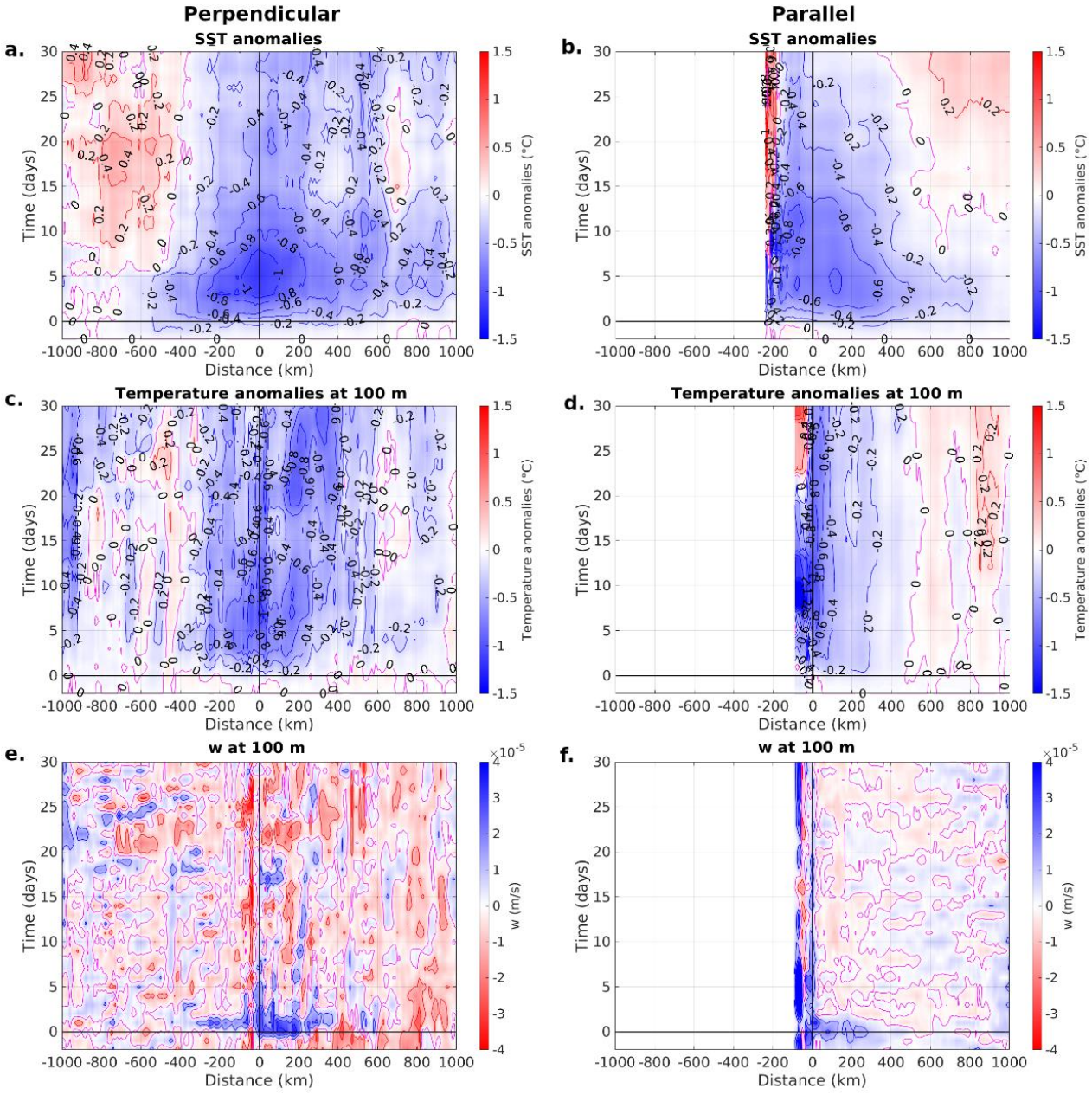

Figure 5.20: Cross-track Hovmoller diagram for TCs moving perpendicular (left column, 53 TC data points) and parallel (right column, 108 TC data points) to the coast: (a), (b) SST anomalies; (c), (d) temperature anomalies at 100 m depth (contours every 0.2 °C); and (e), (f) vertical currents at 100 m depth (contours every 1 x10^5 m/s).

5.4.1.1 TCs perpendicular to the coast

TCs moving perpendicular toward the coast develop maximum SST cold anomalies directly beneath the TC centre approximately 5 days after the TC passage (Fig. 5.20a), which are slightly stronger than for the "all TCs" composite (Fig. 5.5). The maximum SST anomaly is initially asymmetric to the left of track and then switches to the right of track after Day 5. After Day 15, the cold anomalies beneath the TC centre have recovered to values similar to those for all TCs. However, there is an area of substantial warming to the left of track beyond 700 km beginning Day 0, that expands inward to 400 km and intensifies after Day 5. In comparison, the "all TCs" composite (Fig. 5.5) develops only very weak warming beyond 800 km on the left of track beginning Day 0. There is also a slot of warming that develops on the right of track near 650 km beginning Day 5, which steadily increases through Day 15 and it is present until Day 25 (Fig. 5.20a). There is no similar right-of-track warming in the "all TCs" composite.

At 100 m depth, TCs that move perpendicular to the coast produce a larger variation of the temperature anomaly with the distance from the track and in time than at the surface. While this is still likely to be because of the lower number of data points considered in the composite, there are also strong internal tides and cyclone induced internal waves that can last several days after its passage that may affect the composite structure (Davidson and Holloway, 2003). In general, at 100-m depth the largest temperature cold anomaly is still located beneath the TC centre (Fig. 5.20c) coincident with the surface anomaly. Strong upwelling out to 400 km either side of the TC track from Day 0 to Day 3 drive the central cold anomalies (Fig. 5.20e). After Day 3 the vertical currents reverse to downward in bands. This alternating pattern of upward and

downward motion with the distance from the track has a wavelength of approximately 100 km and could be due to internal waves that are not completely averaged out in the composite and in BRAN daily output, due to the low number of TC data points in the composite. There is a secondary cold maximum on the right-of-track at 100-m depth that coincides with the shift of the temperature asymmetry at the surface to right-of-track after Day 5. This secondary maximum, which is located near 200 km from the centre coincides with strong upwelling at that radius that remains in place through Day 15 (Fig. 5.20e). The warming on the left of track is also evident at 100 m depth although it is located closer to the TC centre and exhibits a strong lateral banding structure coincident with the bands of upwelling and downwelling after Day 3. At 100 m depth the warming on both sides of the track decays slowly and it is still strong after 30 days from the TC passage (Fig. 5.20c).

5.4.1.2 TCs parallel to the coast

TCs that move parallel to the coast develop SST cold anomalies with two peaks near Day 4, one on each side of the track (Fig. 5. 19b). These peaks are located closer to the coast, where the shallow shelf depth allows the cooling to occur more rapidly and to a greater extent, and just off the shelf edge (situated on the right of track), where the cold water upwells along the edge. The right-of- track anomaly decreases over time, similar to the general shelf case. However, the left-of-track anomaly maintains intensity over time through Day 12 perhaps because of enhanced upwelling driven on the coast due to the orientation of the TC winds along the coast.

To confirm the locations of the two peaks in Fig. 5.20b, Fig 5.21 shows the SST anomalies for shallow TC data points with bathymetry < 30 m situated along the coast (Fig. 5.21c) and for TC data points along the shelf edge (with bathymetry

between 100 and 200 m depth, Fig. 5.21d). TC data points over shallow water present a strong peak under their track (Fig. 5.21a) where the bathymetry is shallow and the water cools easily, and a smaller peak at around 100 km over the right of the track, where the shelf edge is located and the cold water is upwelled. TC data points along the shelf edge (Fig. 5.21d) show a peak on the left of track, where the coast and shallow water is situated and a larger peak beneath the track and slightly on the right of it, where the shelf edge is located (Fig. 5.21b). Furthermore, for data points over the shelf edge (Fig. 5.21b) the temperature anomaly beneath the track reaches its maximum around Day 10 and lasts longer than for the general case, suggesting the development of a long-lasting upwelling along the shelf slope. The cold anomalies are stronger and cover a larger region on both sides of the track for TC data points over the shelf edge, likely due to the strong convergence that develops at the bottom of the shelf slope which triggers strong upwelling of colder water along the slope. Although the coarser resolution BRAN data do not permit further study into the detailed development of temperature anomalies over the shelf edge, this analysis does confirm that the spatial pattern of the temperature anomalies that develop following a TC that passes over the shelf and parallel to it depends also on the distance from the coast and the underlying bathymetry (Davidson and Holloway, 2001).

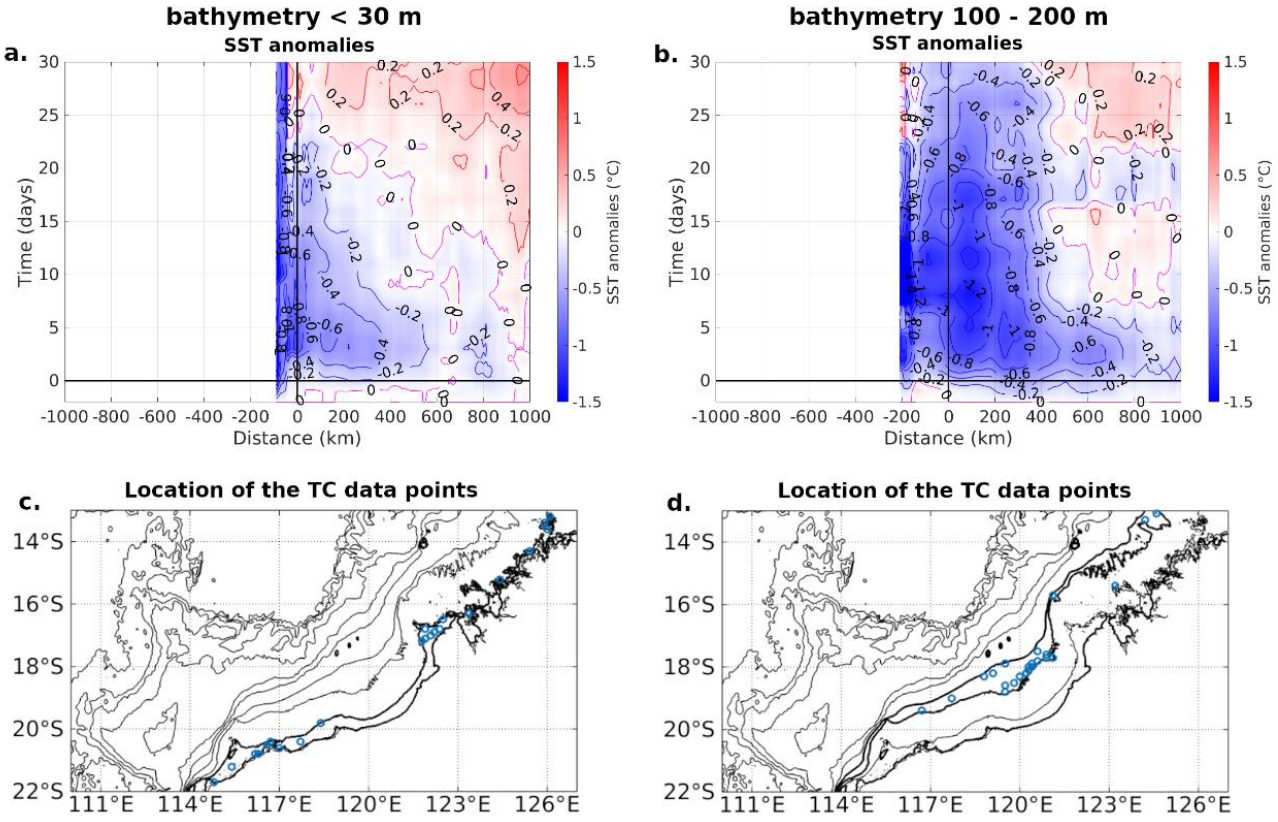

Figure 5.21: (a), (b) Cross-track Hovmoller diagram of SST anomalies (contours every 0.2 °C) in time; and (c), (d) map of the location of the data points on the NWS for TCs moving parallel to the coast for bathymetry shallower than 30 m (left column, 22 TC data points) and near the shelf edge with bathymetry between 100 and 200 m (right column, 25 TC data points).

TCs that move parallel to the coast exhibit increasing cold temperature anomalies at 100 m depth, which reach a maximum between Day 8 and 10 (Fig. 5.20d). These anomalies are stronger than at the surface and reach up to more than 1.2 °C and are located just to the left of the track and are likely bounded by the presence of the shelf edge and rising sea bottom in that location. Strong vertical currents lie across the TC track from the coast on the left-of-track to 400 km to the right-of track at Day 0 to Day 2 (Fig. 5. 19f) supporting the initial development of the cold anomaly from the coast out to approximately 400 km and from 100-m depth to the surface. The strong upward vertical currents continue along and to the left of track through Day 30 except for a thin ribbon of relatively strong downwelling that develops at 50 km on the sides of the track after Day 6. The very strong upwelling and cooling that occurs on and left-of-track to the coast possibly explains the longer duration of the cold anomalies at 100 m depth beneath the track and could have implications for the ecologically sensitive littoral zone along the NWS. Strong warm anomalies at 100 m depth also develop on the right of track corresponding to the SST warm anomalies (Fig. 5.20b), although they develop from Day 0 at 100 m, with a similar patter to the general case on the right of the track (Fig. 5.11c). These anomalies are likely located over the open ocean rather than on the shelf and they could be due to the weak downwelling motion away from the track that develops to compensate the strong upwelling beneath it, as in the general case.

In summary, although BRAN does not allow a detailed study of the TC-induced currents and temperature anomalies over a shallow bathymetry, it is clear that TC data points over the shelf present different behaviour depending on the direction of movement compared to the shelf edge (Davidson and Holloway, 2001). In particular,

TCs that move south-westward parallel to the coast develop much stronger cold anomalies beneath the track, especially at 100 m depth and strong upward currents beneath the track that last for up to 30 days after the TC passage.

5.4.2 Deep Ocean TCs moving parallel to the shelf

As shown in the previous section, the presence of the continental shelf has considerable impacts on the ocean conditions associated with TCs moving parallel to the coast. A question arises whether the orientation of the NWS affects the ocean processes over deep ocean locations. To explore this a little further, deep ocean TC data points moving parallel to the coast in the region (110° - 127° E, 13° - 22°S) are divided into data points at locations within 200 km from the coast, between 200 and 400 km from the coast and at more than 400 km from it (Fig. 5.22a, b and c).

As the cyclone passes parallel to the shelf at distance, the cyclonic winds at distance to the left of track (where the shelf is located) are predominantly north-easterly parallel to the coast, driving Ekman downwelling because of the wind-coast interaction. Enhanced warming at depth is produced on the left of track by TCs that move parallel to the shelf compared to the general population (Fig. 5.22g-l compared to Fig. 5.11c, f). This enhanced warming is more significant at 300 m depth for TCs that pass further away from the coast and it is correlated with strong downward currents over the left of track at 100 m depth (Fig. 5.22i, l and o). This is possibly due to the north-easterly TC winds over the left of track at distance over the shelf edge, that are weaker but last for longer and drive downwelling for a longer time, although with a limited sample (87 TC data points) it can't be excluded that this could be due to the effect of some particular strong TC. There is not much warming signal over the left of the track at depth for data points very close to the shelf slope (Fig. 5.22a, g, j),

as the coast is too close on that side and the bathymetry too shallow. At the surface, at more than 600 km to the left of the track, the SST anomalies driven by TCs that pass further from the coast are positive from Day 0 and Day 2 before starting to decrease after Day 3 (Fig. 5.22f). The decrease of SST is concurrent with an increase in temperature anomalies at depth further than 200 km on the left of the track (Fig. 5.22f, i, l), which suggests that there is significant mixing on the left of track in the days following the TC passage. The mixing near the shelf edge could be enhanced by the strong internal waves, which are not fully captured by BRAN daily output. At 100 m depth there is considerable warming extending from less than 200 km from the centre of the TC to over 1000 km (Fig. 5.22k, l) driven by much stronger downwelling (Fig. 5.22n, o) compared with the general case (Fig. 5.12c). After Day 4 the vertical motion pattern to the left of track shows a similar lateral downwelling, upwelling pattern observed for the "on-shelf" TC data points (Figs. 5.22m, n, o, 5.20f) suggesting an influence by internal waves generated by the continental shelf. While these shifts affect the overall warming pattern on the left of track and closer to the coast at 100 m, the general warming of the ocean remains through at least Day 30 after the TC passage.

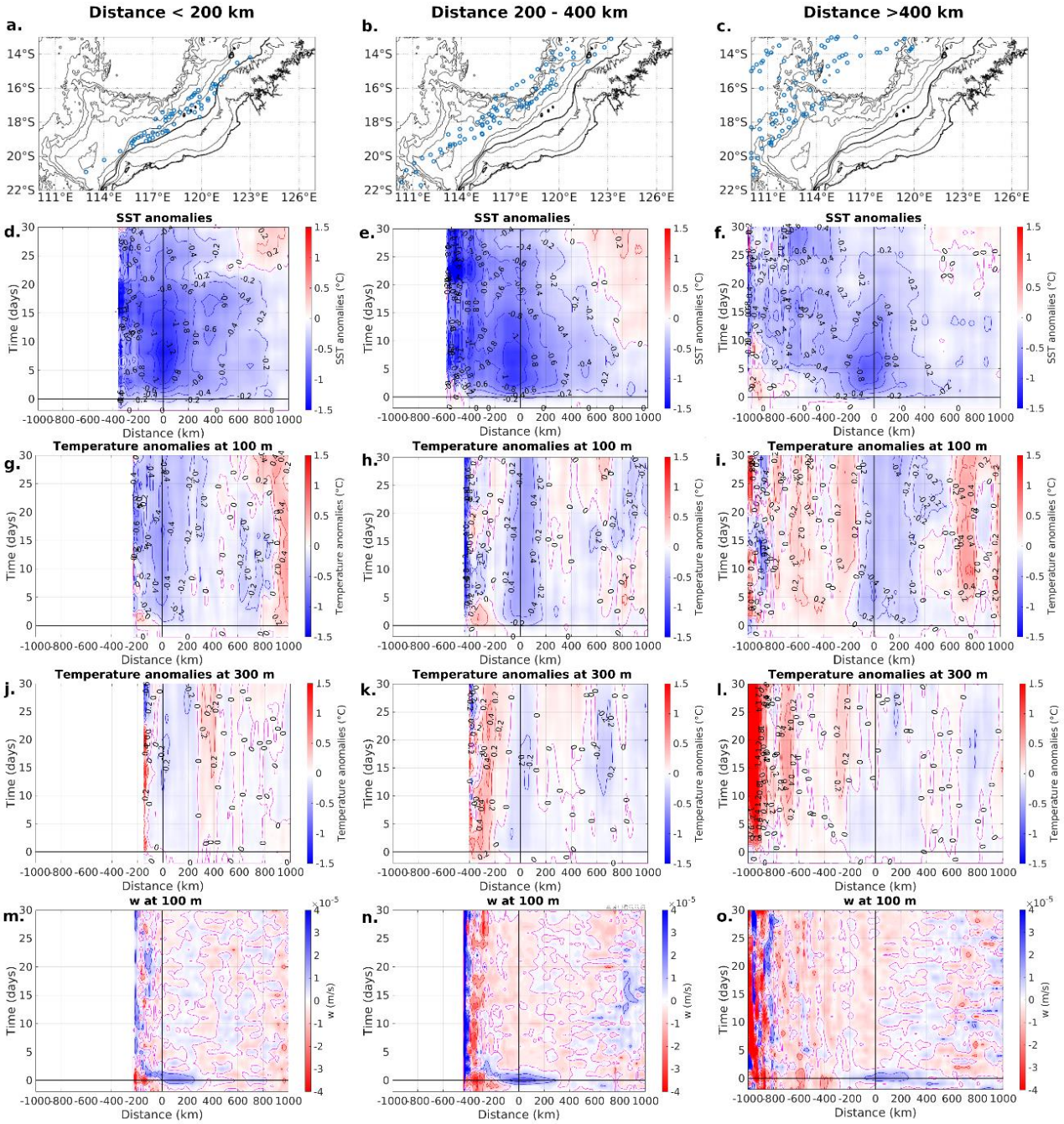

Figure 5.22: (a)-(c) Maps of TC data points with tracks moving parallel to the coast over the deep ocean in the region (110° - 127°E, 13° - 22°S); Cross-track Hovmoller diagram of: (d)-(f) SST anomalies (contours every 0.2 °C); (g)-(i) temperature at 100 m anomalies (contours every 0.2 °C); (j)-(l) temperature at 300 m anomalies (contours every 0.2 °C); and (m)-(o) vertical velocity at 100 m depth (contours every 1 x 10^{-5} m/s in time for data points within 200 km from the coast (left column, 57 TC data points), between 200 and 400 km from the coast (middle column, 79 TC data points) and at more than 400 km from the coast (right column, 87 TC data points).

5.5 Impact of different seasons on the ocean temperature anomalies recovery after the TC passage

To study the impact of the period of the year when the TC occurs on the ocean recovery, the deep ocean TC dataset is divided into two seasons: 1) the "warming season", which occurs between November and February when the ocean temperature is generally warming, and 2) the "cooling season", which occurs after February, when the ocean starts to cool down as autumn approaches. The recovery of the temperature anomalies for TC data points during the warming season and cooling season changes with depth (Fig. 5.23). At the surface the cold anomaly recovers faster during the warming season, when the incoming solar radiation and the net heat flux entering the ocean surface is higher (Fig 5.24). This is further confirmed by the anomaly to a 20-year climatology of the net heat flux warming the ocean (Fig. 5.24a, b). In fact, during the warming season the incoming shortwave radiation is higher and drives a faster recovery at surface than during the cooling (Fig. 5.24c, d). Furthermore, after the TC passage the latent heat flux losses are reduced compared to the climatology (positive anomalies compared to the climatology, Fig. 5.24e and f), and the effect of the higher shortwave radiation flux on the net heat flux into the ocean during the warming season is enhanced. The e-folding recovery time within 100 km of the TC centre (Fig. 5.23g) shows a difference of almost 10 days between the recovery time at the surface for warming- versus cooling-season TCs. The difference in the e-folding recovery time is much less between 100 and 150 m depth where the solar radiation effect in warming the ocean is reduced. In fact, at 100 m depth the development of the cold anomalies during the warming and cooling season is similar, although the maximum cold

anomalies are slightly colder during the warming season and recover at the same time than during the cooling season (Fig. 5.23c and d). Below 200 m depth the e-folding recovery time decreases to less than 10 days in the cooling season. This may be because the downwelling that drives the temperature recovery at depth is stronger during the cooling season compared to the warming season when the wind regime around the shelf edge could drive upwelling motion. This is confirmed by Fig. 5.25 that shows that the downward vertical currents that develop beneath the track after the passage of a TC are stronger during the cooling season and that in general the vertical currents at the side of the tracks following a TC are mostly upward during warming season and downward during the cooling season.

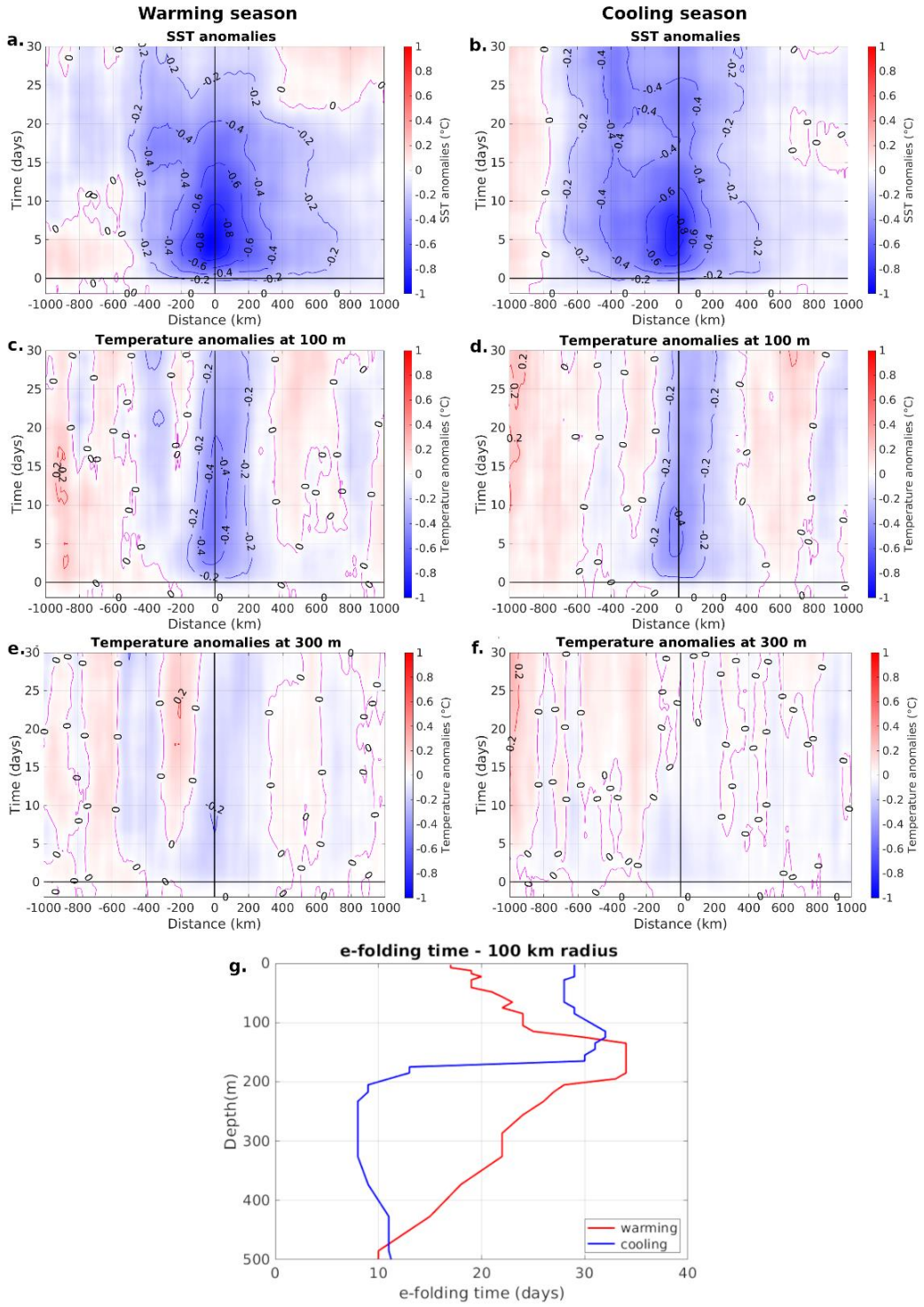

Figure 5.23: Cross-track Hovmoller diagram for: (a), (b) SST anomalies; (c), (d) temperature anomalies at 100 m depth; and (e), (f) temperature anomalies at 300 m depth (contours every 0.2 °C) in time for data points during warming season (left column, 454 TC data points) and cooling season (right column, 483 TC data points); and (g) e-folding time for TC data points during the warming season and during the cooling season.

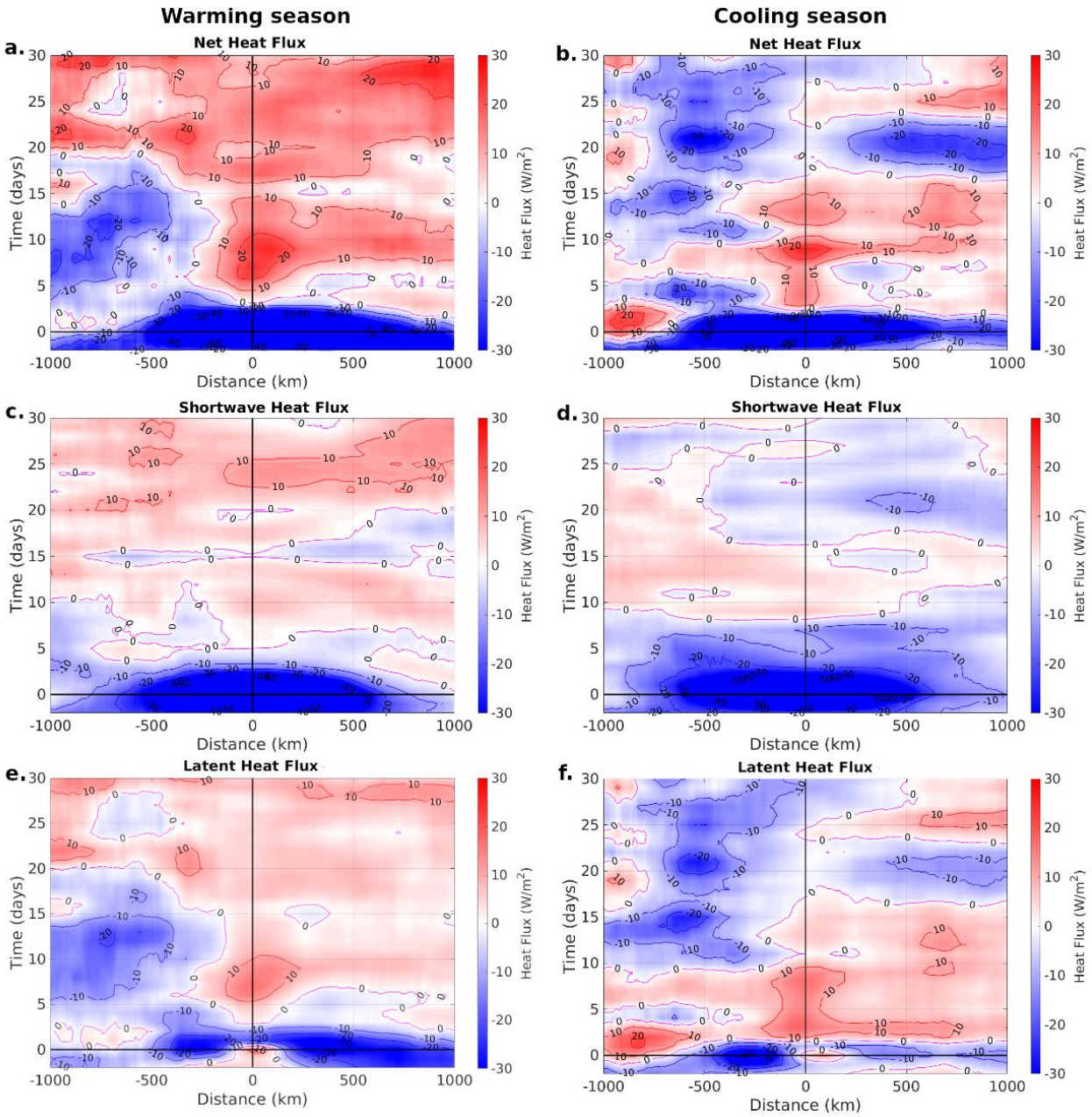

Figure 5.24: Cross-track Hovmoller diagram for: (a), (b) net heat flux; (c), (d) shortwave heat flux; and (e), (f) latent heat flux (contours every 10 W/m^2) in time for data points during warming season (left column, 454 TC data points) and cooling season (right column, 483 TC data points). Anomalies are calculated from the 20-year climatology.

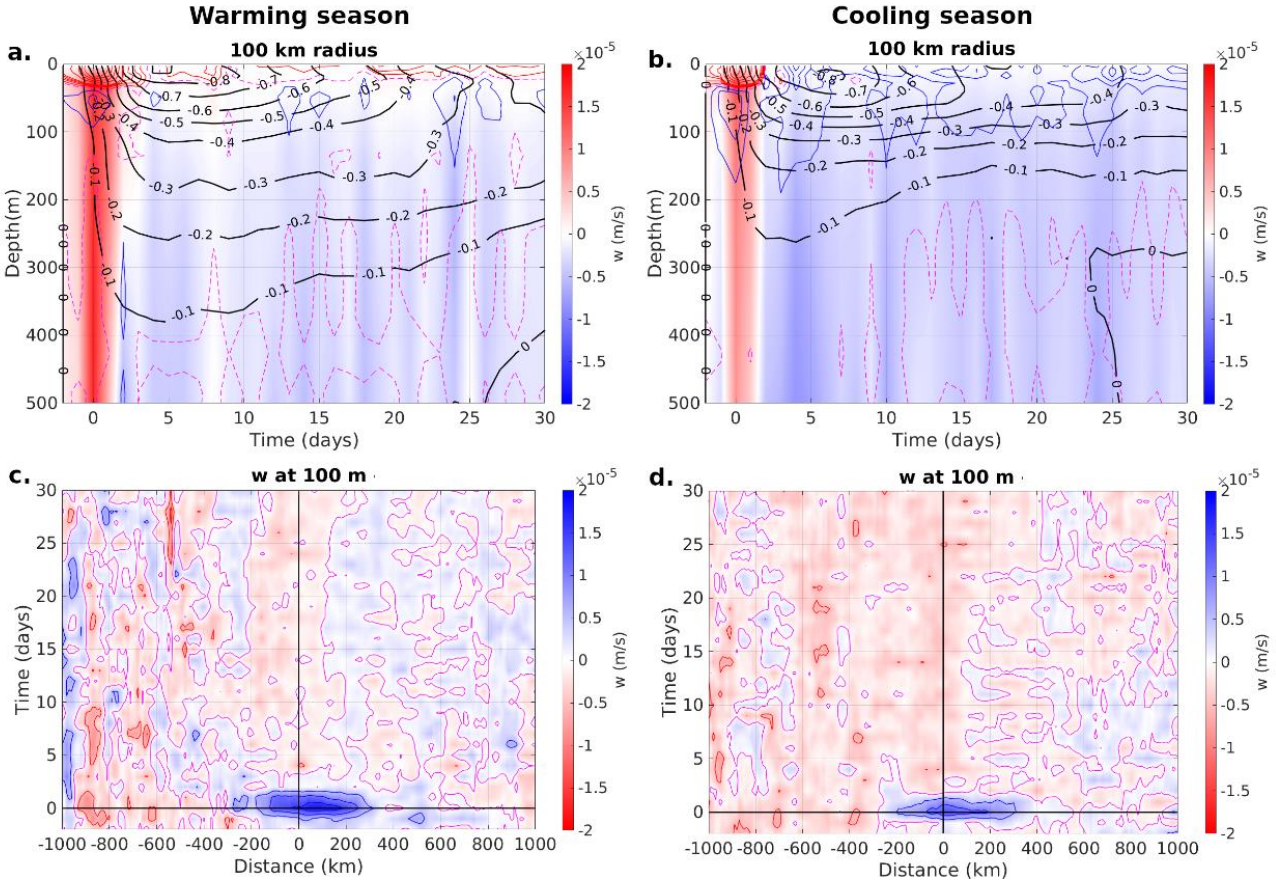

Figure 5.25: (a), (b) Depth-time cross-sections averaged over a 100 km radius circle centred on the TC of temperature anomaly (black contours every 0.1 °C), vertical velocities (shaded, units: x 10^{-5} m/s) and divergence (units: x 10^{-8} s^{-1}, red (+ve) and blue (-ve) contours every 2 x10^{-8} s^{-1}); and (c) (d) cross-track Hovmoller diagram of vertical velocity (contours every 0.2 x10^{-6} m/s) in time for data points during warming season (left column, 454 TC data points) and cooling season (right column, 483 TC data points).

5.6 Strong versus weak and fast versus slow TC effects

The characteristics of the thermal changes induced over the ocean by a TC depends strongly on the intensity and on the translation speed of the TC (Haackman et al., 2019; Lin et al., 2017; Mei and Pasquero, 2013). Initially, the TC data points were separated into 4 groups based on current Australian intensity categories (Category 1 (17.5-24 m/s), Category 2 (25-32 m/s), Category 3 (33-44 m/s), Category 4 and above (> 44 m/s)) and into 4 groups depending on their translation speed (< 2 m/s, 2 m/s - 4 m/s, 4 m/s - 6 m/s, and > 6 m/s), for a total of 16 groups. The number of TC data points included in the composite for each group is presented in Table 5.2.

Table 5.2: Number of TC data points included in the composite for each combination of the 4 groups of translation speed and category.

	Cat 1	**Cat 2**	**Cat 3**	**Cat 4-5**
0-2 m/s	68	22	28	22
2-4 m/s	115	100	66	56
4-6 m/s	131	112	63	57
>6 m/s	41	42	4	10

Fig. 5.26 shows the cross-track SST anomalies for the 30 days following the TC passage for the 16 groups. At the ocean surface, the cold anomalies are more intense for stronger and slower TCs (Fig. 5.26, bottom right). The wake is wider and extends further away from the TC track for slower TCs (bottom row), while it is narrower and shifted more towards the left side of the track for TCs that move faster

(Fig. 5.26, top row). Fig. 5.27 shows the average temperature anomalies within 100 km of the TC centre for the 16 groups. The cold temperature anomalies are more intense for more intense TCs, especially in the surface layer (Fig. 5.27, right column). The translation speed of the TCs influences the temperature anomalies at different depths, as slow-moving TCs produce colder anomalies through the entire water column (Fig. 5.27, bottom row), while fast-moving TCs cool significantly only the layer close to the surface (Fig. 5.27, first row). For the most intense (> Cat 4) fast-moving TCs, there is a net warming below the ML through a deep layer in the ocean (Fig. 5.27, top, right panel).

Because of their similar characteristics, the 16 groups are arranged into 4 more comprehensive groups (Table 5.3, Figs. 5.28 and 5.29): weak and fast TCs, including Cat 1-2 TCs with speed > 4m/s, strong and fast TCs, including TCs of Cat. 3-5 and speed faster than 4 m/s, weak and slow TCs, with TCs of Cat 1-2 and speed < 4m/s and strong and fast TCs of Cat 3-5 and translation speed lower than 4 m/s. Figs. 5.28 and 5.29 clearly illustrate the preceding discussion that slower TCs produce a colder wake that extends symmetrically far from the track and deeper, while faster TCs produce a more asymmetric left of track surface cooling, that is relatively shallower. For simplicity, this division will be used for the following analysis.

Table 5.3: Number of TC data points included in the composite for each combination of fast/slow translation speed and weak/strong intensity.

	weak	**strong**
fast	305	172
slow	326	134

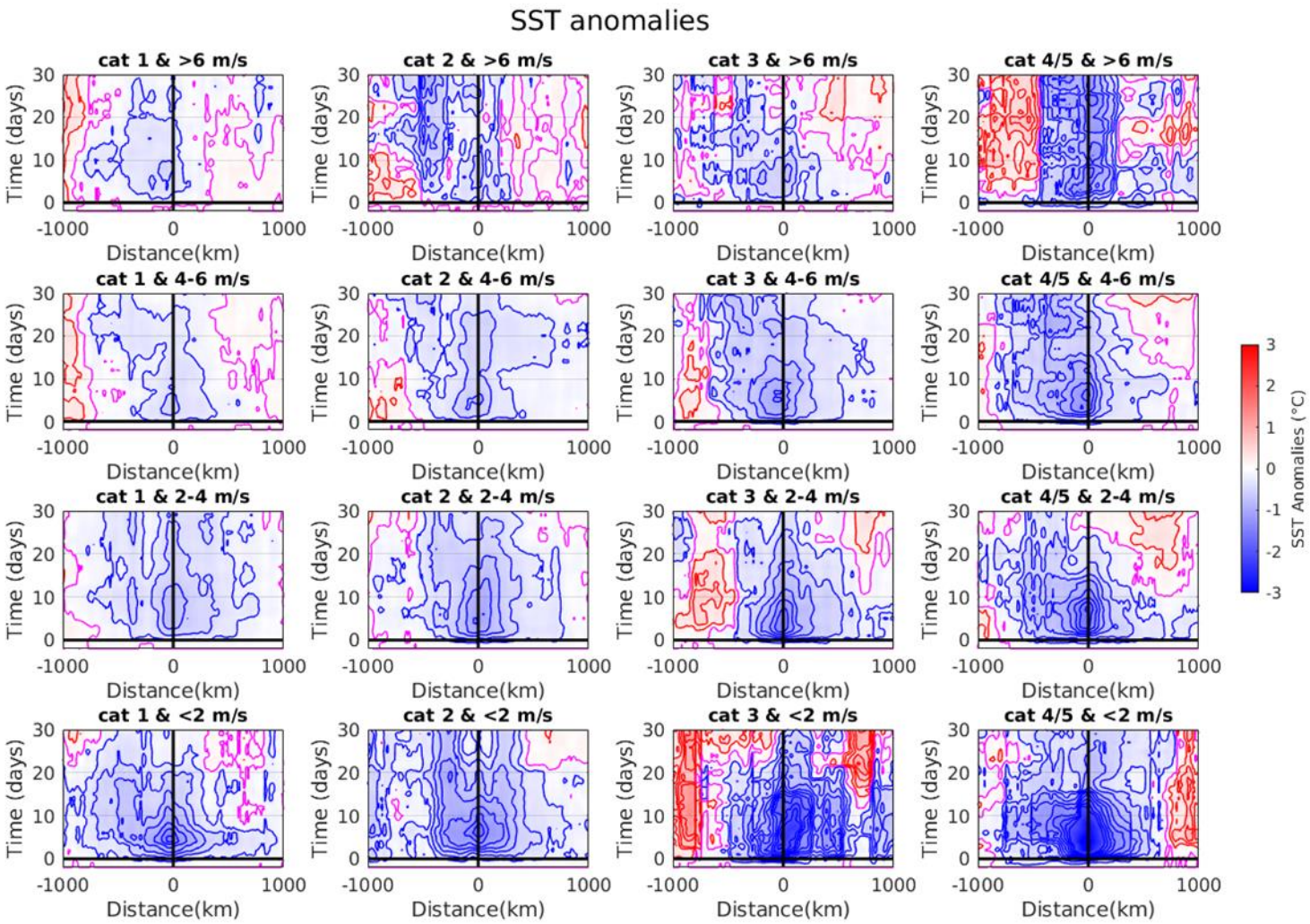

Figure 5.26: Hovmoller diagram of cross-track SST anomaly (contours every 0.2 °C) in time for 16 combinations of TC translation speeds and categories.

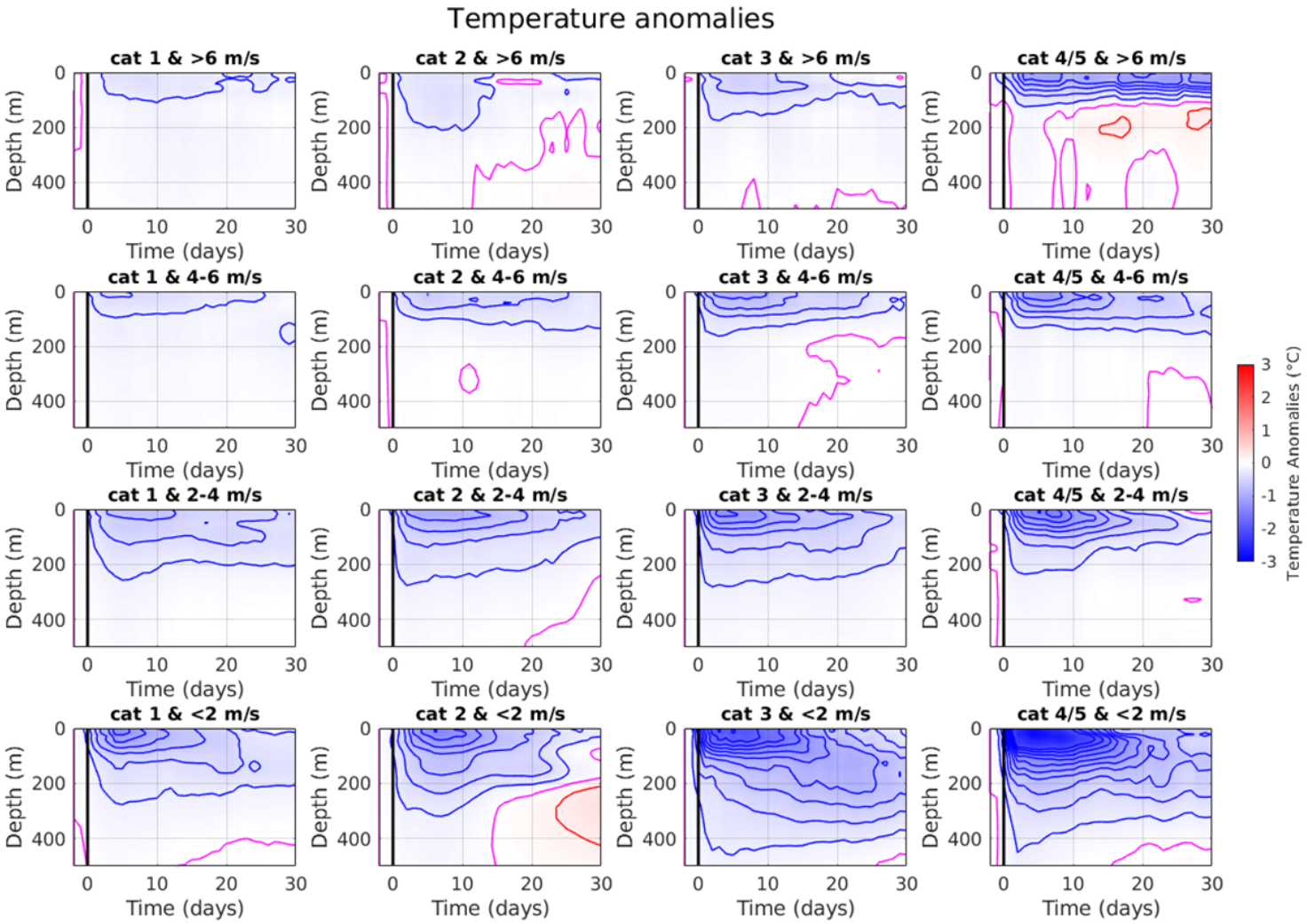

Figure 5.27: Depth-time cross-section of the temperature anomalies (contours every 0.2 °C) averaged within 100-km of the TC centre for 16 combinations of translation speeds and categories.

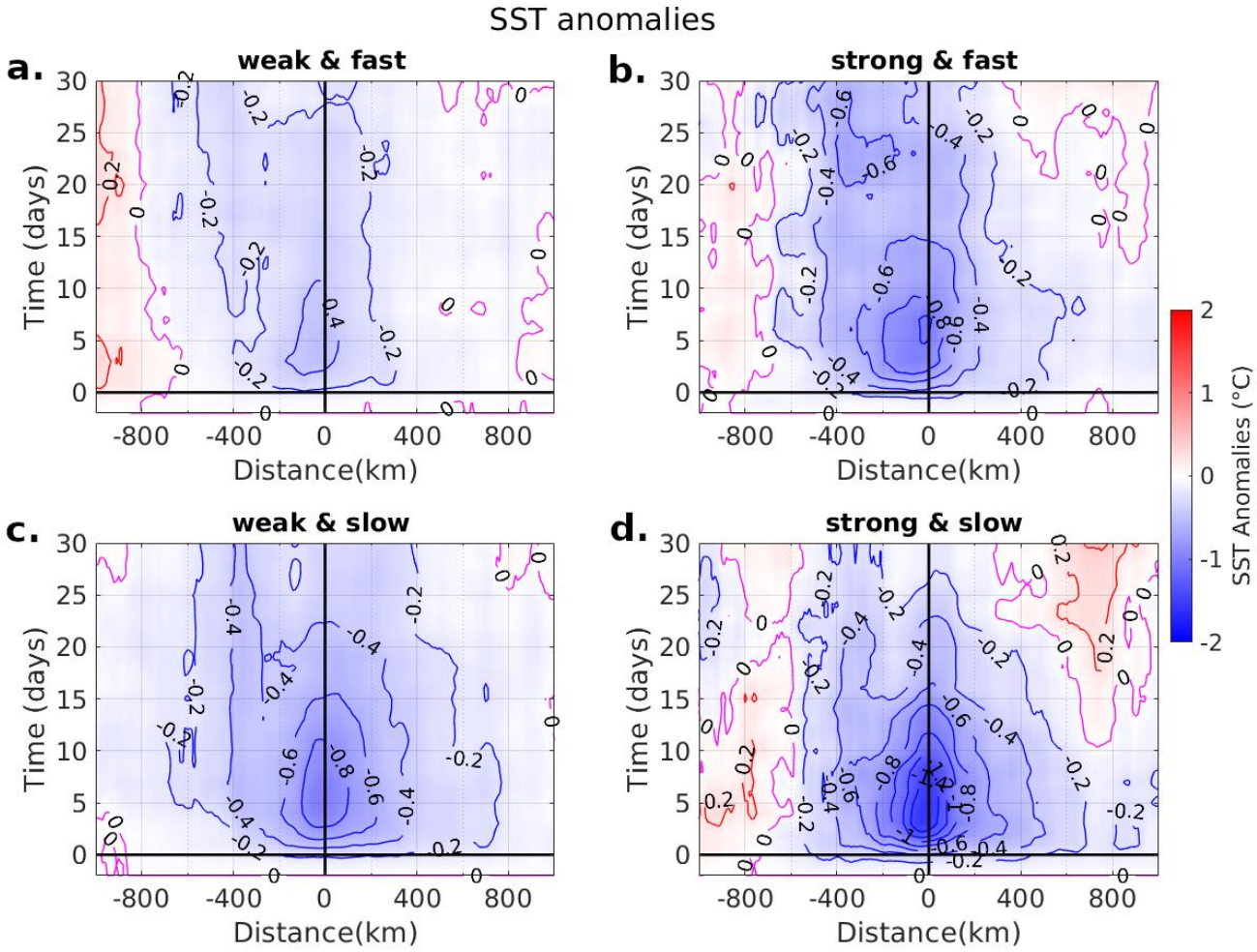

Figure 5.28: Hovmoller diagram of the cross-track SST anomaly (contours every 0.2 °C) in time for the 4 combinations of TC translation speeds and categories.

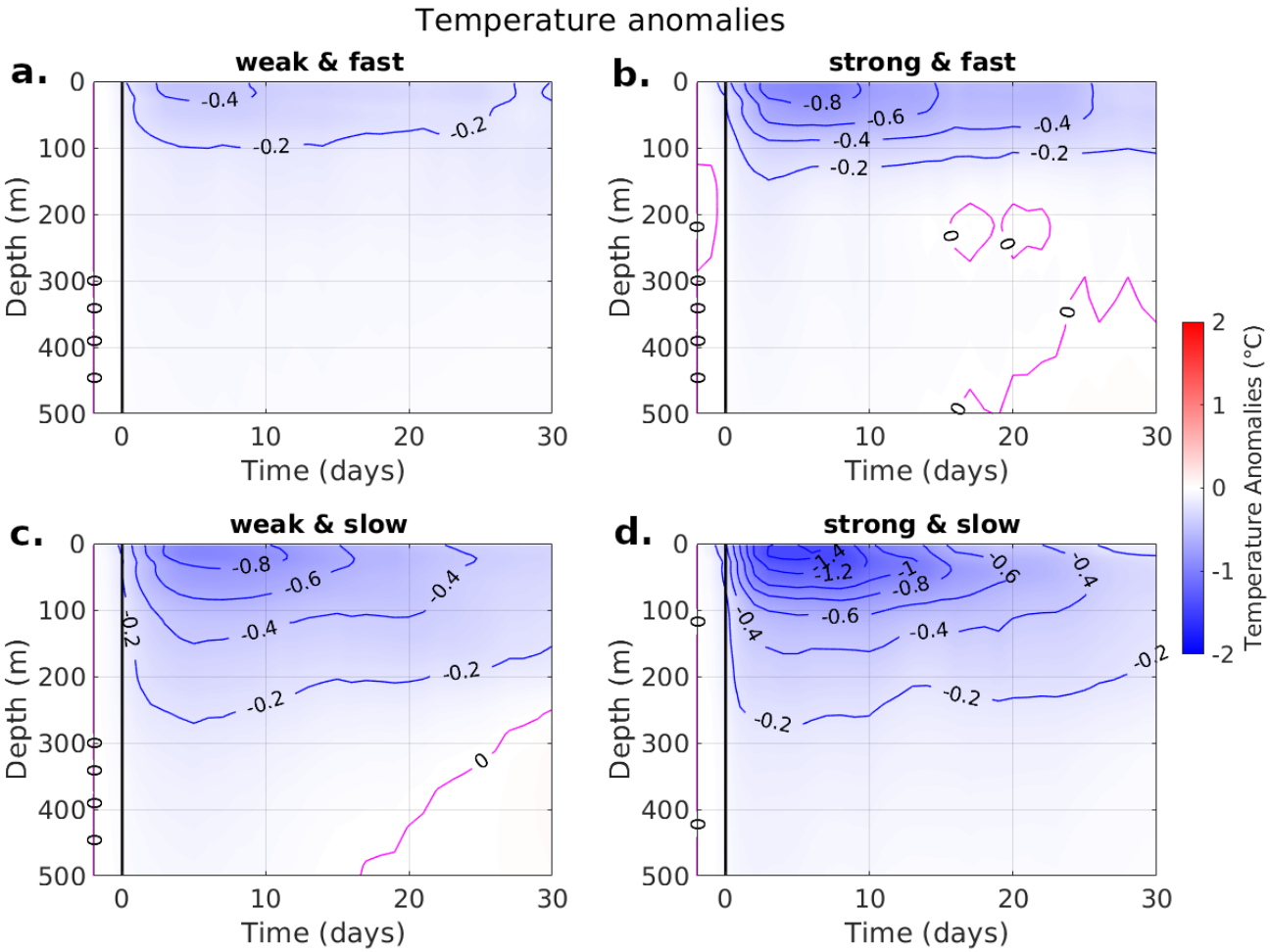

Figure 5.29: Depth-time cross-section of the temperature anomalies (contours every 0.2 °C) averaged within 100 km of the TC centre for the 4 combinations of translation speeds and intensity categories.

Heat flux losses during the TC passage contribute to the development of the cold anomalies at surface. On Day 0, the net heat flux becomes negative and the ocean transfers heat to the atmosphere (Fig. 5.30). The heat loss in the ocean is greater for stronger TCs and contributes more significantly to the development of the SST cold anomalies. The net heat flux losses are not symmetrical around the track, as there is a stronger heat loss on the left side of track. The asymmetry is particularly evident for strong and fast TCs and is well correlated with stronger cold anomalies over the left of the track (Fig. 5.28b). The net heat flux on Day 0 is divided into its components in Figs. 5.31, 5.32, 5.33 and 5.34. The shortwave solar radiation, which warms the surface of the water is strongly reduced especially for strong TCs, as thicker clouds cover the region (Fig. 5.31). The longwave heat loss from the ocean to the atmosphere is reduced below the TC as the SST starts to decrease in the region, especially for strong and slow TCs (Fig. 5.32). The latent component of the heat flux provides the higher contribution to the ocean heat loss and is the major term responsible for the asymmetry in the net flux on Day 0 (Fig. 5.33). In fact, the latent heat loss is much stronger for more intense storms and shifted more to the left of the track for fast-moving TCs, where the faster translation speed adds to the wind speed (as they are in the same direction) and enhances the heat loss. The sensible heat flux loss to the atmosphere is also stronger and shifter more to the left of track for more intense TCs (Fig. 5.34).

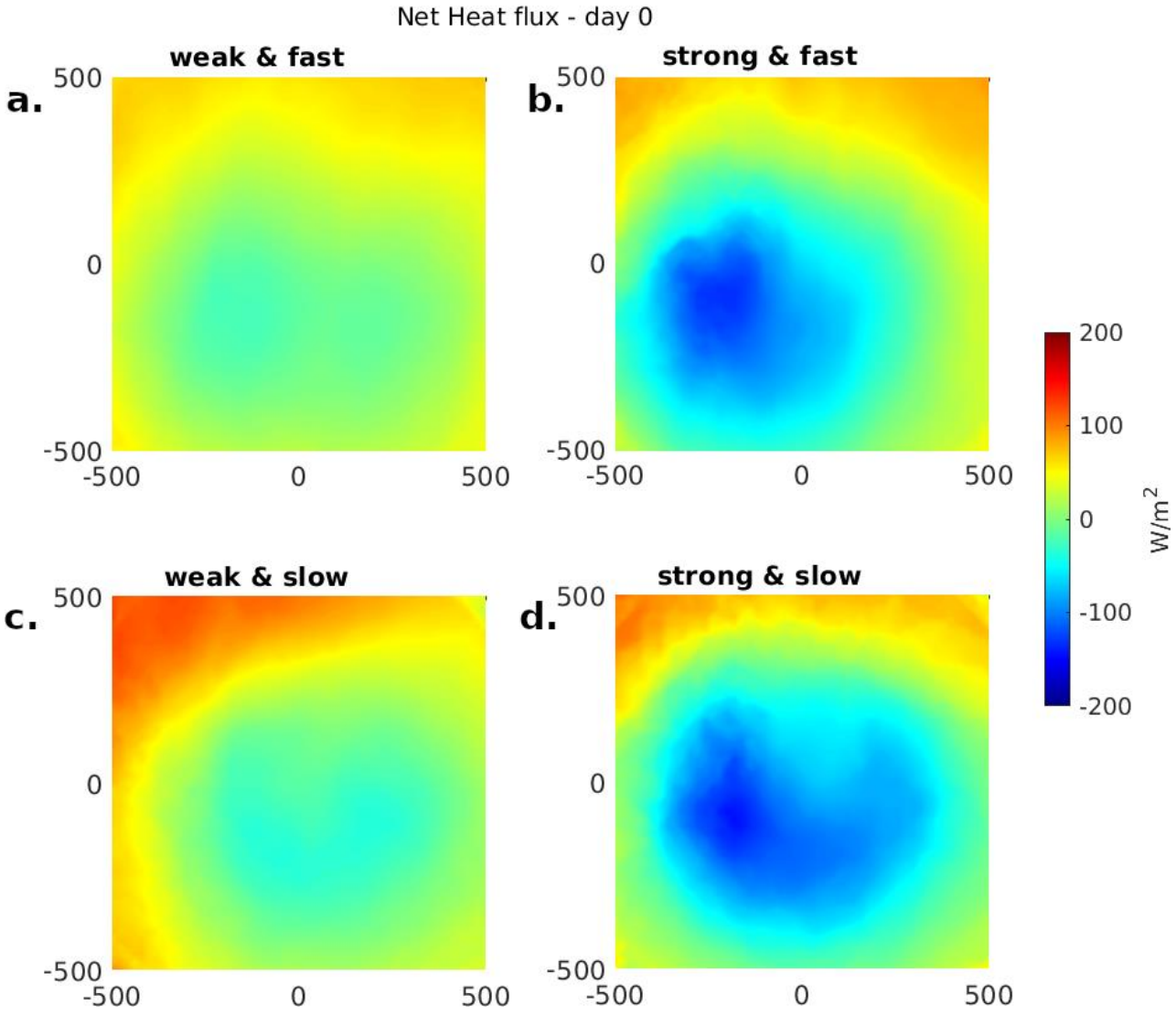

Figure 5.30: Net heat flux on Day 0 over the region for 4 combinations of different translation speeds and categories.

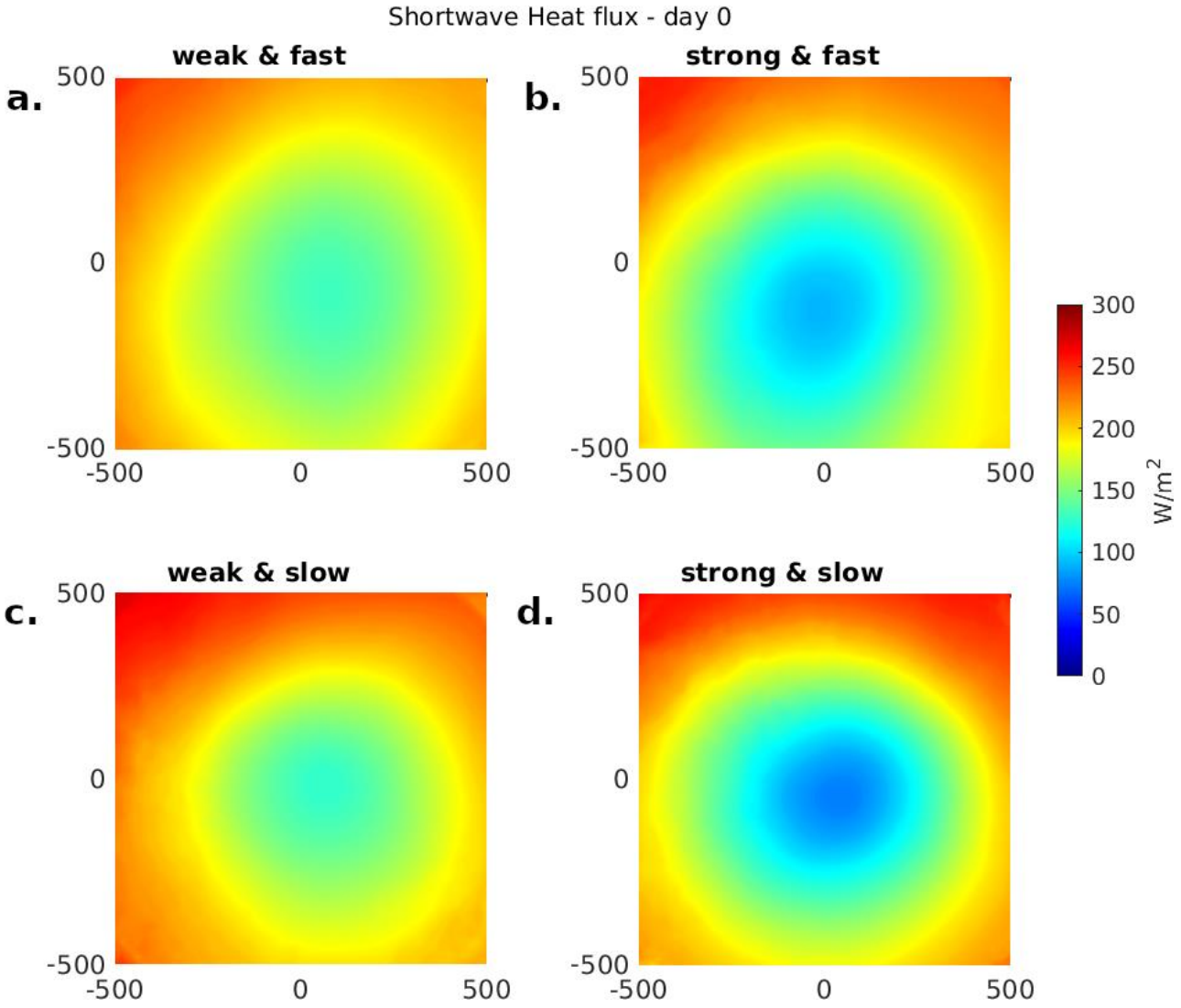

Figure 5.31: Shortwave radiation heat flux on Day 0 over the region for 4 combinations of different translation speeds and categories.

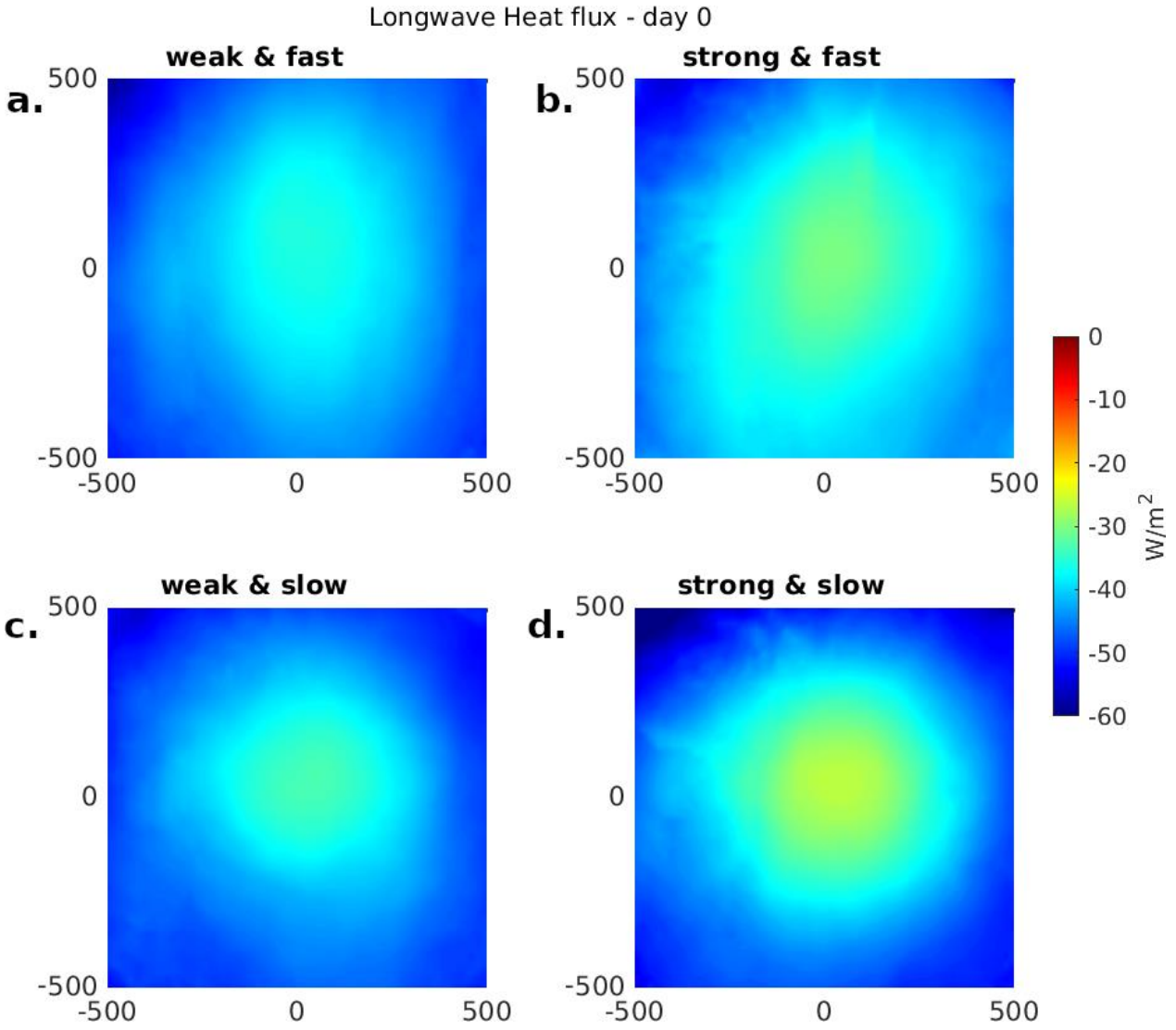

Figure 5.32: longwave radiation heat flux on Day 0 over the region for 4 combinations of different translation speeds and categories.

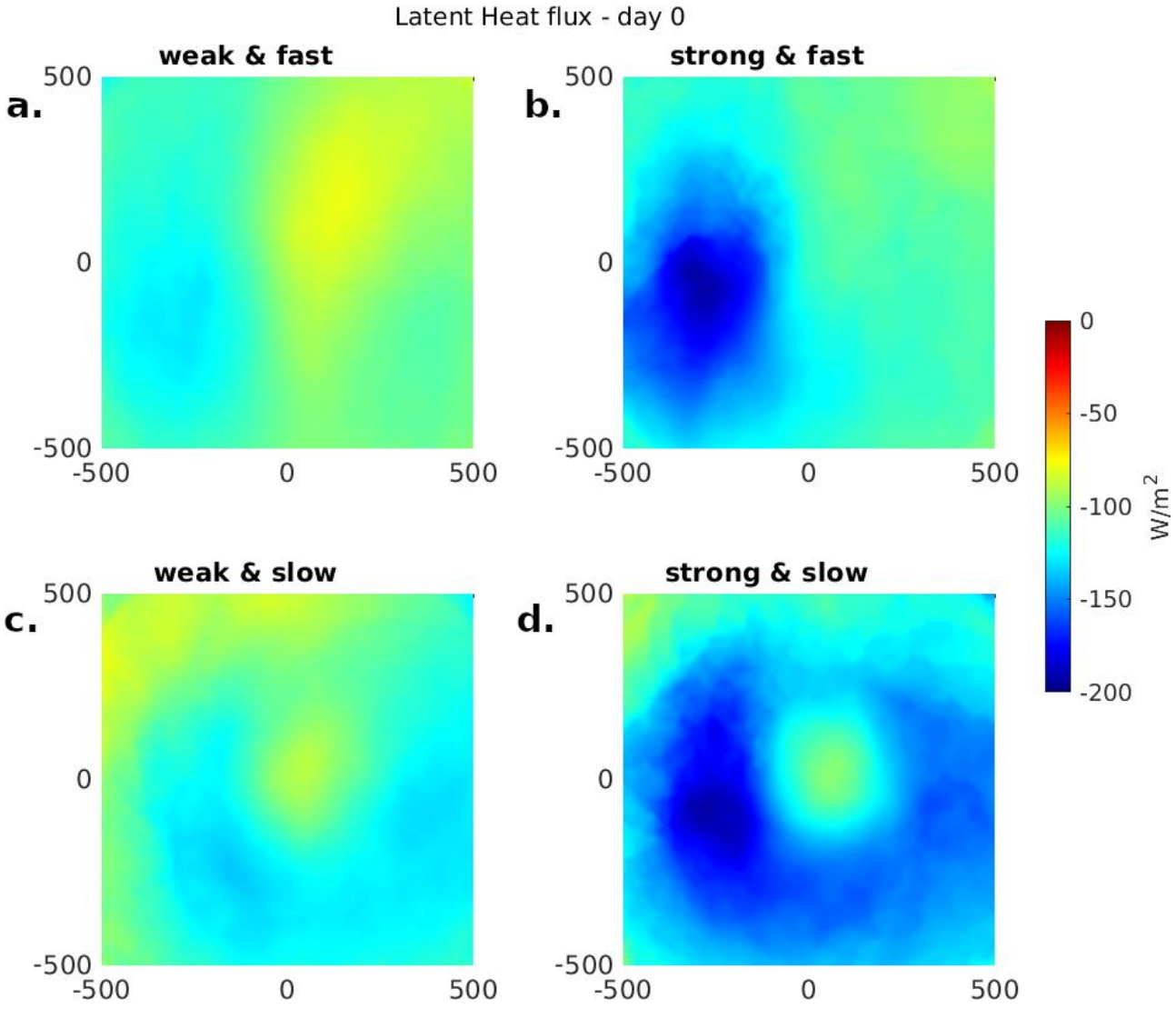

Figure 5.33: Latent heat flux on Day 0 over the region for 4 combinations of different translation speeds and categories.

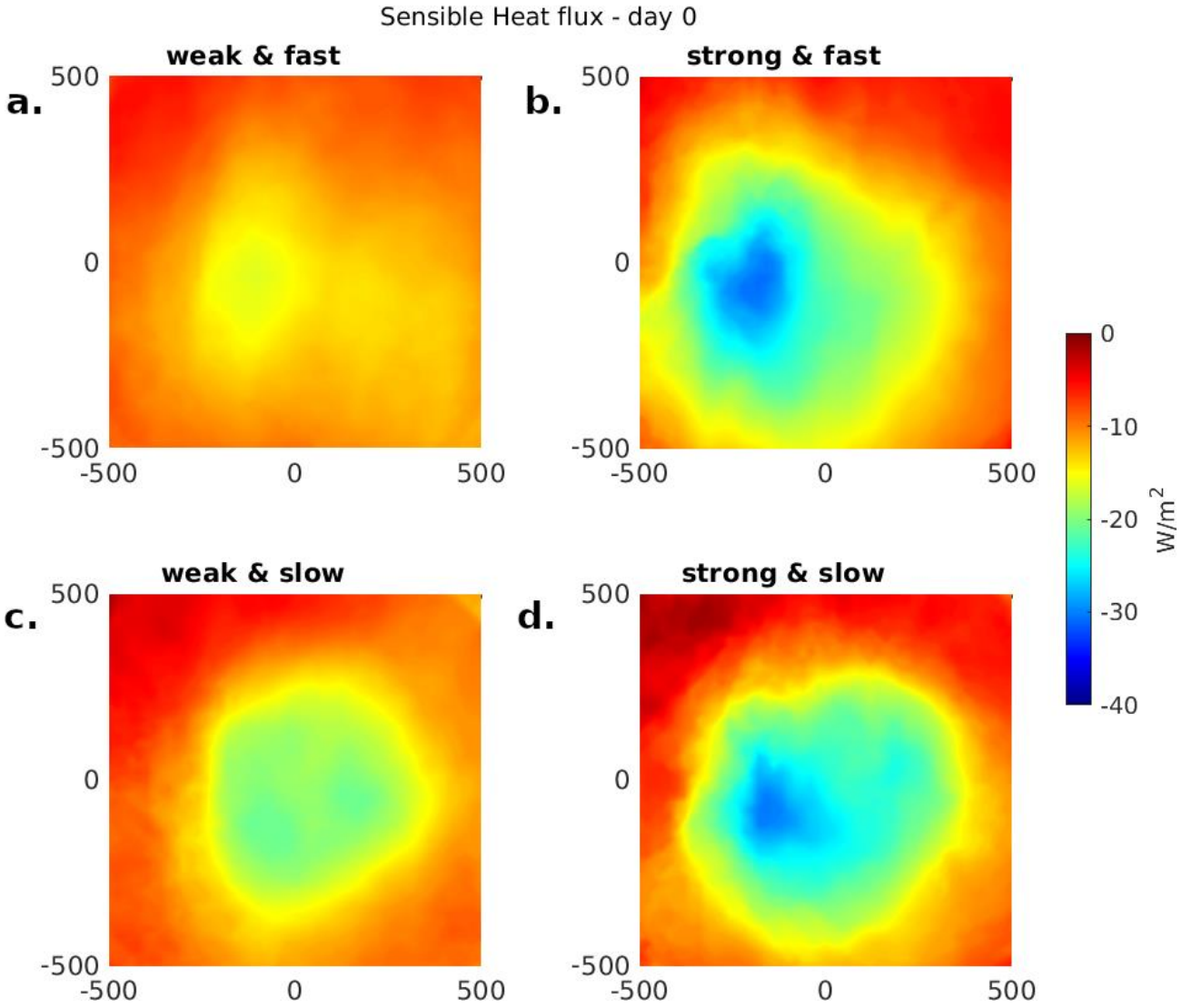

Figure 5.34: Sensible heat flux on Day 0 over the region for the four combinations of translation speeds and categories.

Figs. 5.35, 5.36 and 5.37 show the development of the temperature anomalies in time at 100 m, 200 m and 300 m depth. Below the track, the cold anomalies are shifted slightly to the right of track, especially for slow-moving storms, and stronger cold anomalies develop at depth for slow-moving TCs (Figs 5.35c and d, 5.36c and d, Fig. 5.37c and d). This right-of-track asymmetry in the cold temperature anomalies is driven by strong upward motion shifted right-of-track that lasts longer for slower moving TCs (Fig. 5.38c and d). The stronger upward motion (Fig. 5.38c and d) upwells more cold water from below and produces generally stronger cold anomalies during and after the TC passage for slower moving TCs (e.g., Fig. 5.35c and d). After reaching its maximum development, the cold anomalies start to decrease faster for slow-moving TCs, as the downwelling motion that follows the initial strong upwelling is stronger for slow-moving TCs (Fig. 5.38c and d). This strong persistent downwelling from Day 4 warms and restores the temperature at depth below the track. At the sides of the track beyond approximately 200 km, warm temperature anomalies develop at, or shortly after, the TC passage and are especially strong between 100 and 200 m depth for strong TCs (Figs. 5.35b and d and 5.36b and d). In particular, for slow-moving strong TCs and to a lesser extent for fast-moving strong TCs, the warm anomalies appear over a large area on the left of track and in two narrower bands over the left of track, between 200 and 400 km and at more than 600 km (Fig. 5.35b and d).

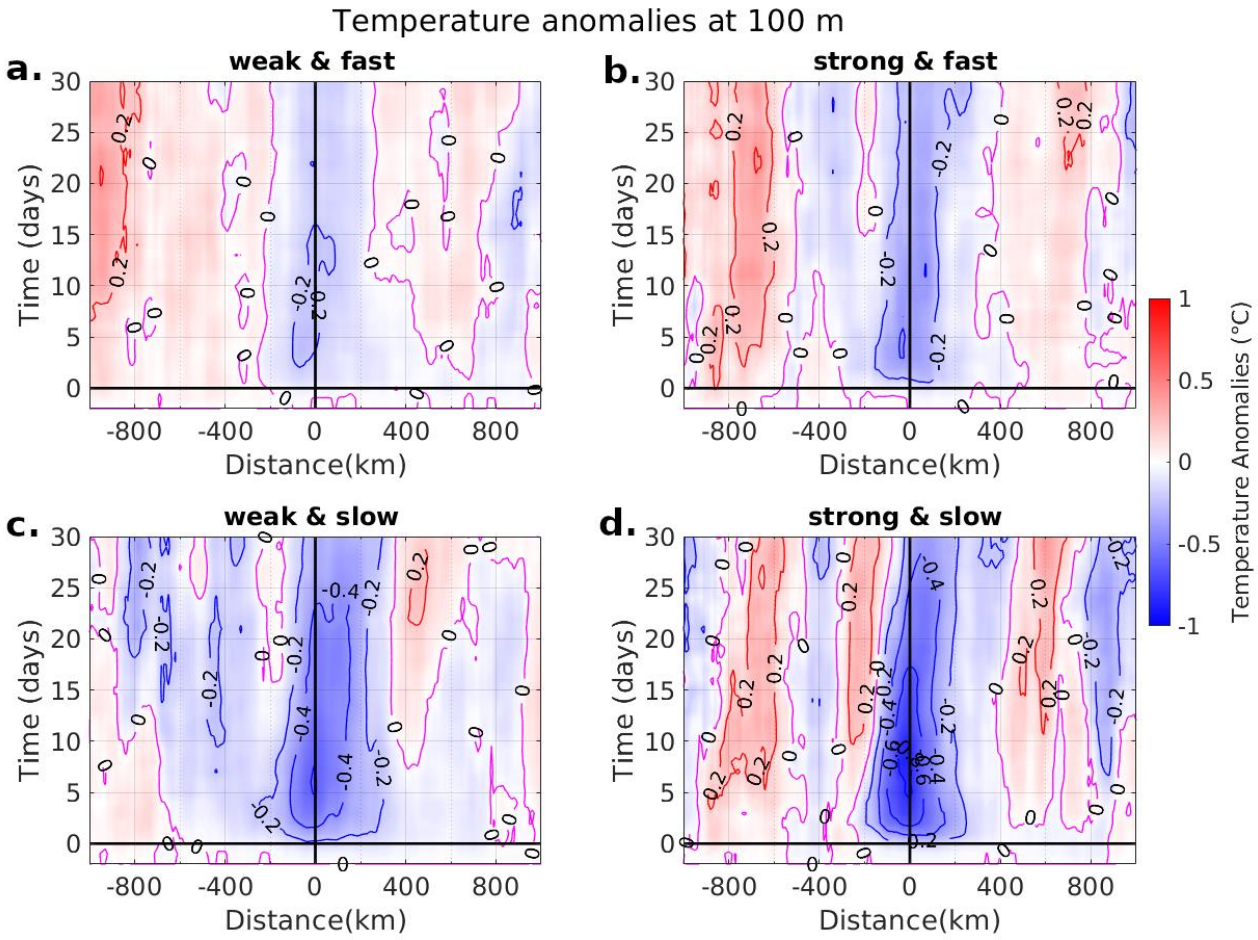

Figure 5.35: Cross track Hovmoller diagram of temperature anomaly (contours every 0.2 °C) in time at 100 m depth for 4 combinations of different translation speeds and categories.

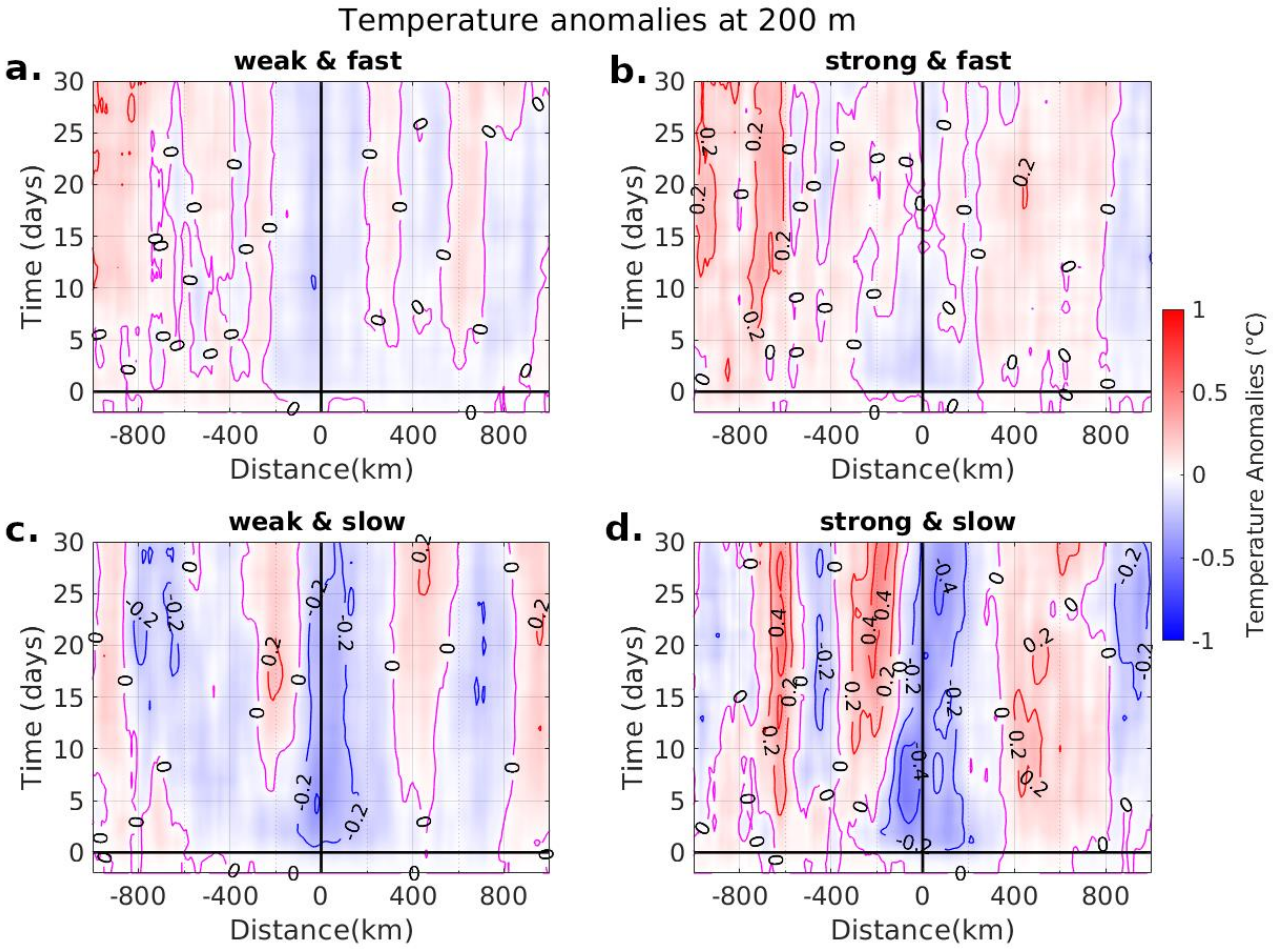

Figure 5.36: Cross track Hovmoller diagram of temperature anomaly (contours every 0.2 °C) in time at 200 m depth for 4 combinations of different translation speeds and categories.

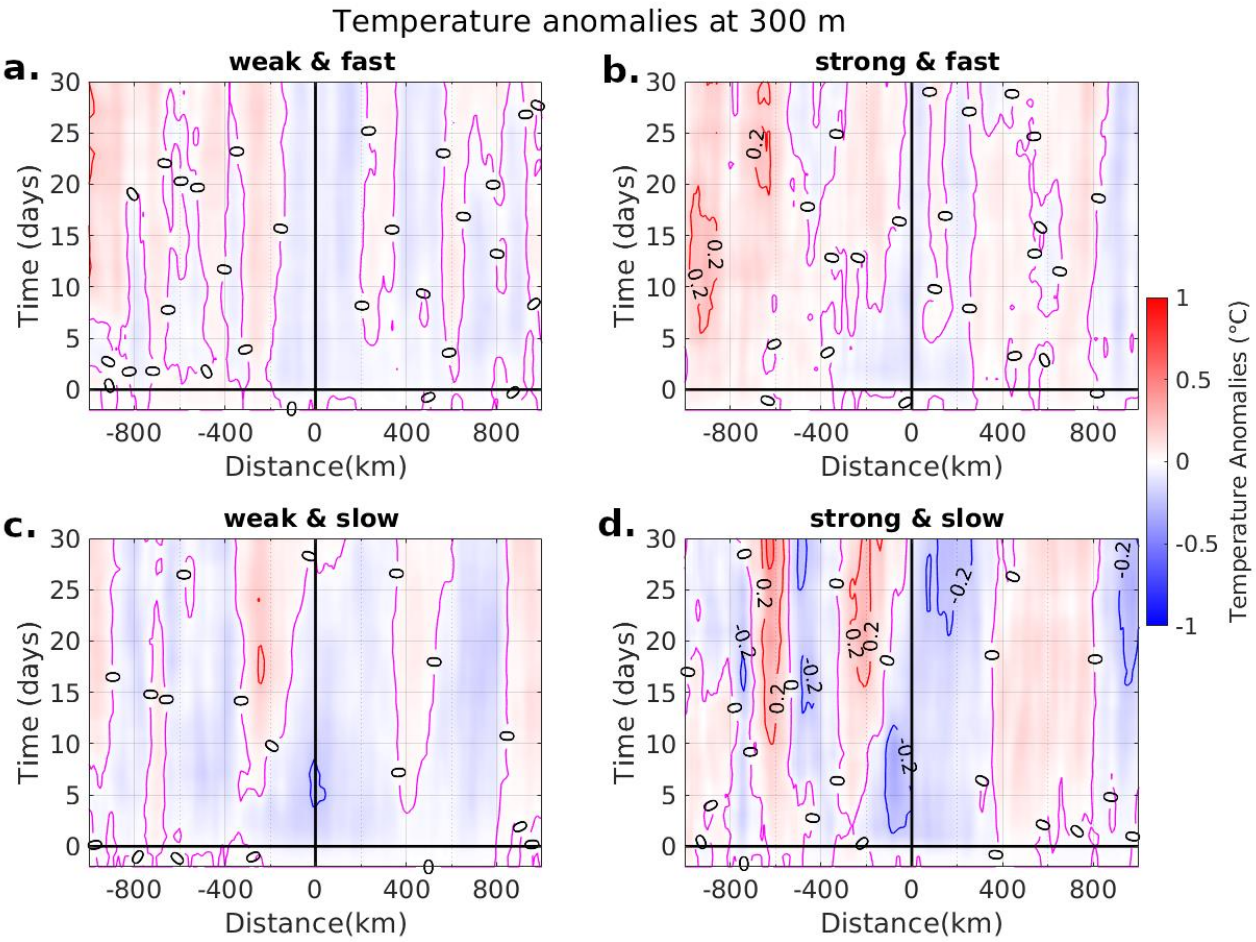

Figure 5.37: Cross track Hovmoller diagram of temperature anomaly (contours every 0.2 °C) in time at 300 m depth for 4 combinations of different translation speeds and categories.

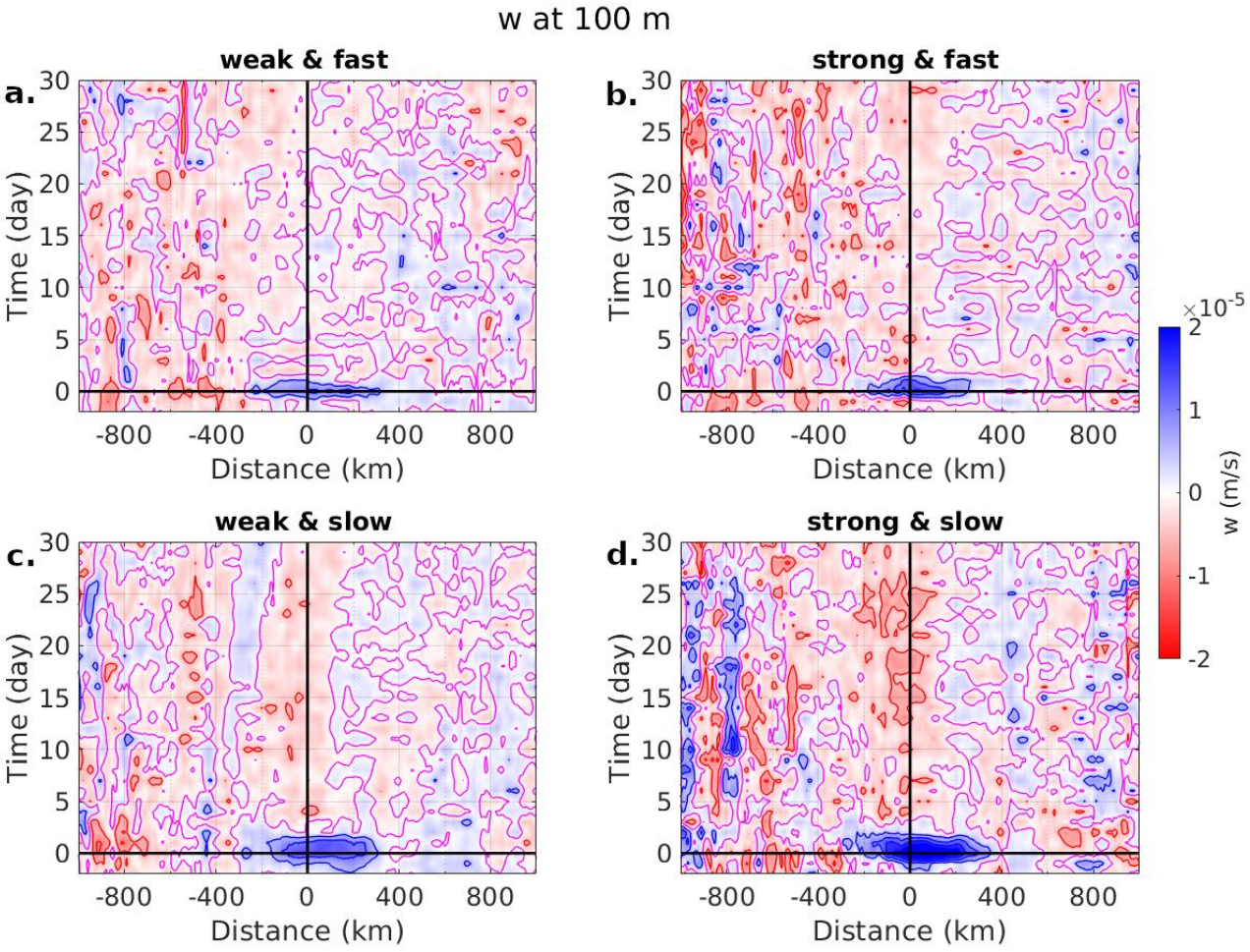

Figure 5.38: Cross track Hovmoller diagram of vertical velocity (contours every 0.5 x10^5 m/s) in time at 100 m depth for 4 combinations of different translation speeds and categories.

The cross-track section of the temperature anomalies at Day 5, when the cold anomalies are maximum, highlights the more intense cold anomalies at depth and extending both sides of the TC track at the surface, which happens for strong and for slow-moving TCs (Fig. 5.39d). There is more cooling at depth for slow-moving TCs regardless of intensity, which is probably due to the stronger vertical currents and more intense upwelling driven by the longer residence time (Figs. 5.39d and 5.40d). The warming in the subsurface appears on both sides of the track and it is more intense for intense TCs regardless of speed of translation, on the left of track (Fig. 5.39b and d). The regions where the highest subsurface warming develops correspond well to the regions where during the days prior to Day 5 there is a strong vertical shear between the surface currents and the currents in the layer below, especially on the left of track (e.g. Fig. 5.30, that shows strong horizontal currents in the first 20 m that decay rapidly with depth), and where vertical mixing and ML entrainment is expected to occur (Price et al., 1981; Shay 2019).

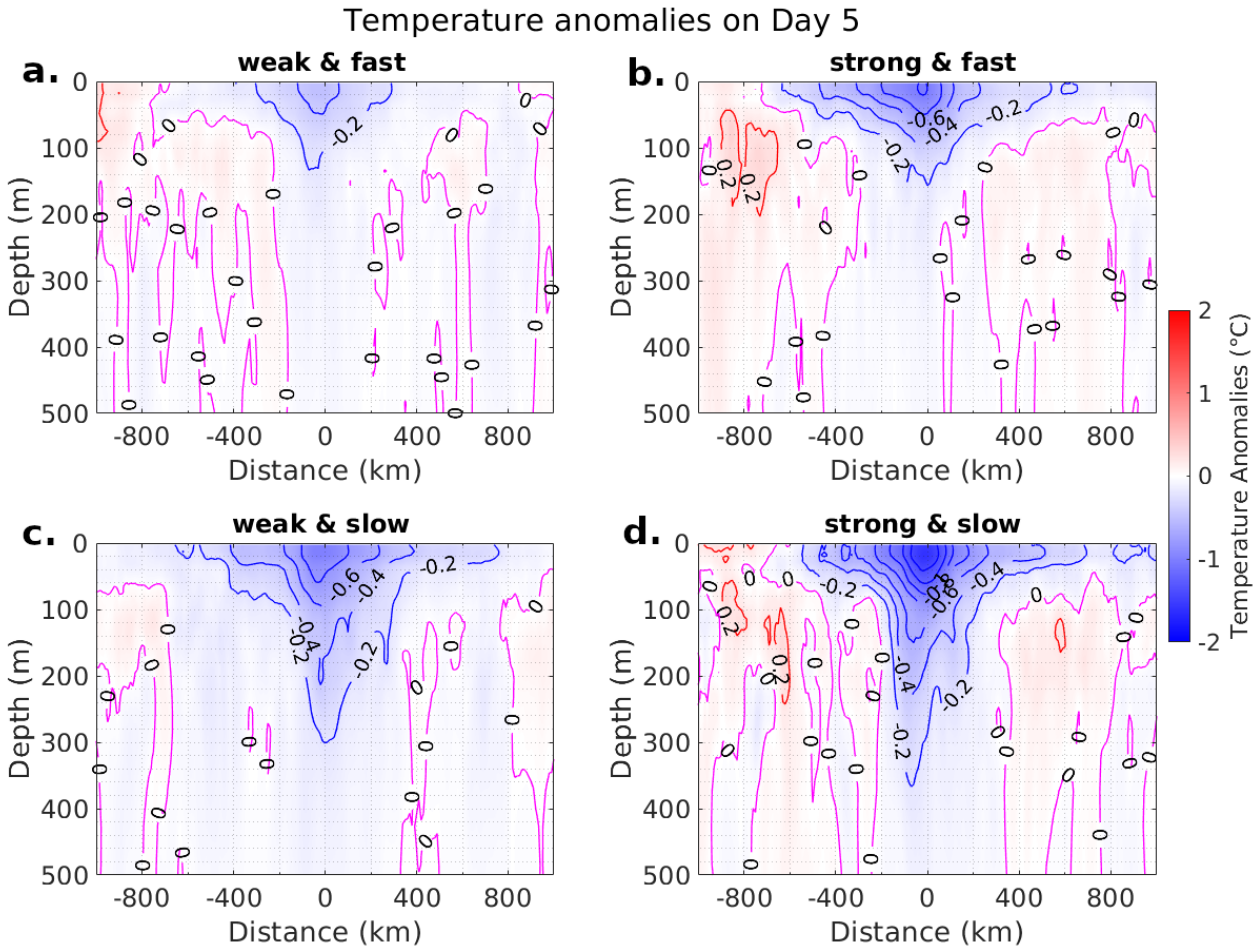

Figure 5.39: Cross section of the temperature anomalies (contours every 0.2 °C) at Day 5 after the TC passage for the four combinations of different translation speeds and intensities.

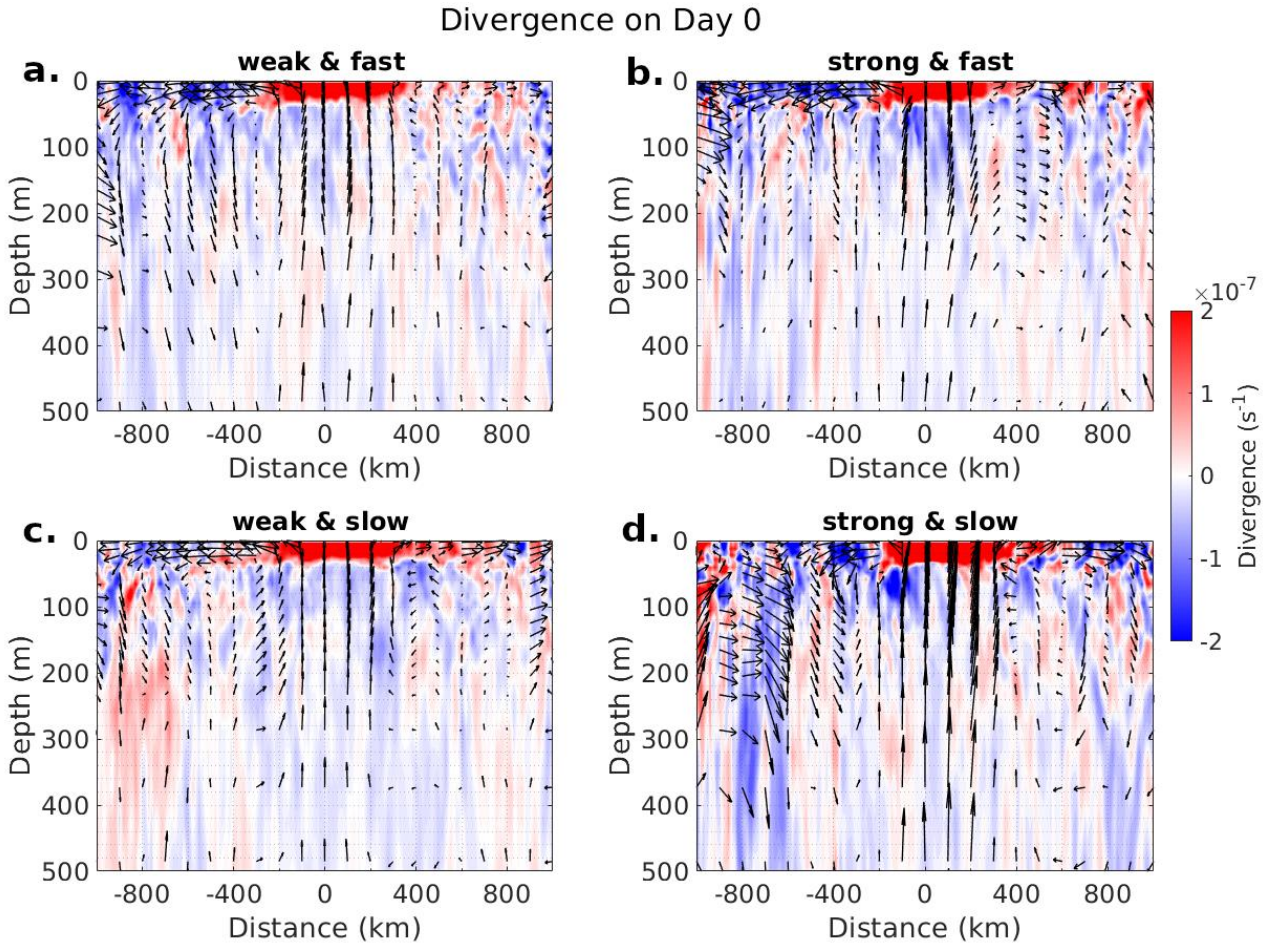

Figure 5.40: Cross section of the divergence pattern and current vectors during the day of the TC passage for 4 combinations of different translation speeds and categories.

The inner core vertical currents (shaded) and the alternating pattern of divergence and convergence (red and blue contours) are shown in Fig. 5.41 over the temperature anomalies (black contours) for fast/slow and weak/strong TCs. The upwelling underneath the TC lasts longer for slow-moving TCs compared to fast-moving TCs, as they have a longer residence time over the location (Fig. 5.41c, d compared to a, b). Furthermore, the upwelling is stronger for strong TC regardless of translation speed (Fig. 5.41b, d compared with a, c). Following the period of upwelling, the downward currents are stronger for slow TCs and for more intense TCs. The periods of divergence and convergence of the horizontal currents alternating at the surface correspond well with the vertical currents underneath. In particular weak and fast TCs are followed by longer periods of divergent surface currents and weak vertical currents in the column below, while strong and slow TCs are followed by strong horizontal currents that alternate periods of strong then weaker convergence at the surface, corresponding to strong then weaker downwelling below the track (Fig. 5.41).

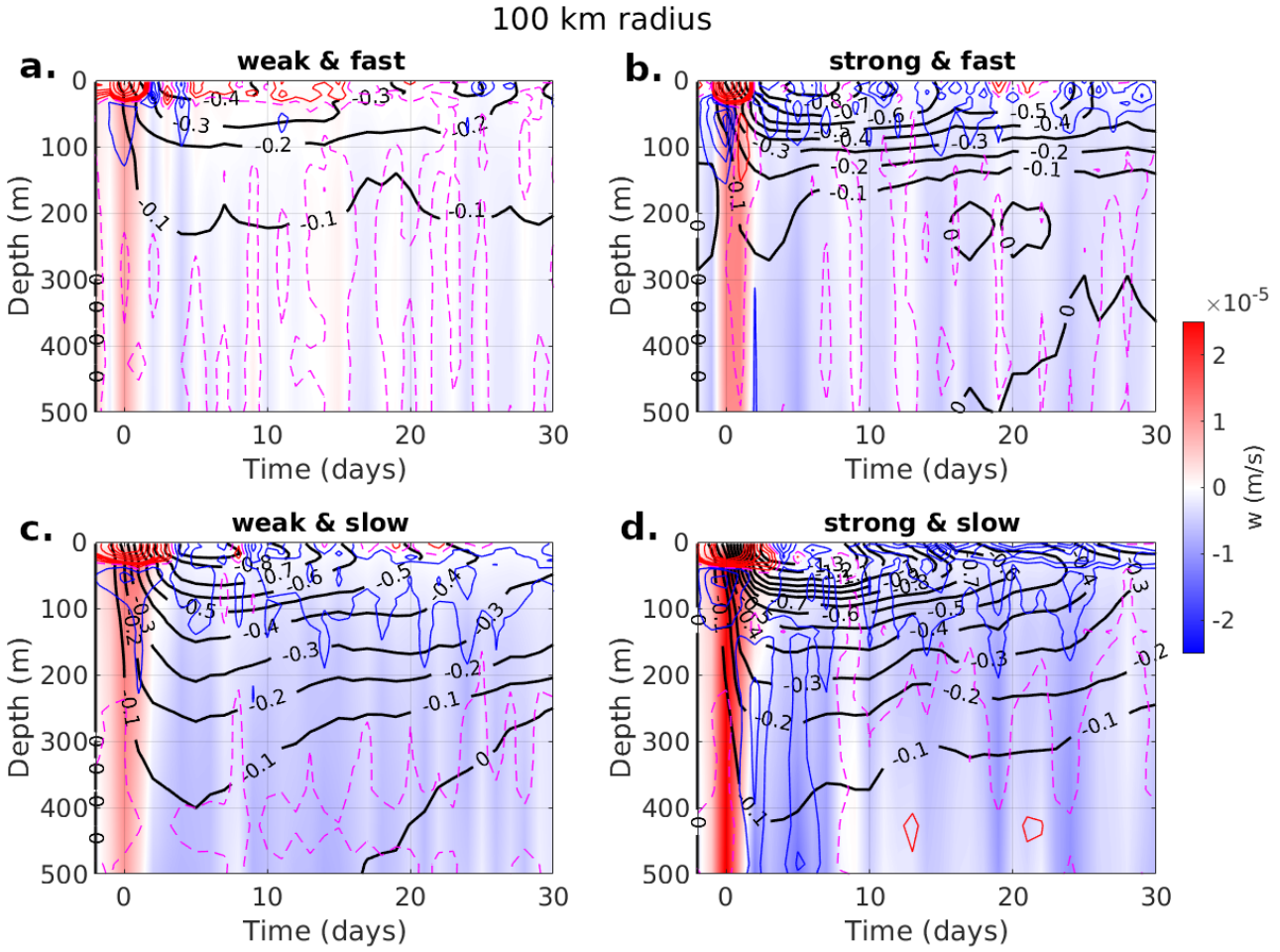

Figure 5.41: Depth-time cross-section of the temperature (units: °C, black contours every 0.1 °C), vertical velocity (shaded, x 10^{-5} m/s), and divergence of the horizontal currents (units: x 10^{-8} s^{-1}, red (+ve) and blue (-ve) contours every 2 x10^{-8} s^{-1}) averaged over a 100 km radius circle centred on the TC centre for 4 combinations of different translation speeds and categories.

Fig. 5.42 shows the changes in the e-folding time for the temperature recovery for strong and weak data points and for slow and fast data points. The colder wake at the surface induced by a strong TC recovers more quickly than the weaker cooling of a weak TC, but at depth the cold anomalies last for longer (Fig. 5.42a). In general, fast-moving TCs take longer to recover through the water column than slow-moving TCs (Fig. 5.42b).

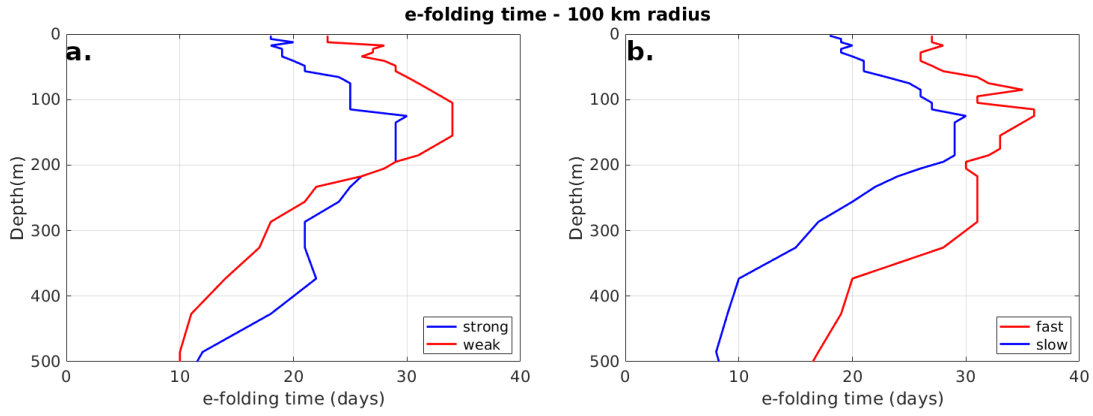

Figure 5.42: e-folding time (days) for the temperature recovery at different depths for: (a) weak and strong data points; and (b) fast and slow-moving data points.

5.7 Barrier layer effects

The effects of the presence of a deep barrier layer prior the passage of a TC inhibits vertical mixing and entrainment between the surface layer and the colder water underneath. To study the effect of a barrier layer of different thickness on the temperature anomalies we decided to focus on the annulus region between 100 and 300 from the TC centre (Fig. 5.43), as the mixing is overwhelmed by the strong upwelling signal directly under the TC centre (Fig. 5.10).

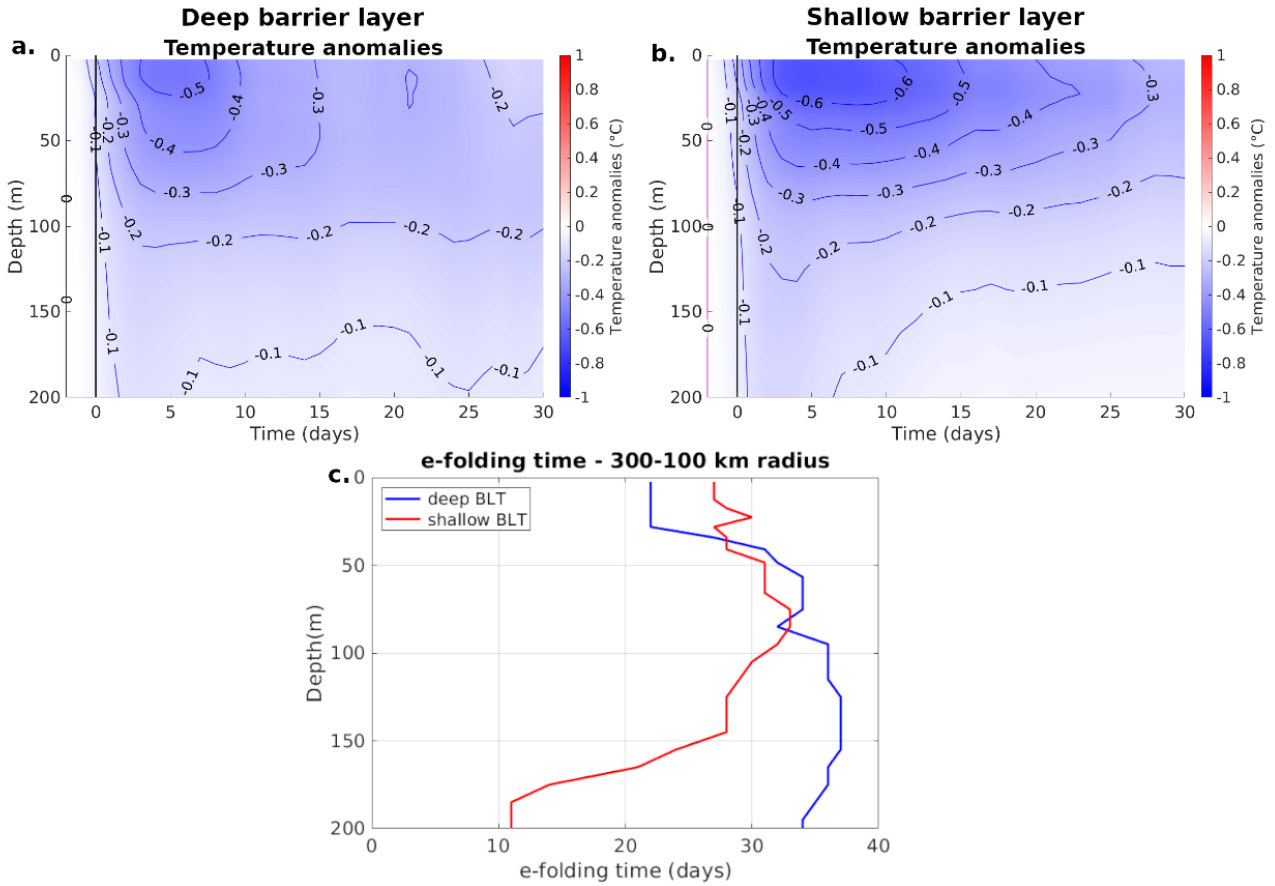

Figure 5.43: Depth-time cross-section of the temperature anomalies (contours every 0.1 °C) averaged in the annulus between 100 and 300 km from the TC centre for: (a) deep barrier layer (365 data points); (b) shallow barrier layer (562 data points); and (c) e-folding time (days) for deep barrier layer and shallow barrier layer data points with depth.

The maximum SST anomaly produced by the passage of a TC is greater for the shallow barrier layer data points compared to when a deep barrier layer is present (Fig. 5.43) with the main differences occurring in the top 50 m, where the entrainment of colder water from below the thermocline is the most efficient cooling process (Fig. 5.43). This suggests that the mixing across the thermocline induced by the currents below the TC is less effective for a thicker barrier layer compared with a thinner barrier layer. The cold anomalies in the top 150 m of the water column recovery more slowly for the shallow barrier layer data points (Fig. 5.43a and b) with e-folding times of approximately 30 days. In comparison, the deep barrier layer data points exhibit two e-folding times: just over 20 days for the layer above 50 m; and approximately 35 days for the layer below 50 m, where the anomalies recover very slowly (Fig. 5.43c). This suggests that the presence of a deep barrier layer affects the recovery through the water column by more effectively trapping the solar radiation warming in the top 50 m of the water column compared with a shallow barrier layer.

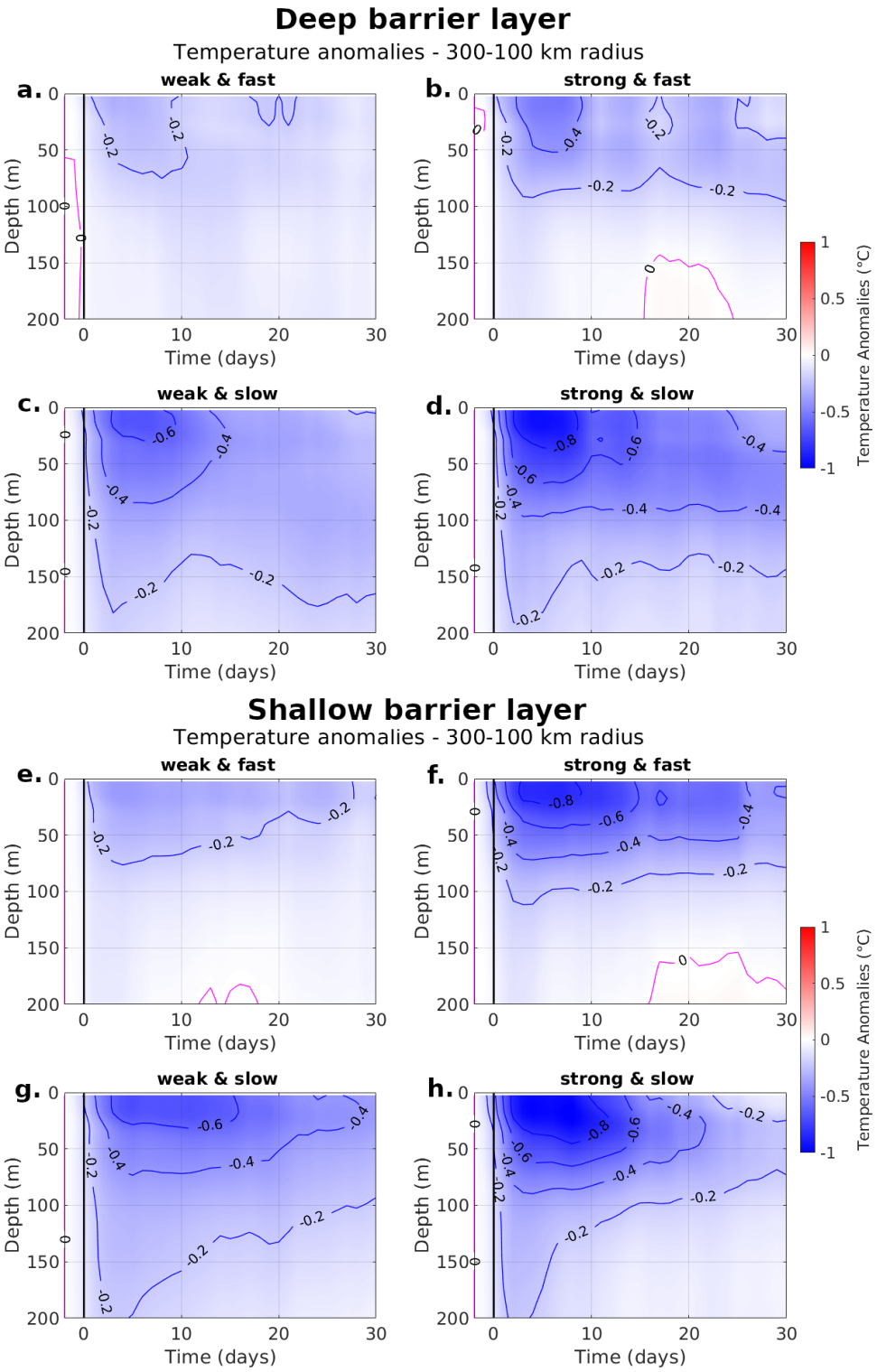

Figure 5.44: Depth-time cross-section of the temperature anomalies (contours every 0.2 °C) averaged in the annulus between 100 and 300 km from the TC centre for: (a)-(d) deep barrier layer and (e)-(h) shallow barrier layer, for the 4 combinations of different translation speeds and categories.

Fig. 5.44 shows the effects of the presence of a deep barrier layer and stable stratification for the cooling induced by weak or strong storm and slow-moving or fast-moving TCs. A major difference in the ML cooling occurs for fast-moving TCs (Fig. 5.44b and f). While slow-moving storms spend more time in a location and can eventually overcome even a thick barrier layer and entrain colder water in the surface layer, for fast-moving TCs the entrainment occurs over a shorter period and can be efficient only if there is no barrier layer that inhibits the entrainment processes. Furthermore, slow-moving TCs, which spend more time in a location produce a stronger upwelling effect in the water underneath, pushing the isotherms upward and further intensifying the entrainment and the cooling through the whole water column, which helps to overcome a deep barrier layer (Fig. 5.44).

5.8 Summary and discussion

The passage of a TC over the NWS region drives strong thermal changes in the ocean in a wide region underneath and around the TC track. A 20-year composite shows that cold temperature anomalies develop over a wide region at the ocean surface and at depth underneath the TC centre, while warm anomalies develop in the subsurface on the sides of the track, stronger at 700 to 900 km on the left of track between 100 and 200 m depth. Strong divergent surface currents develop, driven by the TC winds. These currents drive strong Ekman upwelling in the region underneath the track, which are responsible for the cooling through the water column, and the currents' strong shear on the sides of the track drives MLD entrainment and the temperature anomalies, cold at surface and warm in the subsurface, over the two sides. During the month following the passage of the TC the surface cold anomalies recover, although not completely, due to the increase in the air-sea net heat flux into the ocean. After 2 days, the divergent surface currents reverse and become convergent and drive weak downwelling in the region underneath the track, that helps the recovery of the cold anomalies at depth. The temperature anomalies in the subsurface underneath the track and the warm anomalies at the sides take longer to recover.

Data points over the shelf or over the deep ocean and of TCs with different characteristics have been composited together to assess how the ocean and TC properties affect the thermal changes. Table 5.4 presents a summary of the characteristics of the cooling within 100 km from the track for the different cases studied and provides an insight of the meaningfulness of the differences.

Table 5.4: Summary of inner core SST cooling, cooling at 300 m (subsurface), and vertical currents at 100 m depth for the various cases. Values highlighted in italics represent cases with a statistically significant difference from the case indicated in the second column (t-test with $p < 0.05$).

	Compared against	**Inner core SST anomaly - Day 5 (°C)**	**Inner core Temperature anomaly at 300 m - Day 5 (°C)**	**Inner core w at 100 m ($x10^{-5}$ m/s)**
General case	-	-0.87	-0.12	1.2
Deep Ocean	General case	-0.84	-0.12	*1.3*
Shelf	Deep ocean	*-0.92*	-	*0.8*
Shelf - parallel to the coast	Shelf	*-0.77*	-	0.7
Shelf – perpendicular to the coast	Shelf	*-1.09*	-	1.3
Deep ocean – parallel to the coast	Deep ocean	*-0.99*	-0.11	*1.7*
Warming season	Cooling season	*-0.91*	*-0.17*	*1.5*
Cooling Season	Warming Season	*-0.78*	*-0.08*	*1.1*
Weak and fast	Deep ocean	*-0.46*	*-0.07*	*0.9*
Strong and fast	Deep ocean	-0.92	*-0.06*	1.2
Weak and slow	Deep ocean	*-0.93*	*-0.18*	1.3
Strong and slow	Deep ocean	*-1.40*	*-0.18*	*2.5*
Shallow barrier layer	Deep barrier layer	*-0.93*	*-0.14*	*1.4*
Deep barrier layer	Shallow barrier layer	*-0.71*	*-0.11*	*1.2*

The difference in cooling produced by TCs over the deep ocean is not significant compared to the general case (Table 5.4). Over the shelf, the direction of motion of the TCs and the interaction of the TCs induced currents and the shelf influence the temperature anomalies development. TCs over the continental shelf produce strong cold anomalies at the surface over a larger area and over the inner core (Table 5.4), while vertical currents beneath the TC inner core show a large variability with depth, being less intense at 100 m depth (Table 5.4), but stronger below (Fig. 5.17a). Moreover, the direction of TC motion over the shelf affects the development of the currents and the associated thermal changes. TC data points that move perpendicular to the shelf edge drive stronger upward vertical currents that last for a month following the TC passage and stronger SST anomalies (Table 5.4). However, TCs parallel to the coast drive colder temperature anomalies at depth (Fig. 5.20). TCs over the deep ocean moving parallel to the shelf are also affected by the interaction between the wind induced currents and the shelf edge, and although the difference depends on the distance from the shelf, they are generally characterized by stronger upwelling and colder anomalies at the surface (Table 5.4). The time of the season affects the development of the vertical currents, as a general downwelling regime over the region is in contrast to the TC induced upwelling during the cooling season. Stronger upward currents develop during the warming season and produce colder temperature anomalies, both at the surface and subsurface (Table 5.4). The intensity and translation speed of the TC has a strong effect on the development of the temperature anomalies. Slow-moving and strong TCs drive colder temperature anomalies over a wider region, and slow-moving TCs drive more upwelling and colder anomalies deeper through the water column beneath the TC centre (Table.5.4). The

stratification of the water column and the presence of a deep barrier layer prior to the passage of the TC can inhibit the development of cold anomalies at the surface (Table 5.4), especially for fast-moving and strong TCs.

The recovery of the inner core temperature anomalies is also affected by the characteristics of the ocean and of the TC (Table 5.5). In general, the e-folding recovery time at the surface of TCs on the shelf is slightly higher than for TCs on the deep ocean. However, the more intense SST anomalies of the TCs on the shelf that move parallel or perpendicular to it have a lower e-folding time compared to the general shelf case (Table. 5.5). The cold anomalies of TCs over the deep ocean and parallel to the shelf have an e-folding time similar to the general deep ocean cases at the surface but recover faster at 200 m depth, possibly due to stronger restorative downwelling (Table 5.5). Moreover, the time of the season when the TC passes over the region strongly affects the recovery of the temperature anomalies. The surface cold anomalies take longer to recover for TC data points that occur later in the season, when the temperatures are generally cooling and the solar radiation is decreased. At depth, the presence of downwelling regime events later during the TC season speeds up the recovery of the cold anomalies, while the cold anomalies at depth for TCs that occur earlier in the season recover more slowly (Table 5.5). At the surface, the colder anomalies that develop after stronger TCs recover at a faster rate. At 200 m depth, strong and fast TCs recover most rapidly, possibly as the anomalies are not very intense but the restorative downwelling is quite strong. The stratification of the ocean prior to the TC passage seems to affect the inner core recovery time of the cold anomalies, with faster recovery at the surface over strong stratification, but slower in the subsurface as the left-over barrier layer inhibits warming underneath (Table 5.5).

Table 5.5: Summary of the e-folding time for the cold anomalies recovery at surface and at 200 m for the different cases analyzed.

	Inner core e-folding time at surface (days)	**Inner core e-folding time at 200 m (days)**
General case	22	27
Deep Ocean	21	30
Shelf	23	-
Shelf - parallel to the coast	18	-
Shelf – perpendicular to the coast	19	-
Deep ocean – parallel to the coast	21	21
Warming season	17	33
Cooling Season	29	11
Weak and fast	23	29
Strong and fast	19	9
Weak and slow	21	27
Strong and slow	13	31
Shallow barrier layer	22	29
Deep barrier layer	19	31

The intensity and location of the warm anomalies at the sides of the track for the different cases analysed is presented in table 5.6. In general, most of the cases develop maximum warm anomalies at less than 800 km to the left of track (negative

distances in Table 5.6) and at around 100 m depth. Stronger warm anomalies develop for on-shelf cases (Table 5.6), although they have high spatial variability (Fig. 5.16), possibly due to the localized downwelling that develops from the interaction of the ocean TC-driven currents and the shelf edge. The presence of the shelf can also affect the TCs that are located farther from the shelf over deeper water by driving Ekman downwelling near the coast when TCs move south-westward and parallel to it, which contribute to the development of stronger warm anomalies on the left side of the TC track. The season does not appear to influence the maximum warm anomaly (Table 5.6), although at depth the warm anomalies cover a slightly larger area during the cooling season (Fig. 5.23), as they are driven by a general downwelling regime. Strong TCs drive higher warming, especially at the left of the track (Table 5.6, Figs. 5.35, 5.36 and 5.37), because they induce stronger horizontal currents and more vertical mixing at the sides of track. Weak and slow TCs develop only a very weak maximum warm anomaly compared with the other three categories (Table 5.6), likely because they drive only weak mixing and downwelling. Although the maximum warm anomaly appears to be higher for deep barrier layer cases, this may not be very significant as the barrier layer is calculated beneath the TC centre and may not be an applicable indicator for variations away from the inner core where the subsurface warm anomalies develop.

Table 5.6: Summary of the maximum warm anomaly and its location for the different cases analyzed.

	Max warm anomaly - Day 10 (°C)	Distance from the track (km)	Depth (m)
General case	0.17	-750	115
Deep Ocean	0.17	-770	115
Shelf	0.25	-740	85
Shelf - parallel to the coast	0.23	600	115
Shelf – perpendicular to the coast	0.46	-10	135
Deep ocean – parallel to the coast	2.46	-950	287
Warming season	0.22	-770	145
Cooling Season	0.22	-1000	95
Weak and fast	0.37	-1000	85
Strong and fast	0.36	-740	115
Weak and slow	0.19	930	175
Strong and slow	0.41	-680	145
Shallow barrier layer	0.21	-1000	95
Deep barrier layer	0.30	710	125

There are several limitations to the composite approach with BRAN data. BRAN has a daily temporal resolution that doesn't allow an extensive study of the

near-inertial currents that develop following the TC passage and of the internal waves driven by the interaction of the TC-induced currents with the shelf edge, that could be strong on the NWS (Davidson and Holloway, 2001). Furthermore, the composite averages the effect of the interaction with ocean eddies or masks the presence of upwelling or downwelling events not related to the passage of the TC in the region. By averaging the currents and temperature anomalies over the region within 100 km from the track the asymmetry of the upwelling region, which is stronger on the right of track, also is not considered.

Chapter 6. Tropical cyclones effect on the Ocean Heat Content on the NWS

6.1 Introduction

The passage of a TC induces strong thermal changes in the ocean around its track and modifies the OHC of the surrounding region. It has been postulated that the development of warm temperature anomalies in the subsurface, in combination with a faster recovery of the surface cold anomalies, could lead to a change in the OHC that could eventually be transported away from the region and influence the global climate (Emanuel 2001; Sriver and Huber 2007, Sriver et al. 2008) or even provide long-term sequestration of energy at depth (Nguyen 2021). However, the development and the intensity of the subsurface warm anomalies depends on the TC and ocean characteristics, and the increase of OHC in the subsurface is not always comparable to the surface cooling (Cheng et al., 2015). Here, we focus on quantifying the OHC changes during the passage of a TC and in the month following over the NWS region in order to understand the conditions that could lead to an increase in OHC and what processes are driving the OHC changes. We use a composite approach to evaluate the OHC changes within different areas around the TC track. A heat budget over a cross-track section is calculated to study the processes that drive the OHC changes during the passage of a TC and during the month following at different distances from the track. The effect of the season during which the TC occurred, and TC translation speed and intensity is investigated to assess which conditions drive major OHC changes in the region.

6.2 General case

The passage of a TC affects the heat content of the ocean over a large region. In Figs. 6.1 and 6.2 the average OHC changes through different depths of the ocean following deep ocean TC passage are illustrated for the inner core (within 100 km of the TC centre; Fig. 6.1) and whole circulation (1000 km; Fig. 6.2). These layers include averaged OHC from the surface to different depths through 2000 m (Figs. 6.1a and 6.2a) to analyse the total OHC changes, 500-m layers in the top 2000 m (Figs. 6.1b and 6.2b) to more closely analyse the deeper ocean changes, and 50-m layers in the top 1000 m (panels c and d in Figs. 6.1 and 6.2) to further analyse the depths most affected by TCs. These changes are analysed through the recovery period, defined as the period from Day 5 to Day 30. Overall, the effect of the TC passage is to decrease the OHC during the first 5 days after the event followed by a slow recovery to near pre-TC conditions.

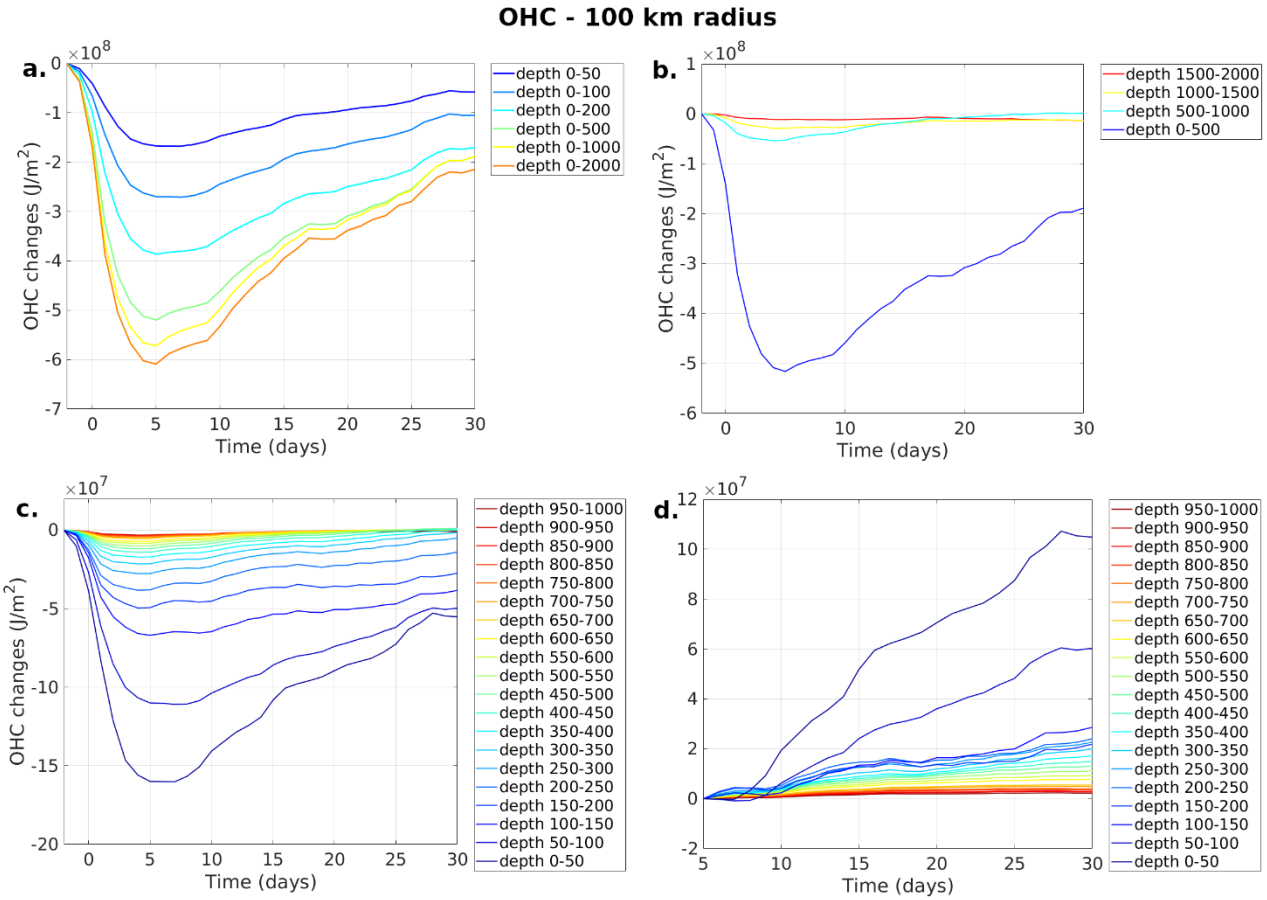

Figure 6.1: OHC changes from 2 days before the passage of the TC in the inner core (within 100 km of the TC centre) calculated for: (a) layers from the surface to various depths; (b) layers of 500-m depth from 0 to 2000 m; (c) layers of 50-m depth from 0 to 1000 m; and (d) same as (c) but starting from 5 days after the passage of the TC. Note the use of different scales for the OHC.

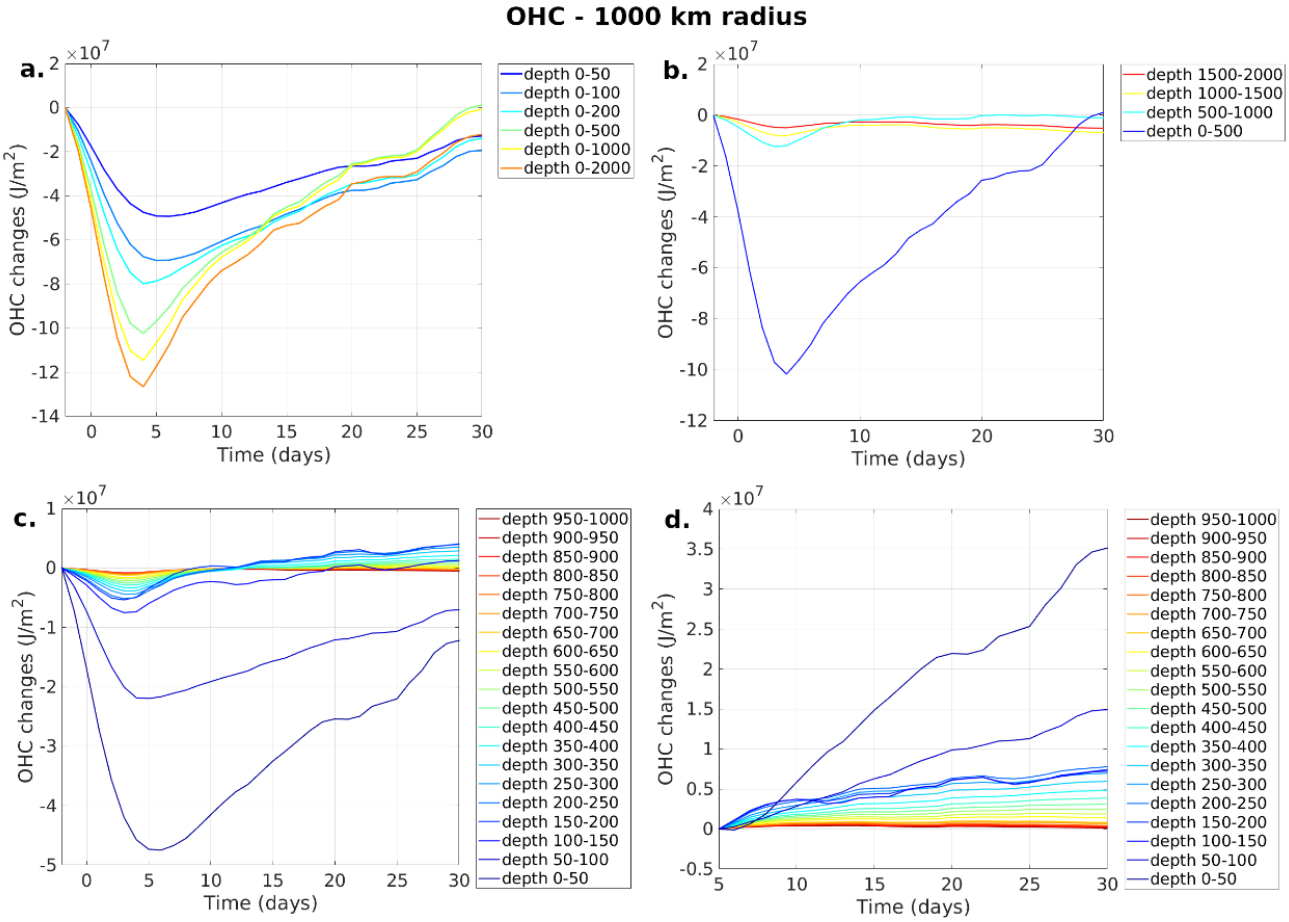

Figure 6.2: As in Figure 6.1 except averaged over the whole circulation within 1000 km of the TC centre.

The majority of the OHC losses following the TC passage occur in the inner core (within 100 km of the TC centre) (Fig. 6.1 compared to Fig. 6.2, note difference in scale). Almost 95% of the initial OHC loss within the inner core through 2000 m depth occurs in the top 1000 m subsurface layer (Fig. 6.1 a), with more than 85% loss occurring in the upper 500 m (Fig. 6.1 a). In the top 100 m, the OHC reaches a minimum near Day 5-6, while below 150 m, the minimum OHC occurs earlier, around Day 3 (Fig, 6.1c), suggesting that different processes drive the OHC reduction at different depths. In the surface layer, the decrease of the OHC lasts for longer than it does below 150 m as the horizontal current shear (Fig. 5.10) continues to drive mixing and entrainment of colder water into the surface layer. The surface cooling is further enhanced due to upwelling driving cold water up toward the surface and mixing with the warm surface water (Price, 1981). All 50-m layers within the first 1000 m show a decrease in their OHC following the TC passage (Fig. 6.1c).

The OHC anomalies are strongly connected with the cold temperature anomalies, averaged for 50 m layers (to match with Figs. 6.1c and 6.2c), which are shown in Fig. 6.3, along with the vertical currents. The region in which the cold anomalies develop below 100 m corresponds with the region where the upward vertical currents are the most intense (blue contours in Fig. 6.3c, d, e and f). This demonstrates that within the inner core, the reduction of OHC at depth and the cold anomalies are driven by strong upwelling that occurs during the TC passage and the day after in the region within 300 km from the track (coloured contours in Fig. 6.3).

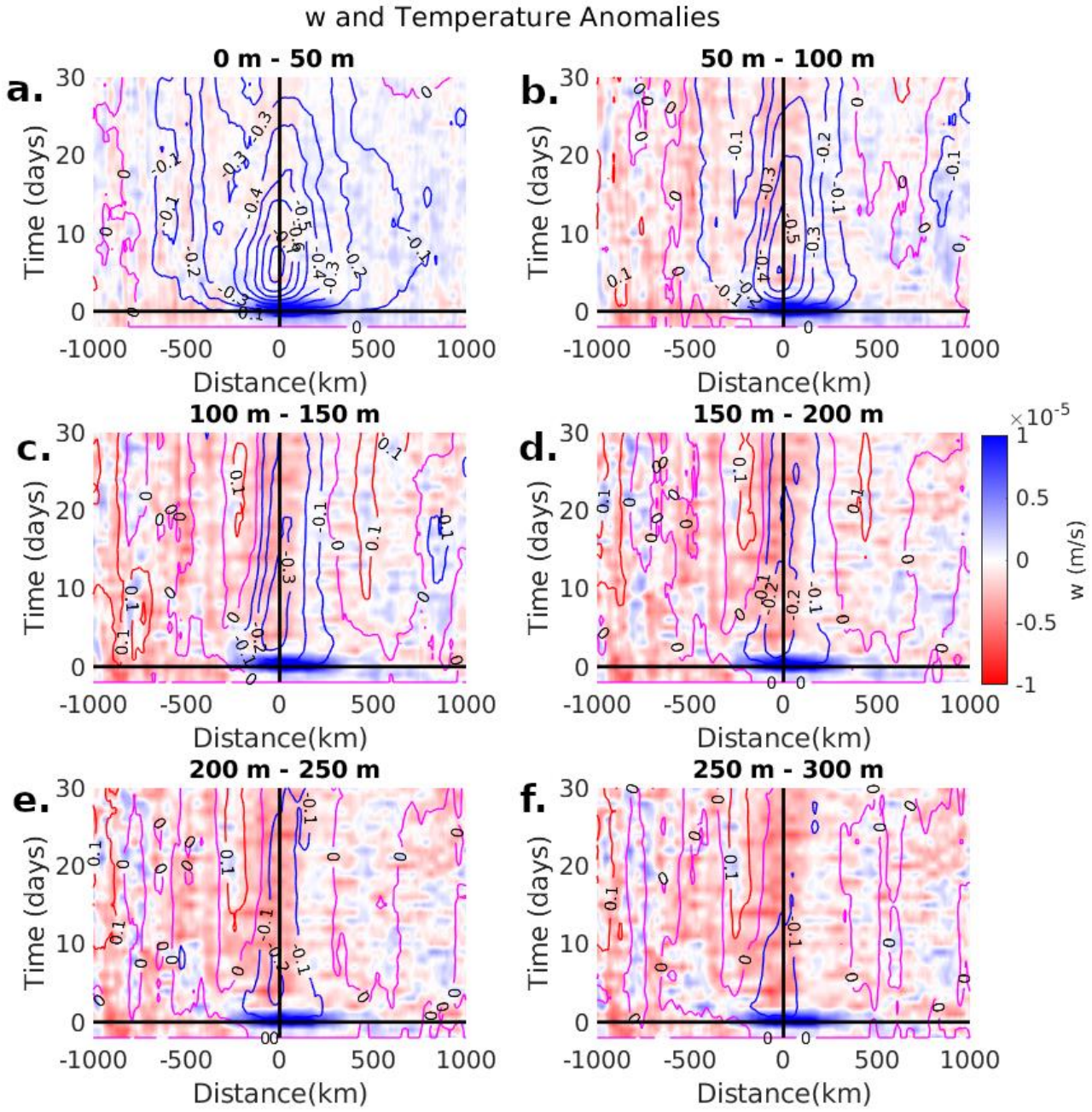

Figure 6.3: Cross-track Hovmoller diagram of vertical velocities (w (x 10^{-5} m/s), shaded in blue for upward and in red for downward vertical velocities) and temperature anomalies (contours every 0.1 °C, blue for negative anomalies and red for positive anomalies) in time for the average of 50 m depth layers between 0 and 300 m.

Within the inner core the OHC in the top 300 m never completely recovers in the first 30 days, although considerable increase in OHC occurs from 5 days after the TC passage (Fig. 6.1d). The strongest OHC recovery occurs in the surface layer, due to the high rate of warming from incoming solar radiation. Between 400- and 1000-m depth, the OHC fully recovers to pre-TC conditions around Day 25 (Figs. 5.14 and 6.1c) due to strong downwelling that begins after Day 2 and continues beyond Day 30 (Figs. 5.14, 6.4). However, the integrated OHC through 1000 or 2000 m depth within the inner core does not recover, at least in the first 30 days after the TC passage.

Over the larger whole circulation region (1000 km average), approximately 80% of the OHC loss occurs in the top 500 m (Fig. 6.2a) and 55% occurs in the top 100 m, suggesting that in the outer region subsurface cooling is strongly reduced compared to the inner core (25% of the OHC losses between 100 and 500 m in the whole region, compared to 50% in the inner core) and mixing across the thermocline dominates the surface OHC loss, especially in the most external region.

Dividing the layers into smaller, 50-m layers provides more insight. The OHC averaged over the whole region decreases in the days following the TC passage for any 50 m depth layer between the surface and 1000 m (Fig. 6.2). After a month the OHC within 1000 km of the TC centre has not recovered to pre-TC conditions in the surface 0-100 m layer (Fig. 6.2c) in spite of the high rate of OHC increase in that layer (e.g., Fig. 6.2d) most likely due to the positive net heat flux into the ocean (Fig 5.7). However, below 100 m the OHC in the whole region increases above pre-TC conditions as early as Day 10 in some layers (Fig. 6.2c), as weak downwelling occurs over a large region, especially to the left of track (Fig. 6.3).

The OHC from the surface to 1000 m, comprising over 90% of the OHC loss within 1000 km of the TC centre, recovers to pre-TC conditions within 30 days (Fig. 6.2a). This suggests that contributing physical processes including surface fluxes, mixing, and horizontal and/or vertical advection after TC passage are strong enough to offset the large amount of cooling and OHC loss that occurs in the TC inner core (Figs. 6.1 and 6.2) only if the larger region is considered. Beneath 1000 m where the OHC loss is quite small (< 10% of the total), other processes external to the TC, such as regional upwelling events or cold currents, may be occurring which result in slight continual OHC loss through the period. However, the resolution of BRAN data at these depths is too coarse to allow in depth study of this. In fact, beneath 1000 m the OHC decreases slightly in the first 4-5 days after TC passage, then begins to recover through days 8-15 and then decreases again through Day 30 (Figs. 6.2b).

The decrease of surface layer OHC and the increase of deeper (below 100 m) OHC (Fig. 6.2c) is balanced after a month to 1000 m depth (Fig. 6.2a). This is because the large OHC decrease within the inner-core region is offset by an OHC increase in the large outer region below 100-m depth. In fact, outside the inner core the major effect of the TC passage is vertical mixing of the surface and subsurface waters due to vertical current shear (Figs. 5.10 and 5.13). This results in a decrease of surface layer OHC and increase in the layer below, especially between 100 and 300 m (Fig. 6.2c). The comparison between the location of the 0°C anomaly in the surface 50-m layer (Fig. 6.3a) and in the layer below (Fig. 6.3b) shows that the majority of the mixing occurs between 500 and 800 km to the left of track, where at Day 5 the surface has cooled and the subsurface has warmed.

The OHC changes within 100-km annulus bands from the TC centre are shown in Figs. 6.4 and 6.5. Between 100 and 500 km from the TC centre, the OHC does not recover from the surface to any depth (Fig. 6.4a, b, c and d). By Day 30, the OHC in the top 1000 m of the ocean has recovered to at least pre-TC conditions in the 500-600 km band (Fig. 6.4e) and the OHC has increased compared to pre-TC conditions in all bands further than 600 km from the TC centre. The OHC decrease in the top 100 m completely recovers by Day 30 in the bands located further than 700 km from the TC centre (Fig. 6.4g, h and i).

The OHC changes every 50 m layer between the surface and 1000 m is shown in Fig. 6.5 to better understand where the warming occurs that balances the surface cooling. Within 300 km of the TC centre, the OHC does not increase relative to pre-TC conditions in any 50-m layer in the ocean down to a depth of 1000 m during the month following the TC passage (Fig. 6.5a and b). However, in the 300-400 km band the OHC recovers and shows positive anomalies after Day 15 for layers below 200 m depth (Fig. 6.5c). In the 400-500 km band, OHC becomes positive below 150 m depth and in the 500-600 km band it it becomes positive below 100 m approximately 10 days after the TC passage. At distances greater than 700 km from the TC centre, there is an increase in OHC in the layers below 100 m and a decrease above 100 m in the days following TC passage, suggesting that mixing is likely the main process that leads to OHC losses in the surface in the outer regions of the TC and warming in the subsurface (Fig. 6.5g, h and i). Furthermore, in the outer region, the OHC increase in deeper layers during TC passage is further enhanced by downwelling (Fig. 6.4, shaded in red), which occurs more than 600 km from the TC centre, and is expected to happen to compensate for the strong upwelling in the inner core.

In summary, the passage of a TC drives strong OHC losses within 300 km from the track at any depth and OHC gains in the subsurface in the outer regions to depths near 1000 m. The heat losses are strongest within 300 km of the center of the TC (Figs 6.1, 6.4a and b, and 6.5a and b) and in the ocean surface 100 m over the whole region (Fig. 6.2c). An increase in OHC occurs in ocean layers below 100 m in the outer region (Fig. 6.5g, h and i), at distances greater than 700 km from the TC centre most likely due to mixing and downwelling. Over the whole region, the OHC is reduced following the TC passage, but is balanced after a month when considering the ocean to a depth of 1000 m (Fig. 6.2a). Thissuggests that, although the OHC in the core after 30 days is still negative, there is an OHC increase in the large outer region that balances the OHC losses in the central region (Fig. 6.4g, h and i). In fact, at Day 30 the OHC in the outer region shows strong positive anomalies for any layer considered (Fig. 6.5g, h and i). After Day 10, the warm anomalies on the sides of the track that developed during TC passage remain trapped in the subsurface (Fig. 6.3c, d, e and f) and any further recovery of the cold anomalies at depth in the inner core and in the surface layers drives an overall increase of the OHC to above pre-TC conditions in the whole region.

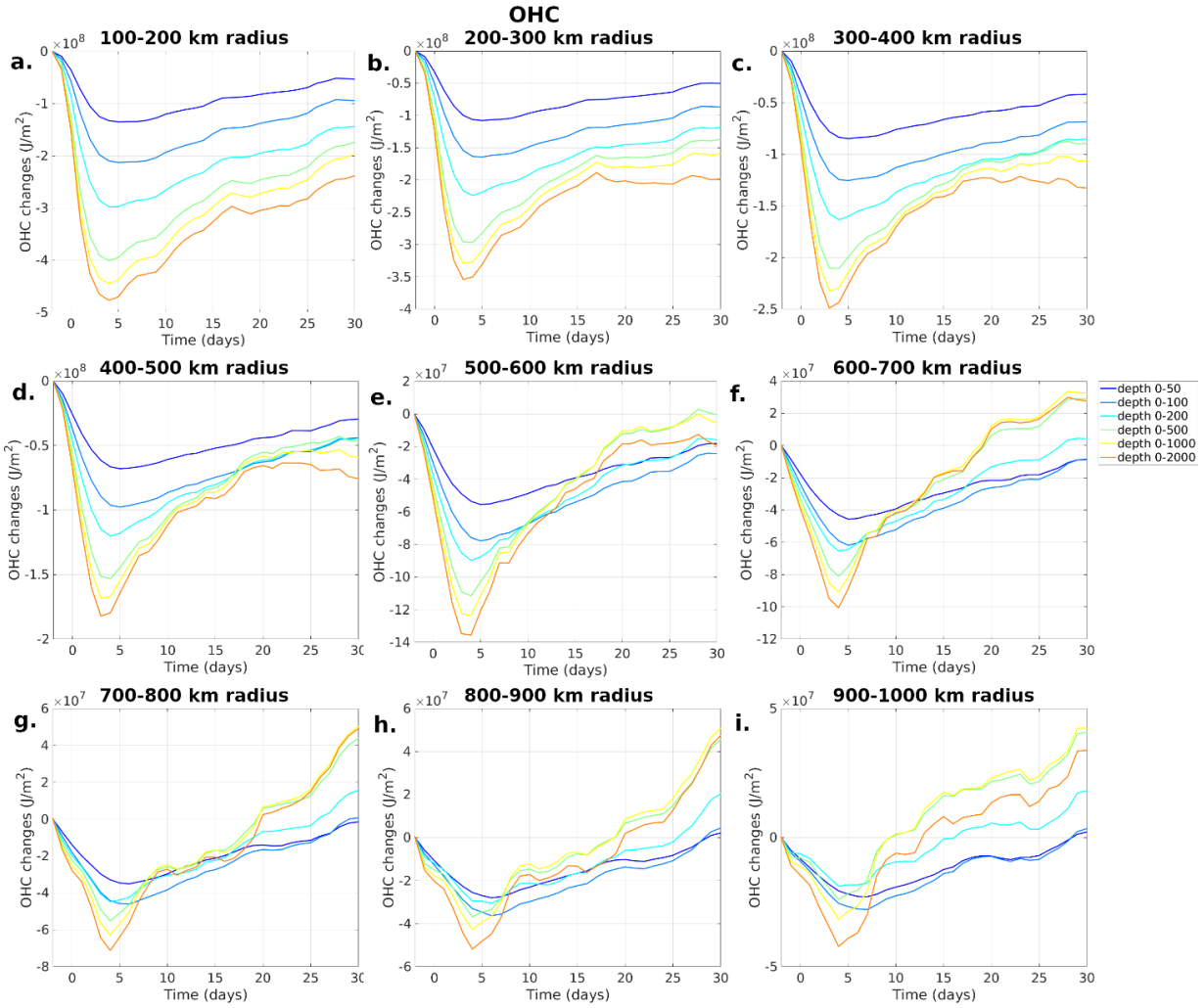

Figure 6.4: OHC changes from 2 days before TC passage of the TC calculated for layers from the surface to various depths averaged in regions at different distances from the TC centre.

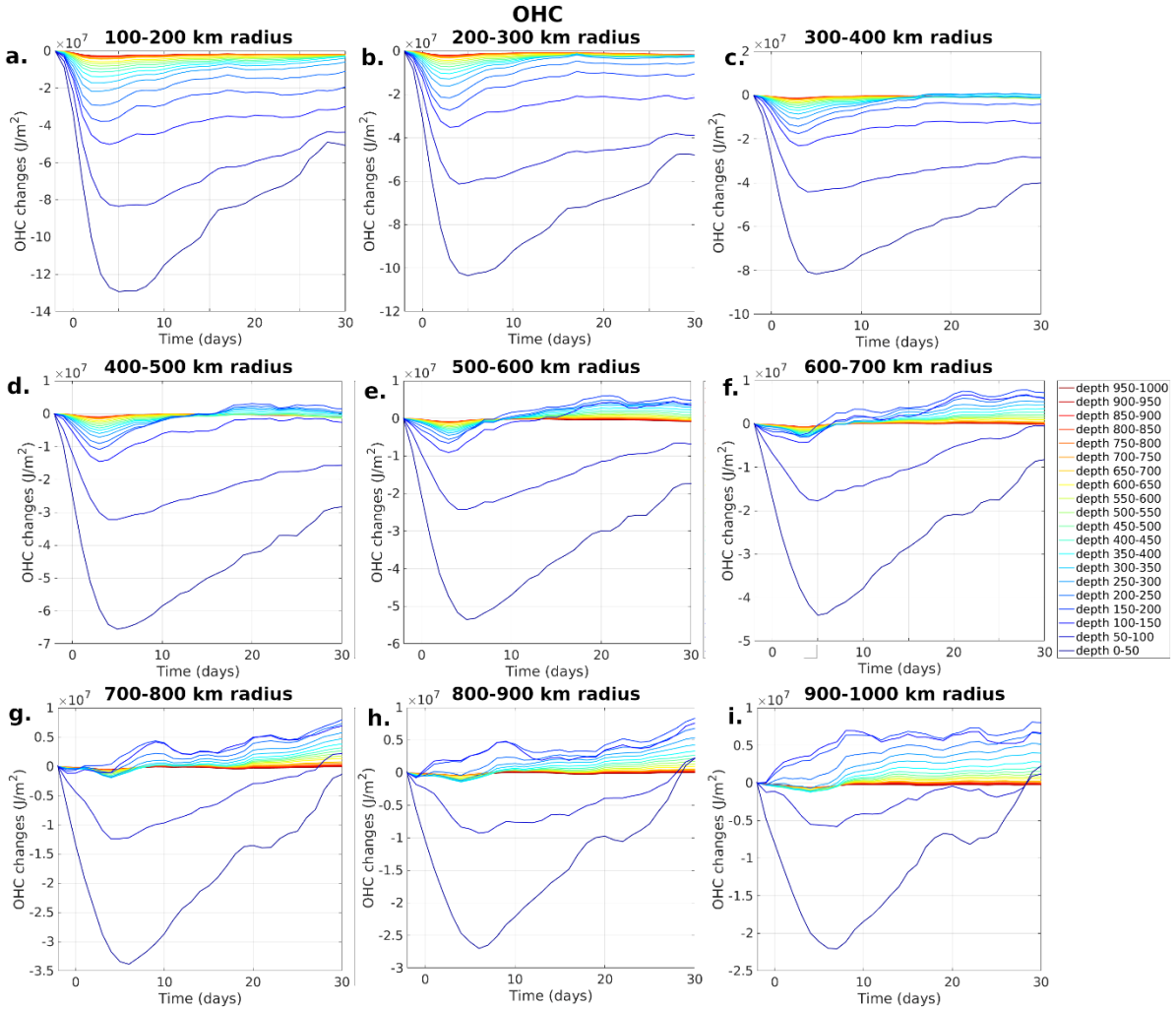

Figure 6.5: OHC changes from 2 days before the passage of the TC calculated for layers of 50-m depth from 0 to 1000 m averaged in regions at different distances from the TC centre.

6.2.1 OHC budget

The OHC changes during the passage of a TC (and their recovery) are driven by several mechanisms occurring at different distances from the TC centre. In this section the OHC budget is studied without removing the seasonal cycle from the temperature data, thus Fig. 6.6 shows the differences between the OHC changes from 2 days before the TC passage and the OHC rate of change calculated removing (panels a and c) and not removing the seasonal cycle (panels b and d). The cross-track section of OHC anomalies from 2 days prior to TC passage, integrated from the surface to 500 m (Fig. 6.6a and b), shows a strong OHC reduction between 200 km to the left to 300 km to the right of track and an OHC increase over the sides, which by Day 30 covers the region further than 200 km. Fig. 6.6c and d show a strong OHC decrease beneath the track between Day 0 and Day 5 (in agreement with Fig. 6.1c) and a general increase over the sides from Day 0 (in agreement with Fig. 6.5g-i) and beneath the track from Day 5 when the OHC losses start to recover (in agreement with Fig. 6.1d). The effect of the seasonal cycle on the composited OHC is an increase in OHC during the recovery stage in the month following the passage of the TC (Figs. 6.6b and d compared to Figs. 6.6a and c). This could be due to a seasonal trend of temperature warming during the TC season over the NWS, which is not removed in Figs. 6.6b and d.

To further investigate the processes driving OHC changes at different distances from the track, the components of the OHC budget integrated in the first 500 m are calculated and shown in Fig. 6.7. Furthermore, to demonstrate the effect of different processes at depth during and after the TC passage a cross-track section of OHC budget components are shown for the forcing stage (Day -2 to 5, from two days before

the TC passage to 5 days after), recovery stage (Day 5 to 30), and for the whole period (Day -2 to 30) in Figs. 6.8 to 6.10.

Fig. 6.7a shows that during the forcing stage (Days -2 to 5), the OHC is strongly reduced beneath the TC track, slightly reduced on the right of track, and slightly increased on the left of track . The overall effect at Day 5 is a general reduction in OHC in the surface 50 m between 800 km to the left and 900 km to the right of track and a reduction in the subsurface between 100 km to the left and 400 to the right of track (Fig. 6.8a). However, on both sides further than 300 km from the track, there is an increase of OHC in the subsurface, especially strong between 50 and 200 m depth and 200 to 600 km on the left of track (Fig. 6.8a), in agreement with where the cold and warm anomalies develop following a TC (Fig. 6.3). This pattern agrees with an overall reduction of the OHC in every 50 m layer, especially strong near the surface, for any region considered (Figs. 6.1c, 6.2c and 6.5) but not below the surface layer for the outer region (Fig. 6.5f-i).

During the TC passage and the day following, the negative vertical advection indicates strong upwelling beneath the TC centre (Figs. 6.7b and 6.8b), which also extends out to 900 km to the right of track at a lower intensity. This agrees with upward vertical currents due to Ekman pumping driven by strong divergent surface currents (Figs. 5.10 and 6.3) and with the stronger OHC decrease in every 50 m layer for the inner core (Fig. 6.1c). At the same time, positive vertical advection drives warming at more than 300 km to the left of track and helps the development of the warm anomalies in the subsurface (Figs. 6.3c-f, 6.7b and 6.8b), and likely driving the increase of OHC in the outer region below 100 m (Fig. 6.5f-i).

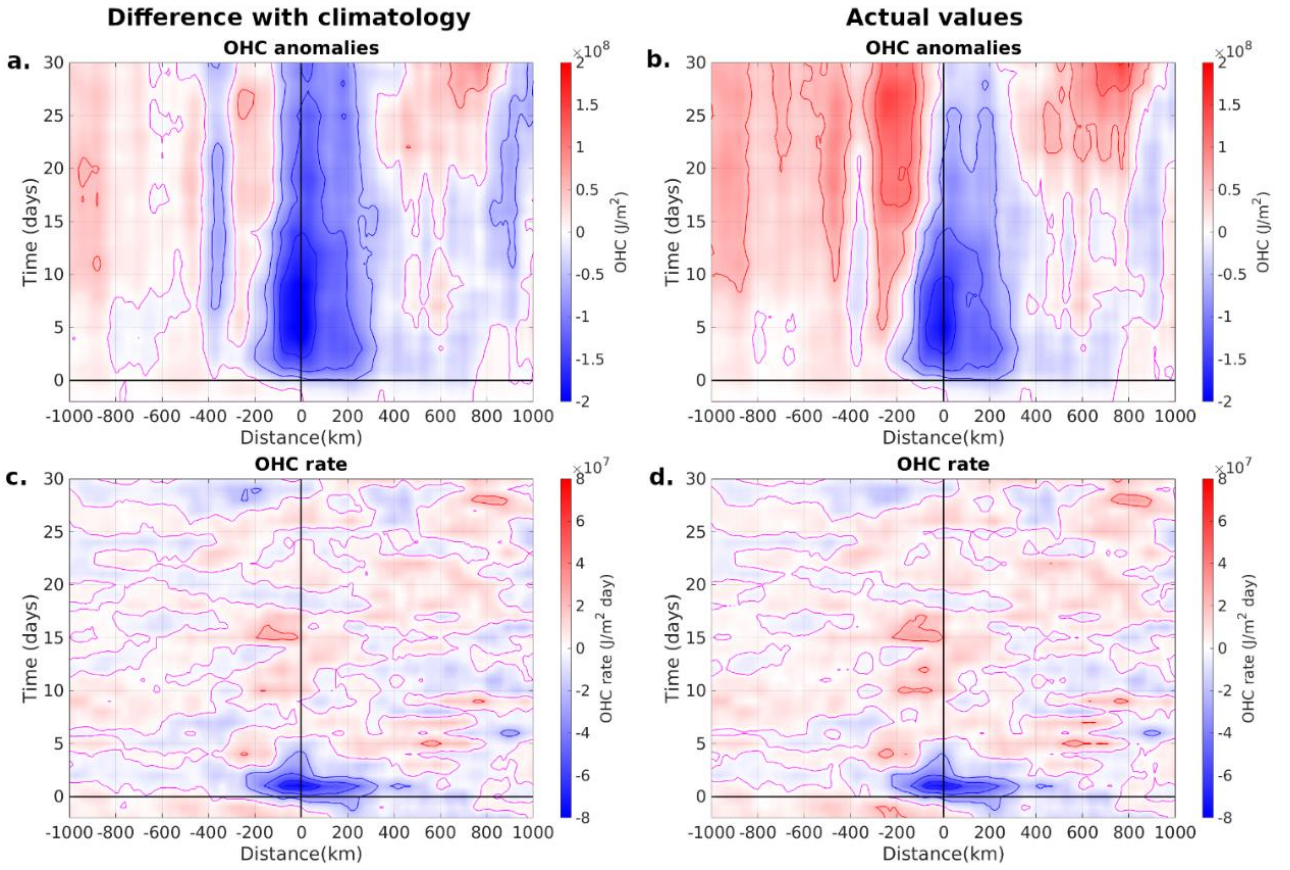

Figure 6.6: Cross-track Hovmoller diagram of OHC integrated from the surface to 500 m showing: (a), (b) OHC anomalies from 2 days before TC passage; and (c), (d): OHC rate of change . The left and right columns show, respectively, seasonal cycle removed and not removed.

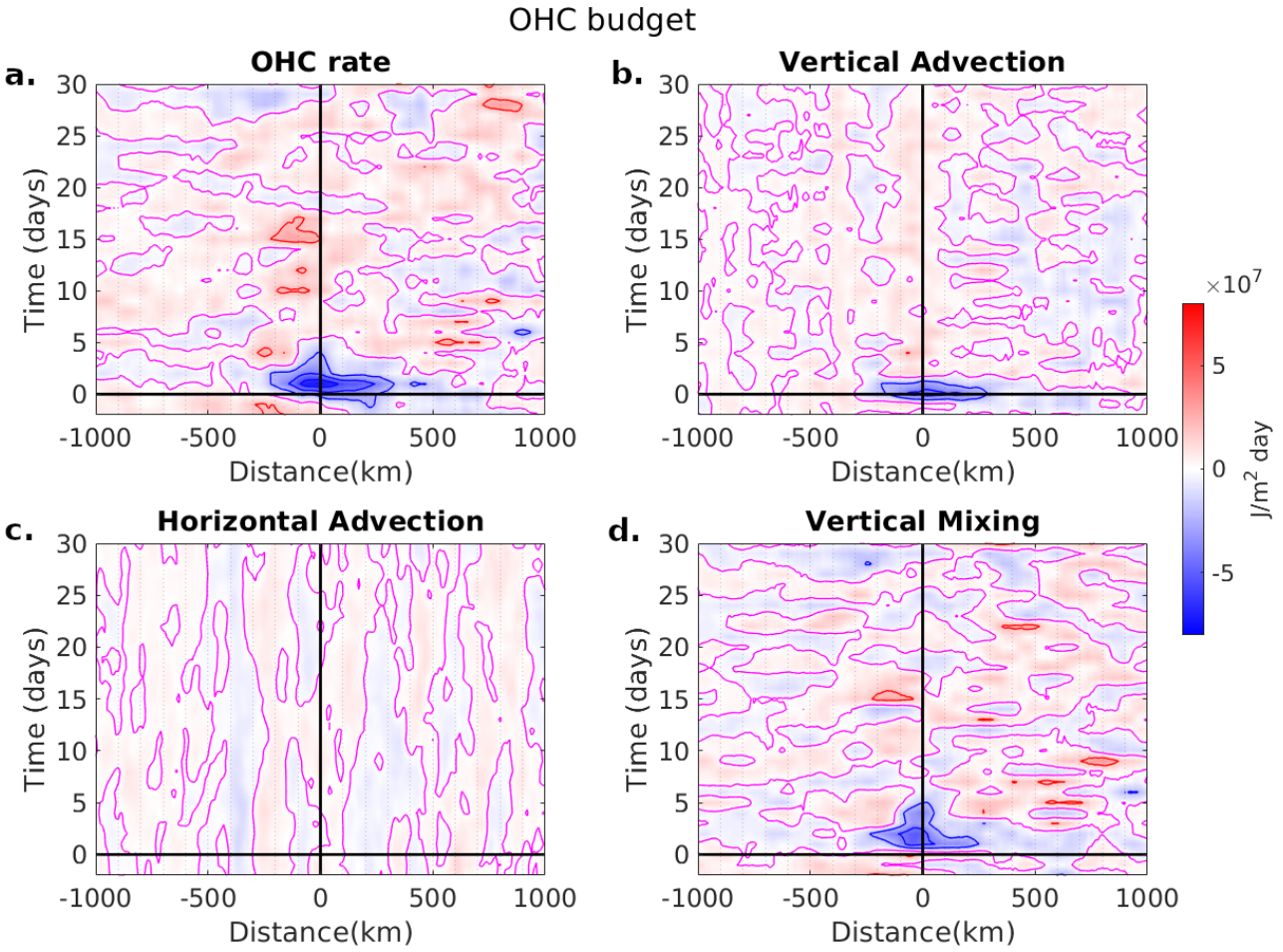

Figure 6.7: Cross-track Hovmoller diagram of OHC rate of change in time integrated in the first 500 m depth (terms of eq. 3.10) for: (a) the total rate; (b) changes due to vertical advection; (c) horizontal advection; and (d) vertical mixing and surface fluxes.

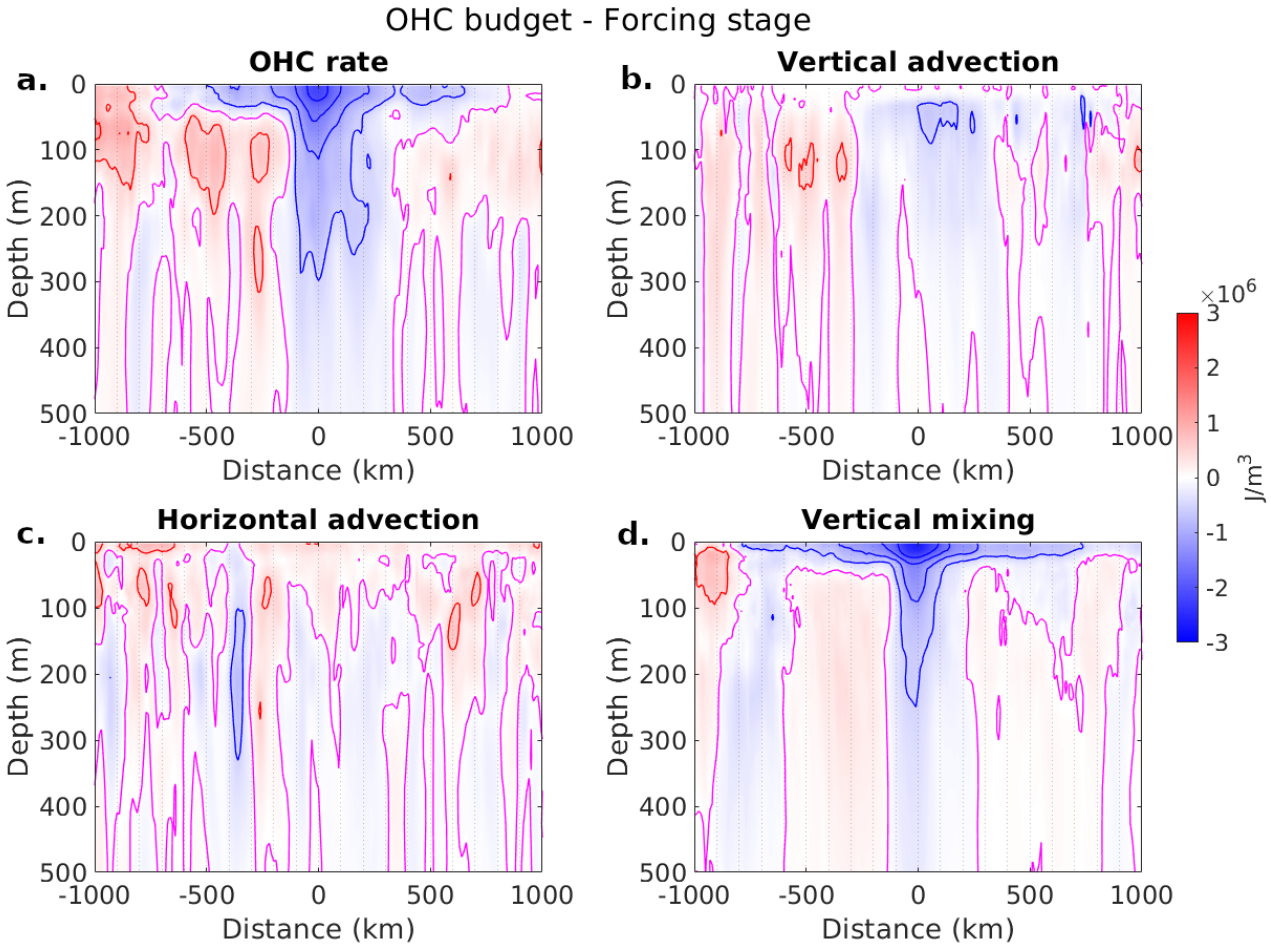

Figure 6.8: Cross-section of the OHC changes integrated in time during the forcing stage (from Day -2 to Day 5) for: (a) the total rate; (b) changes due to vertical advection; (c) horizontal advection; and (d) vertical mixing and surface fluxes.

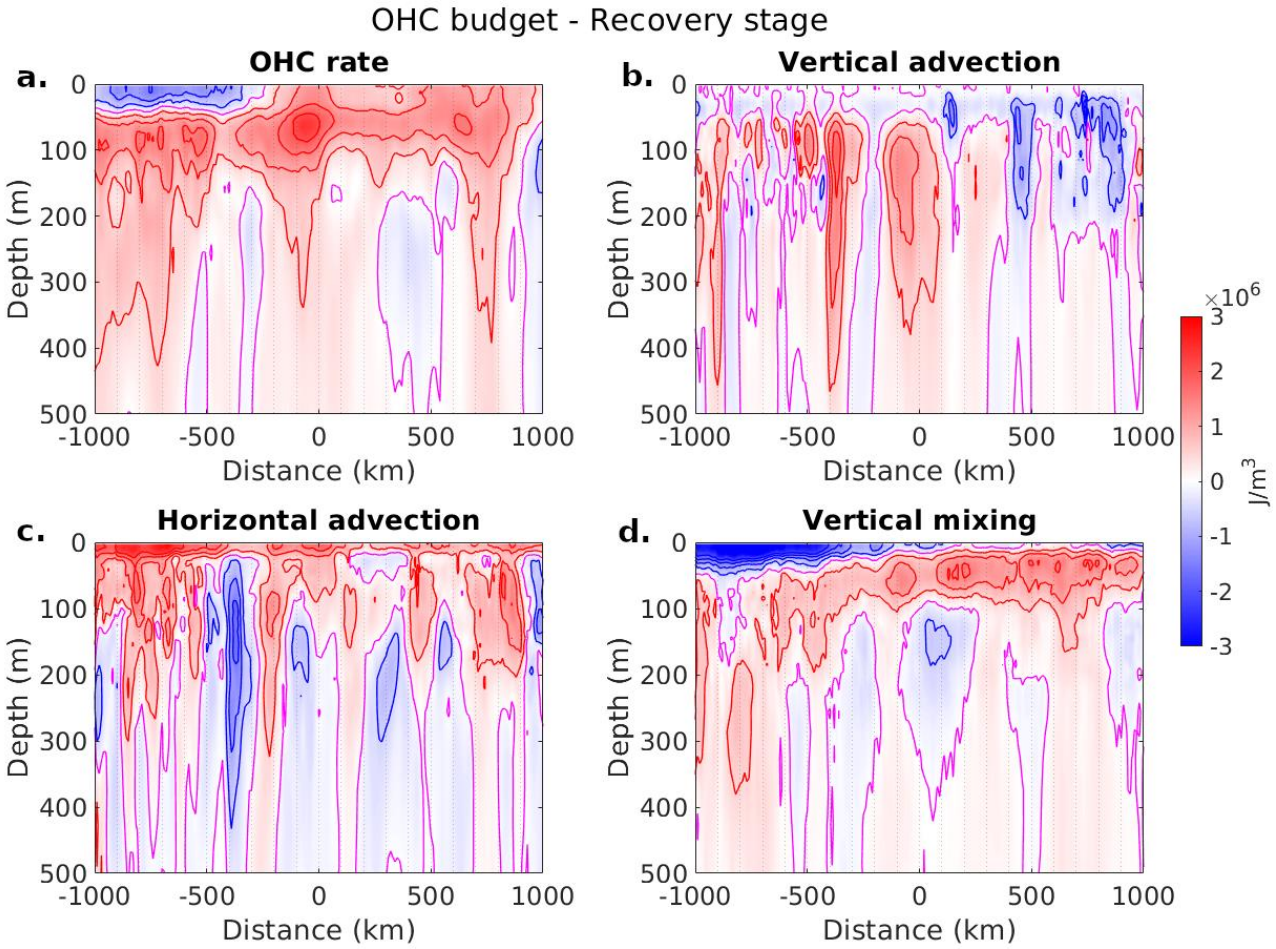

Figure 6.9: As in Figure 6.8 but during the recovery stage (from Day 5 to Day 30).

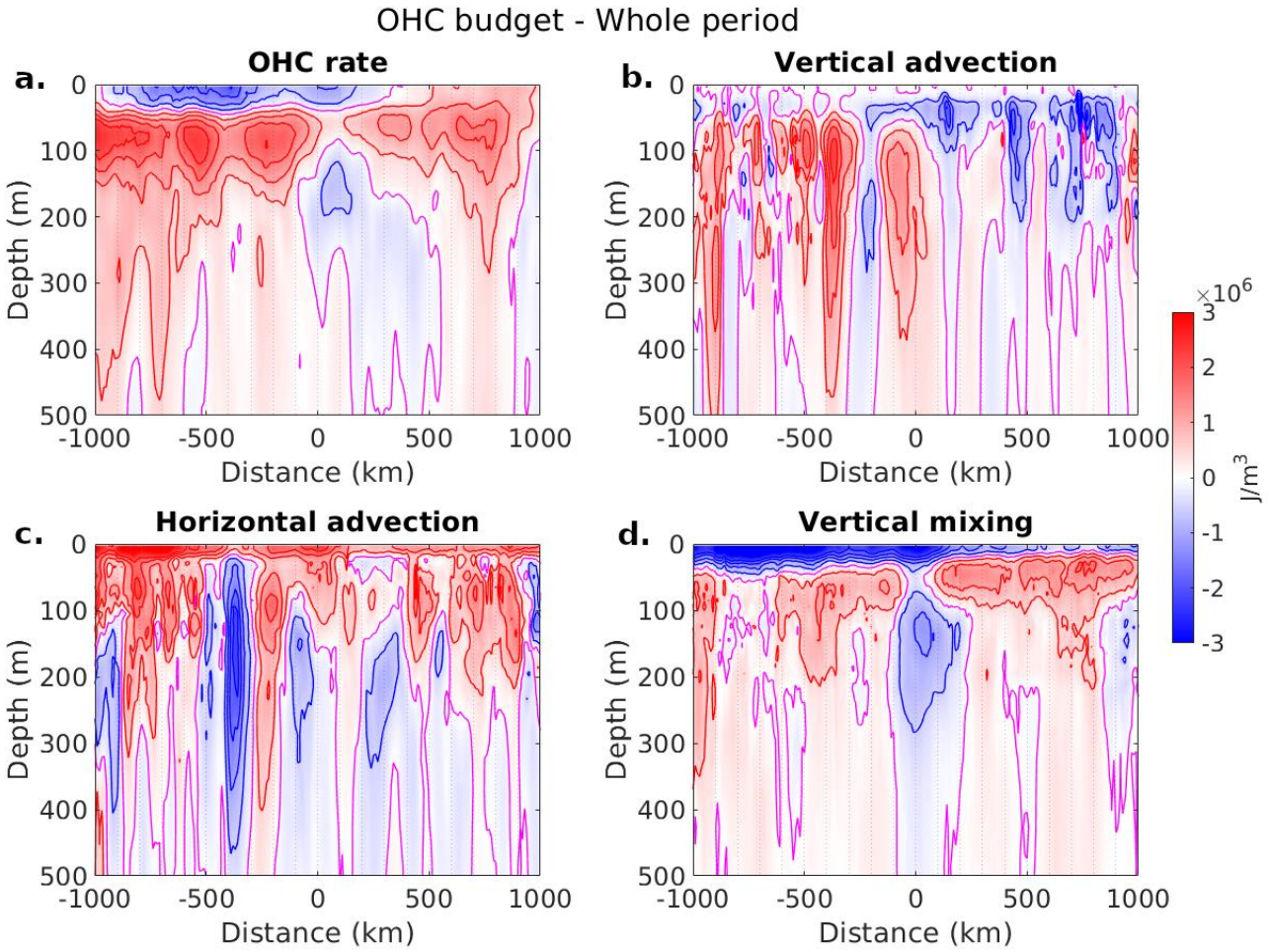

Figure 6.10: As in Figure 6.8 but for the whole period (from Day -2 to Day 30).

Horizontal advection integrated in the first 500 m contributes weakly to the OHC changes and is generally positive, but with two negative regions between 300 and 500 km to the left of track and 100 and 500 km to the right of track (Fig. 6.7c). At depth, the horizontal advection during the forcing stage is positive in the first 100 m and mostly negative below (Fig. 6.8c).

The vertical mixing contribution to the OHC change in the top 500 m of the ocean is negative during the forcing stage in the whole region and is especially strong within 200 km of the TC centre (Fig. 6.7d). This vertical mixing drives the strong OHC reduction in the surface 50 m layer out to 1000 m radius (Figs. 6.1c, 6.2c and 6.5). At depth, the contribution of the vertical mixing during the forcing stage is generally to reduce OHC in the surface 50 m layer and to increase OHC in the subsurface layers at both sides of the track (Fig. 6.8d). This is expected and is in correspondence with regions where the MLD is entrained following the TC passage and the warm water at the surface is mixed with the colder water underneath (Fig. 5.13), and where OHC does not decrease in the subsurface following TC passage (Fig. 6.5g-i). The contribution of mixing is negative and stronger at the surface beneath the track from 100 km to the left to 300 km to the right of track (Fig. 6.8d) and could be due to the combined effects of mixing and upwelling being captured in the vertical mixing component since this is calculated as the residual of the budget (Fig. 6.1a and c). Furthermore, vertical mixing includes the surface net flux component of the budget, which is negative during the forcing stage due to enhanced heat loss from the ocean to the atmosphere as the cyclone passes over the region (Figs. 5.6 and 5.15).

During the recovery stage, the OHC in the first 500 m generally increases as the cold temperature anomalies recover (Fig. 6.7a), in agreement with Figs. 6.1d and

6.2d. Fig. 6.9a shows that the OHC recovers from Day 5 to Day 30 at depth, with general warming everywhere except for the 20 m surface layer more than 300 km to the left of track.The warming is generally strongest in the subsurface, between 50 and 150 m (Fig. 6.9a). In the region further than 300 km to the left of track, the mixing continues after Day 5 and the MLD continues to deepen (Fig. 5.13a), causing the decrease of the OHC in the surface layer and the increase in the subsurface.

The contribution of vertical advection during the recovery stage is generally to increase the OHC in the first 500 m with some decrease between 400 and 1000 km to the right of track from Day 5 to Day 20 (Figs. 6.7b and 6.9b). There is a region of strong positive vertical advection contribution beneath the TC centre between 50 m and 350 m, where the restorative downwelling occurs following the reversal of the horizontal surface currents to convergence (Figs. 5.10 and 6.3). This contributes to the higher rate of OHC increase during the recovery stage in the inner core (Fig. 6.1d).

The pattern of horizontal advection during the recovery stage is similar to the pattern during the forcing stage (Figs. 6.7c, 6.8c and 6.9c). In the first 150 m near the surface the contribution from horizontal advection is mostly to increase OHC but with a decrease below (Fig. 6.9c). The narrow band of negative horizontal advection between 300 and 500 km to the left of track below 50 m depth is still present during the recovery stage (Fig. 6.9c). It is unclear what the cause of this persistent feature is.

Depth integrated vertical mixing during the recovery stage alternates positive and negative contribution to OHC changes (Fig. 6.7d). At depth, between Day 5 and Day 30, it contributes strong warming in the subsurface below 50 m and to some cooling at the surface on the left of track, which corresponds to the region where OHC

decreases during recovery (Fig. 6.9d and a). The region on the left of track where there is cooling at the surface and warming underneath suggest that the mixing between these layers continues after Day 5, which agrees with a further entrainment of the ML on the left of track during recovery (Fig. 5.13).

Fig. 6.10 shows the overall OHC changes from before the TC passage to a month after as well as the contributions from the different components. In the surface 50-m layer OHC decreases up to 1000 km to the left and up to 400 km to the right, mostly due to vertical mixing (Fig. 6.10a and d), while the horizontal advection at the surface is positive and contrasts this cooling (Fig. 6.10c). In the subsurface, between 50 and 150 m the OHC is mostly increased at Day 30, driven by a combination of vertical mixing, and horizontal and vertical advection (Fig. 6.10c and d) on the left of track, where the vertical currents are mostly downward during both the forcing and recovery stage (Fig. 6.3 and 6.10b). Below 200 m depth, the OHC is mostly increased, although to a lesser extent from the subsurface layer at the sides of the track, in agreement with the OHC increase in Fig. 6.5e-i. However, between the TC centre and 500 km to the right of track, the OHC below 100 m is decreased, driven by vertical mixing with some minor contribution from the horizontal and vertical advection components (Fig. 6.10). The pattern of the OHC over the whole period corresponds well with the OHC changes over the whole region a month after TC passage. At Day 30 the surface 50 m layer has not yet recovered, but the 50 m layers below 100 m have not only recovered but also increased their OHC from Day -2 (Fig. 6.2c). Overall, there is recovery in the top 500 m over the whole region (Fig. 6.2a), but not within the inner core (Fig. 6.1), where the OHC is decreased not only at surface but also over a large region underneath (Figs. 6.1a and c and 6.10a).

The OHC budget over a cross-track section shows how horizontal and vertical advection and vertical mixing contribute between the forcing and recovery stages at different depths. Horizontal advection constantly drives an OHC increase at the surface and a decrease below 200 m (Figs. 6.8 and 6.9). Vertical advection drives strong upwelling beneath the track during the forcing stage, which later reverses to downwelling. Vertical contributions are mostly positive over the left and mostly negative over the right of track for the whole period. Overall vertical mixing shows a cooling of the surface layer and an OHC increase in the subsurface at the sides of track during the forcing stage. This continues during the recovery stage as the ML continues to entrain. Vertical mixing is calculated as the budget residual and thus can be influenced by other terms not properly captured by the horizontal and vertical advection. The OHC budget is calculated without removing the seasonal cycle and, as the comparison in Fig. 6.6a to d shows, results in overestimating the warming during the recovery period. This is likely connected to overestimating the warming terms in Figs. 6.8 and 6.9 compared to Figs. 6.1, 6.2, 6.4 and 6.5 where the OHC changes are calculated removing a 20-year temperature climatology. Furthermore, in Figs. 6.1 and 6.2 the total OHC changes are calculated as the average of a circular region which gives more weight to the center of the track, while the budget in Figs. 6.7 to 6.10 is studied for a cross-track section to emphasize the different processes at distance from the track.

6.3 Seasonal effects on the OHC changes

The season in which a TC passes over the region influences the development of the temperature anomalies and their recovery in different ways (section 5.5). Within the inner core (Fig. 6.11) the OHC decrease is stronger for TCs during the warming season, especially when considering deeper layers to > 100 m depth (Fig. 6.11a compared to 6.11b), due to the generally stronger upwelling beneath the track during the warming season (Fig. 5.25). The stronger OHC decrease is larger between 100 to 500 m depth (Fig. 6.11c and d) which agrees with the development of stronger cold anomalies in the warming season in Fig. 5.23c.

The OHC also recovers much faster within the inner core during the warming season, especially closer to the surface (Fig. 6.11e and f), which is likely driven by the larger surface heat fluxes which warm the region in the following month (Fig. 5.24a). At Day 30 the OHC is closer to the pre-TC conditions during the warming season compared to the cooling season (Fig. 6.11a and b), due to the faster recovery of surface layers (Fig. 6.11c and e). Similar to the general case, no layer fully recovers by Day 30 during either the warming or the cooling season (Fig. 6.11c, d, e and f) .

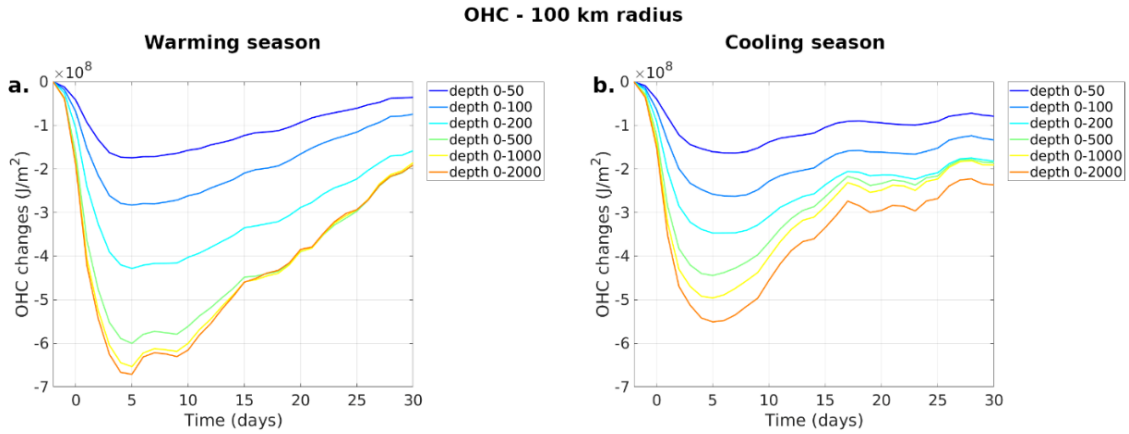

Figure 6.11: OHC changes within 100 km radius from 2 days before the passage of the TC calculated for layers of different depths from the surface for the: (a) warming season (454 data points); and (b) cooling season 487 data points).

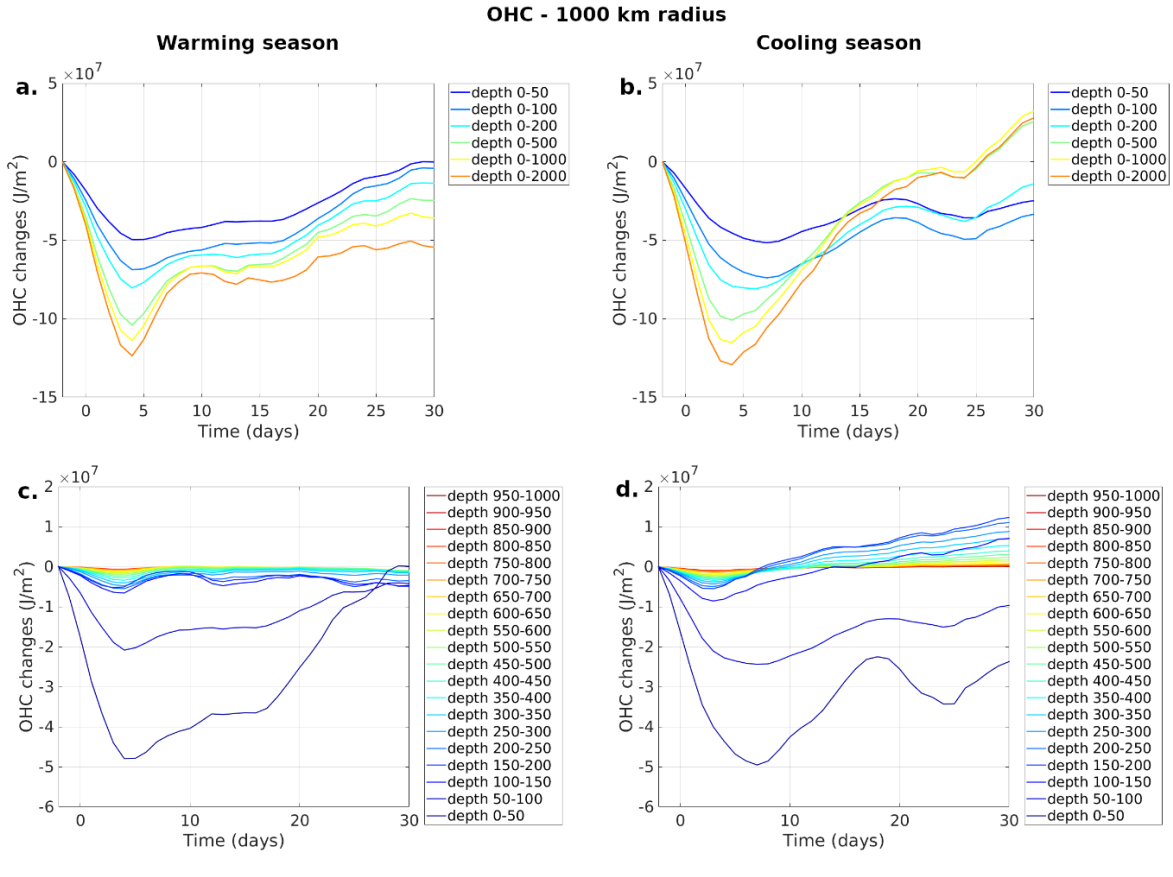

Figure 6.12: OHC changes within 1000-km radius from 2 days before the passage of the TC calculated for layers of different depths for the: (a), (c) warming season (454 data points); and (b), (d) cooling season 487 data points).

Within 1000-km radius during the forcing stage, the differences in OHC decrease between the warming and cooling seasons are less than they are in the inner core, suggesting that the stronger cooling mechanisms are mostly confined within the inner core. However, there are striking differences in the OHC anomalies during their recovery between the warming and cooling seasons (Fig. 6.12). During the warming season, the OHC anomalies recover by Day 30 for surface layers most likely because of the strong net heat flux into the ocean during the warming season that quickly warms the surface layers. However, below 100 m, the ocean does not fully recover (Fig. 6.12a). During the cooling season, the opposite occurs. In the surface 200 m of the ocean, the OHC anomalies do not recover to pre-TC conditions. However, below 100 m depth, the OHC increases relative to pre-TC conditions as early as 10 days after the TC passage (Fig. 6.12b). OHC changes in different bands form the TC centre are shown in Fig. 6.13. Much of the additional OHC gain during the cooling season at all radii is due to OHC increases below 200 m at all distances from the TC centre (Fig. 6.13a).

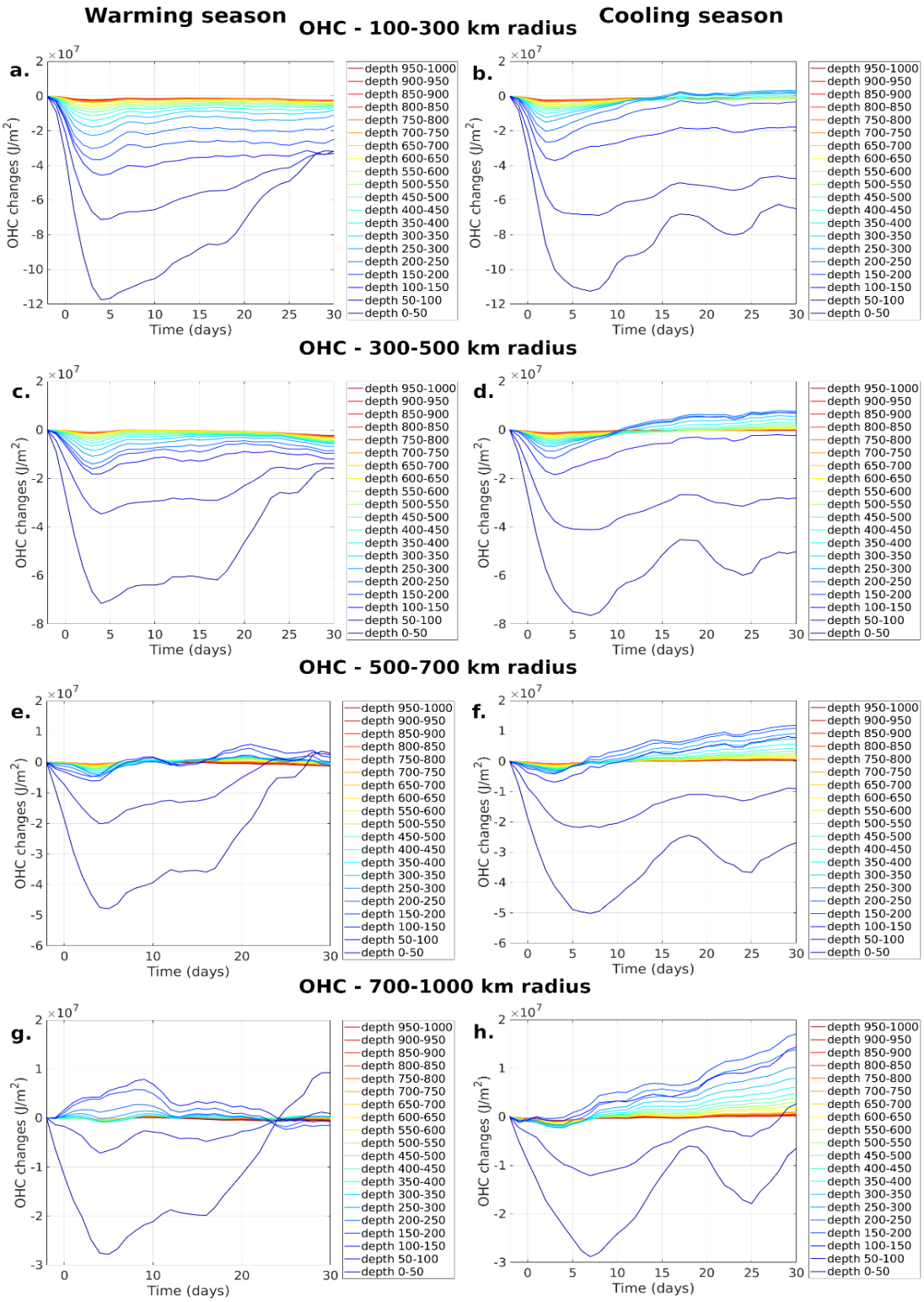

Figure 6.13: OHC changes calculated for 50-m layers in bands from the centre of the TC during the (left) warming season and (right) cooling season for: (a), (b) 0-300 km; (c), (d) 300-500 km; (e), (f) 500-700 km; and (g), (h) 700-1000 km.

The differences of the OHC changes between the warming and cooling seasons highlight the different processes that occur in different seasons. The higher rate of surface flux anomalies (Fig. 5.24) during the warming season drives an OHC increase and faster recovery in the surface 50-m layer compared to the cooling season (Figs. 6.11c and d, 6.12c and d, and 6.13). Below 100 m the OHC changes during the TC passage are driven by vertical mixing and show a small increase as warm temperature anomalies develop at the sides of the track, slightly stronger during the warming season between 100 and 200 m depth (Figs. 6.13e and g compared to f and h, and 5.23c and d), which is likely connected to the weaker stratification earlier in the season which facilitates mixing. During the recovery stage, the OHC anomalies in the outer region deeper than 100 m are driven mostly by the vertical currents (Fig. 5.25), with downward currents during cooling season driving warming to deeper layers (Fig. 6.13).

In general, although in our analysis the seasonal climatology is removed from the temperature signal, the OHC changes during the warming and cooling season differ. Within the inner core, stronger upwelling during the warming season drives more cooling for deeper layers. During warming season recovery, the surface layer OHC recovers quickly, driven by strong heat fluxes warming the ocean. Below 100 m outside the inner core, the recovery is much faster during the cooling season and the OHC in the subsurface has increased by Day 30 compared to before the TC passage, likely driven by the downward vertical currents. When considering the whole region and layers deeper than 200 m, the general result of TC passage is to decrease OHC during the warming season and increase OHC during the cooling season. The surface layer OHC increase during the warming season could help the development of MHWs and development of more TCs later in the season. The subsurface warm anomalies that

develop during the cooling season could resurface in winter, warming the ocean temperatures in the following months, or stored for longer and possibly be transported away from the region.

6.4 Effects of translation speed and TC intensity

Strong and slow TCs drive the development of colder and deeper temperature anomalies (Section 5.6). This is reflected in the OHC changes within the inner core for TC data points of different translation speed and categories (Figs. 6.14 and 6.15). The largest OHC decrease occurs in strong and slow TCs (Fig. 6.14d and 6.15d), followed by weak and slow (Fig. 6.14c and 6.15c), while weak and fast TCs produce the lowest OHC loss (Fig. 6.14a and 6.15a). The 50-m layer near the surface drives cooling of similar magnitude for strong and fast and for weak and slow TCs (Fig. 6.15b and c). However, below 50 m the cooling is stronger for weak and slow TCs. The major cooling and OHC decrease at depth for slow-moving TCs is likely due to the larger residence time that establishes stronger upwelling.

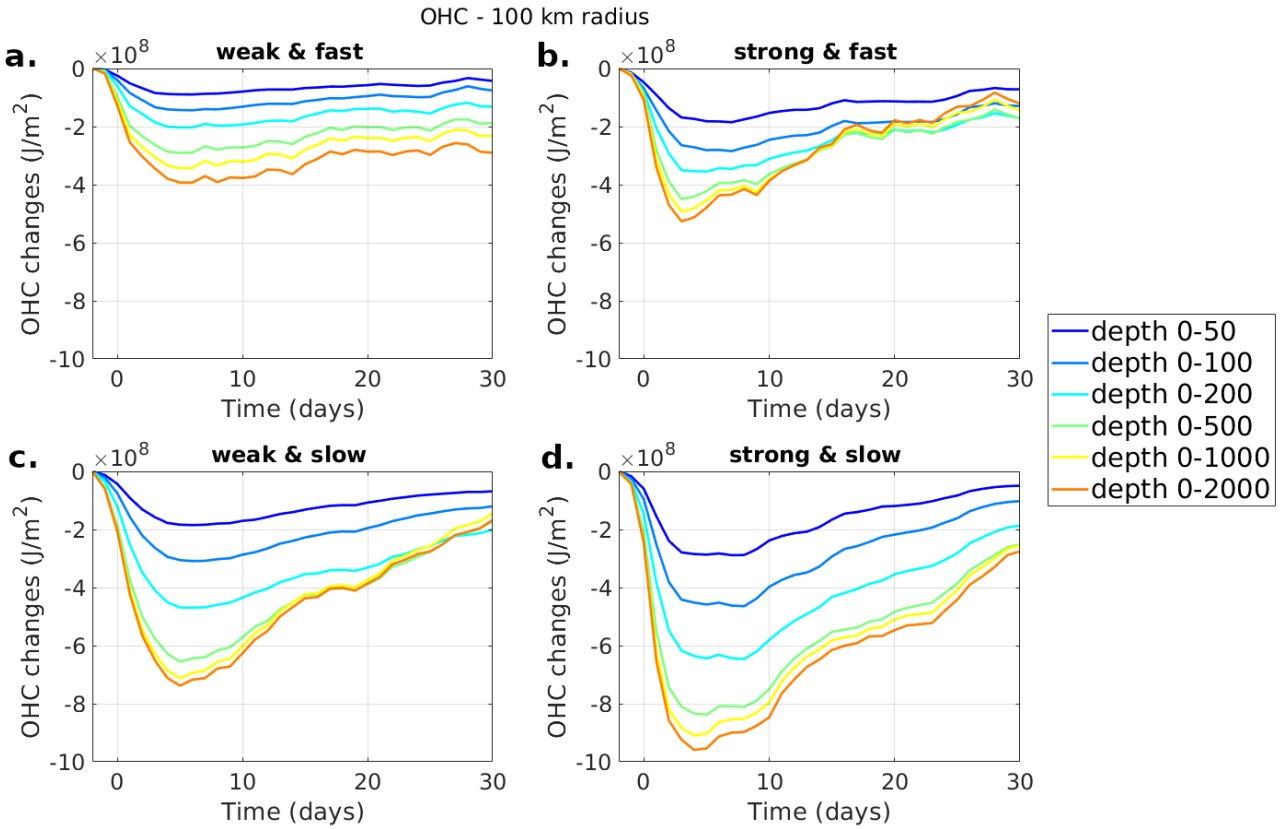

Figure 6.14: OHC changes from 2 days before the passage of the TC calculated for 100 km area average and layers of different depths for different translation speeds and categories.

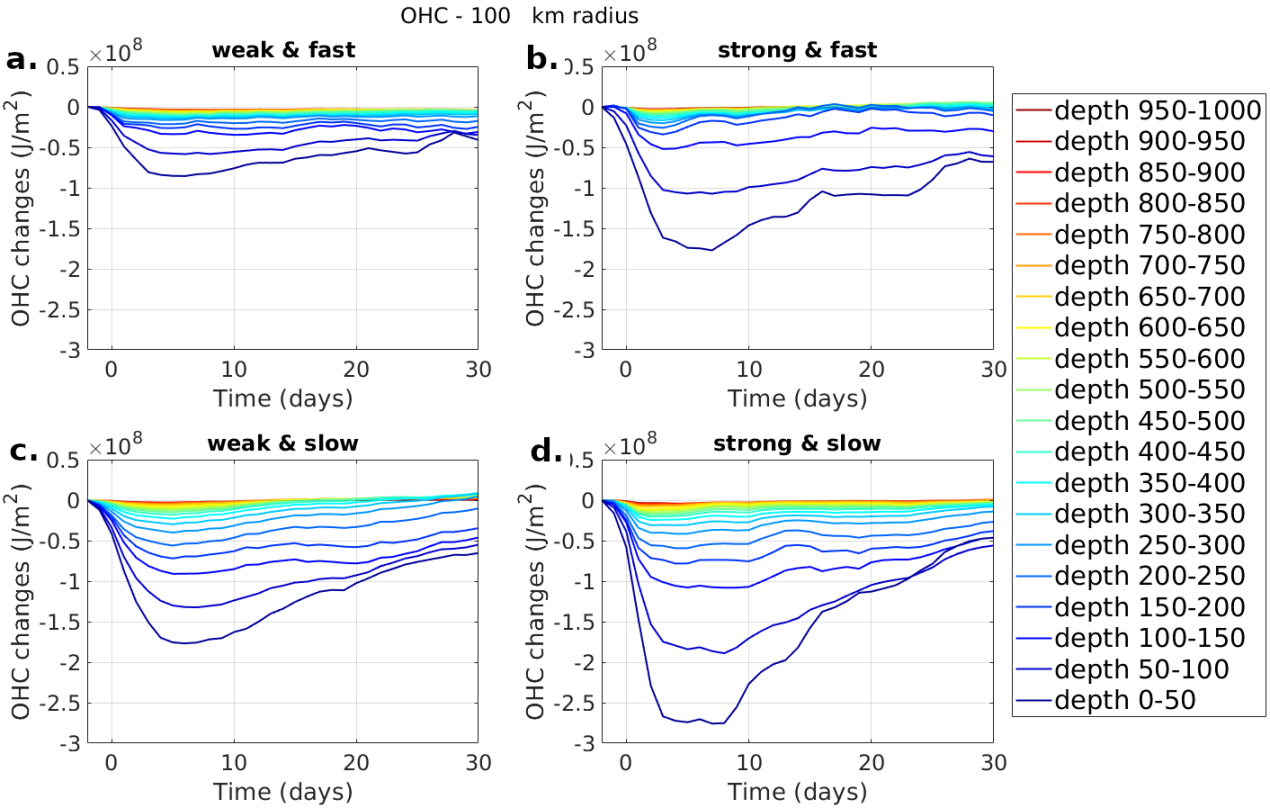

Figure 6.15: As in Figure 6.14 but in 50-m depth layers from the surface to 1000 m.

After the initial rapid OHC loss as the TC passes, the OHC within the inner core gradually recovers although it does not recover to pre-TC conditions for any combination of translation speed and category (Fig. 6.14). However, the OHC recovery is stronger for the surface 50-m layer especially for strong and slow TCs (Fig. 6.15d), where the cooling is also strongest. Although there is not much difference in the downwelling magnitude between forcing and recovery stages (Fig. 5.38), the OHC increase during recovery in deeper layers of the ocean is generally higher for slow-moving TCs, which may simply be because these TCs developed a colder anomaly that warms more rapidly during recovery.

The OHC changes within the whole region (1000-km radius) for different intensities and translation speeds are shown in Fig. 6.16. The difference in OHC decrease between TCs of different intensity and translation speed is less than for the inner core. As in the inner core, colder OHC anomalies develop after strong and slow TCs in the surface 100 m (Fig. 6.16), and below 100 m the weak and slow TCs develop the colder anomalies (Fig. 6.16c). This is highlighted in Fig. 6.17.

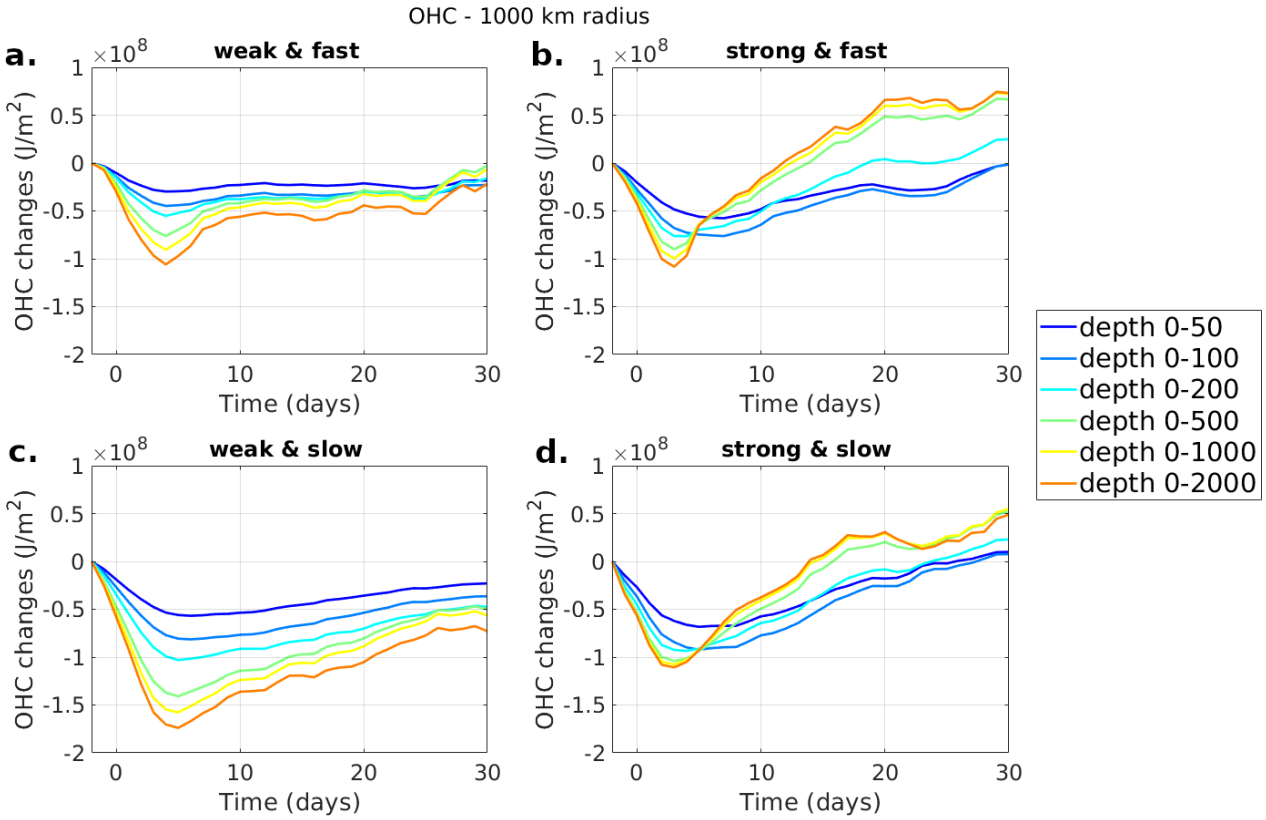

Figure 6.16: As in Fig. 6.14 for the whole region.

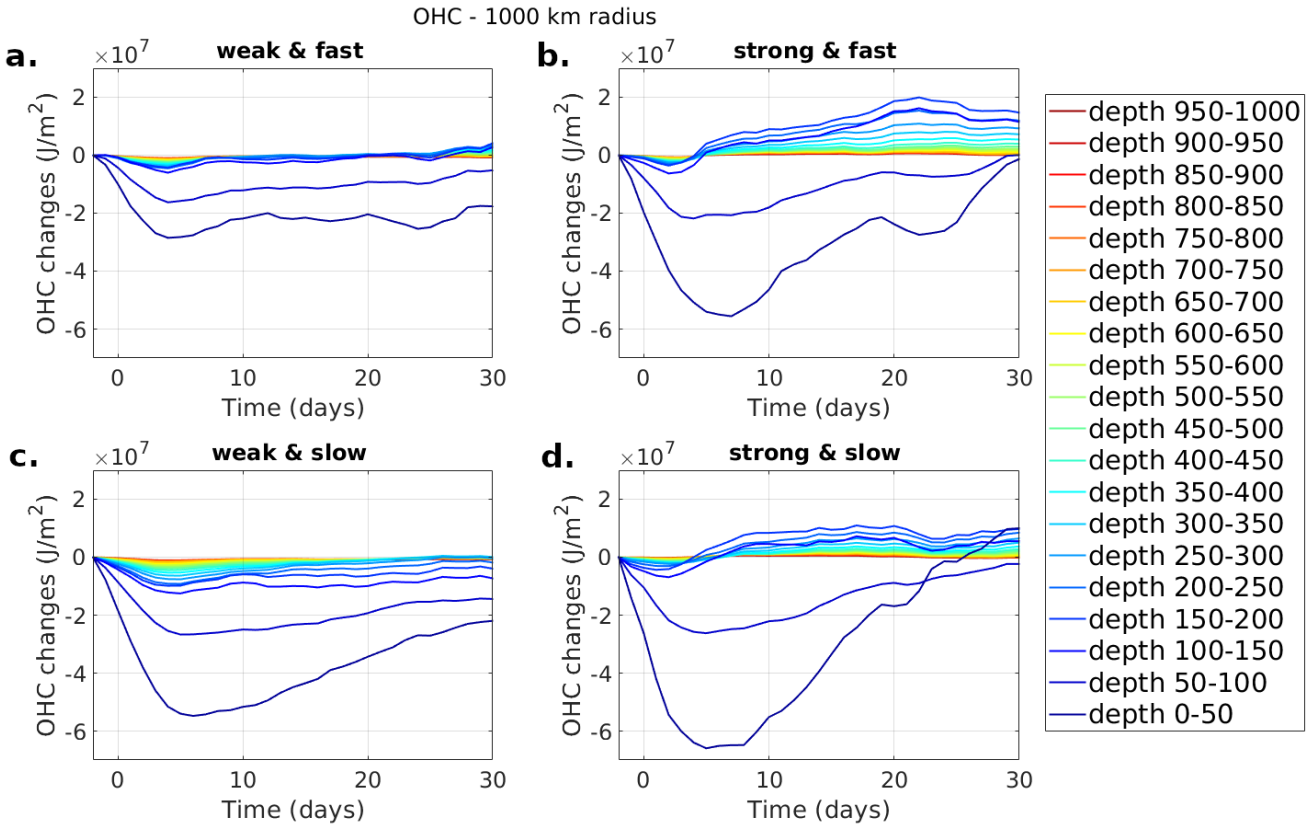

Figure 6.17: As in Fig. 6.15 for the whole region.

The OHC does not recover to pre-TC conditions by Day 30 for weak TCs regardless of their translation speed although weak and fast TCs come close (Fig. 6.16a and c). The OHC recovers for strong TCs and is positive by Day 30 (Fig. 6.16b and d). In fact, for strong TCs all 50-m layers below 100 m depth have developed positive OHC anomalies after Day 5 (Fig. 6.17b and d). During recovery, a larger OHC increase occurs above 100 m depth for strong and slow TCs and below 100 m depth for strong and fast TCs (Fig. 6.18b and d). These differences during recovery between the inner core and the whole region for TCs of different intensities and translation speeds are likely due to the different strengths of the processes happening at various distances from the track. In the outer region mixing drives positive anomalies during recovery below 100-m depth, which are much stronger for strong TCs and not significant for weak TCs. Conversely, within the inner core the recovery below 100 m depth is much stronger for slow-moving TCs (either weak or strong) as it is driven by restorative downwelling.

The OHC changes within a range of annuli bands for different translation speeds and categories are shown in Figs. 6.18 to 6.21. Within the 100-300 km band, the highest cooling from the surface to any depth develops in slow-moving TCs, especially strong TCs (Fig. 6.18), as upwelling is still a major cooling mechanism up to 400 km from the TC centre (Fig. 6.8). Interestingly, during recovery for fast and strong TCs the OHC below 150 m increases to become positive after Day 15 and continues increasing up through Day 30 (Fig. 6.18b). This is probably because strong and fast TCs are characterized by winds strong enough to produce significant mixing, but their residence time is not enough to establish strong upwelling and hence a major

subsurface cooling (Fig. 5.38a and b show less intense upward currents during the forcing stage in a narrower region for fast-moving TCs).

The OHC losses within the 300-500 km band are also higher for slow-moving TCs compared to fast-moving TCs (Fig. 6.19), which is similar to the inner core (Fig. 6.15) and to the 100-300 km band (Fig. 6.18), suggesting that Ekman upwelling is still a major driver out to ~500 km radius from the TC centre. However, during recovery there is a much larger subsurface OHC increase following strong TCs. In fact, strong TCs drive a fast recovery below 150 m, possibly due to the increased mixing between the surface and subsurface layer (Fig. 6.19b and d). The OHC anomalies below 150-m depth following strong and fast TCs become positive at Day 5 (Fig. 6.19b) and at Day 10 for strong and slow TCs (Fig. 6.19 b and d). Of interest, weak and fast TCs, which drive little Ekman pumping also recover to pre-TC conditions below 200 m by Day 30 in the 300-500 km band.

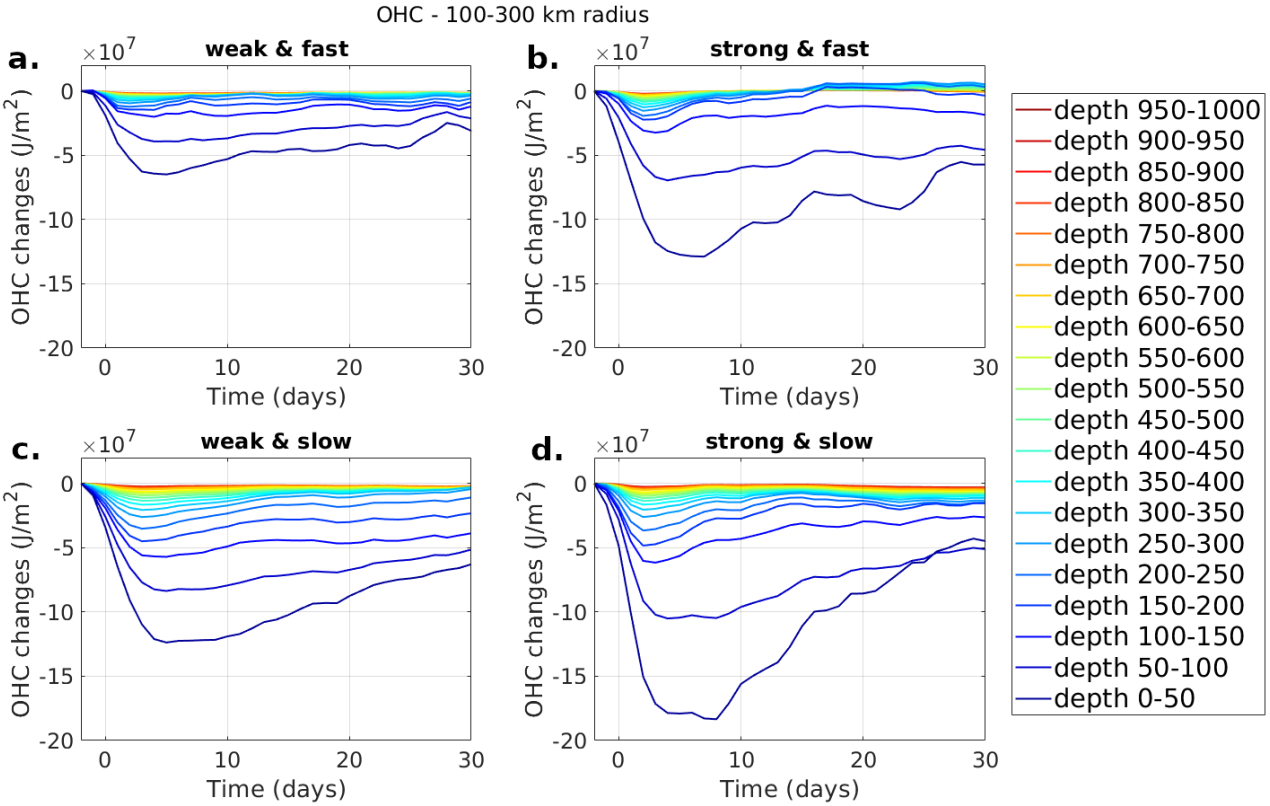

Figure 6.18: As in Fig 6.15 for the annulus between 100 and 300 km.

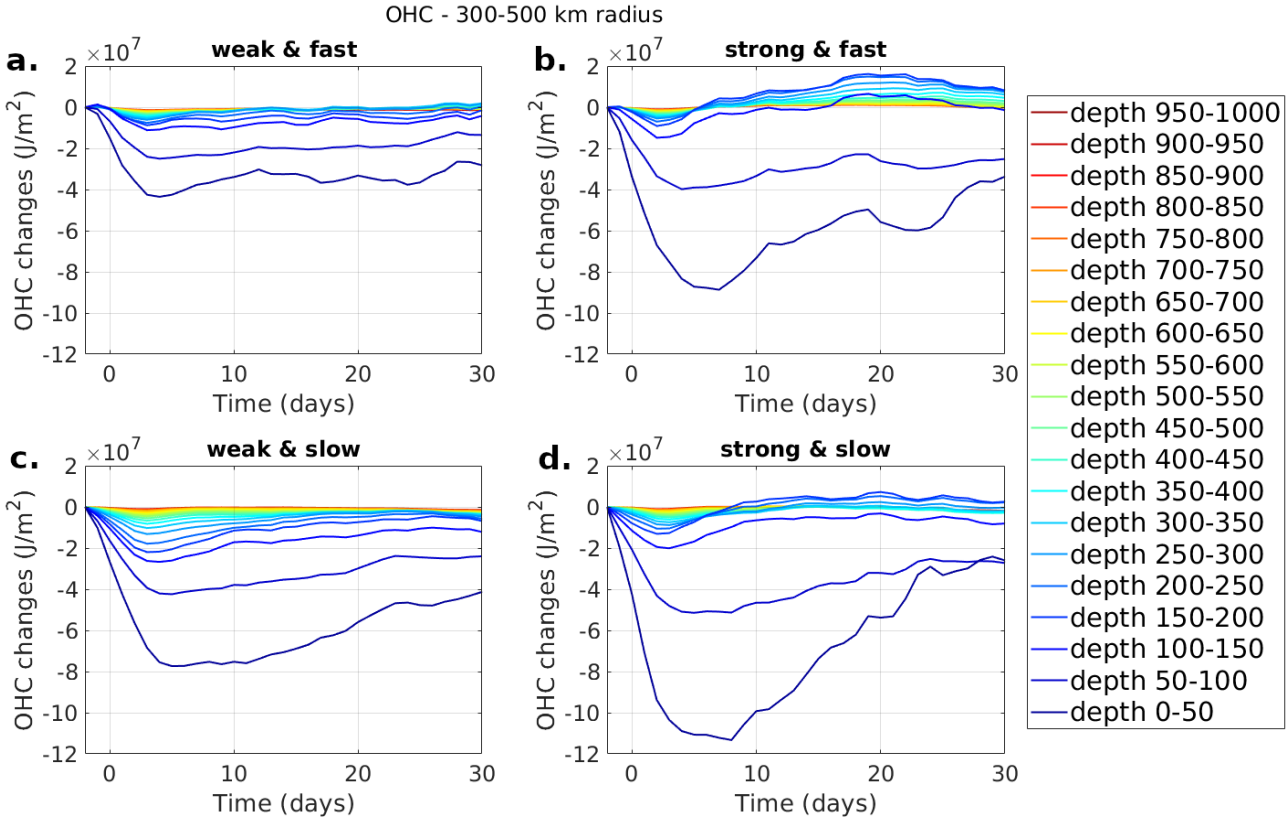

Figure 6.19: As in Fig 6.15 for the annulus between 300 and 500.

In the 500-700 km band the dominance of mixing processes over Ekman pumping become apparent particularly for the strong TCs with little change in the OHC below 100-m depth (Fig. 6.20). This is particularly evident for strong and slow TCs (Fig. 6.20d) where there is almost no difference in the OHC calculated between 0-100 and 0-2000 m. This indicates that all the OHC change in strong and slow TCs at these radii is occurring in the top 100 m of the ocean and is due to mixing. This compares with weak and slow TCs (Fig. 6.20c) where the OHC changes depending on the depth over which it is calculated suggesting that upwelling is affecting the OHC. The magnitude of OHC loss is also lower for strong TCs compared with the weak TCs at this radii (Fig. 6.20). Below 200 m depth, strong TCs, whether fast or slow develop positive OHC starting at Day 2 at all layers below 100-m depth (Fig. 6.21b, d) and are almost neutral (fast) or positive (slow) in the surface 100 m by Day 30 in this band. Weak TCs are also near zero or positive (Fig. 6.21a, c) below 100 m by Day 30. This happens as within this region mixing is the main driver of the OHC changes, and it is more efficient for fast-moving TCs and for strong TCs. This agrees with the positive SST anomalies that develop in the region further than 500 km on both sides of the track (Fig. 5.28b and d).

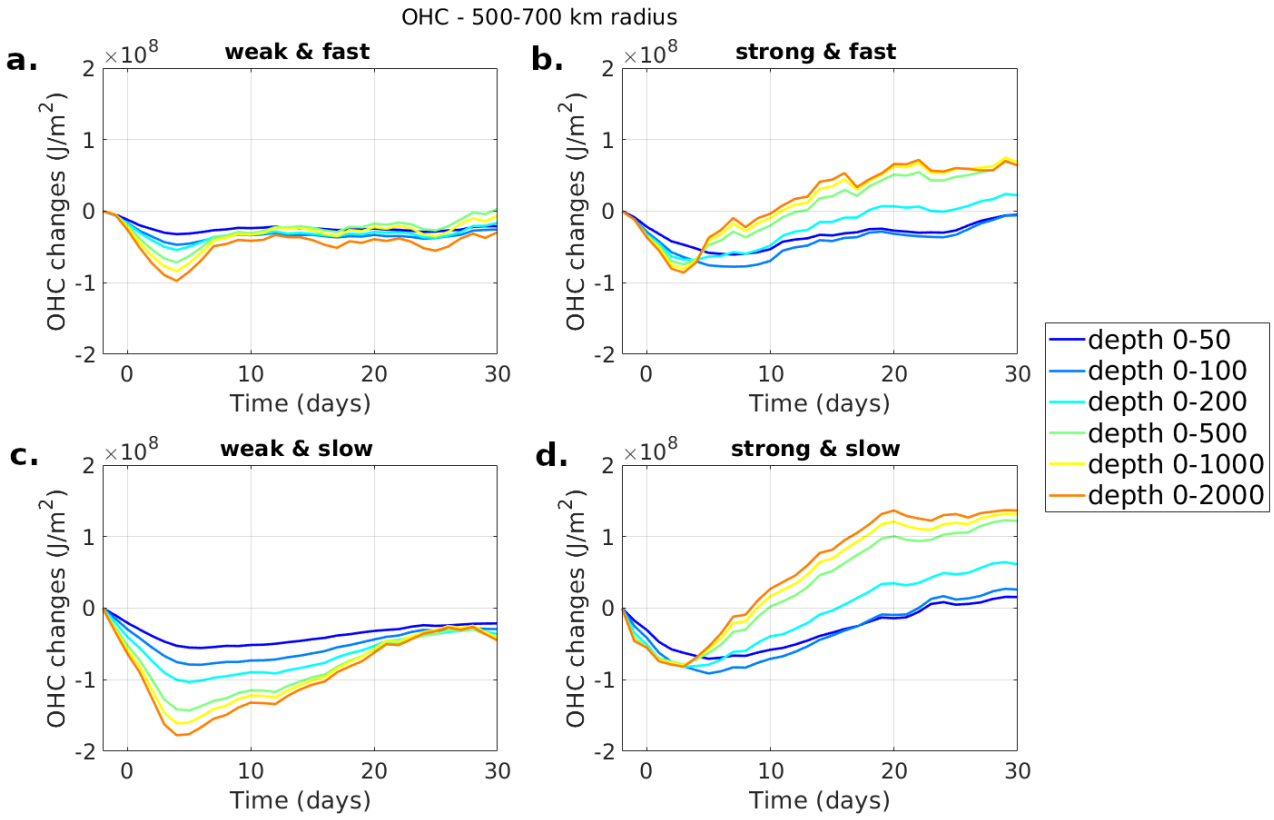

Figure 6.20: As in Fig 6.14 for the annulus between 500 and 700 km.

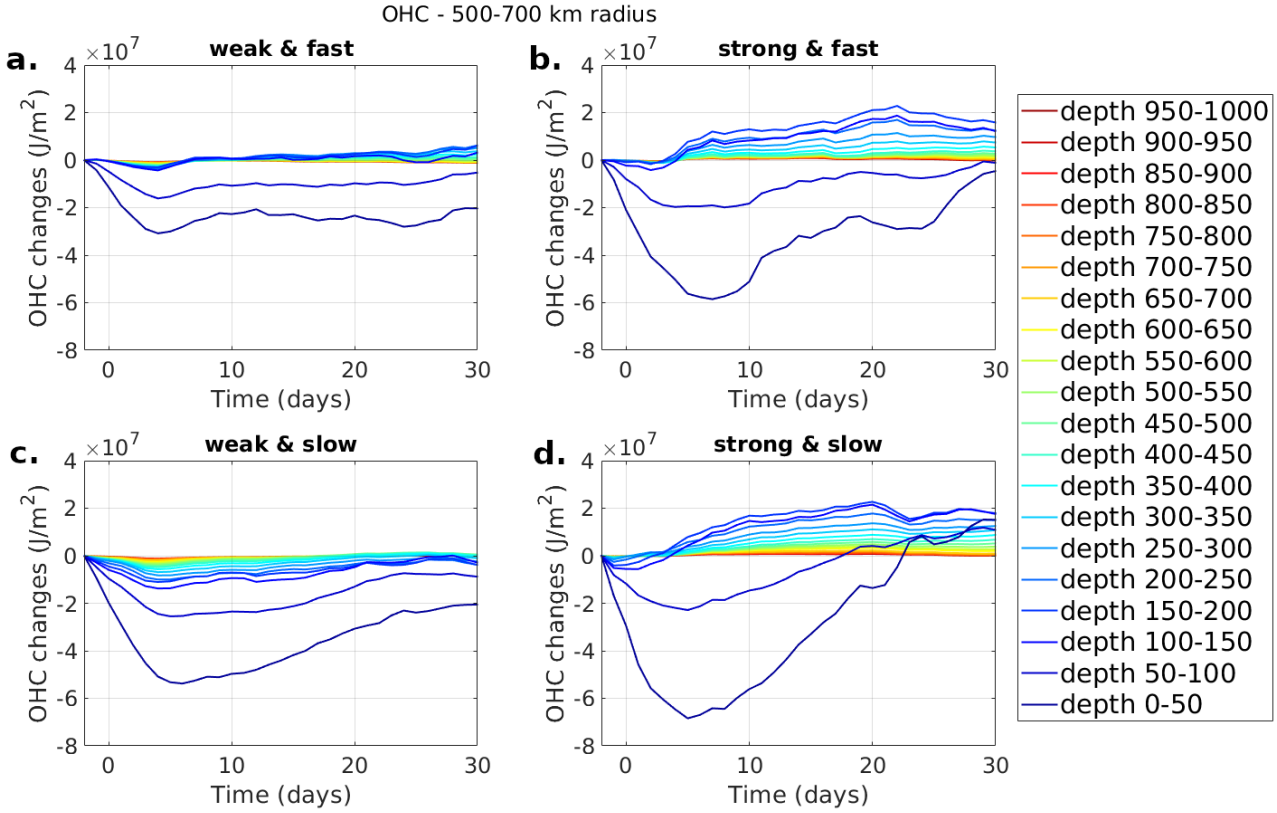

Figure 6.21: As in Fig 6.15 for the annulus between 500 and 700 km.

The OHC changes within the 700 to 1000 km outer annulus are similar to those for the 500-700 km band (not shown). Although weaker in magnitude, the OHC changes are similar in structure and follow the thesis that mixing processes dominate in the outer radii of the TC and downwelling drives positive temperature anomalies and positive OHC.

In summary, within 300 km of the TC centre, the OHC decreases more after the passage of slow TCs, followed by weak and slow then fast and strong TCs. Negative anomalies are greater for slow-moving TCs especially below 100 m, as TCs with longer residence time produce stronger upwelling and cool the subsurface more efficiently. Within these inner regions, the OHC in the ocean layer down to 2000 m does not recover to pre-TC conditions by Day 30 for any translation speed and intensity. However, when considering the 1000-km radius area, the OHC changes due to strong TCs recover and increase compared to pre-TC conditions before Day 30 through the ocean depth to 2000 m. Thus, strong TCs provide a positive energy input to the ocean, both at the surface and in the subsurface driven by processes both during the TC passage and up to at least 30 days after. In contrast, weak TCs result in a net negative OHC input into the ocean. The OHC increase in all TCs occurs because mixing processes become the dominant driver of temperature and hence OHC changes beyond 500 km from the TC centre. Mixing traps warm water in the subsurface while the corresponding decrease in the OHC in the surface layer recovers faster and becomes positive, likely driven by net heat flux.

6.5 Summary and discussion

In general, over the deep ocean in the North West of Australia the passage of a TC produces strong cooling that reduces the OHC within the inner core region due to a combination of mixing and strong upwelling driven by Ekman pumping. Outside of this inner-core region, the mixing dominates and OHC can increase below the mixed layer in the outer region. Overall, this provides a net neutral change in OHC in the top 1000-m depth within the whole region. An ocean heat budget in the first 500 m of the ocean demonstrated that the stronger cooling within the inner core is driven by upwelling beneath the TC centre and by vertical mixing, while within the outer regions the surface is cooled by vertical mixing and the subsurface is warmed by a combination of weak downwelling and mixing of warm surface water down. During recovery, defined as 5-30 days subsequent to the TC passage, the heat budget shows that both surface and subsurface OHC increase is driven by vertical mixing and heat fluxes over a large region on the right of track, while on the left of track, vertical mixing drives stronger warm anomalies in the subsurface. Beneath the TC centre, the initial upwelling changes to downwelling, which drives an increase in OHC during the recovery period. Horizontal advection appears to be generally warming the top 200 m of the ocean and cooling the water underneath. By Day 30, the overall effect from before the TC passage is a significant OHC increase in the subsurface at both sides of the track, which is stronger on the left, and a weak OHC decrease in a large surface region and in the water column beneath the TC centre.

Within the whole region, for TCs that occur during the warming season the OHC losses recover in the surface layer by Day 30 but not in the deeper layers, while

TCs occuring during the cooling season drive an OHC decrease at the surface and an increase in the subsurface layers. The overall effect of TC passage is OHC decrease during the warming season and OHC increase during the cooling season. Even though slow and strong TCs drive higher OHC losses during their passage, the OHC of the whole region increases within a month for strong TCs, while weak TCs drive an overall OHC decrease.

Overall, the results indicate that the OHC changes in the month following the TC passage drive an increase in the thermal energy of the whole region for strong TCs and for TCs that occur later in the season, when the ocean temperatures are already cooling but downwelling drives stronger subsurface warm anomalies. This may be important as TC characteristics and the period of the year may be influenced by the changing climate, and an increase of strong TCs or TCs later in the year due to the warming of the ocean could produce a positive feedback with further OHC increase.

Moreover, the higher OHC in the surface layer in the outer regions of strong TCs may contribute to the development of regional warming events such as MHWs similar to the 2012-2013 MHW discussed in Chapter 4, which was affected by the passage of two strong TCs, TC Narelle and TC Rusty. The OHC stored in the subsurface could be trapped for longer periods and either transported away from the region or be re-absorbed into the deepening ML during winter and warm the region in the following months. Under climate change, it is currently projected that there will likely be less TCs overall, but a higher frequency of the more intense TCs (Knutson et al., 2010; Mendelsohn et al., 2012; IPCC 2021) and this may have a positive impact on OHC in the ocean and drive a positive feedback.

Although our analysis provides a general description of how OHC is modified by TCs over Australia's North West Shelf and of the processes driving the changes, it has limitations. The choice of OHC averaging within column and annulus regions from the TC centre gives more weight to processes directly under the TC centre as it moves through the region than to the processes that occur on the sides. Moreover, the processes are not symmetric with respect to the TC track therefore the effect of asymmetry is not considered. BRAN reanalysis data are produced using the OFAM3 model, which does not have a mixing parameterization and atmospheric forcing specific for representing TCs , so a TC-specific model could provide higher confidence in the heat budget results. Furthermore, as the seasonal cycle is not removed for the OHC budget calculation, the results of the recovery stage could be influenced by seasonal processes that are not connected to TC passage, and that could not be fully averaged out by the composite.

Chapter 7. Conclusions and future work

The NWS of Australia is subject to extreme events, in particular MHWs and TCs. This thesis focused on studying the physical drivers of the summer 2012/2013 MHW and on the effect of TCs on the thermal energy budget of the region.

7.1 Part 1: The 2012/2013 marine heatwave

In Chapter 4, a numerical model based on ROMS is used to identify the hydrodynamic drivers of the summer 2012/2013 MHW on the inner shelf north of North West Cape, which happened during a non-canonical Ningaloo Niño (Feng et al., 2015). The MHW developed rapidly during December 2012 and lasted for more than 2 months, overcoming the threshold of twice the difference between the 90th percentile and the 30-year climatology in region 2 (Fig. 4.1), which defined it as a "strong" MHW, for a week at the end of February 2013. A heat budget analysis, comparing summer 2012/2013 to a 7-year model climatology, suggests that the increase in air-sea heat flux and positive advection anomalies were the major causes leading to the development of the MHW during December. During January and February, a decrease of advective cooling and a decrease in vertical mixing (which normally entrains colder water up) compared to the climatology contributed to maintain the warm anomalies. The delayed onset of the Australian monsoon, which usually begins around December 13, could have contributed to the onset of the MHW. In fact, weaker north-easterly winds during December 2012 forced an anomalous south-westward flow over the NWS, bringing warmer northern waters to the region. The reduced wind speed

produced stronger stratification and a shallower MLD during summer 2012/2013, which contributed to reduce the cooling effect from the vertical mixing. The SLP anomalies pattern over the NWS during December could correspond to a locally amplified Ningaloo Niño described by Kataoka et al. (2014), which happens when warm SST anomalies produce low SLP anomalies, triggering northerly wind anomalies that cause downwelling anomalies and further increase warming.

7.2 Part 2: Effect of tropical cyclones on the ocean thermal balance

The effect of TCs on the ocean thermal balance is analysed in Chapter 5, with a focus on the development of temperature anomalies and TC-induced vertical currents, and in Chapter 6, which focuses on the OHC changes following the passage of a TC. Our analysis is based on a 20-year composite and shows that following the passage of a TC cold temperatures anomalies develop over a wide region at the ocean surface and at depth underneath the track, while warm anomalies develop in the subsurface at the two sides of the track, stronger on the left of it. The extensive cooling through the water column in the region underneath the TC centre appears to be driven by strong divergent surface currents which produce Ekman upwelling. On the sides of the track, the surface cooling with subsurface warming is caused by vertical mixing generated by the strong TC winds, which drives MLD entrainment. The recovery of the cold anomalies at the surface is driven by air-sea heat fluxes and beneath the TC centre, the cold anomalies at depth recovers thanks to weak but persistent downwelling, while the warm anomalies to the side of the track take longer to recover and are still present one month after the TC passage.

Compared to TCs over the deep ocean, TCs over the continental shelf drive stronger cold anomalies at the surface over a larger area, with stronger vertical currents underneath. The direction of motion of the TCs over the shelf can further impact the development of currents on the shelf and, thus, influence the temperature anomalies, which are colder at depth for TCs moving parallel to the coast moving south-westward. TC data points over the deep ocean that move south-westward parallel to the coast are also impacted by the presence of the shelf edge as they trigger stronger warm anomalies on the left of their track near the coast, where the interaction between the TC winds and the coast drives Ekman downwelling. The recovery of the temperature anomalies differs between TCs occuring earlier in the season, when the solar radiation is stronger and the surface cold anomalies recover faster, and TCs occuring later in the season, when the general downward vertical currents help a faster recovery of the cold anomalies at depth. The development of the temperature anomalies is affected by the intensity and translation speed of the TC data points, as slow-moving and strong TC data points drive colder temperature anomalies over a wider region. As their residence time is longer, upwelling is enhanced for slow-moving TC data points, which produces stronger cold anomalies at depth beneath the track. The presence of a deep barrier layer before the passage of the TC can inhibit mixing and reduces the development of cold anomalies at surface, especially for fast-moving and strong TC.

In Chapter 6 the 20-year composite of the OHC changes in regions of different size around the TC centre is analysed for TC data points over the deep ocean. The results show that in general the OHC of the region within 1000 km from the TC location for a layer of 500 m depth from the surface recovers after a month from the TC passage. This happens because, although within the inner core regions cold

anomalies are not completely recovered by Day 30, within the outer region the subsurface OHC increases following the passage of the TC and balances the heat losses of the core region. A heat budget calculation shows that upwelling drives the strong cooling within the inner core region, while vertical mixing and MLD entrainment drive the OHC losses at the surface and OHC increase in the subsurface within the outer region. The recovery appears to be driven by downwelling beneath the track and vertical mixing over a large region at the surface and subsurface right of the track, while on the left of the track the MLD keeps entraining and the surface continues to cool as the subsurface warms more. After a month from the TC passage, the OHC of the surface layers is increased for TCs earlier in the season and decreased for TCs occuring during the cooling season. However, TCs later in the season drive an increase of the OHC in the subsurface layers, which overwhelms the surface cooling when considering the top 500 m of the ocean. Within the whole region the effect of the TC intensity appears to be greater than TC translation speed as one month after the TC passage strong TCs drive a strong increase in the OHC through the ocean depth, while weak TCs result in a reduction of the OHC of the region.

7.3 Limitations of this study and possible future research

Chapter 4 presents an extensive analysis on the processes leading to the development of the summer 2012/2013 MHW over the NWS of Australia. However, our work has some limitations, and it could be improved with further studies. The 2012/2013 MHW happened during a non-canonical locally amplified Ningaloo Niño. To better capture the ocean-atmosphere feedbacks that led to the development of the

Ningaloo Niño and the influence of remote wind forcing from the Kimberly coast that drove the MHW, a regional coupled ocean-atmosphere model may be more suitable. A coupled model extending to include a larger region could allow to further research on the large-scale drivers of a delayed monsoon onset. Moreover, further research could investigate in more detail the decaying period of the MHW and its causes. The potential cooling influence of TCs Narelle and Rusty on the warm temperature anomalies that developed during the MHW could be investigated in further studies, especially as the decay of the MHW happened concurrently to the passage of TC Rusty and a subsequent upwelling event.

Part 2 provides further knowledge on the effect of the passage of TCs over the north-western region of Australia on the thermal balance of the ocean, using a composite approach with BRAN data. The main limitation of BRAN data is the daily temporal resolution, which does not allow a detailed study of the near-inertial currents that develop following the passage of a TC and of the internal waves produced from the interaction of the TC-induced currents with the shelf edge. Future studies could focus on further analysing the processes that happen at shorter time scales, with higher temporal resolution data, and allow the analysis to be conducted in terms of inertial periods in order to focus more on the ocean dynamics. In addition, the coarse spatial resolution of BRAN limits the analysis, especially for locations over the shelf and a model with finer resolution could reproduce better the interaction between coastal currents and shallow bathymetry with TC induced currents. High resolution ocean modelling of the atmosphere-ocean interaction due to TC passage should be done over many TC intensities and over both the deep ocean and over the shelf in the NWS region in order to investigate the importance of the mixing and the interaction between

TC-induced currents and the coastal processes occurring over the shelf edge. Furthermore, the use of a model that includes TC specific parameterization for wave turbulence and a different drag formulation during high winds can improve ocean simulations under TC conditions (Hwang, 2018; Stoney et al., 2017; Stoney et al., 2018).

Moreover, we focused on a composite study, but analysis of specific TCs could provide further insight on how specific TC characteristics impact the ocean over the NWS, and would enable a focus on the interaction between the TC induced currents and the eddies present over the region. In particular, focusing on case studies over the shelf region could help understand better the interactions between the direction of movement of the TC and the underlying bathymetry and coastal currents.

A further OHC budget study with a TC- specific ocean model to analyse in more detail the processes leading to the development of OHC anomalies in the region could lead to further insights. A NWS model able to fully capture the effects of the passage of a TC could allow to investigate how the subsurface OHC increases caused by the passage of a strong TC evolve in a longer period after the TC passage. In fact, whether the subsurface warm anomalies are released back to the atmosphere during the winter following the TC passage or are trapped in the ocean for longer, and if they are transported away from the region, is still unknown.

Climate change could impact TC activity and it is predicted that as the ocean temperatures increase, the frequency of intense TCs will increase in the future (Knutson et al., 2010; Webster et al., 2005). Our study shows that strong TCs drive an increase in the OHC of a large region around the track after a month from their passage

while weak TCs drive a decrease in the OHC. This could lead to a positive feedback mechanism, if the frequency of strong TCs increases in the future. Moreover, if the translation speed of TCs decreases in the future (Hassim and Walsh, 2008; Kossin 2018), TCs could also lead to an increase in upwelling events. Further studies on the effect of TCs over the ocean over the NWS region in different climate change scenarios could be crucial to be able to protect the unique environment of the region.

References

Acil Tasman Ltd, 2009. Nation builder: how the North West Shelf Project has driven economic transformation in Australia. ACIL Tasman, Melbourne.

Aijaz, S., Kepert, J. D., Ye, H., Huang, Z., & Hawksford, A. (2019). Bias Correction of Tropical Cyclone Parameters in the ECMWF Ensemble Prediction System in Australia. *Monthly Weather Review*, 147(11), 4261-4285.

Andreas, E. L., & Emanuel, K. A. (2001). Effects of sea spray on tropical cyclone intensity. *Journal of the atmospheric sciences*, 58(24), 3741-3751.Bahmanpour, M. H., Pattiaratchi, C., Wijeratne, E. S., Steinberg, C., & D'Adamo, N. (2016). Multi-year observation of Holloway current along the shelf edge of north western Australia. *Journal of Coastal Research*, (75), 517-521.

Balaguru, K., Foltz, G. R., Leung, L. R., Asaro, E. D., Emanuel, K. A., Liu, H., & Zedler, S. E. (2015). Dynamic potential intensity: An improved representation of the ocean's impact on tropical cyclones. *Geophysical Research Letters*, 42(16), 6739-6746.

Barnier, B., Siefridt, L., & Marchesiello, P. (1995). Thermal forcing for a global ocean circulation model using a three-year climatology of ECMWF analyses. *Journal of Marine Systems*, 6(4), 363-380.

Benthuysen, J., Feng, M., & Zhong, L. (2014). Spatial patterns of warming off Western Australia during the 2011 Ningaloo Niño: quantifying impacts of remote and local forcing. *Continental Shelf Research*, 91, 232-246.

BOM 2012: Madden-Julian Oscillation (MJO). http://www.bom.gov.au/climate/mjo/, accessed 8 April 2020.

BOM 2013a: Bureau of Meteorology Seasonal Climate Summary for Northern Territory. http://www.bom.gov.au/climate/current/season/nt/archive/201304.summary.shtml, accessed 30 March 2020.

Bueti, M. R., Ginis, I., Rothstein, L. M., & Griffies, S. M. (2014). Tropical cyclone–induced thermocline warming and its regional and global impacts. *Journal of Climate*, *27*(18), 6978-6999.

C3S, Copernicus Climate Change Service (2017). "ERA5: Fifth Generation of ECMWF Atmospheric Reanalyses of the Global Climate. Copernicus Climate Change Service Climate Data Store (CDS)." https://cds.climate.copernicus.eu/cdsapp#!/home

Caputi, N., Feng, M., Pearce, A., Benthuysen, J., Denham, A., Hetzel, Y., ... & Chandrapavan, A. (2015). Management implications of climate change effect on fisheries in Western Australia Part 1: Environmental change and risk assessment. *FRDC Project*, (2010/535).

Chapman, D. C. (1985). Numerical treatment of cross-shelf open boundaries in a barotropic coastal ocean model. *Journal of Physical oceanography*, 15(8), 1060-1075.

Chaudhuri, D., Sengupta, D., D'Asaro, E., Venkatesan, R., & Ravichandran, M. (2019). Response of the salinity-stratified Bay of Bengal to cyclone Phailin. *Journal of Physical Oceanography*, 49(5), 1121-1140.

Cheng, L., Zhu, J., & Sriver, R. L. (2015). Global representation of tropical cyclone-induced short-term ocean thermal changes using Argo data. *Ocean Science*, 11(5).

Chi, N. H., Lien, R. C., D'Asaro, E. A., & Ma, B. B. (2014). The surface mixed layer heat budget from mooring observations in the central Indian Ocean during Madden–Julian Oscillation events. *Journal of Geophysical Research: Oceans*, 119(7), 4638-4652.

Chiang, T. L., Wu, C. R., & Oey, L. Y. (2011). Typhoon Kai-Tak: An ocean's perfect storm. *Journal of Physical Oceanography*, *41*(1), 221-233.

Clarke, A. J., & Liu, X. (1994). Interannual sea level in the northern and eastern Indian Ocean. *Journal of Physical Oceanography*, *24*(6), 1224-1235.

Condie, S., & Andrewartha, J. (2008). Circulation and connectivity on the Australian North West Shelf. *Continental Shelf Research*, 28, 1724-1739.

Cresswell, G. R., & Golding, T. J. (1980). Observations of a south-flowing current in the southeastern Indian Ocean. *Deep Sea Research Part A. Oceanographic Research Papers*, 27(6), 449-466.

Cresswell, G., Frische, A., Peterson, J., & Quadfasel, D. (1993). Circulation in the Timor Sea. *Journal of Geophysical Research: Oceans*, 98(C8), 14379-14389.

D'Adamo, N., Fandry, C., Buchan, S., & Domingues, C. (2009). Northern sources of the Leeuwin current and the "Holloway Current" on the North West Shelf. *Journal of the Royal Society of Western Australia*, 92, 53-66.

D'Asaro, E. A. (2003). The ocean boundary layer below Hurricane Dennis. *Journal of Physical Oceanography*, 33(3), 561-579.

D'Asaro, E. A., Sanford, T. B., Niiler, P. P., & Terrill, E. J. (2007). Cold wake of hurricane Frances. *Geophysical Research Letters*, 34(15).

Dare, R. A., & McBride, J. L. (2011). Sea surface temperature response to tropical cyclones. *Monthly Weather Review*, *139*(12), 3798-3808.

Davidson, F. J., & Holloway, P. E. (2003). A study of tropical cyclone influence on the generation of internal tides. *Journal of Geophysical Research: Oceans*, *108*(C3).

De'ath, G., Fabricius, K. E., Sweatman, H., & Puotinen, M. (2012). The 27–year decline of coral cover on the Great Barrier Reef and its causes. *Proceedings of the National Academy of Sciences*, *109*(44), 17995-17999.

Di Lorenzo, E., & Mantua, N. (2016). Multi-year persistence of the 2014/15 North Pacific marine heatwave. *Nature Climate Change*, *6*(11), 1042-1047.

Doi, T., Behera, S. K., & Yamagata, T. (2013). Predictability of the Ningaloo Niño/Niña. *Scientific reports*, 3(1), 1-7.

Doi, T., Behera, S. K., & Yamagata, T. (2015). An interdecadal regime shift in rainfall predictability related to the Ningaloo Niño in the late 1990s. *Journal of Geophysical Research: Oceans*, 120(2), 1388-1396.

Domingues, C. M., Maltrud, M. E., Wijffels, S. E., Church, J. A., & Tomczak, M. (2007). Simulated Lagrangian pathways between the Leeuwin Current System and the upper-ocean circulation of the southeast Indian Ocean. *Deep Sea Research Part II: Topical Studies in Oceanography*, 54(8-10), 797-817.

Dufois, F., Lowe, R. J., Branson, P., & Fearns, P. (2017). Tropical Cyclone-Driven Sediment Dynamics Over the Australian North West Shelf. *Journal of Geophysical Research: Oceans*, *122*(12), 10225-10244.

Dufois, F., Lowe, R. J., Rayson, M. D., & Branson, P. M. (2018). A Numerical Study of Tropical Cyclone-Induced Sediment Dynamics on the Australian North West Shelf. *Journal of Geophysical Research: Oceans*, *123*(8), 5113-5133.

Dee, D. P., Uppala, S. M., Simmons, A. J., Berrisford, P., Poli, P., Kobayashi, S., ... & Vitart, F. (2011). The ERA-Interim reanalysis: Configuration and performance of the data assimilation system. *Quarterly Journal of the royal meteorological society*, 137(656), 553-597.

Egbert, G. D., & Erofeeva, S. Y. (2002). Efficient inverse modeling of barotropic ocean tides. *Journal of Atmospheric and Oceanic Technology*, 19(2), 183-204.

Egbert, G. D., Bennett, A. F., & Foreman, M. G. (1994). TOPEX/POSEIDON tides estimated using a global inverse model. *Journal of Geophysical Research: Oceans*, 99(C12), 24821-24852.

Egbert, G. D., & Ray, R. D. (2000). Significant dissipation of tidal energy in the deep ocean inferred from satellite altimeter data. *Nature*, *405*(6788), 775-778.

Eliot, M., & Pattiaratchi, C. (2010). Remote forcing of water levels by tropical cyclones in southwest Australia. *Continental Shelf Research*, *30*(14), 1549-1561.

Emanuel, K. (2001). Contribution of tropical cyclones to meridional heat transport by the oceans. *Journal of Geophysical Research: Atmospheres*, *106*(D14), 14771-14781.

Feng, M., Colberg, F., Slawinski, D., Berry, O., & Babcock, R. (2016). Ocean circulation drives heterogeneous recruitments and connectivity among coral populations on the North West Shelf of Australia. *Journal of Marine Systems*, 164, 1-12.

Feng, M., Hendon, H. H., Xie, S. P., Marshall, A. G., Schiller, A., Kosaka, Y., ... & Pearce, A. (2015). Decadal increase in Ningaloo Niño since the late 1990s. *Geophysical Research Letters*, 42(1), 104-112.

Feng, M., McPhaden, M. J., Xie, S. P., & Hafner, J. (2013). La Niña forces unprecedented Leeuwin Current warming in 2011. *Scientific reports*, 3, 1277.

Feng, M., Biastoch, A., Böning, C., Caputi, N., & Meyers, G. (2008). Seasonal and interannual variations of upper ocean heat balance off the west coast of Australia. *Journal of Geophysical Research: Oceans*, 113(C12).

Feng, M., Meyers, G., Pearce, A., & Wijffels, S. (2003). Annual and interannual variations of the Leeuwin Current at 32 S. *Journal of Geophysical Research: Oceans*, 108(C11).

Flather, R. A., & Heaps, N. S. (1975). Tidal computations for morecambe bay. *Geophysical Journal International*, 42(2), 489-517.

Flather, R. A. (1976). Results from a storm surge prediction model of the north-west European continental shelf for April, November and December, 1973.

Frölicher, T. L., Fischer, E. M., & Gruber, N. (2018). Marine heatwaves under global warming. *Nature*, *560*(7718), 360-364.

Garrabou, J., Coma, R., Bensoussan, N., Bally, M., Chevaldonné, P., Cigliano, M., ... & Ledoux, J. B. (2009). Mass mortality in Northwestern Mediterranean rocky benthic communities: effects of the 2003 heat wave. *Global change biology*, *15*(5), 1090-1103.

Ginis, I. (2002). Tropical cyclone-ocean interactions. *Advances in Fluid Mechanics*, *33*, 83-114.

Glenn, S. M., Miles, T. N., Seroka, G. N., Xu, Y., Forney, R. K., Yu, F., ... & Kohut, J. (2016). Stratified coastal ocean interactions with tropical cyclones. *Nature communications*, *7*(1), 1-10.

Godfrey, J. S., & Ridgway, K. R. (1985). The large-scale environment of the poleward-flowing Leeuwin Current, Western Australia: longshore steric height gradients, wind stresses and geostrophic flow. *Journal of Physical Oceanography*, 15(5), 481-495.

Haakman, K., Sayol, J. M., van der Boog, C. G., & Katsman, C. A. (2019). Statistical Characterization of the Observed Cold Wake Induced by North Atlantic Hurricanes. *Remote Sensing*, *11*(20), 2368.

Harper, B. A., Stroud, S. A., McCormack, M., & West, S. (2008). A review of historical tropical cyclone intensity in northwestern Australia and implications for climate change trend analysis. *Australian Meteorological Magazine*, *57*(2), 121-141.

Hart, R. E., Maue, R. N., & Watson, M. C. (2007). Estimating local memory of tropical cyclones through MPI anomaly evolution. *Monthly Weather Review*, *135*(12), 3990-4005.

Hassim, M. E., & Walsh, K. J. (2008). Tropical cyclone trends in the Australian region. *Geochemistry, Geophysics, Geosystems*, *9*(7).

Hobday, A. J., Alexander, L. V., Perkins, S. E., Smale, D. A., Straub, S. C., Oliver, E. C., ... & Holbrook, N. J. (2016). A hierarchical approach to defining marine heatwaves. *Progress in Oceanography*, 141, 227-238.

Hobday, A. J., Oliver, E. C., Gupta, A. S., Benthuysen, J. A., Burrows, M. T., Donat, M. G., ... & Smale, D. A. (2018). Categorizing and naming marine heatwaves. *Oceanography*, 31(2), 162-173.

Holloway, P. E. (1983). Internal tides on the Australian North-West Shelf: a preliminary investigation. *Journal of Physical Oceanography*, *13*(8), 1357-1370.

Holloway, P. E. (1984). On the semidiurnal internal tide at a shelf-break region on the Australian North West Shelf. *Journal of Physical Oceanography*, *14*(11), 1787-1799.

Holloway, P. E. (1995). Leeuwin current observations on the Australian north west shelf, May–June 1993. *Deep Sea Research Part I: Oceanographic Research Papers*, 42(3), 285-305.

Holloway, P. E. (2001). A regional model of the semidiurnal internal tide on the Australian North West Shelf. *Journal of Geophysical Research: Oceans*, *106*(C9), 19625-19638.

Holloway, P. E., & Nye, H. C. (1985). Leeuwin Current and wind distributions on the southern part of the Australian North West Shelf between January 1982 and July 1983. *Marine and Freshwater Research*, *36*(2), 123-137.

Huang, P., Sanford, T. B., & Imberger, J. (2009). Heat and turbulent kinetic energy budgets for surface layer cooling induced by the passage of Hurricane Frances (2004). *Journal of Geophysical Research: Oceans*, *114*(C12).

Hwang, P. A. (2018). High-wind drag coefficient and whitecap coverage derived from microwave radiometer observations in tropical cyclones. *Journal of Physical Oceanography*, 48(10), 2221-2232.

IMOS. 2019. “Current Velocity Time Series.”. https://portal.aodn.org.au/search

IMOS. 2020. “Argo profiles.”. https://portal.aodn.org.au/search

Jacob, S. D., Shay, L. K., Mariano, A. J., & Black, P. G. (2000). The 3D oceanic mixed layer response to Hurricane Gilbert. *Journal of Physical Oceanography*, *30*(6), 1407-1429.

Jaimes, B., & Shay, L. K. (2015). Enhanced wind-driven downwelling flow in warm oceanic eddy features during the intensification of Tropical Cyclone Isaac

(2012): Observations and theory. *Journal of Physical Oceanography*, *45*(6), 1667-1689.

Jaimes, B., Shay, L. K., & Halliwell, G. R. (2011). The response of quasigeostrophic oceanic vortices to tropical cyclone forcing. *Journal of physical oceanography*, *41*(10), 1965-1985.

Jansen, M., & Ferrari, R. (2009). Impact of the latitudinal distribution of tropical cyclones on ocean heat transport. *Geophysical Research Letters*, *36*(6).

Jansen, M. F., Ferrari, R., & Mooring, T. A. (2010). Seasonal versus permanent thermocline warming by tropical cyclones. *Geophysical Research Letters*, *37*(3).

Jayne, S. R., Roemmich, D., Zilberman, N., Riser, S. C., Johnson, K. S., Johnson, G. C., & Piotrowicz, S. R. (2017). The Argo program: present and future. *Oceanography*, 30(2), 18-28.

Jullien, S., Menkès, C. E., Marchesiello, P., Jourdain, N. C., Lengaigne, M., Koch-Larrouy, A., ... & Faure, V. (2012). Impact of tropical cyclones on the heat budget of the South Pacific Ocean. *Journal of Physical Oceanography*, *42*(11), 1882-1906.

Kajikawa, Y., Wang, B., & Yang, J. (2010). A multi-time scale Australian monsoon index. *International Journal of Climatology*, 30(8), 1114-1120.

Kataoka, T., Masson, S., Izumo, T., Tozuka, T., & Yamagata, T. (2018). Can Ningaloo Niño/Niña Develop Without El Niño–Southern Oscillation?. *Geophysical Research Letters*, 45(14), 7040-7048.

Kataoka, T., Tozuka, T., Behera, S., & Yamagata, T. (2014). On the Ningaloo Niño/Niña. *Climate dynamics*, 43(5-6), 1463-1482.

Kataoka, T., Tozuka, T., & Yamagata, T. (2017). Generation and decay mechanisms of Ningaloo Niño/Niña. *Journal of Geophysical Research: Oceans*, 122(11), 8913-8932.

Katsumata, K. (2006). Tidal stirring and mixing on the Australian North West Shelf. *Marine and Freshwater Research, 57*(3), 243-254.

Knutson, T. R., McBride, J. L., Chan, J., Emanuel, K., Holland, G., Landsea, C., ... & Sugi, M. (2010). Tropical cyclones and climate change. *Nature geoscience, 3*(3), 157-163.

Kossin, J. P. (2018). A global slowdown of tropical-cyclone translation speed. *Nature, 558*(7708), 104-107.

Kusunoki, H., Kido, S., & Tozuka, T. (2020). Contribution of oceanic wave propagation from the tropical Pacific to asymmetry of the Ningaloo Niño/Niña. *CLIMATE DYNAMICS*, 54(11-12), 4865-4875.

Lafratta, A., Fromont, J., Speare, P., & Schönberg, C. H. L. (2017). Coral bleaching in turbid waters of north-western Australia. *Marine and Freshwater Research, 68*(1), 65-75.

Large, W. G., McWilliams, J. C., & Doney, S. C. (1994). Oceanic vertical mixing: A review and a model with a nonlocal boundary layer parameterization. Reviews of Geophysics, 32(4), 363-403.

Lee, T., Fukumori, I., & Tang, B. (2004). Temperature advection: Internal versus external processes. *Journal of physical oceanography*, 34(8), 1936-1944.

Lin, I. I., Pun, I. F., & Wu, C. C. (2009). Upper-ocean thermal structure and the western North Pacific category 5 typhoons. Part II: Dependence on translation speed. *Monthly Weather Review, 137*(11), 3744-3757.

Lin, I. I., Wu, C. C., Pun, I. F., & Ko, D. S. (2008). Upper-ocean thermal structure and the western North Pacific category 5 typhoons. Part I: Ocean features and the category 5 typhoons' intensification. *Monthly Weather Review, 136*(9), 3288-3306.

Lin, S., Zhang, W. Z., Shang, S. P., & Hong, H. S. (2017). Ocean response to typhoons in the western North Pacific: Composite results from Argo data. *Deep Sea Research Part I: Oceanographic Research Papers, 123*, 62-74.

Lorbacher, K., Dommenget, D., Niiler, P. P., & Köhl, A. (2006). Ocean mixed layer depth: A subsurface proxy of ocean-atmosphere variability. *Journal of Geophysical Research: Oceans*, 111(C7).

Marchesiello, P., McWilliams, J. C., & Shchepetkin, A. (2003). Equilibrium structure and dynamics of the California Current System. *Journal of physical Oceanography*, 33(4), 753-783.

Maxime, M., & Ming, F. (2019). Intra-annual variability of the North West Shelf of Australia and its impact on the Holloway Current: Excitement and propagation of coastally trapped waves. *Continental Shelf Research*, 186, 88-103.

Marshall, A. G., Hendon, H. H., Feng, M., & Schiller, A. (2015). Initiation and amplification of the Ningaloo Niño. *Climate dynamics*, 45(9-10), 2367-2385.

Marshall, A. G., & Hendon, H. H. (2014). Impacts of the MJO in the Indian Ocean and on the Western Australian coast. *Climate dynamics*, 42(3-4), 579-595.

Mei, W., Lien, C. C., Lin, I. I., & Xie, S. P. (2015). Tropical cyclone–induced ocean response: A comparative study of the South China Sea and tropical northwest Pacific. *Journal of Climate*, *28*(15), 5952-5968.

Mei, W., & Pasquero, C. (2012). Restratification of the upper ocean after the passage of a tropical cyclone: A numerical study. *Journal of physical oceanography*, *42*(9), 1377-1401.

Mei, W., & Pasquero, C. (2013). Spatial and temporal characterization of sea surface temperature response to tropical cyclones. *Journal of Climate*, *26*(11), 3745-3765.

Mendelsohn, R., Emanuel, K., Chonabayashi, S., & Bakkensen, L. (2012). The impact of climate change on global tropical cyclone damage. *Nature climate change*, *2*(3), 205-209.

Merchant, C. J., Embury, O., Bulgin, C. E., Block, T., Corlett, G. K., Fiedler, E., ... & Eastwood, S. (2019). Satellite-based time-series of sea-surface temperature since 1981 for climate applications. *Scientific data*, 6(1), 1-18.

Meyers, G., Bailey, R. J., & Worby, A. P. (1995). Geostrophic transport of Indonesian throughflow. *Deep Sea Research Part I: Oceanographic Research Papers*, *42*(7), 1163-1174.

Mills, K. E., Pershing, A. J., Brown, C. J., Chen, Y., Chiang, F. S., Holland, D. S., ... & Wahle, R. A. (2013). Fisheries management in a changing climate: lessons from the 2012 ocean heat wave in the Northwest Atlantic. *Oceanography*, *26*(2), 191-195.

Mitchell, D. A., Teague, W. J., Jarosz, E., & Wang, D. W. (2005). Observed currents over the outer continental shelf during Hurricane Ivan. *Geophysical research letters*, 32(11).

Mrvaljevic, R. K., Black, P. G., Centurioni, L. R., Chang, Y. T., D'Asaro, E. A., Jayne, S. R., ... & Sanford, T. B. (2013). Observations of the cold wake of Typhoon Fanapi (2010). *Geophysical Research Letters*, 40(2), 316-321.

Nguyen, K., Hu, L., Alenin, A., Ritchie, E., & Tyo, S. (2021). A satellite-based remote-sensing framework to quantify the upwelling radiation due to tropical cyclones. *IEEE Journal of Selected Topics in Applied Earth Observations and Remote Sensing.*

Oey, L. Y., Ezer, T., Wang, D. P., Fan, S. J., & Yin, X. Q. (2006). Loop current warming by Hurricane Wilma. *Geophysical Research Letters*, *33*(8).

Oke, P. R., Brassington, G. B., Griffin, D. A., & Schiller, A. (2008). The Bluelink ocean data assimilation system (BODAS). *Ocean modelling*, 21(1-2), 46-70.

Oke, P. R., Griffin, D. A., Schiller, A., Matear, R. J., Fiedler, R., Mansbridge, J., ... & Ridgway, K. (2013). Evaluation of a near-global eddy-resolving ocean model. *Geoscientific model development*, 6(3), 591.

Oliver, E. C., Benthuysen, J. A., Bindoff, N. L., Hobday, A. J., Holbrook, N. J., Mundy, C. N., & Perkins-Kirkpatrick, S. E. (2017). The unprecedented 2015/16 Tasman Sea marine heatwave. *Nature communications*, *8*(1), 1-12.

Oliver, E. C., Donat, M. G., Burrows, M. T., Moore, P. J., Smale, D. A., Alexander, L. V., ... & Holbrook, N. J. (2018). Longer and more frequent marine heatwaves over the past century. *Nature communications*, *9*(1), 1-12.

Park, J. J., Kwon, Y. O., & Price, J. F. (2011). Argo array observation of ocean heat content changes induced by tropical cyclones in the north Pacific. *Journal of Geophysical Research: Oceans*, *116*(C12).

Pasquero, C., & Emanuel, K. (2008). Tropical cyclones and transient upper-ocean warming. *Journal of Climate*, *21*(1), 149-162.

Pearce, A. F., & Feng, M. (2013). The rise and fall of the "marine heat wave" off Western Australia during the summer of 2010/2011. *Journal of Marine Systems*, 111, 139-156.

Pearce, A., & Feng, M. (2007). Observations of warming on the Western Australian continental shelf. *Marine and Freshwater Research*, 58(10), 914-920.

Price, J. F. (1981). Upper ocean response to a hurricane. *Journal of Physical Oceanography*, *11*(2), 153-175.

Price, J. F. (1983). Internal wave wake of a moving storm. Part I. Scales, energy budget and observations. *Journal of Physical Oceanography*, *13*(6), 949-965.

Price, J. F., Morzel, J., & Niiler, P. P. (2008). Warming of SST in the cool wake of a moving hurricane. *Journal of Geophysical Research: Oceans*, *113*(C7).

Price, J. F., Sanford, T. B., & Forristall, G. Z. (1994). Forced stage response to a moving hurricane. *Journal of Physical Oceanography*, *24*(2), 233-260.

Purcell, P. G., & Purcell, R. R. (1988). The North West Shelf, Australia-An Introduction.

Rayson, M. D., Jones, N. L., Ivey, G. N., & Gong, Y. (2021). A Seasonal Harmonic Model for Internal Tide Amplitude Prediction. Journal of Geophysical Research: Oceans, 126(10), [e2021JC017570].

Rayson, M. D., Ivey, G. N., Jones, N. L., Lowe, R. J., Wake, G. W., & McConochie, J. D. (2015). Near-inertial ocean response to tropical cyclone forcing on the

Australian North-West Shelf. *Journal of Geophysical Research: Oceans*, *120*(12), 7722-7751.

Ridgway, K. R., Dunn, J. R., & Wilkin, J. L. (2002). Ocean interpolation by four-dimensional weighted least squares—Application to the waters around Australasia. *Journal of atmospheric and oceanic technology*, 19(9), 1357-1375.

Santoso, A., Sen Gupta, A., & England, M. H. (2010). Genesis of Indian Ocean mixed layer temperature anomalies: A heat budget analysis. *Journal of climate*, 23(20), 5375-5403.

Schiller, A., Brassington, G. B., Oke, P., Cahill, M., Divakaran, P., Entel, M., ... & Zhong, A. (2020). Bluelink ocean forecasting Australia: 15 years of operational ocean service delivery with societal, economic and environmental benefits. *Journal of Operational Oceanography*, 13(1), 1-18.

Seneviratne, S.I., X. Zhang, M. Adnan, W. Badi, C. Dereczynski, A. Di Luca, S. Ghosh, I. Iskandar, J. Kossin, S. Lewis, F. Otto, I. Pinto, M. Satoh, S.M. Vicente-Serrano, M. Wehner, & B. Zhou (2021). Weather and Climate Extreme Events in a Changing Climate. In *Climate Change 2021: The Physical Science Basis*. Contribution of Working Group I to the Sixth Assessment Report of the Intergovernmental Panel on Climate Change [Masson-Delmotte, V., P. Zhai, A. Pirani, S.L. Connors, C. Péan, S. Berger, N. Caud, Y. Chen, L. Goldfarb, M.I. Gomis, M. Huang, K. Leitzell, E. Lonnoy, J.B.R. Matthews, T.K. Maycock, T. Waterfield, O. Yelekçi, R. Yu, and B. Zhou (eds.)]. Cambridge University Press. In Press.

Shay, L. K. (2019). Upper ocean structure: Responses to strong atmospheric forcing events. In *Encyclopedia of ocean sciences* (pp. 86-96). Elsevier.

Shay, L. K., & Elsberry, R. L. (1987). Near-inertial ocean current response to Hurricane Frederic. *Journal of Physical Oceanography*, *17*(8), 1249-1269.

Shay, L. K., Elsberry, R. L., & Black, P. G. (1989). Vertical structure of the ocean current response to a hurricane. *Journal of physical oceanography*, *19*(5), 649-669.

Shay, L. K., Goni, G. J., & Black, P. G. (2000). Effects of a warm oceanic feature on Hurricane Opal. *Monthly Weather Review*, *128*(5), 1366-1383.

Shchepetkin, A. F., & McWilliams, J. C. (2005). The regional oceanic modeling system (ROMS): a split-explicit, free-surface, topography-following-coordinate oceanic model. *Ocean modelling*, 9(4), 347-404.

Smith, R. L., Huyer, A., Godfrey, J. S., & Church, J. A. (1991). The Leeuwin current off western Australia, 1986–1987. *Journal of Physical Oceanography*, 21(2), 323-345.

Smith, R. K., Montgomery, M. T., Kilroy, G., Tang, S., & Müller, S. K. (2015). Tropical low formation during the Australian monsoon: The events of January 2013. *Aust. Meteorol. Oceanogr. J*, *65*, 318-341.

Sprintall, J., Wijffels, S. E., Molcard, R., & Jaya, I. (2009). Direct estimates of the Indonesian Throughflow entering the Indian Ocean: 2004–2006. *Journal of Geophysical Research: Oceans*, *114*(C7).

Sriver, R. L., Goes, M., Mann, M. E., & Keller, K. (2010). Climate response to tropical cyclone-induced ocean mixing in an Earth system model of intermediate complexity. *Journal of Geophysical Research: Oceans*, *115*(C10).

Sriver, R. L., & Huber, M. (2007). Observational evidence for an ocean heat pump induced by tropical cyclones. *Nature*, *447*(7144), 577-580.

Sriver, R. L., Huber, M., & Nusbaumer, J. (2008). Investigating tropical cyclone-climate feedbacks using the TRMM Microwave Imager and the Quick Scatterometer. *Geochemistry, Geophysics, Geosystems*, *9*(9).

Stoney, L., Walsh, K., Babanin, A. V., Ghantous, M., Govekar, P., & Young, I. (2017). Simulated ocean response to tropical cyclones: The effect of a novel parameterization of mixing from unbroken surface waves. *Journal of Advances in Modeling Earth Systems*, 9(2), 759-780.

Stoney, L., Walsh, K. J., Thomas, S., Spence, P., & Babanin, A. V. (2018). Changes in ocean heat content caused by wave-induced mixing in a high-resolution ocean model. *Journal of Physical Oceanography*, 48(5), 1139-1150.

Teague, W. J., Jarosz, E., Wang, D. W., & Mitchell, D. A. (2007). Observed oceanic response over the upper continental slope and outer shelf during Hurricane Ivan. *Journal of Physical Oceanography*, *37*(9), 2181-2206.

Thompson, R. O. (1984). Observations of the Leeuwin current off Western Australia. *Journal of physical oceanography*, 14(3), 623-628.

Tozuka, T., & Oettli, P. (2018). Asymmetric Cloud-Shortwave Radiation-Sea Surface Temperature Feedback of Ningaloo Niño/Niña. *Geophysical Research Letters*, 45(18), 9870-9879.

Van Gastel, P., Ivey, G. N., Meuleners, M. J., Antenucci, J. P., & Fringer, O. (2009). The variability of the large-amplitude internal wave field on the Australian North West Shelf. *Continental Shelf Research*, *29*(11-12), 1373-1383.

Vincent, E. M., Lengaigne, M., Madec, G., Vialard, J., Samson, G., Jourdain, N. C., ... & Jullien, S. (2012). Processes setting the characteristics of sea surface cooling induced by tropical cyclones. *Journal of Geophysical Research: Oceans*, *117*(C2).

Vincent, E. M., Lengaigne, M., Vialard, J., Madec, G., Jourdain, N. C., & Masson, S. (2012). Assessing the oceanic control on the amplitude of sea surface cooling induced by tropical cyclones. *Journal of Geophysical Research: Oceans*, *117*(C5).

Vincent, E. M., Madec, G., Lengaigne, M., Vialard, J., & Koch-Larrouy, A. (2013). Influence of tropical cyclones on sea surface temperature seasonal cycle and ocean heat transport. *Climate dynamics*, *41*(7-8), 2019-2038.

Walsh, K. J., & Ryan, B. F. (2000). Tropical cyclone intensity increase near Australia as a result of climate change. *Journal of Climate*, *13*(16), 3029-3036.

Wang, Y., Kepert, J. D., & Holland, G. J. (2001). The effect of sea spray evaporation on tropical cyclone boundary layer structure and intensity. *Monthly weather review*, 129(10), 2481-2500.

Wang, X., Han, G., Qi, Y., & Li, W. (2011). Impact of barrier layer on typhoon-induced sea surface cooling. *Dynamics of Atmospheres and Oceans*, *52*(3), 367-385.

Wang, X. H., & Zhang, H. (2017). Effects of Australian Summer Monsoon on Sea Surface Temperature Diurnal Variation Over the Australian North-Western Shelf. *Geophysical Research Letters*, 44(19), 9856-9864.

Webster, P. J., Holland, G. J., Curry, J. A., & Chang, H. R. (2005). Changes in tropical cyclone number, duration, and intensity in a warming environment. *Science*, *309*(5742), 1844-1846.

Wernberg, T., Smale, D. A., Tuya, F., Thomsen, M. S., Langlois, T. J., De Bettignies, T., ... & Rousseaux, C. S. (2013). An extreme climatic event alters marine ecosystem structure in a global biodiversity hotspot. *Nature Climate Change*, *3*(1), 78-82.

Wheeler, M. C., & Hendon, H. H. (2004). An all-season real-time multivariate MJO index: Development of an index for monitoring and prediction. *Monthly weather review*, 132(8), 1917-1932.

Wijeratne, S., Pattiaratchi, C., & Proctor, R. (2018). Estimates of surface and subsurface boundary current transport around Australia. *Journal of Geophysical Research: Oceans*, 123(5), 3444-3466.

Wijffels, S., & Meyers, G. (2004). An intersection of oceanic waveguides: Variability in the Indonesian Throughflow region. *Journal of Physical Oceanography*, *34*(5), 1232-1253.

Wijffels, S. E., Meyers, G., & Godfrey, J. S. (2008). A 20-yr average of the Indonesian Throughflow: Regional currents and the interbasin exchange. *Journal of Physical Oceanography*, *38*(9), 1965-1978.

Wilkin, J. L. (2006). The summertime heat budget and circulation of southeast New England shelf waters. *Journal of physical oceanography*, 36(11), 1997-2011.

Wyrtki, K. (1987). Indonesian through flow and the associated pressure gradient. *Journal of Geophysical Research: Oceans*, *92*(C12), 12941-12946.

Xu, J., Lowe, R. J., Ivey, G. N., Jones, N. L., & Zhang, Z. (2018). Contrasting heat budget dynamics during two La Nina marine heat wave events along Northwestern Australia. *Journal of Geophysical Research: Oceans*, 123(2), 1563-1581.

Xu, J., Lowe, R. J., Ivey, G. N., Pattiaratchi, C., Jones, N. L., & Brinkman, R. (2013). Dynamics of the summer shelf circulation and transient upwelling off Ningaloo Reef, Western Australia. *Journal of Geophysical Research: Oceans*, 118(3), 1099-1125.

Zhang, H., Beggs, H., Wang, X. H., Kiss, A. E., & Griffin, C. (2016). Seasonal patterns of SST diurnal variation over the Tropical Warm Pool region. *Journal of Geophysical Research: Oceans*, 121(11), 8077-8094.

Zhang, H., Chen, D., Zhou, L., Liu, X., Ding, T., & Zhou, B. (2016). Upper ocean response to typhoon Kalmaegi (2014). *Journal of Geophysical Research: Oceans*, *121*(8), 6520-6535.

Zhang, H., Wu, R., Chen, D., Liu, X., He, H., Tang, Y., ... & Tian, D. (2018). Net modulation of upper ocean thermal structure by Typhoon Kalmaegi (2014). *Journal of Geophysical Research: Oceans*, *123*(10), 7154-7171.

Zhang, L., Han, W., Li, Y., & Shinoda, T. (2018). Mechanisms for generation and development of the Ningaloo Niño. *Journal of Climate*, 31(22), 9239-9259.

Zhang, N., Feng, M., Hendon, H. H., Hobday, A. J., & Zinke, J. (2017). Opposite polarities of ENSO drive distinct patterns of coral bleaching potentials in the southeast Indian Ocean. *Scientific reports*, 7(1), 1-10.

Zheng, J., Fei, J., Du, T., Wang, Y., Cui, X., Huang, X., & Li, Q. (2008). Effect of sea spray on the numerical simulation of super typhoon ‘Ewiniar’. *Journal of Ocean University of China*, 7(4), 362-372.